Light-Emitting Diodes and Photodetectors

Advances and Future Directions

*Edited by Maurizio Casalino
and Jagannathan Thirumalai*

Light-Emitting Diodes and Photodetectors - Advances and Future Directions

Edited by Maurizio Casalino and Jagannathan Thirumalai

IntechOpen

Supporting open minds since 2005

Contributors

Shenghuang Lin, Haoran Mu, Jian Yuan, Mubashir A. Ahmad, Gul-Faroz Ahmad Malik, Farooq Ahmad Khanday, Maurizio Casalino, Teresa Crisci, Luigi Moretti, Mariano Gioffrè, Saluru Baba Krupanidhi, Karuna Kar Nanda, Deependra Kumar Singh, Basanta Roul, Mikhail E. Belkin, Leonid Zhukov, Dmitriy A. Fofanov, Alexander S. Sigov, Mikhail Vasil'ev, Debashish Nayak, Ram Bilash Choudhary, Muhammad M.A.S. Mahmoud, Salvatore Musumeci

Notice
Statements and opinions expressed in the chapters are these of the individual contributors and not necessarily those of the editors or publisher. No responsibility is accepted for the accuracy of information contained in the published chapters. The publisher assumes no responsibility for any damage or injury to persons or property arising out of the use of any materials, instructions, methods or ideas contained in the book.

We are IntechOpen,
the world's leading publisher of
Open Access books
Built by scientists, for scientists

5,400+
Open access books available

134,000+
International authors and editors

165M+
Downloads

156
Countries delivered to

Our authors are among the
Top 1%
most cited scientists

12.2%
Contributors from top 500 universities

BOOK CITATION INDEX
CLARIVATE ANALYTICS
INDEXED

WEB OF SCIENCE™

Selection of our books indexed in the Book Citation Index
in Web of Science™ Core Collection (BKCI)

Interested in publishing with us?
Contact book.department@intechopen.com

Numbers displayed above are based on latest data collected.
For more information visit www.intechopen.com

Meet the editors

Dr. Maurizio Casalino earned a Ph.D. in Electrical Engineering from the University "Mediterranea" of Reggio Calabria, Italy, after obtaining a laurea (summa cum laude) in Electrical Engineering from University of Naples "Federico II." In 2010, he joined the Institute of Applied Sciences and Intelligent Systems, Naples, as a researcher. He taught Optoelectronics at the University of Calabria from 2009 to 2012, physics of the semiconductors and devices and analog electronics from 2013 to 2021, and from 2020 to 2021, respectively, at the University of Campania "Luigi Vanvitelli". He is the author of more than ninety scientific articles focused on the development of optoelectronic and photonic devices. His research activities have been funded by CNR (National Research Council of Italy), public and external organizations, and the European Community.

Dr. J. Thirumalai received his Ph.D. from Alagappa University, Karaikudi, in 2010. He was awarded a post-doctoral fellowship from Pohang University of Science and Technology (POSTECH), Republic of Korea, in 2013. He worked as an assistant professor of Physics, B.S. Abdur Rahman University, Chennai, India, from 2011 to 2016. Currently, he is Assistant Professor of Physics, SASTRA Deemed University, Kumbakonam (T.N.), India. His research interests focus on luminescence, self-assembled nanomaterials, thin-film optoelectronic devices, and spintronics applications. He has published more than sixty indexed papers and ten book chapters. He has also edited six books. Dr. Thirumalai is a member of several national and international societies. His research activities are funded by the Science and Engineering Research Board (SERB), India.

Contents

Preface

French scientist P. Aigrain introduced the term "photonics" in 1967. This term encompasses light generation (lasers or light-emitting diodes [LEDs]), organic LEDs (OLEDs), light transmission (through free space or guided structures), processing (modulation, switching, etc.), and detection of both light and images. This book examines LEDs/OLEDs and photodetectors (PDs).

Section 1, "Light-Emitting Diodes and Organic Light-Emitting Diodes," includes three chapters discussing recent reviews and important modernizations in evaluating lighting systems. Chapter 1 discusses the operation and mechanisms of OLEDs. Chapter 2 presents an overview of LEDs, including information on their economic benefits and ratings of outdoor high-intensity discharge (HID) lights, smart control of road lighting, and intelligent design of indoor LED lights in industrial buildings. Chapter 3 evaluates LED driver circuits based on different supply sources and power requests.

Section 2, "Photodetectors," includes five chapters presenting recent developments in the photo-detection field. Photodetectors (PDs) are devices able to convert light into a measurable electrical signal, mainly taking advantage of two approaches: 1) the use of the incident photon flux to generate excitons within specific materials and 2) the use of materials characterised by strongly temperature-dependent properties. Chapter 4 reports on silicon (Si) PDs, which have been widely developed in the visible spectrum for the realisation of high-performance complementary metal-oxide semiconductor (CMOS) sensors. Nowadays, Si is becoming an ideal platform for detecting the short-wavelength infrared (SWIR) spectral band thanks to the integration of Si with 2D materials. Chapter 5 discusses 2D materials like transition metal dichalcogenides (TMDs), black phosphorous, silicene, and graphene. It also presents the advances of PDs based on 2D materials and the main heterostructures. Chapter 6 introduces a new type of group-10 noble TMDs (NTMDs) that demonstrate the capability to realize PDs characterized by ultra-broad detection waveband (200 nm to 10.6 μm), fast response time, high responsivity and detectivity, and polarization sensitivity. Chapter 7 describes the evolution in the field of III-nitride semiconductors and their employment to the realization of structures for next-generation PDs. Finally, Chapter 8 presents a comparative study of a long-wavelength vertical cavity surface-emitting laser (LW-VCSEL) adapted to work as a PD and the standard PIN PDs.

This book provides readers with a detailed overview of the most recent advances in the fascinating world of both LEDs and PDs as well as explores some possible future directions in the field. This book is for students and scientists working in the field of photonics and advanced technologies.

We thank all the contributors to this book as well as Anja Filipovic and Mia Vulovic at IntechOpen for their valuable assistance during the preparation and publication of this book.

Dr. Maurizio Casalino
Institute of Applied Science and Intelligent Systems "Eduardo Caianiello",
National Research Council,
Italy

Dr. Jagannathan Thirumalai
Department of Physics,
Srinivasa Ramanujan Centre,
SASTRA Deemed University,
Kumbakonam, Tamil Nadu, India

Section 1

Light Emitting Diodes and Organic Light-Emitting Diodes

Conducting Polymer-Based Emissive Layer on Efficiency of OLEDs

Debashish Nayak and Ram Bilash Choudhary

Abstract

Many changes have arisen in the world of display technologies as time has passed. In the vast area of display technology, Organic light-emitting diode is a recent and exciting discovery. Organic light-emitting diodes (OLEDs) have received a lot of curiosity among the researcher in recent years as the next generation of lighting and displays due to their numerous advantages, such as superior efficiency, mechanical flexibility and stability, chemical versatility, ease of fabrication, and so on. It works on the theory of electroluminescence, which is a mechanism in which electrical energy converts to light energy. Organic LEDs have a thickness of 100 to 500 nanometers or 200 times that of human hair. In OLEDs, organic material can be used in two or three layers. The emissive layer plays a key role in OLEDs. Polymers are used in the emissive layer to enhance the efficiency of OLEDs at the same time self-luminescence materials are used in OLEDs. In displays, this self-illuminating property removes the need for backlighting. Compared to LEDs and LCDs, OLED displays are smaller, lighter, and more portable.

Keywords: Conducting Polymer, recombination, OLEDs, luminescence, emissive layer

1. Introduction

Today, using electronics is so much a part of our daily lives that we rarely imagine what life will be like without them. Electronics and mechanical assets are used in a variety of operations ranging from food to music. Because of the high demand for electrons, chemists, physicists, and other scientists and engineers are developing a plethora of novel organic materials that will change how society views technology [1]. Organic printed electronics are being developed for a variety of applications such as organic light-emitting diodes (OLEDs), organic photovoltaic cells (OPVs), electronic journals, portable electronics, and various sensors [2]. It is anticipated that compact, small, and lightweight devices with cost-effective usability can lead creativity into our lives, making research and development (R&D) in this field highly ambitious and universal [3].

OLEDs, as self-emitting devices, have high image efficiency, are ultra-thin, and light in weight [4]. They have become popular with the general public due to their use in mobile phones such as Samsung's Galaxy, iPhone, etc.. For the time being, OLEDs are mass-produced using an evaporation technique. While this method is

feasible for mass manufacture of small-scale to medium-sized OLED displays, but it is still thought that certain technological and cost challenges remain in the manufacturing of large TV displays. The main feature and efficiency of the OLED device depend on the types of materials used for fabrication.

The research of nanomaterials has recently gained increased interest due to their optical, mechanical, electrical, and chemical properties. Metals, semiconductors, carbon, and polymers are among the materials used to create nanoparticles, nanowires, nanotubes, and nanocomposites. These materials' uses cover optical and electronic instruments, as well as chemical and biomedical areas. Over the last century and a half, new groups of advanced materials known as polymers have been developed and researched, not only challenging the old classical materials but also enabling the creation of new goods that have led to the expansion of mankind's range of activities. Polymers are the foundation of many significant industrial products. Aside from social influences, their exponential rise in production is driven by the need to substitute conventional products. G. J. Berzelius, a Swedish chemist, invented the expression "polymer." He found benzene (C_6H_6) to be an ethyne polymer (C_2H_2). Later, this term underwent a minor change. The concept of polymers is one of the twentieth century's great ideas. It first appeared in the 1920s after much debate, and its acceptance is closely linked with the name of H. Staudinger, who won the Nobel Prize in 1953.

Thus, this chapter intended to describe and discuss the polymers used in OLEDs. Types of conducting polymer used and their synthesis process. Moreover, OLEDs mechanism and their structure. How the emissive layer affects OLEDs and their efficiency are reported. Also, types of OLEDs are used in this era and their benefits in day-to-day life.

2. Organic light emitting diode

OLEDs (organic light-emitting diodes) are innovative developments in the field of optoelectrical systems for modeling next-generation versatile displays and devices that use organic thin film as an electroluminescent diode sensitive to current. There are different types of OLEDs classified below according to their light luminescence properties.

2.1 Types of OLED

There are several types of OLEDs which are used for a different purpose in day to day life. These are classified as, passive matrix, active matrix, transparent, top-emitting, bottom emitting, foldable, white, and phosphorescent OLEDs as shown in **Figure 1** [1].

2.1.1 Passive-matrix OLED (PMOLED)

PMOLEDs include a cathode, organic layers, and anode. The anode and cathode are arranged in the way they are parallel to each other. Light is emitted by the pixel due to the intersections of the cathode and anode. External applied voltage helpful for the specific anode and cathode strips, for specifying which pixels light up and which stay dark. Once again, the light of each pixel is equal to the amount of current added. PMOLEDs are simple to produce, but they use more power than other forms of OLEDs, owing primarily to the power necessary for the external circuitry. PMOLEDs are ideally suited for small displays and are most useful for text and icons.
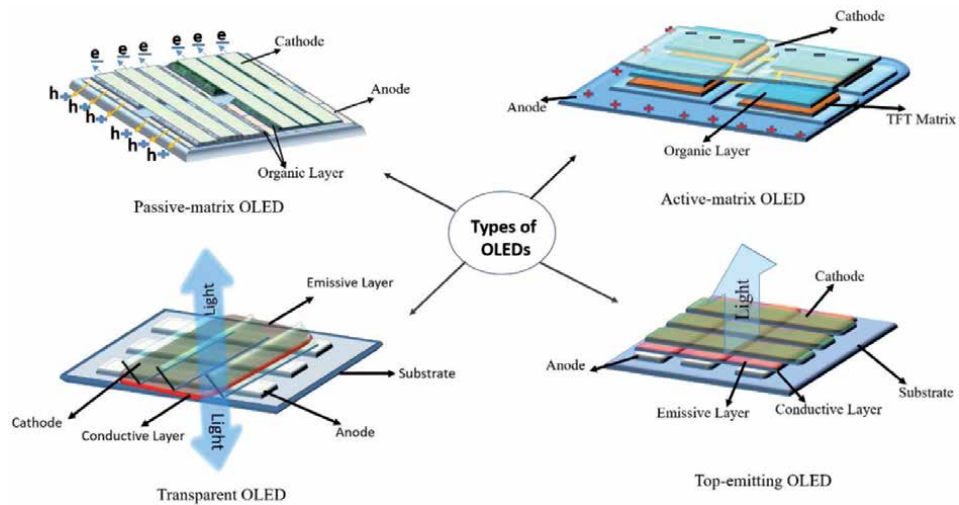
Figure 1.
Schematic diagram of different types of OLEDs [5–8].

2.1.2 Active-matrix OLED (AMOLED)

AMOLEDs include complete layers of a cathode, organic molecules, and anode, but the anode layer is overlaid by a matrix of thin-film transistors (TFTs). The circuitry that decides which pixels are switched on to form an image is the TFT array itself. Since the TFT array consumes less power than other alien electronics. AMOLEDs absorb less power than PMOLEDs, making them ideal for large displays. AMOLEDs also have higher refresh times, making them perfect for the film. Computer displays, large-screen TVs, and electronic signage or billboards are the perfect applications for AMOLEDs.

2.1.3 Transparent OLED (TOLED)

Transparent OLEDs contain translucent components (substrate, cathode, and anode) only, and can be up to 85% transparent when switched off from their substrate. The light will continue in both directions when a clear OLED monitor is enabled. Transparent OLED displays may be either active- or passive-matrix displays. This machine can be used for heads-up displays.

2.1.4 Top-emitting OLED (TEOLED)

The substrates of such OLEDs may be opaque or translucent. Since they are conveniently combined with a non-transparent transistor backplane, they are favored for active-matrix applications. Top-emitting OLED used in smart cards by manufacturers.

2.1.5 Bottom-emitting OLED (BEOLED)

In this type of OLED organic materials are used. BEOLED contains transparent glass, TFT, ITO, an emission layer, and a cathode. Light emits from the bottom of the devices. Manufacture use bottom emitting OLED in smaller as well as larger displays.

2.1.6 Foldable OLED (FOLED)

The substrates of FOLEDs are made of lightweight plastics or metallic foils. They have the benefits of being flexible, durable, and lightweight. Since the material is strong, corrosion and breakage are reduced, so it is used in GPS cameras, cellular phones, and big curved TVs. FOLEDs have many advantages, including higher image resolution and quicker response time. It has implementations in smartphones, GPS receivers, and OLED displays.

2.1.7 White OLED (WOLED)

White OLEDs provide the true color of incandescent lamps that produce brighter white light than fluorescent lights and bulbs that are standard and energization effective. They substitute fluorescent lamps which can reduce energy costs for lighting because they are manufactured in large sheets, are cost-effective, and use less electricity. It fits well for car lighting. White OLEDs are small and light, allowing automobiles to be more lightweight and powerful.

2.1.8 Phosphorescent OLED (PHOLED)

Heat production is minimized by using PHOLEDs. As a result, we will find it in a broad-sized OLED TV or lamps. PHOLEDs can significantly reduce temperature because they are energy-efficient. It also removes the amount of air conditioning needed to remove the heat produced and makes it a key component of a green or environment building strategy. PHOLEDs are used in computer displays, TV screens, and light tables.

2.2 Structure and mechanism of OLEDs

OLEDs operate similarly to traditional diodes and LEDs, but instead of using layers of n-type and p-type semiconductors to contain electrons and holes, they use organic molecules. Eight separate layers consist of an advanced OLED [8]. There are protective glass or acrylic layers on the top and bottom. The upper layer is the seal and the underlying substratum layer. There are a negative terminal and a positive terminal within these layers (called cathode and anode). Finally, two layers between the anode and cathode, the emissive layer (where light is produced). In between the emissive layer and anode, there are two layers to control and ejection of the hole called the hole injection layer and hole transport layer. Similarly, there also two layers in between the emissive layer and cathode called the electron transport layer and blocking layer [9]. **Figure 2** describes the structure and mechanism of OLEDs.

We simply connect a voltage (potential difference) between the anode and cathode to make an OLED light up. The cathode absorbs electrons from the power supply while the energy flows, while the anode loses them (or it "receives holes," if you prefer to look at it that way). An electron from the cathode moves towards the emissive layer through the electron transport layer. At the same time holes moves towards the emissive layer through-hole transport layer. The blocking layer and hole injection layer are used to control the electron and holes. At an emissive layer both electron and hole combined. As a hole (a lack of electron) collides with an electron, the two cancel each other out and emit a fleeting burst of energy in the form of a photon [9]. This is known as recombination, and since it occurs hundreds of times per second, the OLED emits constant light as long as the current flows. Overall, OLED goes through four fundamental steps [11],
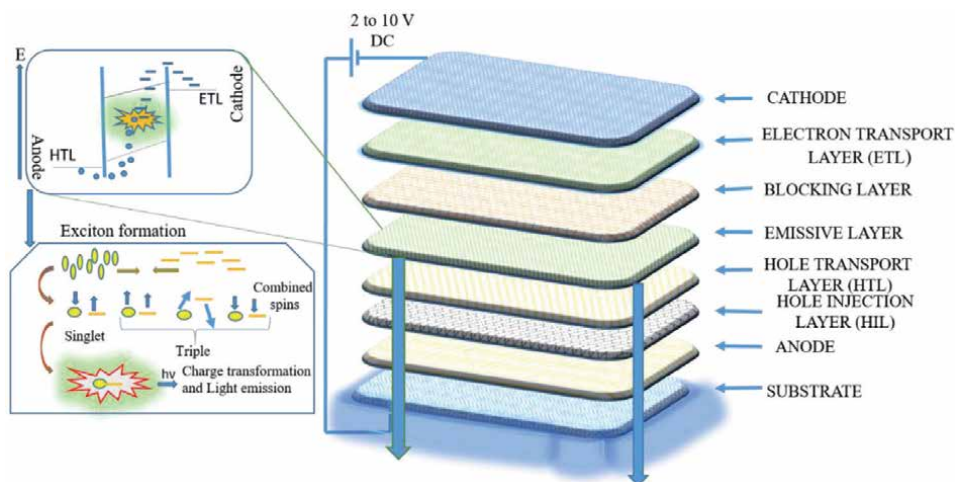
Figure 2.
Schematic diagram of OLEDs and basic process of electroluminescence [10].

   i. Electron and hole injection at the electrodes.

   ii. Charge carriers are transported across the organic layers.

   iii. The shape of electron–hole bound pairs (excitons).

   iv. Radiative exciton decay and light emission.

3. OLED materials

OLEDs are constantly developing and emphasizing the existence of customized functions of organic materials that can be added to well-preserved thin films. As a result, the materials' specifications are diverse, ranging from processability and
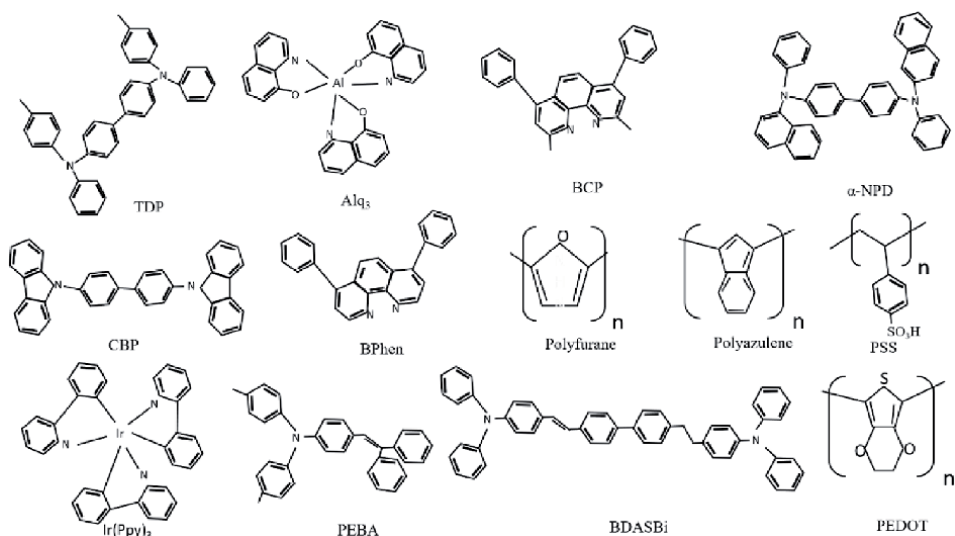
Figure 3.
Types of organic materials used for OLEDs [13].

film formulation to electrical transport, emission, and optical properties [12]. The availability of effective and reliable light emitters over the entire visible spectral spectrum is more important. In this regard, the distinction between fluorescent and phosphorescent materials must be made. The arrival and further creation of emitters based on heavy-metal oriented metal–organic complexes, as seen in **Figure 3**, was a watershed moment. These materials are used in different layers of OLED to enhance properties and efficiency. Powerful spin-orbit coupling in these compounds combines singlet and triplet states even more than in pure hydrocarbons, allowing phosphorescence to become a permitted transfer. Meanwhile, promising efficiency data for OLEDs based on these materials have been published; however, the bottleneck remains the limited supply and stability of deep-blue phosphorescent emitters.

As there are different layers in OLEDs, we need different types of materials for enhancing the properties of OLEDs. The most important layer of the OLEDs is an emissive layer, where recombination takes place and light emits in a specific direction according to device manufacturing.

4. Emissive materials

As seen in **Figure 4**, OLED emissive materials are classified into two groups: small molecules and polymers [8]. Subgroups of the polymer group are known as non-conjugated or conjugated. Small molecule and polymer groups may use dendritic compounds as intermediate materials. Organic material-based electroluminescent (EL) systems have excellent low-power driving voltage and bright emission properties [14]. Tiny molecular organic compounds, conjugated oligomers, and polymers with precise chain lengths are examples of organic light-emitting materials that have distinct electrical and optical properties. The interpretation of the operating process in organic EL devices is dependent on the carrier mobility of organic materials. Conducting polymers must have high conductivity, strong solubility, and mechanical properties. They must also be resistant to acids and bases. Dendrimers are a new kind of polymer that can be used in OLEDs. Bernanose et al. made the first discoveries of electroluminescence of organic materials in the early 1950s [15].
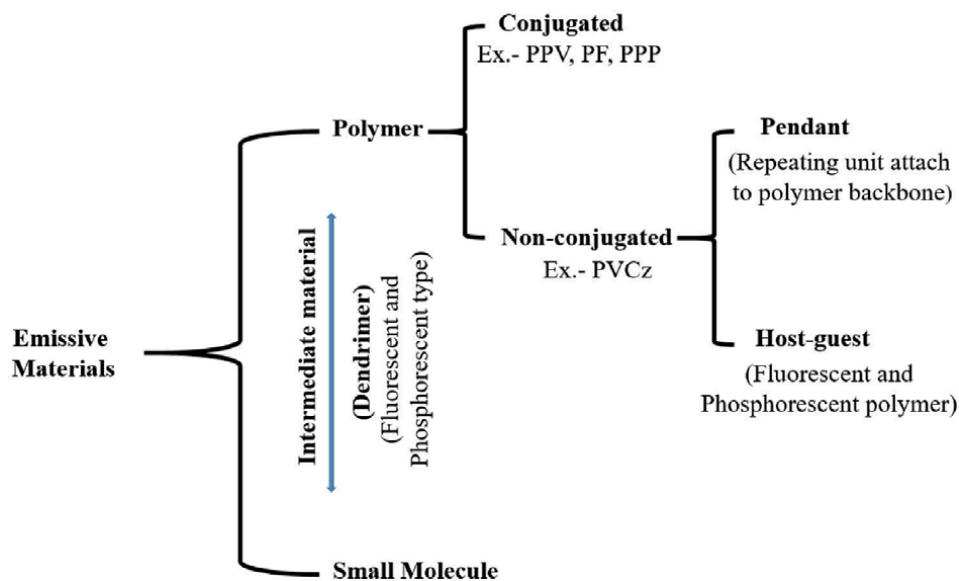

Figure 4.
Schematic classification of emissive materials [16].

4.1 Small molecules

These are materials that are crystalline or semi-crystalline and have high aqueous solubility. Tang et al. were the first to create efficient OLEDs using small molecules [17]. Small molecules have advantages like simple synthesis and purification, and the techniques of vapor deposition allow for the production of complex, high-performance multi-layered layers.

4.2 Polymer used in OLED

The intrinsic versatility of the displays is determined by the material used. Polymers, thin metal tubes, and glass are examples of ductile materials that have been used. Conducting polymers, on the other hand, are more compact, lighter, and less costly. Polymers are widely used material forms for OLEDs because of these advantages [18].

In 1989, a team from Cambridge University discovered electroluminescence (EL) in a conjugated polymer [19]. The system had a very short lifespan of a few minutes and only had a weak emission of 0.1 percent outward quantum efficiency (EQE). After this discovery, the vigorous development of polymer OLED materials and the optimization of system design has started with Sumitomo Chemical Co. Ltd., Covion in Germany, Dow Chemicals in the United States, and Cam-bridge Display Technology (CDT) in the UK. Strong EQE of 51% and a long operational lifespan of many tens of thousands of hours have been reached as the culmination of over 20 years of R&D [20].

Polymer OLEDs, like small-molecule OLEDs, have the following characteristics [15, 21]: (a) high contrast ratio (luminance-on/−off), (b) large viewing angle, (c) bright colors, (d) slim devices, (e) high-speed image switching, and (f) low power consumption. The applicability of a cost-effective fabrication method in mass manufacturing is a noteworthy characteristic of polymer OLEDs.

The color of light emitted by polymers is highly influenced by the form of polymer, its chemical structure, and the existence of the side groups. Thus, a series of soluble luminous polymers that emit from 400 nm to 800 nm across the entire VIS spectrum could be made available by chemical modifications to the polymer structure. A fascinating aspect that affects the colors of light-emitting polymers is the use of emissions additive, also known as dyes. If a small volume of an appropriate dye is applied to a polymer, the energy can be transmitted by light absorption from the dye from the polymer to the dye. Different dyes may be used to adjust the device's color. A blue polymer containing a green dye will emit green light, while a blue polymer containing a red dye will emit red light. When choosing a material for a device, the glass transition temperature (Tg) of the polymer materials is critical. The study of several organic materials as active components is motivated by the need to refine the device's characteristics. Burroughes et al. published a high-quality green light-emitting polymer-based system using poly(p-phenylene vinylene) in 1990, bringing polymer electroluminescence research to a close.

4.2.1 Conducting polymer

In 1976, conductive polymers were discovered. Shirakawa inadvertently produced the first conducting polymer polyacetylene capable of conducting electricity in the mid-1970s. While it was not stable in air, the fact that it could become conductive due to doping has prompted further studies into other recognized conjugated polymers. Many experiments have been conducted on conductive polymers such as Polypyrrole, polythiophene, and polyaniline since 1976 [22].
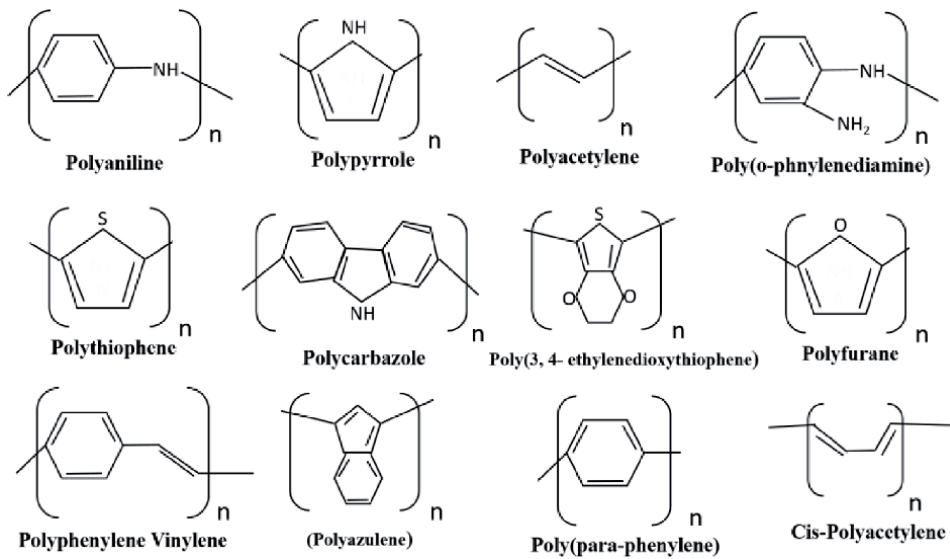
Figure 5.
Chemical structure of conducting polymer [27].

Polymer	Synthesis process	Polymer morphology	Application	Refs.
Polyaniline	1. Chemical oxidation 2. Electrochemical	1. Nanofiber 2. Nanotubes and nanowires	ETL in OLED, FED, OLED	[24, 28]
Polypyrrole	1. Electrochemical	1. Nanotubes and nanowires	FED, OLED, solar cell	[29]
Polyacetylene	RH catalyst	—	Sensor, diode, catalyst.	[30]
Polycarbazole	1. Chemical synthesis, 2. In-situ polymerization 3. Sonochemically	--- 2. Granular 3. Spherical	PH sensor, OLEDs	[31–33]
Polythiophene	1. Solvothermal	—	OLED, Supercapacitor	[34]
Polyfurane	1. Suzuki coupling reaction		OLED, HTL,	[35]
Polyazulene	1. Oxidizing	1. spherical nanoparticle	OLED, electrochemical,	[36]
PEDOT	1. Electrochemical	1. Nanotubes and nanowires	FED, HTL, LED, Diode	[24, 37–39]
	2. In-situ polymerization	2. Nanoflowers		
	3. emulsion droplet electochemisty	3.Nanoparticles		
	4. template-free solution method	4.Nanofibers		

Polymer	Synthesis process	Polymer morphology	Application	Refs.
poly(*p*-phenylene vinylene) (PPV)	1. via witting reaction 2. soluble precursor route 3. electrochemical routes		LEDs, laser, optocouples, triodes, photodiodes, photodetectors.	[40]

Table 1.
Different types of polymer with synthesis process, their morphology, and application.

The Nobel chemistry prize was awarded to MacDiarmid, Shirakawa, and Heeger in 2000 for the discovery and advancement of conducting polymers, demonstrating the significance of driving polymers [23].

Conductive polymers have a backbone that is π-conjugated (alternating single and double bonds), allowing overlapping of bound electrons in the polymeric chain [24]. Through incorporating various electron releasing/withdrawing functional groups into the polymeric backbone and managing the electron–hole injecting/transporting ability of the synthesized conducting polymer, and the conductivity of the polymers can be effectively tuned to achieve emission in the desired luminance range [25]. The creation of charge carriers induces an increase in conductivity. The mechanism of conduction in these polymers is described by a quasi-one-dimensional system and bandgap model. The basic self-localized nonlinear excitation, i.e. a quasi-one-dimensional structure is defined by solitons, polarons, and bipolarons [19, 26]. There are different types of conducting polymer used in OLED shown in **Figure 5**.

Property	Small molecules	Polymers	Dendrimers
Structure	Compact	Noncompact	Compact, globular
Structural control	high	low	Very high
Synthesis	Solution technique	polymerization	Stepwise growth
Shape	Fixed	Random	Spherical
Architecture	Regular	Irregular	Regular
Crystallinity	Semi crystalline/crystalline	Semi crystalline/crystalline	Non crystalline/amorphous
Glass transition temperature		high	low
Aqueous solubility	High	low	High
Nonpolar solubility	high	low	high
Viscosity	Linear relation with a molecular weight	Linear relation with a molecular weight	A nonlinear relationship with a molecular weight
Reactivity	Moderate	low	High
Compressibility		High	low
Polydispersity	Monodisperse	plydisperse	monodisperse

Table 2.
Properties of small molecules, polymer, and dendrimers [8, 41, 42].

4.2.2 Synthesis of conducting polymer

Many researchers have reported different ways for the synthesis of conducting polymer. The structure and properties of the polymer depend on the synthesis process. There are many processes used to increase efficiency, few of them are tabulated in **Table 1**.

4.3 Dendrimers

A light-emitting center is typically connected to one or more branched dendrons in light-emitting dendrimers. Surface groups are bound to the distal end of the dendrons to provide the solubilities needed for solution processing. The center (light emission), branching groups (charge transport), and surface groups can all be modified independently to the dendritic structure (processing properties) tabulated in **Table 2**.

5. Efficiency of OLED

The effectiveness of an OLED depends on a variety of variables including the energy efficiency, the voltage it works with, the recombining efficiency, the number of photons that are released in the photons consumed, and the degree of charge carrier equilibrium injection, etc. Device efficiency can be enhanced by using highly filtered organic complexes to monitor the thickness of the substrate, proper HIL, HTL, ETL, and device structure selection (the process for the co-deposition of the suitable host into organic emission material) [43]. In organic thin-film light-emitting systems, energy transfer from a conductive host to a luminescent dopant can result in high external quantum efficiencies.

5.1 Emission efficiency

The efficiency of OLED emissions can be computed with,

$$\varphi = \gamma \cdot \eta_{e-h} \cdot \varphi \cdot (1-Q)$$

Where φ is electroluminescence quantum efficiency, γ is carrier balance of electrons and holes, η_{e-h} is recombination rate, φ is photoluminescence efficiency and Q is quenching factor by the cathode. Higher photoluminescence and recombination rate, well-controlled electrons and holes injections, and cathode calming removal help to increase OLED efficiency according to the equation.

5.2 Light extraction efficiency

In glass or plastic substratum, the majority of light produced by the OLED will be caught and directed by the waves to the sides; normal, this is about 80% of the total. Current research activities are aimed at different surface treatments that can improve the extraction performance significantly.

5.3 Power efficiency

Power efficiency is one of the amounts that decide how long a mobile unit lives. The efficiency of power is calculated per watt in lumens. The reliability of the power is not influenced only by the device's quantum efficiency, but also by its

voltage [44]. It is therefore critical that low voltages of 3–6 V compared to the load injection barrier be obtained. To provide battery compatibility, this prevents costly voltage up converters.

5.4 Recombination efficiency

Recombination performance normally occurs at or close to unity; i.e., as two charges come close to each other, they are guaranteed to destroy each other. However, if the destruction mechanism does not have energetic obstacles, then quantum spin figures show that, if the state has a single multiplicity, only 25% of the resulting excited states are useful. Though spin emissions in organic molecules are prohibited, progress was made in the development of three-state emitters which contain at least one atom with higher atomic weight. The excited state still will decay not radioactively, even though spin is permitted.

5.5 Luminous efficiency

Three parameters reflect OLED's luminous performance: quantum efficiency, lighting quality and efficiency. Quantum performance can be split into internal quantum performance and external quantum performance [45]. The external quantum efficiency η_{ext} corresponds to the proportion of photons (N_P) released by the OLED in a given direction to the amount of injected (N_C) electrons. OLED is a multilayer structure and the waveguide effect is responsible for absorbs or loses light. The inner quantum efficiency η_{int} corresponds to the real device's luminous effectiveness. The ratio of both reflects the η_C coefficient of optical coupling outside the apparatus in a certain direction.

5.6 Way to increase the efficiency

There are several ways to enhance the efficiency of OLED described below,
Efficiency of OLEDs is reduced since the light emission of undoped systems is only accountable in single states. Recent advances in the collection of the triplets using phosphorescent materials have resulted in increased performance and color selectivity. To produce the primary colors required for display applications, the electric phosphorescence achieved by doping organic metallic phosphorus in a host was successfully used [46].
The doping of the emissive layer of an OLED has been widely used to improve performance, durability, and color. Tang et al., used fluorescent dyes, 3-(2-benzothiazolyl)-7-diethylaminocoumarine (coumarin 540), and DCMs were first developed dopant in Alq3 in 1989 to increase system effectiveness and color purity [47].
Endothermic energy transfer from a molecular organic host (donor) to organo-metallic phosphors (trap) can lead to high-efficiency electron lighting.
One of the most important factors restricting the external quantic power of devices is the low extraction of light and hence improved coupling methods for improved efficiency. In wave directed modes, almost 80% of the light provided by the OLED is lost in the radiation optics because of glass substrates and ITO/organism content, i.e. the majority of light produced is either stuck in or out of the edges of an OLED in the glass substratum or the system [48]. Various light refracting and dispersal approaches to reducing TIR at the interface have been identified to remove the trapped and wave-driven light into external modes, like using the shaped substitute, micro-lenses used on the backside of a substratum are used as a spreading medium and high-refractive-index substrate form the silica micro-sheet [49].

The other method is to inject a very low refractive index of silica aerogels between the glass substrates and the translucent ITO electrode.

6. Advantages

Organic materials, such as OLEDs, have a broad range of uses in electronics due to several advantages, including [50]:

i. Incorporation of versatility by nature-organic synthetic processing has limitless precision in terms of molecule packing and macroscopic properties, (ii) solid-state system that is very small, (iii) lightweight- unlike glass displays in LCD applications, (iv) the substrates are shattered resistant, (v) luminous power efficiency is very high. Other than this there are more benefits described below,

An element of inactive OLED does not generate light or consume fuel to make true blacks. With a quick response time, you can create amusing animations. For the quickest color transfer, LCDs can achieve reaction times as low as 1 ms. Response times for OLEDs are 1000 times higher than 10 microsecond LCD response times. The viewing angle is wide. - OLEDs have a larger viewing range than LCDs because the pixels in OLEDs transmit light directly. The colors tend to be right. As it is self-emitting, there is no need for a backlight source. Color correction for full-color screens. Flexibility – OLED displays are made on flexible plastic substrates, which generate flexible organic LEDs. Cost benefits over inorganic systems- OLEDs are less expensive than LCD or plasma screens. Power use is minimal.

OLEDs use much less power than LCDs because they do not need backlighting. OLEDs are less expensive to make, and since they are made of plastic, they can be made into wide and thin sheets. Video files are more realistic and up-to-date as OLEDs reload quicker than LCDs.

6.1 Current status and future OLED applications

OLEDs are currently used in small-screen applications such as mobile phones, digital cameras, and PDAs. Sony Corporation revealed in September 2004 that it would begin mass production of OLED displays for its CLIE PEG-VZ90 brand of personal entertainment handhelds. In March 2003, Kodak was the first to introduce a compact camera with an OLED view, the Easy Share LS633 [source: Kodak press release]. Several firms have already developed prototype OLED computer displays and large-screen TVs. Samsung Electronics revealed in May 2005 that it had created a prototype 40-inch OLED-based ultra-slim TV, the first of its kind [source: Kanellos]. Also, Sony revealed in October 2007 that it would be the first to market for an OLED television. Customers in Japan will be able to buy the XEL-1 in December 2007. It is priced at 200,000 Yen (approximately $1,700 USD, nearly 1.4 lakh in INR) [source: Sony].

OLEDs have a wide range of applications that we see in our everyday lives. To create digital displays for televisions, mobile phones, PDAs, monitors, car radios, and digital cameras. OLEDs have a wide range of applications in lighting, such as the LUMIBLADE OLED samples developed by Philips. Similarly, in 2011, novaled AG, based in Germany, released the Victory OLED desk lamps. It's used in watches. A fossil (JR-9465) and Diesel (DZ7086) were used for OLED displays. MCC of Mitsubishi Chemical Holdings in 2014 developed a 30,000-hour OLED panel which is twice the lifetime of conventional OLED panels. OLEDs have taken the place of

CRTs (Cathode Ray Tubes) or LCDs (Liquid Crystal Display). Based on a white emitter, Samsung electronics produced full-color AMOLED displays. Top-emission systems provide advantages in the manufacture of TFT-OLED displays.

OLED technology and development are advancing steadily, which may lead to potential developments of heads-up displays, vehicle dashboards, billboard-type displays, home and office lighting, and modular displays [51]. As the rate of OLEDs is almost 1,000 times higher than that of LCDs, an OLED device can almost change data in real-time. More detailed videos and daily revisions should be made. The newspaper of the future could be an OLED show that updates with breaking news (think "Minority Report") – then, like a normal newspaper, you could fold it up and stuff it in your bag or briefcase when you are finished reading it.

7. Conclusions

Organic light-emitting diodes, which are more energy consuming, allow computer display more comfortable. OLED is so groundbreaking that it is being celebrated as the first invention since Edison in the field of illumination. Today, OLED technology is commonly considered to be the next-generation flat panel display component and will play an important role in the development of flexible displays. They are more compact and thinner than the crystalline layers in an LED or LCD. They have wide fields of view and they generate their light. We can improve efficiency by taking some precautions and by using appropriate polymers.

This chapter has seen the different types of OLEDs that have been implemented to date in order to increase their functionality and serve various purposes. The operation and mechanisms of oleds are discussed. The output of OLEDs is dependent on their layers, with the emissive layer playing a critical role. Various formulations are used for the emissive coating, depending on the material's properties. A number of factors must influence lead performance, which can be improved with some tweaking. At the moment, OLEDs are gaining popularity for the future transforming age, and many more studies are being conducted to achieve remarkable performance.

Acknowledgements

Conflict of interest

"The authors declare no conflict of interest."

Author details

Debashish Nayak* and Ram Bilash Choudhary
Nano Structured Composite Materials Laboratory, Indian Institute of Technology
(Indian School of Mines), Dhanbad, Jharkhand, India

*Address all correspondence to: debashishiitism@gmail.com

IntechOpen

References

[1] N. Thejo Kalyani and S. J. Dhoble, "Organic light emitting diodes: Energy saving lighting technology—A review," Renew. Sustain. Energy Rev., vol. 16, no. 5, pp. 2696-2723, Jun. 2012, doi: 10.1016/j.rser.2012.02.021.

[2] D. Li, H. Zhang, and Y. Wang, "Four-coordinate organoboron compounds for organic light-emitting diodes (OLEDs)," Chem. Soc. Rev., vol. 42, no. 21, p. 8416, 2013, doi: 10.1039/c3cs60170f.

[3] F. Dumur, "Zinc complexes in OLEDs: An overview," Synth. Met., vol. 195, pp. 241-251, Sep. 2014, doi: 10.1016/j.synthmet.2014.06.018.

[4] S. Lee, J.-H. Han, S.-H. Lee, G.-H. Baek, and J.-S. Park, "Review of Organic/Inorganic Thin Film Encapsulation by Atomic Layer Deposition for a Flexible OLED Display," JOM, vol. 71, no. 1, pp. 197-211, Jan. 2019, doi: 10.1007/s11837-018-3150-3.

[5] P. K. Uttwani, B. C. Villari, K. N. N. Unni, R. Singh, A. Awasthi, and Deepak, "Detection of Physical Defects in Full Color Passive-Matrix OLED Display by Image Driving Techniques," J. Disp. Technol., vol. 8, no. 3, pp. 154-161, Mar. 2012, doi: 10.1109/JDT.2011.2168805.

[6] G. R. Chaji and A. Nathan, "Parallel Addressing Scheme for Voltage-Programmed Active-Matrix OLED Displays," IEEE Trans. Electron Devices, vol. 54, no. 5, pp. 1095-1100, May 2007, doi: 10.1109/TED.2007.894608.

[7] H. Zhu, Z. Fang, C. Preston, Y. Li, and L. Hu, "Transparent paper: fabrications, properties, and device applications," Energy Environ. Sci., vol. 7, no. 1, pp. 269-287, 2014, doi: 10.1039/C3EE43024C.

[8] N. Thejokalyani and S. J. Dhoble, "Novel approaches for energy efficient solid state lighting by RGB organic light emitting diodes – A review," Renew. Sustain. Energy Rev., vol. 32, pp. 448-467, Apr. 2014, doi: 10.1016/j.rser.2014.01.013.

[9] N. Sain, D. Sharma, and P. Choudhary, "A REVIEW PAPER ON: ORGANIC LIGHT-EMITTING DIODE (OLED) TECHNOLOGY AND APPLICATIONS," Int. J. Eng. Appl. Sci. Technol., vol. 04, no. 11, pp. 587-591, Apr. 2020, doi: 10.33564/IJEAST.2020.v04i11.103.

[10] M. L. P. Reddy and K. S. Bejoymohandas, "Evolution of 2, 3′-bipyridine class of cyclometalating ligands as efficient phosphorescent iridium(III) emitters for applications in organic light emitting diodes," J. Photochem. Photobiol. C Photochem. Rev., vol. 29, pp. 29-47, Dec. 2016, doi: 10.1016/j.jphotochemrev.2016.10.001.

[11] S.-J. Zou, Y. Shen, F.-M. Xie, J.-D. Chen, Y.-Q. Li, and J.-X. Tang, "Recent advances in organic light-emitting diodes: toward smart lighting and displays," Mater. Chem. Front., vol. 4, no. 3, pp. 788-820, 2020, doi: 10.1039/C9QM00716D.

[12] A. P. Kulkarni, C. J. Tonzola, A. Babel, and S. A. Jenekhe, "Electron Transport Materials for Organic Light-Emitting Diodes," Chem. Mater., vol. 16, no. 23, pp. 4556-4573, Nov. 2004, doi: 10.1021/cm049473l.

[13] J.-H. Jou, S. Kumar, A. Agrawal, T.-H. Li, and S. Sahoo, "Approaches for fabricating high efficiency organic light emitting diodes," J. Mater. Chem. C, vol. 3, no. 13, pp. 2974-3002, 2015, doi: 10.1039/C4TC02495H.

[14] T. Tsutsui, H. Tokuhisa, and M. Era, "Charge carrier mobilities in molecular materials for electroluminescent diodes," Apr. 1998, p. 230, doi: 10.1117/12.305425.

[15] A. Bernanose, "Electroluminescence of organic compounds," Br. J. Appl.

Phys., vol. 6, no. S4, pp. S54–S55, Jan. 1955, doi: 10.1088/0508-3443/6/S4/319.

[16] C. Sekine, Y. Tsubata, T. Yamada, M. Kitano, and S. Doi, "Recent progress of high performance polymer OLED and OPV materials for organic printed electronics," Sci. Technol. Adv. Mater., vol. 15, no. 3, p. 034203, Jun. 2014, doi: 10.1088/1468-6996/15/3/034203.

[17] C. W. Tang and S. A. VanSlyke, "Organic electroluminescent diodes," Appl. Phys. Lett., vol. 51, no. 12, pp. 913-915, Sep. 1987, doi: 10.1063/1.98799.

[18] C. Zhan, G. Yu, Y. Lu, L. Wang, E. Wujcik, and S. Wei, "Conductive polymer nanocomposites: a critical review of modern advanced devices," J. Mater. Chem. C, vol. 5, no. 7, pp. 1569-1585, 2017, doi: 10.1039/C6TC04269D.

[19] J. H. Burroughes *et al.*, "Light-emitting diodes based on conjugated polymers," Nature, vol. 347, no. 6293, pp. 539-541, Oct. 1990, doi: 10.1038/347539a0.

[20] S. P. Mucur, T. A. Tumay, S. E. San, and E. Tekin, "Enhancing effects of nanoparticles on polymer-OLED performances," J. Nanoparticle Res., vol. 14, no. 10, p. 1214, Oct. 2012, doi: 10.1007/s11051-012-1214-9.

[21] M. Y. Wong, "Recent Advances in Polymer Organic Light-Emitting Diodes (PLED) Using Non-conjugated Polymers as the Emitting Layer and Contrasting Them with Conjugated Counterparts," J. Electron. Mater., vol. 46, no. 11, pp. 6246-6281, Nov. 2017, doi: 10.1007/s11664-017-5702-7.

[22] R. Balint, N. J. Cassidy, and S. H. Cartmell, "Conductive polymers: Towards a smart biomaterial for tissue engineering," Acta Biomater., vol. 10, no. 6, pp. 2341-2353, Jun. 2014, doi: 10.1016/j.actbio.2014.02.015.

[23] M. S. AlSalhi, J. Alam, L. A. Dass, and M. Raja, "Recent Advances in Conjugated Polymers for Light Emitting Devices," Int. J. Mol. Sci., vol. 12, no. 3, pp. 2036-2054, Mar. 2011, doi: 10.3390/ijms12032036.

[24] B. H. Kim, D. H. Park, J. Joo, S. G. Yu, and S. H. Lee, "Synthesis, characteristics, and field emission of doped and de-doped polypyrrole, polyaniline, poly(3,4-ethylenedioxythiophene) nanotubes and nanowires," Synth. Met., vol. 150, no. 3, pp. 279-284, May 2005, doi: 10.1016/j.synthmet.2005.02.012.

[25] H. L. Smith *et al.*, "n-Doping of a Low-Electron-Affinity Polymer Used as an Electron-Transport Layer in Organic Light-Emitting Diodes," Adv. Funct. Mater., vol. 30, no. 17, p. 2000328, Apr. 2020, doi: 10.1002/adfm.202000328.

[26] D. Feldman, "Polymer History," Des. Monomers Polym., vol. 11, no. 1, pp. 1-15, Jan. 2008, doi: 10.1163/156855508X292383.

[27] D. S. Correa, E. S. Medeiros, J. E. Oliveira, L. G. Paterno, and L. H. C. Mattoso, "Nanostructured Conjugated Polymers in Chemical Sensors: Synthesis, Properties and Applications," J. Nanosci. Nanotechnol., vol. 14, no. 9, pp. 6509-6527, Sep. 2014, doi: 10.1166/jnn.2014.9362.

[28] R. Kandulna and R. B. Choudhary, "Robust electron transport properties of PANI/PPY/ZnO polymeric nano-composites for OLED applications," *Optik (Stuttg).*, vol. 144, pp. 40-48, Sep. 2017, doi: 10.1016/j.ijleo.2017.06.094.

[29] R. Singh, R. B. Choudhary, and R. Kandulna, "Delocalization of π electrons and trapping action of ZnO nanoparticles in PPY matrix for hybrid solar cell application," J. Mol. Struct., vol. 1156, pp. 633-644, Mar. 2018, doi: 10.1016/j.molstruc.2017.12.013.

[30] B. Koz, B. Kiskan, and Y. Yagci, "Synthesis and Characterization of Polyacetylene with Side-chain

Thiophene Functionality," Int. J. Mol. Sci., vol. 9, no. 3, pp. 383-393, Mar. 2008, doi: 10.3390/ijms9030383.

[31] B. Gupta, R. Prakash, and A. Melvin, "Chemical Synthesis of Polycarbazole (PCz), modification and pH sensor application," in *2012 Sixth International Conference on Sensing Technology (ICST)*, Dec. 2012, pp. 365-369, doi: 10.1109/ICSensT.2012.6461702.

[32] U. Baig, W. A. Wani, and L. Ting Hun, "Facile synthesis of an electrically conductive polycarbazole–zirconium(IV) phosphate cation exchange nano-composite and its room temperature ammonia sensing performance," New J. Chem., vol. 39, no. 9, pp. 6882-6891, 2015, doi: 10.1039/C5NJ01029B.

[33] U. Riaz, S. M. Ashraf, T. Fatima, and S. Jadoun, "Tuning the spectral, morphological and photophysical properties of sonochemically synthesized poly(carbazole) using acid Orange, fluorescein and rhodamine 6G," Spectrochim. Acta Part A Mol. Biomol. Spectrosc., vol. 173, pp. 986-993, Feb. 2017, doi: 10.1016/j.saa.2016.11.003.

[34] J. Ohshita, Y. Tada, A. Kunai, Y. Harima, and Y. Kunugi, "Hole-injection properties of annealed polythiophene films to replace PEDOT–PSS in multilayered OLED systems," Synth. Met., vol. 159, no. 3-4, pp. 214-217, Feb. 2009, doi: 10.1016/j.synthmet.2008.09.002.

[35] S. P. Mucur, C. Kök, H. Bilgili, B. Canımkurbey, and S. Koyuncu, "Conventional and inverted organic light emitting diodes based on bright green emmisive polyfluorene derivatives," *Polymer (Guildf).*, vol. 151, pp. 101-107, Aug. 2018, doi: 10.1016/j.polymer.2018.07.063.

[36] E. Grądzka, P. Makowska, and K. Winkler, "Chemically formed conducting polyazulene: From micro- to nanostructures," Synth. Met., vol. 246,

pp. 115-121, Dec. 2018, doi: 10.1016/j.synthmet.2018.10.002.

[37] S. Kirchmeyer and K. Reuter, "Scientific importance, properties and growing applications of poly(3,4-ethylenedioxythiophene)," J. Mater. Chem., vol. 15, no. 21, p. 2077, 2005, doi: 10.1039/b417803n.

[38] M. W. Lee, D.-J. Kwon, J. Park, J.-C. Pyun, Y.-J. Kim, and H. S. Ahn, "Electropolymerization in a confined nanospace: synthesis of PEDOT nanoparticles in emulsion droplet reactors," Chem. Commun., vol. 56, no. 67, pp. 9624-9627, 2020, doi: 10.1039/D0CC03834B.

[39] Q. Zhao, R. Jamal, L. Zhang, M. Wang, and T. Abdiryim, "The structure and properties of PEDOT synthesized by template-free solution method," Nanoscale Res. Lett., vol. 9, no. 1, p. 557, 2014, doi: 10.1186/1556-276X-9-557.

[40] J. Gruber, R. W. Chia Li, and I. A. Hümmelgen, "Synthesis, properties, and applications of poly(p-phenylene vinylene)S," in *Handbook of Advanced Electronic and Photonic Materials and Devices*, Elsevier, 2001, pp. 163-184.

[41] G. Franc *et al.*, "Synthesis and Properties of Dendrimers Possessing the Same Fluorophore(s) Located Either Peripherally or Off-Center," J. Org. Chem., vol. 72, no. 23, pp. 8707-8715, Nov. 2007, doi: 10.1021/jo701462f.

[42] O. Nuyken, S. Jungermann, V. Wiederhirn, E. Bacher, and K. Meerholz, "Modern Trends in Organic Light-Emitting Devices (OLEDs)," Monatshefte für Chemie - Chem. Mon., vol. 137, no. 7, pp. 811-824, Jul. 2006, doi: 10.1007/s00706-006-0490-4.

[43] W. Brütting, J. Frischeisen, T. D. Schmidt, B. J. Scholz, and C. Mayr, "Device efficiency of organic light-emitting diodes: Progress by improved light outcoupling," Phys. status solidi,

vol. 210, no. 1, pp. 44-65, Jan. 2013, doi: 10.1002/pssa.201228320.

[44] H.-W. Chen, J.-H. Lee, B.-Y. Lin, S. Chen, and S.-T. Wu, "Liquid crystal display and organic light-emitting diode display: present status and future perspectives," Light Sci. Appl., vol. 7, no. 3, pp. 17168-17168, Mar. 2018, doi: 10.1038/lsa.2017.168.

[45] N. Sun, C. Jiang, Q. Li, D. Tan, S. Bi, and J. Song, "Performance of OLED under mechanical strain: a review," J. Mater. Sci. Mater. Electron., vol. 31, no. 23, pp. 20688-20729, Dec. 2020, doi: 10.1007/s10854-020-04652-5.

[46] R. J. Holmes *et al.*, "Blue organic electrophosphorescence using exothermic host–guest energy transfer," Appl. Phys. Lett., vol. 82, no. 15, pp. 2422-2424, Apr. 2003, doi: 10.1063/1.1568146.

[47] C. W. Tang, S. A. VanSlyke, and C. H. Chen, "Electroluminescence of doped organic thin films," J. Appl. Phys., vol. 65, no. 9, pp. 3610-3616, May 1989, doi: 10.1063/1.343409.

[48] B. W. D'Andrade, J. Brooks, V. Adamovich, M. E. Thompson, and S. R. Forrest, "White Light Emission Using Triplet Excimers in Electrophosphorescent Organic Light-Emitting Devices," *Adv. Mater.*, vol. 14, no. 15, p. 1032, Aug. 2002, doi: 10.1002/1521-4095 (20020805)14:15<1032::AID-ADMA1032>3.0.CO;2-6.

[49] K. Neyts and A. Ullan Nieto, "Importance of scattering and absorption for the outcoupling efficiency in organic light-emitting devices," J. Opt. Soc. Am. A, vol. 23, no. 5, p. 1201, May 2006, doi: 10.1364/JOSAA.23.001201.

[50] N. 2018. W. 17 A. 2021. <https://www. ukessays. com/essays/engineering/advantages-and-disadvantages-of-organic-light-emitting-diodes-engineering-essay. php?vref=1. "Advantages And Disadvantages Of Organic Light Emitting Diodes Engineering Essay." UKEssays. ukessays. com, "No Title."

[51] J.-H. Lee *et al.*, "Blue organic light-emitting diodes: current status, challenges, and future outlook," *J. Mater. Chem. C*, vol. 7, no. 20, pp. 5874-5888, 2019, doi: 10.1039/C9TC00204A.

Economic Applications for LED Lights in Industrial Sectors

Muhammad M.A.S. Mahmoud

Abstract

After the Introduction, which discuss the main advantages and disadvantage of LED from Economics angle, the entire Chapter is presented in three sections. The first section discusses the economic benefits of replacing different types and rating of outdoor HID lights, typically installed in an industrial plant, with LED lighting. The section determines important economic indicators to evaluate direct and indirect benefits that can be achieved from using LED lights. In second section an efficient, safe and cost effective design to automate LED lighting system used for long roads with low-traffic is provided. The section provides smart control using image recognition for cost saving of road lighting operation and gives economic analysis for this lighting system. In third section, design of intelligent daylight utilization to achieve efficient indoor lighting intensity control for LED lights that are used in industrial building is provided. Comprehensive evaluation of the lighting system economics is discussed.

Keywords: LED economics, LED verses HID, lighting economic norm, control technology with LED, LED in industrial application smart road lighting

1. Introduction

Light emitting diodes are rapidly developing in light output, color rendering, efficiency, and reliability. Achieving good level of maintenance-free in harsh environment, while keeping product competitive, is the largest challenge which only few manufacturers manage to achieve. The latest high quality LED technologies are already exceeding all other available technologies by all technical parameters. According to its numerous advantages, even higher initial cost quickly pays for itself due to vastly reduced cost of electricity and maintenance. But to fully benefit from the outstanding advantages it is important to educate and recognize the difference between low quality and latest state of the art LED technologies, since low quality LED alternatives have quickly spread all over the world [1, 2].

1.1 General advantages of high quality LED lights

1.1.1 Less energy consumption

LED lights use 40–80% less electricity and have at least 5 times the life expectancy than regular High Pressure Sodium (HPS) fixtures. LED lamps are 7 times more energy efficient than incandescent and twice as efficient as fluorescent lamps.

1.1.2 Higher efficiency and low light pollution due to directional light

LED lights with a lower lumen output can replace conventional lamps with a higher output. For example, a 30 W LED street light can often replace an 80 W High Pressure Sodium lamp. The reason for this is directionality. LED street lamps are very directional and the light output is much more than other street lamps. Also there is little or no hot spot under the LED lamp. The light emitted from the LED lamp is directed downwards, spread throughout the entire area it covers. This means that a lower amount of light is needed to properly illuminate the area. This also dramatically reduces glare and light pollution which affects the mood of human beings, navigation in birds and insects, mating behavior in animals and flowering in plants.

1.1.3 Long life: up to 100.000 hours

LED lights last much longer than conventional lamps (4 to 8 times longer). This result in less expense in replacing the lights themselves but also the labor to replace the lamp is needed less often. This provides a great cost savings by itself.

Also the loss of brightness or lumen depreciation is slower over the life of an LED lamp than that of sodium or other lamp. So not only does the LED have a longer life span than the conventional lamp, but it stays brighter longer than other lamps. The long life span reduces maintenance expenses and makes these bulbs particularly suitable for difficult to reach locations and for streetlights where main-tenance costs can be significant.

Lifetime and Lumen maintenance compression between LED and HID lights is illustrated in **Figure** 1. The comparison shows that relamping of HID fixture is required to be done 5 times to achieved one base life time of LED, considering the relamping is required when the Lumen reduces to 70% of initial lamp Lumen [1].

1.1.4 Great operating characteristics

LED operates at efficiently at low and high temperatures, and unaffected by on/off cycling. This makes them safer and efficient in special indoor applications such
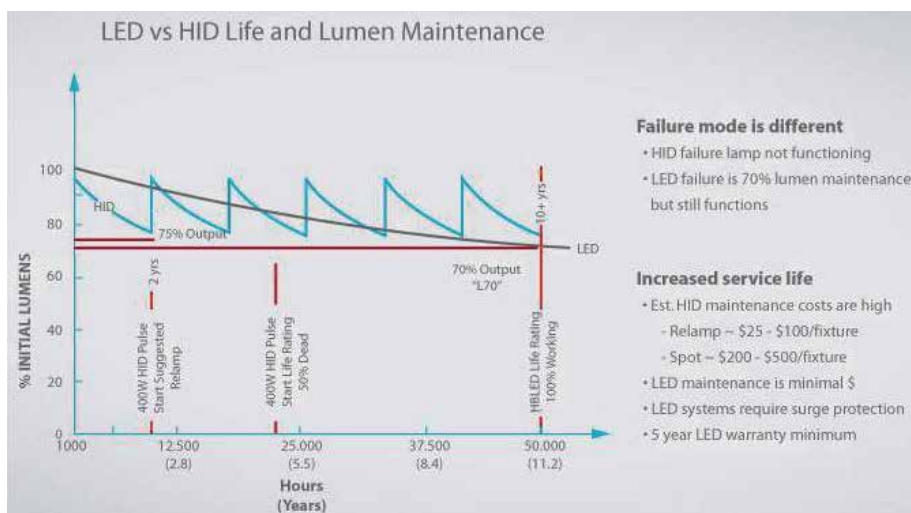

Figure 1.
Lifetime and lumen maintenance compression between LED and HID.

as refrigerator lights, cold room lights, offices, industrial plants and better for applications requiring frequent switching on and off lights. These bulbs are shocks and vibrations resistant making them the best choice for places like offshore platforms, oil refineries, steel factors, skids and similar applications.

1.1.5 Easily controllable

The light is easily controllable with intelligent systems. The light can be turned on and off instantly and can be dimmed for added energy savings at dawn, dusk, and also during hours of low traffic. Switching on–off and dimming does not affect the life-time of the luminaire as in the case of fluorescent lights.

1.1.6 Reducing carbon footprint

The carbon footprint of LED street lights is smaller than other lights due to lower energy usage. Moreover, LEDs last 4 to 8 times longer than any other bulbs, further reducing the carbon footprint of manufacture over the life time. From another angle, wide range application of LED in a country my give better chance to sale there international quota in CO_2 emission to other countries.

1.1.7 Dark-sky friendly

Because of the directional light, light is carefully distributed exactly where it is meant to go and therefore there is no or little light which is wasted by illuminating the night sky or very low background light contribution. This is a considerable plus especially if the local community has a Dark-sky Initiative.

1.1.8 Natural light specter: Color rendering index

It is worth to mention here that for example LED street lamps with color temperature 3.500–4.200 K are rendering more natural light than the yellow of sodium lamps or green of fluorescent streetlights. Also no UV or IR radiation is emitted from the LED street lamps. Color rendering index (CRI) is high (80–90) and displays natural colors of illuminated objects. This reflect actual color of the objects.

1.1.9 Free of harmful substances and lower environmental impact

LED luminaires contain no harmful substances, like mercury, lead or other hazardous chemical and gasses. Spent LED lamps can be thrown away without any special handling or disposal requirement, since they are recyclable and environmentally friendly. Other lighting bulbs often have hazardous materials such as lead and mercury which require special handling and waste management procedures which have both economic and environmental costs.

1.2 International and National Directives

European Commission issued the Regulations EC No. 245/2009 for tertiary lighting products on 18 March 2009. On the basis of these Regulations, about 1 billion lighting products have to be replaced by LED type by the year 2015 only in the area of the EU, which translates to 100 million street lamps for street lighting and industry. The remaining 900 million refer to neon lamps.

Similarly, the Energy Information and Security Act of 2007 began the process of restricting the sale of inefficient lamps in the US. By 2012, with a few exceptions, the result of the legislation will be that inefficient incandescent lamps cannot be sold [1].

2. Economic benefits of replacing different types and rating of outdoor HID lights by LED

2.1 Survey and problem definition

High-intensity discharge lamps (HID lamps) are a type of electrical gas-discharge lamp which produces light by means of an electric arc between tungsten electrodes housed inside a translucent or transparent fused quartz or fused alumina arc tube. This tube is filled with noble gas and often also contains suitable metal or metal salts. The noble gas enables the arc's initial strike. Once the arc is started, it heats and evaporates the metallic admixture. Its presence in the arc plasma greatly increases the intensity of visible light produced by the arc for a given power input, as the metals have many emission spectral lines in the visible part of the spectrum.

Many lighting application use HID bulbs for the main lighting systems, although some applications are now moving from HID bulbs to LED because of the LED advantages [2].

By about 2010 LED technology came to dominate the outdoor lighting industry; earlier LEDs were not bright enough for outdoor lighting. A study completed in 2014 concluded that color temperature and accuracy of LED lights was easily recognized by consumers, with preference towards LEDs at natural color temperatures [3]. LEDs are now able to match the brightness and warmer color temperature that consumers desire from their outdoor lighting system.

By comparing the power characteristics and lighting characteristics for LED verse traditional lighting, it can be concluded that using LED lighting to replace the traditional lighting devices are possible and recommended. However, still protection circuits such as current, voltage and temperature are still needed to be revised to increase the reliability. In order to make such mission become truth, the first important thing should be done is to lower the unit cost and secondary to have a proper and reliable power circuit with less loading and less electrical faults probabilities. Also suitable optics is needed to control the light pattern from the LEDs including focus, diffusion, reflection, and light amplification [4, 5].

For indoor Lighting, seven criteria are proposed to assess the technical and economic characteristics of LED luminaires and ensure their compliance with European Norms regarding office lighting. The proposed decision support system can be applied to any type of luminaire and can be used by professionals who want to evaluate different luminaire suppliers and determine the optimal luminaire tender for the lighting of any indoor space [6].

Other researches concentrated in Road lighting to compares mainly the life cycle costs (LCCs) of two typical alternatives in current road lighting: the HPS and LED luminaires. These studies have considered only the road lighting design criteria, but the esthetics and visual attractiveness are excluded from the comparison. The comparison and the results have considered only the direct energy operating cost [7]. Also an Economic cost analysis comparison between LED and HPS flood lights for an outdoor design, but using solar PV as a power supply, has been carried as a part of renewable energy design [8].

Feasibility study of LED lamp in replacing the conventional fluorescent lamp was conducted. Analysis and comparison have been carried out on the two lighting

systems in terms of electrical and photometrical performance. The study did not cover any HID outdoor lighting [9].

Comprehensive techno-economic analyses that considered the Company and National economic benefits that can be achieved from the high service life of the LED light fittings (up to 100,000 Hours) and its low power consumption compared with HPS was carried out. However, this analysis is limited only for 400 W HPS lighting case.

For the above survey, it can be found that several efforts carried out economic analysis of replacement different light fittings with LED. But, none of these works has considered the economics for replacement the HID lamps by LED lamps in industrial plants. Moreover, none of these researches have presented any type of economic index to support such type of lighting projects, except [10], which limited the research the replacement of only HPS type used in access road of a gas production company.

Based on the above survey, the first goal of this chapter is to discuss the economic benefits of replacing outdoor different type of HID lights with different rating installed in an oil and gas plant, as typical "Case-Study" for industrial plant, with suitable equivalent number of LED lighting fittings, to provide even better lighting effect level, without changing the lighting poles. The second goal is to determine the global saving norm based on two main aspects. "Company Benefits", in which the Company can gain it directly, and "National Benefits" that can be achieved by creating better gas sales opportunity for the county and by the reduction of the CO2 emission and hence the pollution.

2.2 Case-study: techno-economic model analysis for replacement of HID lamps with LED lamp in oil and gas plant

In this section, firstly, comprehensive economic study is introduced to replace 241 pieces of 150 W Metal Halide, 103 pieces of 400 W HPS lighting, 20 pieces of 1000 W MH lighting and 162 pieces of 70 W Bollard lighting by equivalent number of LED lighting fittings. Next, economic discussion is to carried out to provide four important economic indicators. Finally, summary, conclusion and recommendation are given.

2.2.1 Economic study methodology

The methodology in this economic study is carried out to estimate the financial benefits of replacement of outdoor HID (High intensity discharge) lights in an oil and gas plant by the equivalent LED (Light Emitting Diodes) lighting fixture. The Study has considered the following factors:

A. Company (Direct) Benefits:

  a. The initial cost of the replacement the lighting fixtures.

  b. The energy saving.

  c. The maintenance cost.

B. National (Indirect) Benefits:

  d. Natural Gas Sales opportunity

  e. Pollution Cost

In Company Benefits, calculation for "Luminaire Cost", "Power Consumption" and "Maintenance Cost" are given based on offers and prices collected on 2015–2016 from different bidders, contractors and suppliers to find the lowest prices.

In National Benefits, two benefits are considered. First benefit is the gas sales opportunity that will be gained from the reduction of the power consumption in case LED light is used. Natural gas valued using the wholesale price of $4.618/MMBtu based on US Energy Information Administration Henry Hub/NYMEX futures prices; Equivalent energy rate of 5.6 ¢/kWhr is used to value the energy produced over 10 years, assuming 1% annual escalation factor and Euro to USD exchange rate of 1.2 [10, 11] Accordingly,

$$\text{Annual Natural Gas Sale Opportunity} = 1.2 \times 0.056 \times \Delta \text{kWhr} \quad (1)$$

Where Δ kWhr is the reduction in the power consumption.

However, the second benefit is the cost saving due to the reduction of the CO_2 emission, and hence less pollution. Carbon credits based on current market is typically 6 euro/ton. Where, CO_2 emission is considered to be 0.83 kg/kWh. Assuming Euro to USD exchange rate of 1.2, the annual saving in pollution reduction can be calculated as following [10, 11]:

$$\text{Annual Saving in Polution} = \frac{0.83 \times \Delta \text{kWhr} \times 6 \times 1.2}{1000} \ \$ \quad (2)$$

The economic study is categorized based on HID lamp type that is needed to be replaced in the plant under the study. Typical study is summarized in the following **Table 1** for 150 W Metal Halide luminaire replaced by 65 W GREE LED luminaire. Where.

$$\text{Company Saving N} = \frac{\text{Annual Company Net Saving}}{\text{Total kW for the Replaced HID Lighting}} \quad (3)$$

$$\text{Total Saving N} = \frac{\text{Total Net Average Anual Saving}}{\text{Total kW for the Replaced HID Lighting}} \quad (4)$$

Similar to the typical economic study that is carried out for 150 W Metal Halide lighting, economic study is done for the remaining types of lighting; 103 pieces of 400 W HPS lighting, 20 pieces of 1000 W MH lighting and 162 pieces of 70 W Bollard lighting. Summary Tables (**Tables 2–5**) are provided hereinafter to show the Total Benefit and the Economic Analysis for these luminaire types.

Base on the above techno-economic, following **Table 5** is developed to summarize the main project economics indicators that can be used as good guide line for future similar projects that consider the replacement of HID lighting by LED Lighting.

2.2.2 Economic discussion

Based on the Saving Norm calculated for individual luminaire type in the above from **Tables 1–4** the Global Saving Norm can be calculated based on the following Eq.:

$$\text{Global Saving Norm} = \frac{1}{n} \left(\sum_{1}^{n} Norm_n \right) \quad (5)$$

Where "n" is the number of replaced lighting types in the study.
Using Eq. (7), the calculated Global Company Saving Norm is (355.19$/kW).

Company Benefits

I. LUMINAIRE PRICE ANALYSIS

S/N	Description	150 W MH Metal Halide [12]	65 W CREE LED [13]	Remarks
1	Initial Fixture cost	$227.52	$449.59	
2	Total quantity	241	241	
3	Total quantity Cost	0	108351.4986	
4	Cost/lamp manpower, crane, dumping etc. …	108.9918256	108.9918256	This estimate taking into consideration replacement cost, man power, vehicle, manpower to divert/block traffic, cost of loading/unloading & installation
a	Therefore initial investment for LED	0	**$134,618.53**	Additional investment for using LED luminaire.

II. POWER CONSUMPTION ANALYSIS

S/N	Description	150 W MH Metal Halide [12]	65 W CREE LED [13]	
1	Wattage per fixture	150	72	System Wattage includes losses
2	No of fixtures in the lighting circuit	241	241	
3	Total power consumed (kW)	36.15	17.352	
4	Hence total Power consumed per year (kWHr)	145142.25	69668.28	Average daily operating time is considered 11 Hours
5	Cost per kWHr	0.026948229	0.026948229	As agreed with Utility
6	Annual cost	3911.326574	1877.436755	
7	Service Life Range	16,000–20,000	60,000–100,000	
8	Average Service life (Hrs)	18,000	80,000	
b	Therefore the saving in 10 Years	**$20,338.90**		

S/N	Description	150 W MH Metal Halide [12]	65 W CREE LED [13]	Remarks
	Service Life Range	16,000–20,000	60,000–100,000	
1	Average Service life (Hrs)	18,000	80,000	
2	Number of Lamps change cycle in 10 Year	2.230555556	0	LEDs have no downtime against MH lamps which fail arbitrarily
3	Total No. of Lamps	538	0	
4	Cost/lamp manpower, crane, dumping etc	108.992	0	The estimate take into consideration new lamp cost, man power, vehicle, manpower to divert/block traffic, cost of loading/unloading & installation.

S/N	Description	150 W MH Metal Halide [12]	65 W CREE LED [13]	Remarks
c	Therefore savings in lamp maintenance in 10 Years	**$181043.6**		

IV. MAINTENANCE COST SAVING ANALYSIS- IGNITORS / BALLASTS / CAPACITORS

S/N	Description	150 W MH Metal Halide [12]	65 W CREE LED [13]	Remarks
1	Rated life (Hrs)	15,000	N/A	
2	Life in 10 years	2.676666667	N/A	
3	Total No. of Ballasts	241	N/A	
4	Thus component to be replaced in 10 Years	645	N/A	
5	Cost/lamp manpower, crane, dumping etc. ...	81.74386921	N/A	This estimate takes into consideration new ballast cost, man power, vehicle, manpower to divert/block traffic, cost of loading/unloading & installation.
c	Therefore savings in component maintenance in 10 Years	**$52,731.06**	N/A	

SUMMARY OF 10 YEAR COST SAVINGS USING LED LIGHT FITTINGS

a	**INITIAL INVESTMENT ON LED**	**$134,618.53**
b	**ENERGY**	**$20,338.90**
c	**MAINTENANCE - LAMPS**	**$181043.6**
	MAINTENANCE - COMPONENTS	**$52,731.06**
	TOTALL COST SAVING IN 10 YEARS	**$254,113.36**
	Total Average Annual Saving	**$25,411.336**
	Company Net Saving in 10 Years	**$119,495**
	Annual Company Net Saving	**$11,949.5**
	National Benefits	

V. Natural Gas Opportunity Cost:

d	Natural gas valued using the wholesale price of $4.618/ MMBtu based on US Energy Information Administration Henry Hub/NYMEX futures prices; Equivalent energy rate of 5.6¢/kWh used to value the energy produced over 10 years, assuming 1% annual escalation factor.	$5071.85

VI. Pollution cost

e	Carbon credits –based on current forward market @ 6 euro/ton, CO_2 emission in kg/kwh: 0.83, Euro to USD exchange rate of 1.2.	**$451**
	National Benefit Saving in 10 Years	**$5522.887**
	Total Benefits	
	Total Saving in 10 Years Operation	**$125017.88**
	Total Net Average Annual Saving	**$12501.788**
	Company Saving Norm = Annual Saving / kW (5) [10]	**$330.55**

S/N	Description	150 W MH Metal Halide [12]	65 W CREE LED [13]	Remarks
	Total Saving Norm = Total Net Average Annual Saving/ kW (6) [10]			$345.83
	Economic Analysis			
	Company Payback Period in Years (Initial investment for LED/Annual Company Net Saving			11.27 Years
	Company Annual Return on Investment "ROI" in Percentage			8.88%
	Total Payback Period in Years (Initial investment for LED/Annual Company Net Saving			10.77 Years
	Total Annual Return on Investment "ROI" in Percentage			9.29%

Table 1.
Summary of economic study for replacement of 150 W metal halide luminaire by 65 W LED luminaire.

Total Benefits:	
Total Net Average Annual Saving	**$14,899.66**
Company Saving Norm = Annual Saving / kW (3) [10]	$184.02
Total Saving Norm = Annual Saving / kW (4) [10]	$360.29
Economic Analysis	
Payback Period in Years	4.632 Year
Annual "ROI" in Percentage	21.59%

Table 2.
Replacement of 400 W HPS lighting with (100–130) W CREE LED.

Total Benefits:	
Total Net Average Annual Saving	**$2543.09**
Company Saving Norm = Annual Saving / kW (3) [10]	$ 107.15
Total Saving Norm = Annual Saving / kW (4) [10]	$127.15
Economic Analysis	
Payback Period in Years	10.93 Years
Annual "ROI" in Percentage	19.15%

Table 3.
Replacement of 1000 W MH lighting with (426) W CREE XAX LED.

From **Table 2**, it can be concluded that replacement of HPS lighting by LED lighting have the highest Total Net Average Annual Saving. Therefore, it is highly recommended to use LED lights instead of HID lights in industrial lighting applications.

It is also observed from **Table** 4 that replacement Bollard Light Lamps by LED Lamp has highest economic value because of the very short lifetime Bollard Light Lamps compared with LED lifetime.

Total Benefits:	
Total Net Average Annual Saving	**$9291.03**
Company Saving Norm = Annual Saving / kW (3) [10]	$799.05
Total Saving Norm = Annual Saving / kW (4) [10]	$819.31
Economic Analysis	
Payback Period in Years	8.657 Year
Annual "ROI" in Percentage	11.55%

Table 4.
Replacement of 70 W bollard lighting with (34) W CREE EDGE LED.

Project Total Investment	**$339,550.41**
Project Total Average Annual Saving	**$39,235.9**
Project Total Payback Period (Average)	**8.654 Year**
Project Annual Return on Investment "ROI" %	**11.55%**

Table 5.
Project economics.

In **Table 4**, project main economic indicators are illustrated with very attractive total payback period of 8.654 years and Project Annual Return on Investment of 11.55% which is higher approximately 10 times than the international bank rate for dollar deposit. This indicator supports the decision of investment in such scope of work.

In this Section, comprehensive economic study is carried out to calculate the Global Saving Norm for the replacement of High-intensity discharge lamps with different types by LED lamp in an Oil and Gas plant, which includes also the operational cost per year. The study considered Company direct benefits and National indirect benefits in evaluating project economic indicators and in calculating the Global Saving Norm as well. The result is compared and validated with previous research effort. Four important economic indicator were provided in this Section; Global Total Saving Norm ($433.37/kW), Global Company Saving Norm ($355.19/kW), typical total payback period of (8.654 year) and typical Project Annual Return on Investment of (11.55%). These four figures are important for both project decision makers and for cash-flow controllers.

2.2.3 Summary and conclusion

In Section 2 of this chapter, comprehensive economic study is carried out to calculate the Global Saving Norm for the replacement of High-intensity discharge lamps with different types by LED lamp in an Oil and Gas plant as "Case Study" representing industrial plant. The analysis considered Company direct benefits and National indirect benefits in evaluating project economic indicators and in calculating the Global Saving Norm as well. Four important economic indicator were provided in this Section; Global Total Saving Norm ($433.37/kW), Global Company Saving Norm ($355.19/kW), typical total payback period of (8.654 year) and typical Project Annual Return on Investment of (11.55%). These four figures are important for both project decision makers and for cash-flow controllers.

3. Smart LED lighting system used for long -roads with low-traffic for remote industrial plant

3.1 Survey and problem definition

Various road classifications are existed in terms of traffic flow. Principal arterials, minor arterials, rural collectors, local roads and very low-volume roads. The last is what our concern in this section. Statistically, for low-traffic roads the flow rate of the vehicles is assumed to be 400 vehicles per day [14]. In these roads, even simple lighting system is not installed mostly, and authorities rely on vehicle lights to illuminate the roads, which putting people life and valuable product passing in these roads under the risk. The main reason of non-lighting system is the desired of saving electrical energy. The main reason of non-lighting system is the desired of saving electrical energy. However, continuously lightened fully roads cause wastage of electricity, as only one vehicles may appear every three or four hours and even more during the night time. Each of these two scenarios are contradicting and are extremely significant issues.

Several researchers did some projects and published their work related to this topic, however, none of them has considered the lighting automation system on low traffic road. Articles are mainly related to smart or automated main street lighting systems or parking areas. In the following paragraphs, several researches' results is discussed, and main points are drawn into attention.

Some studies proposed a suggestion to use two sensors in order to consume less power with maximized efficiency of a system [15]. Light Dependent Resistor (LDR) sensor is utilized to measure the sun light intensity to control the switching action of LED streetlights, and Passive Infrared Resistor (PIR) motion sensor is used for changing the intensity of LED light when there is no motion of object in the street at mid-night, then all the streetlights are dimmed. However, [16] indicates that LDR and PIR sensor are used for same purpose, but without dimming the light, just switched on or off. In [17], the author worked on this topic using Infrared Resistor (IR) sensors which measure the heat of an object as well as detects the motion, in contrast to previous researchers did. They developed the system using Arduino Uno R3 while [18] achieved the same by Raspberry Pi 3 micro controller.

Another research effort offered Zigbee Based Smart Street Light Control System Using LabVIEW. Here, movement is detected by motion sensors, communication between lights is enabled by Zigbee technology. So, when a passer-by is detected by a motion sensor, it will communicate this to neighboring streetlights, which will brighten so that people are always surrounded by a safe circle of light [19].

Another author developed Intelligent Street Lighting System Using GSM technology. The aim is to achieve the energy saving and autonomous operation on economical affordable for the streets by installing chips on the lights. These chips consist of a micro-controller along with various sensors like CO_2 sensor, fog sensor, light intensity sensor, noise sensor and GSM modules for wireless data transmission and reception between concentrator and PC. The emissions in the atmospheres would be detected along with the consumption of energy and any theft of electricity [20].

Automatic street-light control system using wireless sensor networks is also proposed in some design. The system contains lamp station and base station [21]. Each lamp station consists of Arduino Uno board as microcontroller, PIR sensor, emergency switch, LDR sensor, nRF24L01 transceiver, ultrasonic sensor, relay, LED light and a solar panel as energy source. The base station consists of Raspberry Pi as processor, nRF24L01 transceiver, and a GSM module. The automatic

streetlight turns on under three conditions. Firstly, when PIR sensor detects a human or a moving object vehicle LED light is turned on. Secondly, an ultrasonic sensor is used to detect distance objects and turn on the light accordingly. Lastly, a switch is included for manual operation in case of maintenance work. The LDR sensor is included to measure the light intensity for identification of the day and night. There nRF24L01 wireless transceiver transmits the sensor information and the light status to the Raspberry web server to upload on the web page. Also, it receives commands sent from the web page to turn on or off the light at a particular node. The entire system is powered using solar cells making it more energy efficient.

The problem of high operational cost of low traffic light that use HPS lighting is partially solve by using LED light fitting instead of HPS luminaries [10].

Many real projects and researches have been done on this area [22–24], but few of them are focused in this topic exactly. Most of them consider street, campus, parking, park or any small area lighting system. The rest of them is devoted to road light and control systems. Brief analysis, discussion and comparison will be introduced hereinafter.

From the above literature review, firstly, all systems mentioned above used LDR sensor to sense night-time to operate the control system itself. In the system prosed in this Section, the same day/night sensor idea is also use to know exact hours of night-time or any dark time during the day time due to heavy cloud or any other reasons.

Secondly, all systems above have used motion sensors to detect the object movement whatever this object is, even if it is not vehicle, and hence control the lights in terms of switching ON/OFF or dimming. IR sensors and PIR sensor were the preferred sensors used to detect the object. These type of sensors detect mainly warm object and their movement. But, for the suggested system in this Section that need to be used for low traffic road, movement of only vehicle is needed to be recognized and hence switch on the light or dim them. The proposed system need to be designed to avoid any other motion such as animals, birds, or other objects which may be detected by IR or PIR sensors as this unnecessary detection of motion can cause unjustified energy consumption. Therefore, it is needed to give new approach to tackle with such problems. New approach could be to add the night vision smart camera to the system in order to recognize only the vehicles among all other objects that the camera detects.

Thirdly, some systems control the illumination by measuring the intensity of the objects movement and change the dimming of the lights accordingly. But for illumination system of low traffic roads, the intensity of the vehicles is continuously very low, and hence dimming technique is not effective solution.

Fourth, using LED light continuously operate during the night for low traffic roads can reduce the cost of illuminating the road compared with any other HID lighting, but still this is not best solution because the utilization of this system by this operational philosophy is not an efficient utilization because most of the time the light is ON unnecessary.

Fifth, in general, previous researches have been done on lighting automation system for the roads which serve both pedestrians and vehicles. But, this Section tries to design automation lighting system for long road with low traffic, where no need to switch on the lights for movement of any object except the vehicles.

In this section, efficient, safe and cost effective solution to design automated lighting system suitable for long roads with low-traffic is provided. First, description of the entire system design is discussed. Then, methodology and the programing of vehicles recognition using camera images are illustrated. Economic analysis for the proposed system is carried out. Finally, conclusion is given.

3.2 System design description

Lighting automation system in low traffic roads is intended to implement in the illuminated roads. It is supposed to have source power supply, feeder pillar with controller, light poles with day/night sensor. Such conventional system can be upgraded by new automated system. The methodology of lighting automation system in low traffic roads is achieved by applying the moving object recognition technique using cameras. Firstly, the road is sectionalized into several zones. Each zone depends on how much distance is existed between two feeder pillars, typically 400 meters. So, light poles in each zone will be switch on/off together. It means that each zone will have its feeder pillar (control panel) with controller, day/night sensor, motion sensor, and camera. Night vision cameras are installed on the road in such way to detect the vehicle arrival-to and departure-from each zone. The controller is designed to illuminate only the zones in which the vehicle is detected. The type and span of the zone are calculated based on the road design considering straight spans and roundabout.

3.2.1 Lighting control conceptual design

The control scheme of the automatic lighting system is illustrated in **Figure 2**. Day/night switch detects darkness status to start the controller and hence motion sensor and night vision cameras. Now, let us consider that there are two adjacent zones (Zone N) and (Zone N + 1), and vehicle enters to Zone (N + 1). Mainly, day/night sensor and motion sensors of (Zone N + 1) need to be installed before the camera of (Zone N + 1), while camera of (Zone N + 1) need to be installed in (Zone N) near to the end. This is because camera need to start capture the moving objects images only after motion sensor detects any object in advance and sends the signal to the camera to start operation, and hence the controller takes the proper decision for switch the light of (Zone N + 1) before the object enter the zone.

For that, camera is installed on a light pole about 80 m before each zone. This distance provides approximately 2 seconds for data processing and control assuming maximum speed is approximately 60 km/hour. **Figure 3** illustrates the installation location of (Zone N + 1) camera, day/night sensor and motion sensors in (Zone N).

The software in the controller extracts the image from the camera and analyze it to determine whether the object is vehicle or not. If the object is not a vehicle, no action is taken by controller. In case the object is vehicle, signal shall be sent to Zone N + 1 lighting feeder pillar to switch on light of Zone N + 1 Simultaneously signal shall be sent to Zone N controller to switch off lightning system of Zone.
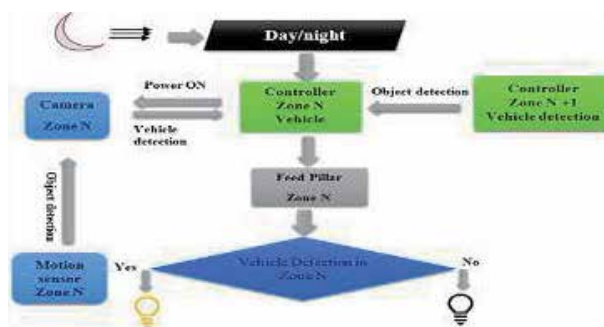
Figure 2.
Automatic lighting system schematic.
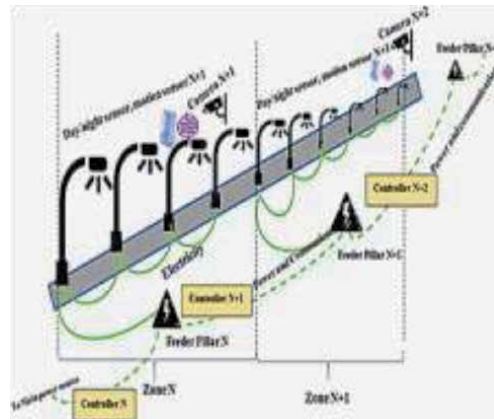
Figure 3.
Zone definition.

3.2.2 Switching on/off lighting system for a zone

As we explained above, each Zone has its own lighting control system consists of Day/night switch, motion sensor, night vision camera, controller and feeder pillar.

When the controller of any zone detect "vehicles" the digital counter inside this controller counts the number of these detected vehicle (Nin). In the same time, the same controller receives from the digital counter inside the controller of next Zone updated number of the vehicle interring the next zone (Nout). The communication between the controllers can be achieved by Power Line Telecommunications method. or RS-485 cable. If the difference between the these to numbers (Nin-Nout) is zero, this means that no vehicles exist in this zone, and the controller switches "Off" the light. As long as (Nin- Nout) is not zero, the light of the zone will be kept "On". This methodology insures that the lighting system for any zone is kept "On" if any vehicle(s) still in that zone for any reason such as accident, maintenance or temporary parking. Also, this methodology insures that the lighting system of the zone free of any vehicle is "OFF".

In **Figure 4**, flow chart for two consequent lighting system control logic is illustrated.

3.3 Vehicle image recognizing

Several researches are done to recognize the vehicle at night based on vehicle lamp detection [25, 26]. This method will not work in case the vehicle lights are switches off for any reason. Another researches are carried out to detect the information in vehicle number-plate using artificial intelligent methods [27, 28]. However, using artificial intelligent method is time consuming and not useful for the application of the proposed system. In this application, recognition of the number-plate rectangular frame is simple method and more than enough to confirm that the moving object is "Vehicle".

3.3.1 Methodology

The process of detection of vehicle number-plate consists of the following steps: capture of image, pre-processing, plate region extraction (**Figure 5**).
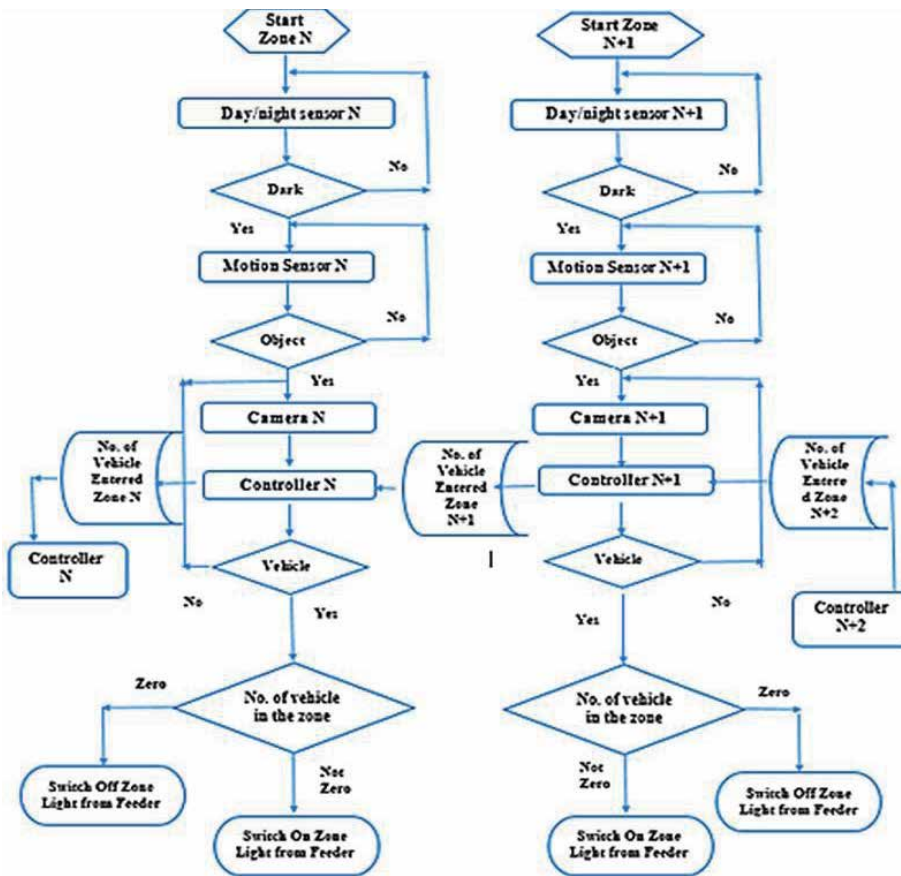
Figure 4.
Control flow chart for zone N and zone N + 1 lighting system.

Figure 5.
Vehicle recognition flowchart.

3.3.2 Capture of image

In this step, the image is captured by electronic devices such as infrared digital camera or any other camera suitable for night time. The image captured is stored in JPEG format. After that the captured image is converted into gray scale image.

3.3.3 Pre-processing

The next step after capturing the image is the pre-processing of the image. When the image is captured a lot of noises present in the image. Reducing the noises from the image are required to obtain an accurate result.

The RGB image is then converted into a gray scale image for easy analysis as it consists of only two color channels.

The aim of this pre-processing is to improve the quality of the image. Image enhancement techniques are used in this step. Image enhancement techniques consists process of sharpening the edges of image, contrast manipulation, reducing noise, color image processing and image segmentation.

3.3.4 Plate region extraction

The most important stage is the extraction of number-plate from eroded image significantly. The extraction of number-plate can be done by using image segmentation method. Mathematical morphology is used to detect the region of interest and Sobel operator are used to calculate the threshold value.

In general, any vehicle has its own number-plate which is always in rectangular shape consists characters. Accordingly, the basic approach in the detection of a vehicle is to recognize its number-plate which is mainly frame with characters (Numbers and letters). So, it is necessary to detect two criteria: the edges of the rectangular plate and there are characters within the rectangular.

A morphology based approach for detection number-plates is used. Our proposed method applies basic mathematical morphology operations like dilation and erosion.

The software model using the image processing technology is designed. The programs are implemented in MATLAB. The algorithm is divided into following parts: capture image, pre-processing, plate region extraction, characters recognition.

3.3.5 MATLAB code for number-plate recognition

The following MATLAB code is written to implement the above mentioned parts:

- Image capturing from camera
  % Read Image
  Input_image = imread('Car.jpg');

- RGB to gray scale
  % Convert the truecolor RGB image to the grayscale image

- I = rgb2gray (Input_image);
  The following steps are used:
  Image capturing from camera
  % Read Image
  Input_image = imread('Car.jpg');
  RGB to gray scale
  % Convert the truecolor RGB image to the grayscale image
  I = rgb2gray (Input_image);

- Edge detection
  % Sobel Operator Mask
  Mx = [−1 0 1; −2 0 2; −1 0 1];
  My = [−1–2 -1; 0 0 0; 1 2 1];

```
% Sobel Masking for filtering image
S = imfilter (I, Mx,'replicate');
```

- Vertical and Horizontal Dilation

```
% Vertical Dilation
Dy = strel('rectangle', [80,4]);
Iy = imdilate (M,Dy);
Iy = imfill(Iy,'holes');
% Horizontal Dilation
Dx = strel('rectangle', [4,80]);
Ix = imdilate(M,Dx);
Ix = imfill(Ix,'holes');
% Joint Places
JP = Ix.*Iy;
Dy = strel('rectangle', [4, 29]);
ID = imdilate(JP,Dy);
ID = imfill(ID,'holes');
```

- Erosion

  The process of erosion reduces removing unwanted details from a binary
  image.

```
% Erosion
E = strel('line',50,0);
IE = imerode(ID,E);
```

- Filtering of digits

  By filtering, the unwanted substances or noise can be removed or filtered out
  that is not a character or digits. Small objects or connected components should
  be removed and then the frame line that is connected to the digits should be
  identified and separated.
  Bwareaopen (Image Processing Toolbox) is applied for removing all the
  connected components from the binary image that have value less than P
  pixels.

```
image2 = bwareaopen(image, min(numberofpixel, 100));
```

  Stats = regionprops (L, properties) is applied for measuring a set of properties
  for each labeled region in the label matrix L.

```
stats = regionprops (image2,'all');
```

- Detect plate from image

3.3.6 Program validation process

The validation of the of the number-plate recognition program, and hence the
detection of vehicle, is done by two tests.

3.3.6.1 Number-plate recognized

In this first test it needs to insure that the program recognizes any object, that is
captured by the camera, has number plat. Therefore, the test is carried out to detect
the number plat for different vehicle models and types with different orientations.
The test result is illustrated in **Figure 6**. The program succeeded to detect the
number-plate as rectangular frame include characters. It is worth to highlight here
that it is not part of the program function to "read" the number-plate.
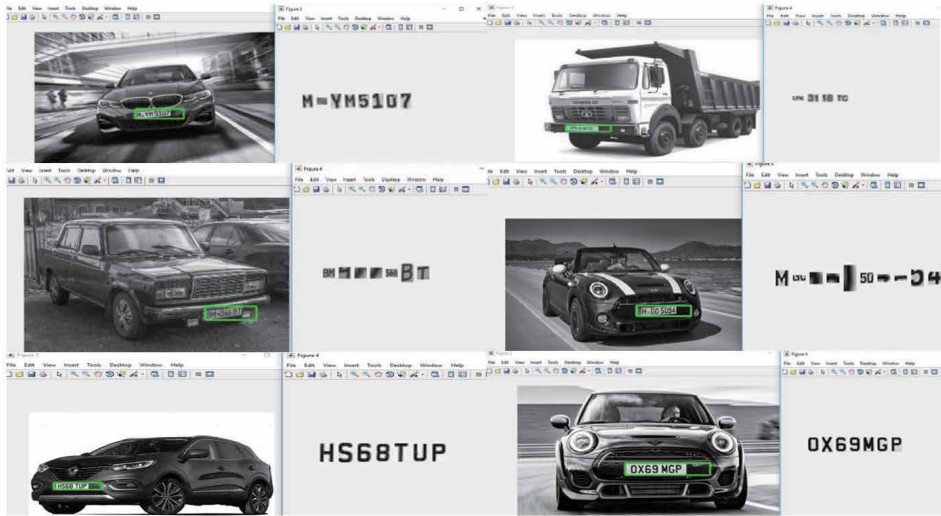
Figure 6.
The results for objects with number-plate.

3.3.6.2 No number-plate recognized

The objective of the second test is to ensure that for any object that does not have number plat, the program shall detect no number-plate. The test is done using four images for different objects consist of peoples and animals - Camels and Dog- (**Figure 7**). The program also succeeded to detect no number-plate.
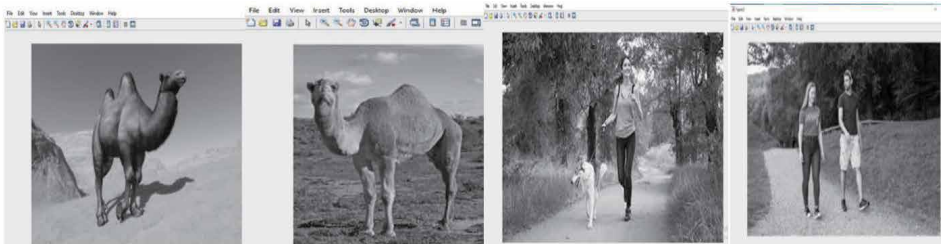
Figure 7.
The results with non-car images.

3.3.7 Object recognition in the road

Any moving object enters any zone of the road shall be subject to two steps of recognition process: the first recognition process is by the motion sensor which detects that there is a moving object leaving the zone (serves-zone) and enters the next zone. The second recognition process is carried out by the image processing software that detects the moving objects which has rectangular plate with characters (Vehicle). If the two condition is satisfied simultaneously, the intelligent lighting system puts ON the road lighting of the next zoon (vehicle entering zoon) and switch off the lighting of the service-zoon after short time delay (vehicle leaving zoon).

3.4 Economic analysis

Comprehensive economic study is carried out with the same methodology discussed is Section 2, but to estimate the financial benefits of using the proposed

lighting automation system for the low traffic roads. The Study considers also Direct Benefit and Indirect Benefits [10] in order to evaluate the entire economic value of the system.

Assuming for low traffic; the vehicle flow is 400 vehicles per day [14], vehicle speed is 60 km/hour, zone distance is 400 meter, lighting pole span is 40 meter, LED fixture consumption per pole is 75 Watts [30] and electricity tariffs is typically (0.053$) per kWh [29].

From the above assumptions, flow rate of the vehicle can be calculated to be 17 vehicles per hour. Considering worst road operation scenario, at which the 17 vehicles are driven with constant speed of 60 km/hour and equal distances from each other, it is obvious to conclude that one vehicle shall enter the first zone each 212 seconds and leaving the zone (400 meter) after approximately 24 seconds. Accordingly, the zone lighting fixtures shall be switched on for 29 seconds and switched of for 183 second approximately. From that, the percentage saving in power consumption using the proposed controller compared with the power consumption when road is illuminated continuously during the night is approximately $183 \times 100/212 = 86\%$ saving.

Considering 4 km low traffic road operating for typically 50 years, Direct benefits and Indirect benefits can be calculated as following:

3.4.1 Direct benefit

3.4.1.1 Initial cost of the new control system

Considering the cost of; camera (approximate number), day/night sensor, motion sensor, controller (simplest version) [31], signal transmission between zones by RS-485 network [32], and installation [10] (lamp, manpower, crane, dumping etc. ...), **Table 6** can be obtained. The table illustrates that approximately $26,662.88 is needed to provide the proposed automation lighting system for 4 km.

3.4.1.2 Energy saving

Table 7 illustrates the comparison of energy consumption between using the proposed automation lighting system versus conventional system which operates all night, considering that both systems utilize LED fixtures with 75-Watt as minimum consumption for the conventional system. The table shows reduction in the power consumption of 86.31%. This reduces drastically the electrical fault probability in the lighting electrical circuits [33, 34].

S. No	Definition (in 4 km)	With controller	Without Controller
1	Total Quantity of LED	100	100
2	Quantity of Day/Night sensor, Motion sensor, Camera & Controller	10	0
3	Unit price for Day/Night sensor, Motion sensor, Camera & Controller including maintenance	$107.40	$0
4	Total cost for item 3	$1074.00	$0
5	Signal transmission between zones	$14,698.88	$0
6	Total Cost of Installation	$ 10,890.00	$0
a	**Initial Investment**	**$26,662.88**	**$0**

Table 6.
Initial investment.

S. No	Description	With Controller	Without controller
1	Wattage per fixture (Watt)	75	75
2	№ fixtures in 4 km	100	100
3	Total power Consumed (Watt)	7500	7500
4	Operating hours (hour) per day	1.643	12
5	Daily operating cycle %	6.8458%	50%
6	Operating hours (hour) in 50 Years	29990.83	219,000
7	Power consumed per day (kWh)	12.325	90
8	Power consumed for 50 years (kWh)	224931.25	1,642,500
9	Total Cost for per day ($)	0.65	4.77
10	Total Cost in 50 years ($)	11,921.36	87,052.50
b	**Saving in 50 years**	**$75,131.14**	

Table 7.
Energy saving.

3.4.1.3 Saving in maintenance cost

Table 8 indicates the maintenance cost saving [10] (in terms of light fixture) such as lamp, manpower, crane, etc. for 50 years' operation of the proposed automation lighting system and the conventional system.

3.4.2 Indirect benefits

In indirect saving, two benefits of implementing the lighting system will be drawn into attention [10].

3.4.2.1 Natural gas sales opportunity

First benefit is natural gas sales opportunity (**Table 9**) gained from reduction of the power consumption calculated based on Eq. (1).

3.4.2.2 Saving in pollution

Second benefit is the cost saving due to reduction of the CO_2 emission, hence less pollution. (**Table 10**) calculate the related saving based on Eq. (2).

S. No	Description	With Controller	Without controller
1	Rated Life (Hours)	100,000	100,000
2	Operating hours in 50 years	29990.83	219243.33
3	Rate of maintenance in 50 years	0	2
4	Maintenance Cost per lightening pole	108.9	108.9
5	Total Maintenance $	$0.00	21,780.00
c	**Saving in Maintenance in 50 years**	**$21,780.00**	

Table 8.
Saving in maintenance cost.

S. No	Description	With Controller	Without controller
1	Annual Power consumption (kWh)	4498.63	32,850
2	Reduction in Power Consumption (kWh)	28351.38	
3	Annual Natural Gas Sale Opportunity	$1587.68	
d	**Natural Gas Sale Opportunity in 50 years**	**$79,383.85**	

Table 9.
Natural gas sales opportunity.

S. No	Description	With Controller	Without Controller
1	Annual Power Consumption (kWh)	4498.625	32,850
2	Power Consumption in 50 years (kWh)	224931.25	1,642,500
3	Annual Saving in Pollution	$1694.2752	
e	**Saving in Pollution in 50 years**	**$84,713.76**	

Table 10.
Saving in pollution.

3.4.2.3 Total saving analysis

Table 11 summaries the calculations in direct and indirect savings. It is obvious that total saving for only 4 km road in 50 years is $ 234,238.47.

3.4.3 Discussion

To sum up, huge amount of money can be saved if such technique is implemented. In case that this system is applied to only 100 km road, total annual saving becomes about $117,119.24; total saving in 50 years becomes $5,855,961.75. It means that such system saves huge amount of energy and hence expenditure saving that can be utilized in other projects' investment. From is discussion, it is also possible to calculates the "Saving Norm" for the proposed system to be $1171.19/km/Year (Eq. (3)).

3.5 Summary and conclusion

This Section provided automation design for the illumination system for low traffic roads in order to solve the problem of operating the road not only economically but also safely. Image recognition techniques was used based on identification

a	**Initial Investment**	**$ 26,770.28**
b	**Saving in Energy**	**$ 75,131.14**
c	**Saving in Maintenance**	**$ 21,780.00**
d	**Saving in Natural Gas**	**$ 79,383.85**
e	**Saving in Pollution**	**$ 84,713.76**
F	**Total Saving Cost**	**$234,238.47**
f	**Total Saving in 50 years**	**$ 234,238.47**

Table 11.
Net saving analysis in 50 years.

of vehicle number-plate to recognize the objects, is it vehicles or not? Image recognition algorithm was tested on different objects. The result from test has proved the validity of the algorithm that is used to detect different types of vehicle. Comprehensive techno-economic analysis was carried out and the result showed a great saving can be achieved, and hence, "Saving Norm" of $1171.19/km/Year was calculated for the proposed system too. This "Saving Norm" is a good index to supports project management for both project decision makers and for cash-flow controllers. The calculated value of this "Saving Norm" index encourages the implementation of this technique in any Low-Traffic Long-Roads. This index is expected to be much higher, and hence more cost saving, in case road lighting uses HID bulbs instead of LED bulbs.

4. Smart utilization of background lights for efficient indoor lighting intensity control

The ways which are used today in order to light houses, offices, and most of indoor areas are inefficient as a lot of energy is consumed unnecessarily during the day time. This problem is also one of the design concern in Green Building. In this section, a solution to this problem and a method for people's comfort is presented. Lights switch on automatically when there is somebody in the room and switch off when there is no occupancy. In addition to this known technique, adjustment of the brightness level of the lights will be possible via the personal computer or any other smart device. In this method, for the illumination of the lights in the area, where is needed to be controlled, light automatically is measured by sensor and considering the amount of background light coming from outside, the brightness of lights automatically controlled to reach the preset level. By the means of this method, it is possible to provide both user comfort and energy saving [35].

4.1 Survey and problem definition

The energy wasting created by lighting is very significant in places where is multi-occupant, especially in offices. In Today's world, a lot of companies provide methods in order to minimize energy consumption, because energy consumption becomes a significant problem in developing world. Many researches show that lighting system accounts for approximately 30% of energy consumption [36]. Especially, departmental stores and big offices located in city territories causes a lot of energy consumption. In offices, lighting system consume approximately twice more than printers and computers [37]. One of the main causes of this problem is that people leaves lights "on" in unoccupied places. In almost 23% of the daytime this event occurs [38]. Another problem that causes to waste of energy is called over-illumination. Over-illumination occurs when lights are brighter than needed to illuminate room. In addition to this, researches demonstrate that excessive lighting can give rise to negative health effects [38]. This problem, however, still occurs in many structures everywhere, particularly in offices. Researches indicates that lights are off for just 1 percent of daytime while the room is unoccupied [39]. And this fact shows that over-illumination occurs during daytime because of external daylight coming into the room. And, in order to overcome these problems, implementation of intelligent lighting system can be a great solution.

The direct advantage of automated lighting system is to reduce energy consumption and maintenance cost. Energy consumption is reduced, because intelligent lighting system considers external daylight coming into the room and occupancy status, hence reduce the amount of power consumed. And, maintenance cost is minimized, since lifetime of the light bulbs is better utilized and this factor

extends the life span of light bulbs. In addition to this, indirect advantages of proposed solution are that it allows the country to export more oil and gas, since the consumption of fuel that is needed to generate electricity will be reduced due to the energy savings caused by intelligent lighting system. Also, a reduction in pollution can be considered as positive advantage as well, because when less energy is consumed, the amount of carbon dioxide emission released by power generation plants is reduced.

It is important to highlight that during the engineering phases of indoor lighting system, because of uncertainty of the amount of daylight and any other background light which penetrates the room, engineers ignore this factor in the design which consequently introduce several drawbacks in the operation and maintenance cost of lighting system. Typical level of illuminance for indoor lighting is given in **Table 12** [35].

It is clear from the minimum level of illuminance indicted in **Table 12** for each application that the design engineer has to consider the given value as Minimum. This make the designer not only ignore any background lighting contribution, but also it considers "Minimum" illumination level that allows the designer to go to higher values to satisfy other design criteria such as symmetrical distribution of lighting inside the room. Also, this "Minimum" value of the illuminance level considered the worst calculation safety-factors that may not be applicable in all cases. Therefore, in general, most of the time in day extra unnecessarily lux level can be obtained inside the room, and hence additional money for operation and maintenance need to be spent.

For better control of the indoor lighting and reduce the operation and maintenance cost of the lighting system, there are many methods to implement intelligent lighting system in order to provide more efficient lighting [40]. First method is to use occupancy sensor in offices, homes etc. In this method, sensor is used to detect occupancy in order to control lights. If there is somebody in the room, lights switch on, otherwise lights switch off automatically. This is a good straight forward and easy method reduce energy consumption but it is not the optimum solution as the method still ignoring the contribution of background lighting, therefore it cannot be considered as high efficient way to control the indoor lighting intensity.

Second method is to utilize daylight to adjust brightness to a preset level. Energy savings are controlled by using dimming technique in which percentage of illumination of light bulbs change according to daylight coming into the room. Researches show that dimming technique reduces energy consumption up to 30% compared to non-dimmable light bulbs [41]. Daylight utilization can be accomplished by using light sensors which is used in order to detect level of illuminance inside the room and adjust brightness of the light bulbs on the basis of amount of daylight measured in the room and desired set-point. The energy saving can increase depending on the performance of light sensors used. It is reported by Electric Power Research

Facility type	Area or task type	E_{min}(lux)
general	Entrance halls or corridors	100
offices	Typing, Writing, Reading	500
offices	Technical drawing/Working on computer	500–750
offices	Conference rooms/Archives	200–500
restaurant	Kitchen/Dining room	300–500
schools	Classrooms/Library and Laboratories	300–500
hospital	Waiting rooms/Operating theater	200–1000

Table 12.
Design average level of illuminance for various places.

Institute that daylight utilization can increase energy savings up to approximately 40% [42]. In addition, researches indicate that energy savings can enhance up to 76% by taking into account daylight and occupancy status [43].

In this section, both above mentioned approaches are considered to develop intelligent lighting system in order to minimize power consumption and provide sustainable lighting system. Economic analysis is required to be carried out to evaluate this new approach.

This integrated approach enables us to adjust brightness of lamps to a preset level, considering daylight coming into the room and also prevent unnecessary lighting in unoccupied places. In the economic analysis, LED lighting type is selected as its power consumption is the lowest among other types of light bulbs, and hence it is expected minimum energy cost saving to be achieved. In case, other type of bulb is used, such as fluorescent or incandescent bulb, the energy saving due to using this intelligent lighting system shall be much higher.

4.2 Lighting control procedure

Energy consumption can be reduced significantly when light bulb's output is controlled automatically. Two methods are commonly used for lighting control. First method uses individual lighting control system in which each light bulb's output is adjusted independently according to light output level of its neighbor bulbs, the second method is networked lighting control system, which is more effective than the first method because all bulbs communicate intelligently with each other in order to achieve the required level for the room light intensity.

Networked lighting control system can be classified as DLCS (distributed lighting control system) for first method, or CLCS (centralized lighting control system) for second method. in DLC systems, each light bulb's sensing data is received by the controller, and they can communicate with neighbors in order to adjust their output level according to each other's state. However, in central unit CLCS which receives the status of each node based on information obtained from the sensors, and then performs control actions via actuators. In this system, central unit determines the output level of each light bulb on the basis of data obtained from sensors. In CLCS, many tasks are performed by central unit, such as, acquiring sensors' data from each node, estimating the optimal state where each light bulb will meet light requirements of the room (**Figure 8**).
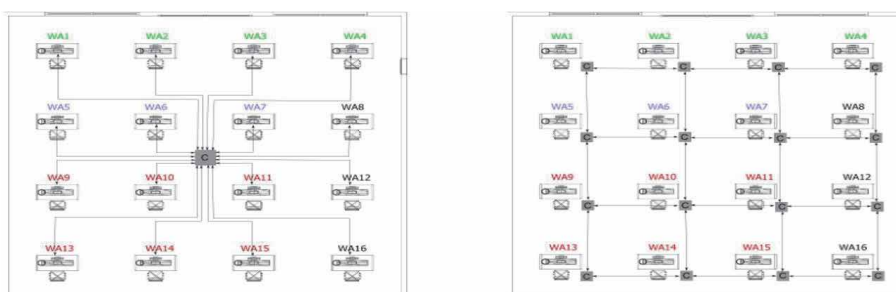
Figure 8.
C LC system and DLC system.

4.3 System description

PIR (Passive infrared) sensor is used to sense occupancy in places. PIR sensor detects occupancy at places and send commands to the controller to switch on or off

lights. Light intensity sensor(s) is used to give the controller the required data. The control unit sends signal to light dimmer(s) to control the LED light imitation to achieve the preset Lux level required for the room considering daylight.

4.3.1 Intelligent lighting systems methodology

The term called intelligent luminaire is connected to a smarter level of illumination where devices are capable of creating lighting comfort, energy efficiency, and easy controllability. The concept which is named intelligent lighting system corresponds to a system that communicates and cooperates with many luminaires, creating a node that satisfies user requirements. The key goal of this kind of system is to save energy and, at the same time user comfort by the means of network communication. In **Figure 9** the block-diagram of intelligent lighting system is illustrated. It is assumed that lighting system is dimmable (controllable) in order to provide intelligent method to tune the Lux level to the present value determined by the controller.

Firstly, this system checks for occupancy. If there is no occupancy, Arduino controller sends commands to AC light dimmer (which is controlling the intensity of light bulbs) to switch off lights. If there is somebody in the room, PIR sensor detects occupancy inside the room and activate Arduino controller. Consequently, the controller sends signal to the dimmer(s) to switch on the light and tune the lux of the room to achieve the preset value based on the input provided by the light intensity sensor(s).
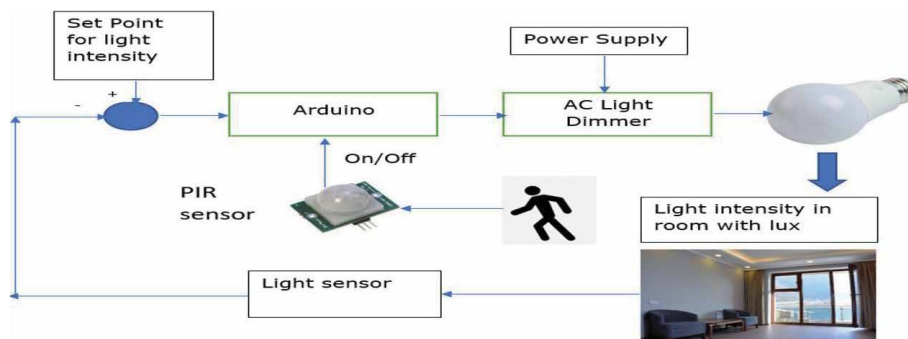
Figure 9.
Block diagram of intelligent lighting system.

4.3.2 Intelligent lighting system components

The intelligent lighting system contains PIR sensor, BH 1750 light sensor, Arduino Mega, AC light dimmer, LED and light bulb.

PIR sensor is used to detect occupancy in the room. Light sensor is used to measure the amount of light in lux. Arduino Mega is used as a controller. Ac light dimmer is used in order to adjust the brightness of LED bulb. To monitor the amount of light (PV) and set point (SP), LCD is used. LED bulb is used to provide illumination in the room.

PIR sensor is one of the simplest and inexpensive type of occupancy sensors and this type of sensor is widely used around the world. It is capable of measuring various air temperatures in the room. When there is somebody in the room, sensor sends a signal to turn on or off lights. When object is moved in the sensor's field of view, infrared lights which is radiating from the objects are measured by PIR

sensor. People have a temperature that is higher than perfect zero and thermal energy is emitted from people in the form of radiation. During the day, the wavelength of radiation is approximately 9–10 micrometers. PIR sensor has capability to detect the wavelength of radiation which only arise when a person comes to sensor's field of view. The radiation emitted by all objects which has temperature above absolute zero cannot be seen by human eye, since it is emitted at infrared wavelengths, however, electronic devices, such as PIR sensor, can detect it. This kind of sensors works totally by sensing the energy emitted by objects. When the amount of heat varies in intensity or position, sensor activates the controller.

PIR sensor which is used in this Intelligent Lighting System possesses pyroelectric sensor module that is designed for the detection of human body. This sensor has sensing range from 3 m to 4 m, and lens angle is about 140 degrees [44]. One of the advantages of PIR sensor compared with other types of occupancy sensor is that it is not complex, effortless to install, and it has compact size which is 28*28 mm. In addition to this, it is highly sensitive, power consumption is very low, and can perform under temperature from −15 to 70 degree. Most significantly, as contrasted with other sensors, it can penetrate walls in which motion can be anticipated and it is cheaper compared with other sensors. However, a constant and slight motion cannot be detected by PIR sensor and this sensor is sensitive to temperature. Another negative side of this sensor is that its field of view is smaller than other type of occupancy sensors. Moreover, this sensor cannot be mounted near the places where temperature changes commonly. But for application of indoor industrial building, this senior is adequate to be used.

BH1750 sensor is used in order to measure light intensity inside the room. This is a digital light sensor and it is used in the majority of mobile phones in order to adjust screen brightness, depending on lights coming from outside. This sensor has capability to measure directly lux value and there is no need to convert measured value to lux. This sensor uses I2C protocol to communicate with the controller. This protocol makes it easy to use with microcontroller. SCL and SDA pins which sensor have are required for I2C protocol. One of the advantages is that there is no need for calculation because we can get directly lux value by the means of this sensor. This sensor measures light intensity based on the amount of light which is hitting on it. The voltage between 2.4 V and 3.6 V and 0.12 mA current is needed to operate this sensor. The main component of BH1750 sensor is illustrated in **Figure 10**.

Arduino Mega is used as a master to control all slaves. It is the brain of this Intelligent Lighting System. It is a type of microcontroller board and uses ATmega 2560 microcontroller. Arduino Mega has 70 I/O pins. Fiftyfour (54) pins of Arduino Mega are digital I/O pin and 14 of them can be used as PWM pin. Other 16 pins are
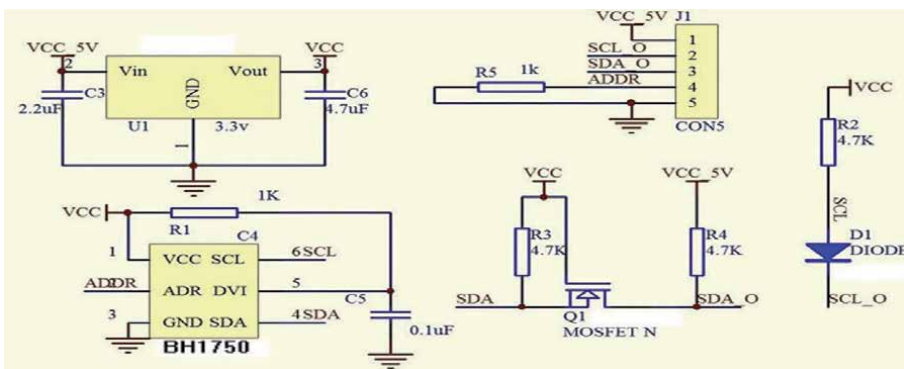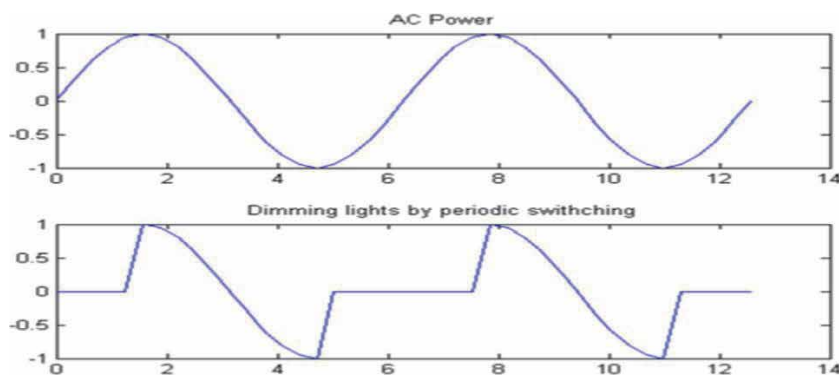

Figure 10.
BH 1750 sensor circuit.

analog I/O. In addition to this, it consists of 4 UARTs, 16Mhz crystal oscillator, USB connection, power jack, ICSP header, and reset button. Arduino Mega can simply be connected to the computer and programmed. There are many types of shields used for several purposes can be added to the Arduino mega [13].

LED light bulbs are the best choice to use in energy saving lighting systems and they have great advantages over the fluorescent lamps and incandescent light bulbs. In these days, LED bulb technology has developed and this technology offer light bulbs which can be used for many applications. In addition to this, this type of light bulbs offer dimmable and non-dimmable options and it creates opportunity to be used in intelligent lighting systems. LED bulbs are very durable and no mercury is used in this type of bulbs. Although the initial cost of LED bulbs is higher than other types of bulbs, they are cheaper to use for overall life of the light bulb compared with fluorescent or incandescent light bulbs. For all of these reasons, it can be beneficial to use led bulbs instead of other types of bulbs in the Intelligent Lighting Systems [44].

AC Light Dimmer is used to adjust the light intensity by dimming the light bulb [45]. There are various methods for dimming, the usual way is to use variable resistor which change the voltage coming into the lamp. Nevertheless, when variable resistance is used in order to change the brightness of lamp, resistance converts some part of energy into the heat that is not used. An effective method for dimming is to turn off AC power regularly and provide only some portion of full wave to the light. It could sound strange at first, because it will produce flicker, however it is not visible by human eye, if the periodic light switches and phase of AC power are locked. In order to accomplish the dimming, two circuits are required, zero-crossing detector and pulse-controlled switch, respectively. This is used in order to maintain switching with the power source in phase. And, to deal with 220 V AC, safety precautions should be implemented. That is why, circuit should be mechanically and electrically isolated from outside by the means of metal box and optoisolators, accordingly. The zero-crossing detector is a full wave rectifier with high power resistors that is used to reduce voltage (**Figure 11**). And, the pulse-controlled switch contains a Diac or Triac.

Figure 11.
Pulse control using AC light dimmer.

4.4 Intelligent lighting system response

The response of system will be illustrated for three different preset values and three background in the room. The response of the system will be represented for occupied conditions. In unoccupied conditions, the intensity of light bulb will be set

automatically to zero lux. In **Figure 12**, the response of the system is illustrated for preset value of 75 lux and external daylight with the amount of 25, 50, and 75 lux, ascending and descending. Another case is considered in **Figure 13** represents the response of the system for setpoint of 150 lux and additional daylight with the amount of 50,100, and 150 lux, ascending and descending. And last test case is considered in **Figure 14** shows the response of the system for setpoint 300 lux and external daylight with the amount of 100, 200, and 300 lux, ascending and descending. It is obvious from the results, the dimmer adjusts the light intensity of light bulb to achieve successfully to the present value, considering the external light coming into the room.

The transient state of the system response is not described in these graphs, only steady state is taken into account, since human's eye does not recognize to the fast changes happen in the amount of light. Moreover, in general, the rate of the change in the daylight occurs slowly and gradually, consequently, the response of the controller will change the intensity of the light emitted from the controlled lighting system in small steps which are comfortable for the eye. Hence, the transient state is not concern for the proposed intelligent lighting system.
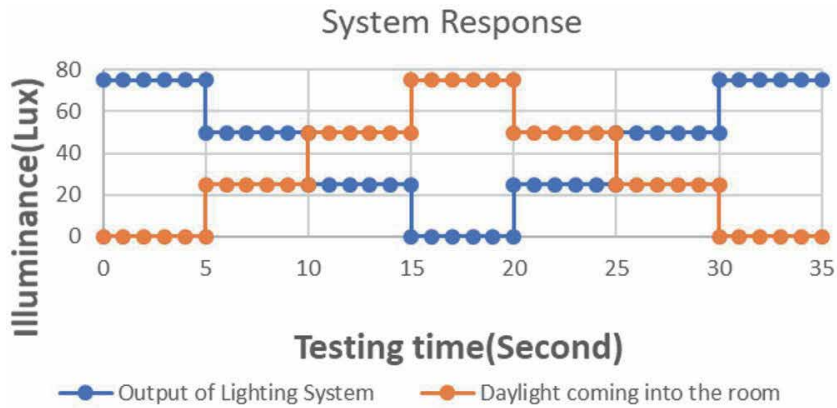
Figure 12.
The response of system for 75 lux SP.
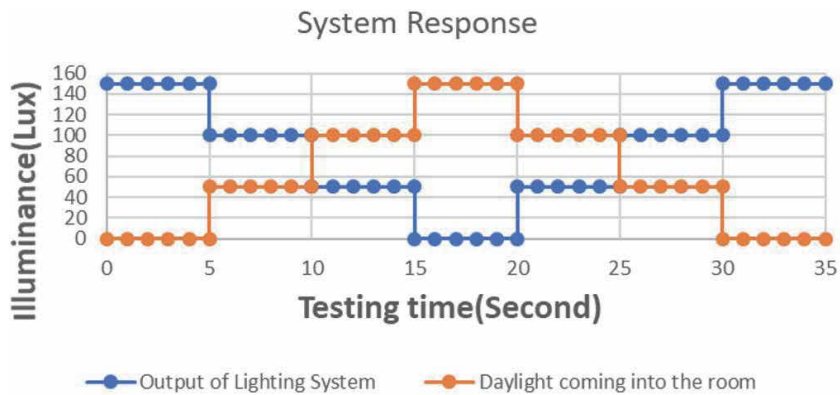
Figure 13.
The response of system for 150 lux SP.
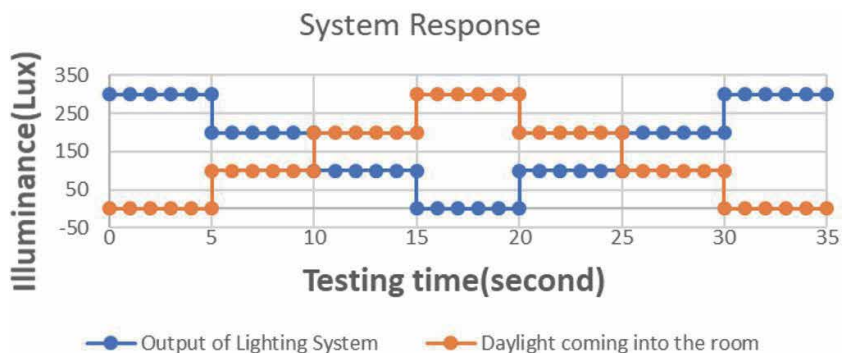
Figure 14.
The response of system for 300 lux SP.

4.5 Economical evaluation

In this section, Techno-Economical evaluation is discussed that includes direct and indirect benefits obtained from using the proposed intelligent lighting system. As mentioned earlier in this Chapter, Direct benefits are categorized in two parts; operational and maintenance cost. However indirect benefit is categorized also into two parts, introducing more oil/gas sale opportunity and reduction of pollution. And, the cost of this intelligent lighting system is negligible compared with other lighting systems [46, 47].

4.5.1 Direct benefits

Direct benefits of the proposed Intelligent Lighting System are explained as following:

4.5.1.1 Reduction of operational cost

This section determines the energy gains that intelligent lighting system can provide during the day. In order to achieve this, the response of controller is assumed to be maintained during the day. By considering occupancy status and level of illuminance during the day, energy savings which intelligent lighting system can provide may be calculated. Survey [37] illustrates that workers' illuminance preference is approximately 300 lux, and energy waste is generated by over-illumination and turning on lights in unoccupied places.

In **Figure 15**, Data of illuminance and occupancy status during the day and workers' illuminance preference in typical open-office are illustrated. In this survey, it is assumed that approximately 60% of daylight is coming into the room. From **Figure 15**, it can be observed that workers arrive at office at approximately 9:00 AM, occupies the working area and turn on the lighting system, because the level of illuminance is less than 300 lux (However, lighting system plus daylight coming into the room provides more than 300 lux). Thus, at the end of working hour, the lighting system was switched off about at 19:00. Also, from It can also be observed that workers leave working area at different times of the day, but lighting system turned on by causing the energy waste. In addition, between 15:00 and 17:00 the illumination which is generated by daylight is sufficient to satisfy the
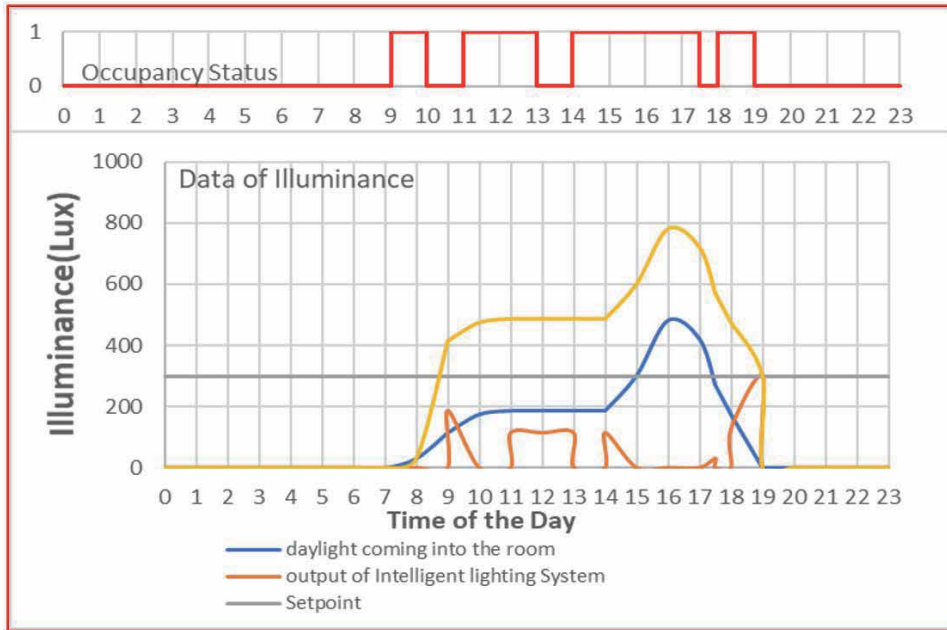
Figure 15.
Data of illuminance and occupancy status in typical open-office.

illuminance requirement at the office and lighting system is however switched on by causing over-illumination.

This data represents that thanks to daylight utilization technique, energy can be saved significantly between 9:00 and 19:00 by controlling the amount of light provided by the lighting system. In addition to this, occupancy sensor will contribute us to save energy by switching off lighting system when there is no occupancy in the working area. Finally, the energy savings can be calculated from the **Figure 15** by comparing the Areas under the curves. In order to find the energy savings, the area of curves, which are generated by the outputs of intelligent lighting system and Setpoint, should be calculated between 9:00 and 19:00. And, using the following equation, the percentage of energy savings accomplished from intelligent lighting system can be estimated.

$$A1 \text{ (Energy for Traditional Lighting System)} = 10 * 300 = 3000 \quad (6)$$

$$A_2 \text{ (Energy for Intelgent Lightting System)} = 95 + 240 + 55 + 8 + 150 = 548$$
$$(7)$$

$$E.S \text{(Energy saving)} = (3000 - 548)/3000 * 100\% = 81.7\% \quad (8)$$

From the equation above, it is calculated that in typical open-office energy savings can be approximately 81.7% by implementing proposed intelligent lighting system.

4.5.1.2 Reduction of maintenance cost

In **Figure 15**, it is clearly seen that operation hours of light bulbs reduce from 10 hours to approximately to 5.5 hours. So, implementation of proposed intelligent lighting system contributes also to reduce maintenance cost. The life span of light bulbs increases significantly, since lights are switched on at certain times of the day.

From **Figure 15**, percentage of reduction of maintenance cost can be calculated by the means of following equation.

$$M.C(\text{maintenance cost}) = (10 - 5.5)/10 * 100 = 45\% \qquad (9)$$

From the equation above, it is calculated that in typical open-office, maintenance cost can be reduced about 45% by implementing proposed intelligent lighting system.

4.5.2 Indirect benefits

Explanation of indirect benefits will be given in detail in the following paragraphs.

4.5.2.1 Annual gas sale opportunity

First benefit is that country can export larger amount of gas, since the consumption of gas will be reduced due to the energy savings caused by proposed intelligent lighting system. By using the selling price of $4.618/MMBtu on the basis of US Energy Information Administration Henry Hub/NYMEX, natural gas valued futures prices. Considering 1% annual escalation factor, equivalent energy rate of 5.6¢/kWhr used to measure the energy generated for one year. And, sales opportunity for the natural gas can be estimated annually by the means of equation Eq.(1) that can be used to calculate the annual gas sale opportunity for any project using this Intelligent Lighting System.

4.5.2.2 Annual saving in pollution

Second indirect benefit is that pollution caused by power plants can be reduced significantly. When the amount of power consumed is reduced, the amount of toxic fumes released by power plants will be reduced. The majority of power plants burn crude oil, coal, fossil fuel etc. Hence, this causes the emission of carbon dioxide that accounts for the majority of pollution. Carbon dioxide is released into the air and causes the absorption of sun's warmth and heat in our atmosphere. When power plants burn more fuel in order to generate more energy, extra carbon waste traps cause too much heat. When carbon dioxide emission is reduced, it will cause less pollution. Eq. (2) can be used to calculate the Annual Saving in Pollution that can be gained in any project using this Intelligent Lighting System.

4.5.3 LED bulbs

Nowadays, energy saving is one of the big problems, that is why energy-efficient lighting systems proceed rapidly over the past ten years [43]. Led light bulbs are the best choice to use in energy saving lighting systems and they have great advantages over the fluorescent lamps and incandescent light bulbs. In these days, led bulb technology has developed and this technology offer light bulbs which can be used for many applications. In addition to this, this type of light bulbs offers dimmable and non-dimmable options and it creates opportunity to be used in intelligent lighting systems. Led bulbs are very durable and no mercury is used in this type of bulbs. Although the initial cost of Led bulbs is higher than other types of bulbs, they are cheaper to use for overall life of the light bulb compared with fluorescent or incandescent light bulbs. For all of these reasons, it can be beneficial to use led bulbs instead of other types of bulbs in lighting systems.

4.5.3.1 Diffused led bulbs

One of the bunch of LED bulbs is diffused LED bulbs. It is covered by lens which have dimple shape, and this shape support to spread light around a big area. Nowadays, because of their tremendous efficiency, people increasingly use this type of bulbs. This type of bulbs is available in standard Edison bases, and they can be used for a lot of purposes, such as, reading lamp, lighting for rooms and offices, and some other applications in which light can remain on for a long time.

4.5.3.2 Flame tip, Candelabra Base LEDs

Flame Tip, Candelabra Base LED bulbs is another type of LED bulbs and it is used in many applications. The purpose of designing such type of light bulbs is to take the place of incandescent candelabra bulbs. This type of light bulbs is significantly effective because they can deliver corresponding light of 25 to 35 W and light does not spread top to bottom as far as typical lights, because of heat sink.

4.5.3.3 Led tube lights

LED Tube Light bulbs is another type of LED light bulbs and it is used in a lot of applications. The purpose of designing this type of light bulbs is to replace typical fluorescent tube lights. They exist in 8 and 16 W. In commercial sites, fluorescent lights are frequently installed in high ceilings and using Led Tube Lights instead of fluorescent tube lights is extra saving, because the frequency of replacing bulbs is significantly decreased.

4.5.3.4 Advantage of led bulbs

The life of LED bulbs is approximately 10 times more than incandescent and fluorescent light bulbs. The main reason why they are more effective is that they do not have filament and they are not destroyed under conditions in which typical incandescent and fluorescent light bulb can be damaged. This type of bulbs does not cause any heat, but common incandescent lamps heat and help to increase the room temperature. LEDs avoid this problem and contribute to reduce the air conditioning cost. In the manufacturing process of LED bulbs, no mercury is utilized and this kind of bulbs use approximately 2–17 W electricity. LED bulbs reduce electricity cost, remain cool and avoid the replacement cost, because they have long life.

4.5.3.5 Cost comparison among light bulbs

Although, initial cost of LED bulbs is higher, this cost compensates over time in electricity saving. The use of LED bulbs commercially adopted, because maintenance and replacement cost was significantly higher. Maintenance and replacement cost in LED bulbs are considerably less compared with others and the initial cost of LED bulbs is continuing to decrease.

4.5.4 Saving norm calculation

Consider standard office with dimension 3mx4m. As per **Table 12**, the design lux level is 500 lux. Using matrix distribution 2x2 with 60cmx60cm light fitting, each consists of 4 lighting tube Fluorescent (25 W) or LED (9 W), the office Traditional lighting load shall be 400 W or 144 W respectively. For 9 hours working duty, the annual consumption shall be 4730kWh and 1314kWh.

Conditions	Led Bulbs	CFL	Incandescent
Light bulb projected Lifespan	50,000 h	10,000 h	1200 h
Watts for per bulb	10	14	60
Cost for per bulb	$35.95	$3.95	$1.25
KWh of electricity used over 50,000 hours	300–500	700	3000
Cost of electricity (0.10per KWh)	$50	$70	$300
Bulbs needed for 50 k hours of use	1	5	42
Equivalent 50 k hours bulb expense	$35.95	$19.75	$52.50
Total cost for 50 k hours	$85.75	$89.75	$352.50

Table 13.
Economic comparison between LED, CFL and incandescent bulbs.

Applying Equation-9, the office annual energy consumption can be reduced to 865.59kWh and 240.462kWh for Fluorescent lighting and LED lighting respectively.

From **Table 13**, cost of electricity (0.10per KWh). Accordingly, from two the values, 865.59kWh and 240.462kWh, Annual Energy Saving Norm/Office for offices using Fluorescent lighting and LED lighting can be calculated to be 86.6 $/ office and 24$/office respectively. For example, if this technique applied on 100 Administration Building with 50 room each, so the total Annual Saving can be 433,000 $ and 120,000$ for Fluorescent lighting and LED lighting consequently. This example gives good impression how much reasonable saving can be obtained by applying such technique in industrial buildings.

4.6 Summary and conclusion

To conclude this section, it can be highlighted that most places are over illuminated because background light is not considered in the design sage. In addition, light is switched on in unoccupied places which causes waste of energy. Therefore, Intellect Lighting System is very essential to overcome this problem to control indoor lighting intensity taking into account occupancy status and background light coming into the room in order to adjust level of illuminance in efficient way. As a result, it is worth to highlighted that Intelligent Lighting System uses properly selected LED bulbs not only reduces power consumption, but also reduces maintenance cost, pollution caused by power plants and increases opportunity for gas sales. Finally, typical Annual Energy Saving Norm (Energy Saving$/Office) is calculated for both cases, offices using Fluorescent lighting and LED lighting.

Author details

Muhammad M.A.S. Mahmoud
Baku Higher Oil School, Baku, Azerbaijan

*Address all correspondence to: mmanar@yahoo.com

IntechOpen

References

[1] Lighting Research Center-Ekobase, Advantage of Using Energy Efficient Lighting for Society and Environment; 2020. https://www.ekobaseglobal.com/index.php/en/learning-center/street-lighting-technology-comparison

[2] Illuminating Engineering Society, Illuminating Engineering Society of North America Had Book (IESNA); 2000.

[3] LED advancements drive quality of light gains (MAGAZINE). LEDs Magazine. 22 April 2014.

[4] Y.K. Cheng, K.W.E. Cheng, "General Study for using LED to replace traditional lighting devices", IEEE 2nd International Conference on Power Electronics Systems and Applications, 2006.

[5] Muhammad M.A.S. Mahmoud, Detection of Single-Line-to-Ground Faults Through Impedance in Mesh Distributed Network, IEEE conference Modern Electrical Power System MEPS-15, Wroclaw, July 2015.

[6] Evangelos-Nikolaos D Madias, Lambros Doulos &, others, A decision support system for techno-economic evaluation of indoor lighting systems with LED luminaires, Journal of Operational Research 2019, DOI: 10.1007/s12351-019-00485-1, SpringerLink,

[7] Leena Tähkämö, Rami-Samuli Räsänen & Liisa Halonen, Life cycle cost comparison of high-pressure sodium and light-emitting diode luminaires in street lighting, The International Journal of Life Cycle Assessment, volume 21, 137–145(2016).

[8] Nibedita Das* , Nitai Pal, Sadhu K. Pradip, Economic cost analysis of LED over HPS flood lights for an efficient exterior lighting design using solar PV,

Building and Environment, Vol. 89, pp 380–392, Elsevier July 2015.

[9] Chin KimGanAhmad Farid SaparYik Chee MunKuan Eng Chong, Techno-economic Analysis of LED Lighting: A CaseStudy inUTeM's Faculty Building, Malaysian Technical Universities Conference on Engineering & Technology 2012, MUCET 2012, Procidia Engineering, Vol 53. Pp 208–216, 2013, Elsevier.

[10] Muhammad M.A.S. Mahmoud, Typical Economic Model for Calculating the Saving Norm of Replacement HPS Street Lighting by LED Fixtures in Access Road of Gas Production Company at GCC, IEEE - International Conferences on electrical and electronics engineering, 4–7 may 2018 (ICEEE 2018) Istanbul.

[11] The Emirates Center for Strategic Studies and Research, Technology and The Future of Energy, 2013.

[12] Lighting Handbook 10th Edition - IES - Illuminating Engineering Society. ISBN # 978–0–87995-241-9.

[13] Cree Edge™ LED Luminaire. Cree Catalogue. Retrieved 9 October 2017.

[14] Cornell University. "What is the traffic volume cut off between high-volume and low volume?" Cornell Local Roads Program. https://www.clrp.cornell.edu/q-a/151-low-volume.html#:∼:text=1%2C000%20vehicles%20per%20day%20is,upon%20context%20including%20functional%20classification.

[15] P. V. K. Bhangdiya, "Low Power Consumption of LED Street Light," International Conference on Global Trends in Signal Processing, Information Computing and Communication, 2016.

[16] Noor Lina Ramli, N. Mohd Yamin, "Implementation of passive infrared sensor in street lighting automation

system," ARPN Journal of Engineering and Applied Sciences, 2015.

[17] Sindhu.A.M, Jerin George, Sumit Roy, Chandra J, "Smart Streetlight Using IR Sensors," IOSR Journal of Mobile Computing & Application (IOSR-JMCA), 2016.

[18] Ms. M. Kokilavani, Dr. A. Malathi "Smart Street Lighting System using IoT," International Journal of Advanced Research in Applied Science and Technology ISSN, 2017.

[19] Faiz Ansari, Saima Khan , Aakash Jaiswar , Pooja Khiste , Milind Nemade, "Zigbee Based Smart Street Light Control System," International Journal of Innovative Research in Science, Engineering and Technology, 2016.

[20] Aman KumarAkash OraonSiddharth Agarwal, "Intelligent Street Lighting System Using Gsm," International Journal of Engineering Science Invention, 2013.

[21] D.SA.S. Rajasri, "Automatic streel light control system using wireless sensor networks," in IEEE international Conference on Power, Control, Signal and Instrumentation Engineering, 2017.

[22] Tvilight, "Energy savings through dynamic dimming on the S100 in Nijmegen", Intelligent Roadway Lighting. https://www.tvilight.com/2016/10/18/case-study-public-roadways/.

[23] Intelilight, "Intelligent Street Lighting," https://intelilight.eu/.

[24] Muhammad M.A.S. Mahmoud "Economic Model for Calculating the Global Saving Norm of Replacement High-Intensity Discharge Lamps with LED Lamp in Oil and Gas Plant", IEEE 61st International Scientific Conference on Power and Electrical Engineering of Riga Technical University (RTUCON) 2020.

[25] Reham Faour, Bassel Shanwar, Nizar Zarka, "Recognition of Vehicle Numberplate using MATLAB", DOI: 10.13140/RG.2.1.1459.8640, 2016.

[26] M. K. B. Ashan and N.G.J.Dias, Recognition of Vehicle License Plates using MATLAB", European International Journal of Science and Technology Vol. 5 No. 6 , August, 2016.

[27] Jing-Ming Guo ; Chih-Hsien Hsia ; KokSheik Wong and others, Nighttime Vehicle Lamp Detection and Tracking With Adaptive Mask Training", IEEE Transactions on Vehicular Technology, Vol. 65 , Issue: 6 , June 2016.

[28] Hazim Hamza Supervisor, Paul WhelanNight, "Time Car Recognition Using MATLAB", M-Eng in Electronic Systems 2013

[29] Republic,"tariffcouncil.gov.a z,"2016. http://www.tariffcouncil.gov.a z/?/az/content/70/.

[30] Pacificlamp.com, https://pacificla mp.com/street-light.asp.

[31] A. A. Circuits, "Low-Cost Programmable Logic Controllers for the Frugal Engineer," https://www.allab outcircuits.com/news/low-cost-progra mmable-logic-controllers-for-the-fruga l-engineer/.

[32] Alibaba, "Signal 2cores twisted pair armoured rs485 cable price," https://www.alibaba.com/product-detail/Signa l-2cores-twisted-pair-armoured-rs485_ 62193928910.html?spm=a2700.7724857. normalList.9.38b06425h3AeQA&s=p.

[33] Muhammad M.A.S. Mahmoud, Electrical Short Circuit Finding in MV Network using Fuzzy Clustering Techniques, Journal of Energy and Power Engineering, JEPE, January 2013.

[34] Muhammad M.A.S. Mahmoud, Zafar Qurbanov, Review of Fuzzy and ANN Fault Location Methods for

Distribution Power System in Oil and Gas Sectors, IFAC, Elsevier 2018.

[35] Ilham Marufov; Muhammad M.A.S. Mahmoud (Advisor), "Intelligent Daylight Utilization for Efficient Indoor Lighting Intensity Control", Graduation Thesis, Baku Higher Oil School, 2020.

[36] James Thompson. "Are Automated daylight control systems working as they should?", "international journal of Electrical Power & Energy Systems". Page 15–20

[37] Bruno Miguel Rodrigues Rocha. "Enhanced Networked Luminaire Controller for Sustainable Ambient Illumination", "international journal of Electrical Power & Energy Systems". Page 3–5

[38] L. Perez Lombard, J. Ortiz, and C. Pout, "A review on buildings energy consumption information," "Energy and Buildings, vol. 40, no. 3". Page 394–396

[39] B. VonNeida, D. Maniccia, A. Tweed, and M. Street, "An analysis of the energy and cost savings potential of occupancy sensors for commercial lighting systems," "Proceedings of the 2000 Annual Conference of the Illuminating Engineering Society of North America". Page 24–27

[40] C. Ehrlich, K. Papamichael, J. Lai, and K. Revzan, "A method for simulating the performance of photosensor-based lighting controls," "Energy and Buildings, vol. 34". Page 14–17

[41] J. S. Edle, A. P. Thakare, and A. M. Agarkar, "Intelligent illumination system to prevail over possible diseases due to over- and under-illumination," "International Journal of Enterprise Computing and Business Systems". Pp 40–44

[42] M. Figueiro, M. Rea, R. Stevens, and *A. rea*, "Daylight and Productivity - A Possible Link to Circadian Regulation," " in Light and Human Health: EPRI/LRO 5th International Lighting Research Symposium, 2002". Page 67–73

[43] P. R. Mills, S. C. Tomkins, and L. J. M. Schlangen, "The effect of high correlated colour temperature office lighting on employee wellbeing and work performance," "Journal of Circadian Rhythms. BioMed Central, vol. 5, Jan. 2007". Page 45–48

[44] "Nabirul Islam, Kazi Tanjib Rizwan, Shamima Islam Nifa", "Smart Departmental Stores", "Dept. of Electrical & Electronic Engineering, BRAC University in partial fulfillment of the requirements for the Bachelor of Science degree in Electrical & Electronic Engineering

[45] "Talha Khan , Hassan Abbas , Shehryar Ali , Waseem Arshad ", "Design & Modeling of Self Configuring Automatic Light Control System", "University of Engineering and Technology".

[46] Muhammad M. A. S. Mahmoud, Leyla Muradkhanli, "Economical and Safe Design for Low-Traffic Long-Roads Illumination Control System by Using Image Recognition Technique", Journal of Electrical and Electronic Engineering, Vol. 8, No. 5, pp. 117–126, 2020. doi: 10.11648/j.jeee.20200805.11 http://www.sciencepublishinggroup.com/journal/paperinfo?journalid=239&doi=10.11648/j.jeee.20200805.11

[47] Muhammad M.A.S. Mahmoud, Leyla Muradkhanl, "Safer Design and Less Cost Operation for Low-Traffic Long-Road Illumination Using Control System Based on Pattern Recognition Technique". Intelligent Control and Automation, 11, 47–62. https://doi.org/10.4236/ica.2020.113005

Chapter 3

Passive and Active Topologies Investigation for LED Driver Circuits

Salvatore Musumeci

Abstract

In this chapter, a survey of LED driver circuits is presented. The driver circuit is a crucial component in the LED light system. It provides the correct voltage and current values for the best brightness and long life. Furthermore, the driver circuits contribute to obtaining high efficiency and reliability light system. Several lighting applications need different driver topologies that meet the use requirement and the energy sources available. In actual applications, passive and active circuits are implemented to satisfy the LED driver electrical requirements and cost-effective demands. The LED driver circuits investigation evaluate the issues and the solutions in the LED lighting systems connected to a DC source such as a battery or AC line. The AC line connection requisites such as the power factor correction and the harmonic distortion are dealt with both the driver topology and control optimization. Also, the volume reduction need is examined in the circuitry choice. Moreover, the different topologies of the power converters isolated and not isolated used in the driver circuits based on both the power request and supply source are described and critically evaluated.

Keywords: LED driver, linear driver circuits, DC-DC converter, Flyback, PFC, LLC converter, multi-channel LED, average current control, peak current control

1. Introduction

Nowadays, LED lights are becoming more and more used in various fields of applications such as domestic and industrial lighting, open space offices or supermarkets lighting, streets lighting, large spaces for sporting or entertainment events, and in transport for lighting and signaling, both on land or sea or air [1, 2]. The power density featured is very variable and depends on the type of application and ranges from a few Watts to thousands of Watts. Furthermore, the power source can be different from direct current (DC source) to alternating current (AC source), presenting different needs for interfacing with Solid-State Lighting (SSL) [3]. In the lighting scenario, a LED light system (light bulb, street-light, floodlight and so on) can be considered as a combination of LED semiconductor materials and a driver circuit.

LED light system is acknowledged as the actual generation of the sustainability light source. It has many benefits compared with incandescent lamp and the fluorescent lamp [4–7]. It features high efficiency, long life, safe and environmental

protection, small size, high reliability and fast response speed. In the last generation of the LED light bulbs, the equivalent lighting effect is achieved with power consumption about 1/10 of incandescent lamp and 1/2 of the fluorescent lamp [8].

The design of the LED driver circuit plays a key role to achieve a performant light system. The light brightness is function to the supplied forward current. Therefore, LED is a current-driven device. The driver circuit must provide the correct level of current for the required brightness as well as comply with other characteristics such as:

- high reliability, necessary in cases of operation in difficult conditions (for example in transport at very low temperatures or generally, for continuity of service needs),

- high efficiency to reduce losses and improve performance and autonomy in the case of portable lighting systems with batteries as a source,

- small volumes of the power converters for arranging the drive circuits to meet the demands of having LED bulbs, light fixtures, and modern lighting systems as compact as possible,

- flexibility and precision in control to adjust the brightness to avoid phenomena such as flicker with the fault-tolerant capability,

- surge protection necessary due to the vulnerability of light emitter diodes to over voltages and low resistance to reverse voltages (for example, high voltage spikes from the power grid can occur in LED streetlights),

- additional protection functions such as input under-voltage, temperature or short circuit of converter power switches,

- high power factor (PF), in the case of AC power supply with a satisfactory power quality waveform and consequently with low Electromagnetic interferences (EMI) contents.

Specifically, in AC connected LED driver a high PF leads a displacement power factor next to one and an input current with quite low total harmonic distortion (THD) [9, 10]. Furthermore, the LED light system must comply with the national and international standards and regulations concerning harmonic currents, such as the standard IEEE-Std-519 and the IEC 61000–3-2.

Other characteristics of the driver circuits concern the circuit structure. The circuits solutions can be passive or active topologies. Active circuits can be classified as linear or switching type. Furthermore, the driver circuits can be non-isolated if the output current is limited and a low voltage source is involved or can be isolated when the safe operative conditions are prevalent and a higher output current is requested [11]. Additionally, the information and communication technologies (ICT) are making the driving of solid-state lamps smarter and smarter, allowing to vary the brightness level (dimming) and the colors through remote and controlled communication systems by means of user interfaces developed according to the needs of the user [12].

This chapter is organized as follows.

In the Section 2, the basics of the LED driver are addressed. Furthermore, the main passive, and active circuit for the solid-state lighting driving are described and classified.

In the Section 3, the main topologies of the DC-DC switching driving circuits are presented and analyzed.

In the Section 4, the switching-type driving circuits and their interfacing with the network AC and DC source are investigated.

2. LED driver circuit basics

In an LED device the emitted light follows the increment of the current. It is almost proportional to the supplied current. However, the relationship between voltage and light output is highly nonlinear. The direct voltage V_F drop and the current I_F are linked by an exponential function typical of the silicon diode. In **Figure 1a** the voltage–current characteristic is depicted for a white LED. The curve has been obtained by a variable voltage source with series resistance to control the diode direct current. In **Figure 1b** the circuit schematic of the LED characterization is shown. From the **Figure 1a**, the diode features rated voltage of 3.5 V and a rated current of 700 mA, while the threshold voltage V_{th} is 2 V. From **Figure 1b** the resistance R_S to obtain the requested current is

$$R_S = \frac{V_S - V_F}{I_F} \qquad (1)$$

The circuit schematic of **Figure 1b** is also the basic linear LED brightness control. Referring to **Figure 1a** two control approaches can be performed. In the first methodology, the LED V-I curve is used to set the voltage needs to generate the requested forward current. In the second driving approach, the LED device is controlled with a constant-current source to drive the LED eliminating the high current changing due to little variations in forward voltage control. Indeed, the high slope of the voltage–current curve leads that a small change of voltage that can carry on a significant change of current through the diode consequently, a considerable change of the emitted light appears. To avoid any flickering, LEDs need a constant current source [13]. Furthermore, constant current control circuits are robustness for the load short-circuit but suffer the load fully open conditions.

The LEDs can be driven by different kind of passive or active circuits. Furthermore, the active driver circuits can be classified in linear or switching topologies.
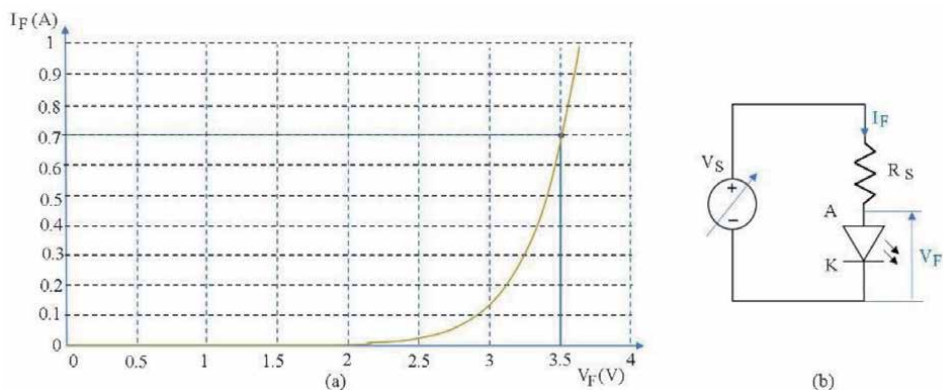
Figure 1.
(a) I-V curve characteristic for a white LED, (b) schematic of characterization circuit.

2.1 Passive drive circuits

The quantities of current and voltage to be supplied to the LED to achieve the required brightness can be provided with different circuits. Passive LED drivers feature the exclusive use of passive components (e.g., resistors, capacitors, magnetic components) and silicon diodes. The simplest and most reliable circuits are passive ones. This simple and cost-effective circuits do not exhibit performance like linear or switching driver circuits and operate without precise control of the output current. They generally provide a DC current with AC current ripple but are still used in those cases where reliability and continuity of service are prevailing parameters comparing to dynamic performance and efficiency. Examples of applications are outdoor street-lights that operating in difficult environmental conditions where complex circuits can be more vulnerable. Use of an impedance between the ac line and the LED light bulb load to fix and limit the current is mandatory. The main drawbacks of these passive topologies are the low PF and THD featured, sometimes not enough to comply with the standards [14]. Passive LED drivers can be arranged in two main categories, lossy and lossless (ideal) passive circuits [15].

The lossy passive driver is usually composed of a transformer that lowers the mains voltage to one compatible with the number of LEDs to be driven (The load is generally composed of LED arrays), a bridge rectifier circuit which rectifies the alternating voltage, an electrolytic capacitor which reduces the AC ripple and finally a resistor in series with the LEDs. The current limitation is achieved by means of a simple resistor. In some LED driver applications, a linear circuit replaces the resistor [16]. The traditional passive circuit described is represented in **Figure 2a**. The step-down transformer reduces the voltage drop on the resistor R_S leading to an increase in the overall system efficiency. Furthermore, the transformer guarantees galvanic isolation. A large electrolytic capacitor C_S is used to reduce the ripple appropriately in order to avoid flickering. The large value of C_S necessary lead to pulsating input currents which high harmonics contents. Generally, the PF of such circuits is low and hardly is comply with the Class D limit [17].

In this type of passive driver, the main cause of the efficiency reduction is the conduction losses of the R_S resistor.

The "lossless" drivers use to limit the current of the LEDs ideally a lossless impedance (such as inductors and capacitors). An inductor positioned on the AC side can be used to limit the current as shown in **Figure 2b**. The inductor L_{in} produces an impedance that withstands the voltage difference between the input voltage V_{AC} and the output voltage V_0 required across the LEDs. The L_{in} impedance does not require the step-down transformer of the previous circuit solution. Furthermore, L_{in} acts as an input filter. As consequence on the DC side, after the rectifier bridge, it is possible to use a capacitor C_S with a smaller capacity and therefore not electrolytic. The use of non-electrolytic capacitors allows a long life of the entire system. The L_S on the DC side is used to convert the rectifier output
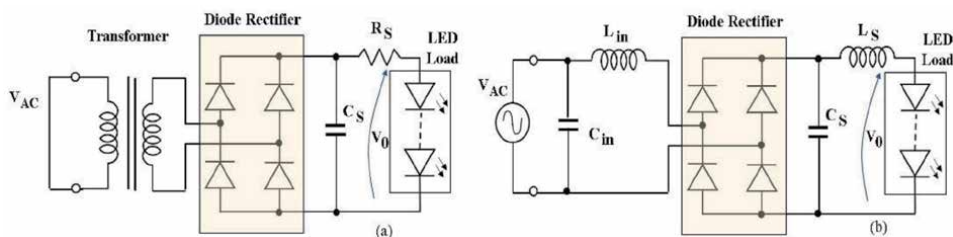
Figure 2.
Passive LED driver circuit. (a) Lossy passive circuit, (b) lossless passive circuit.
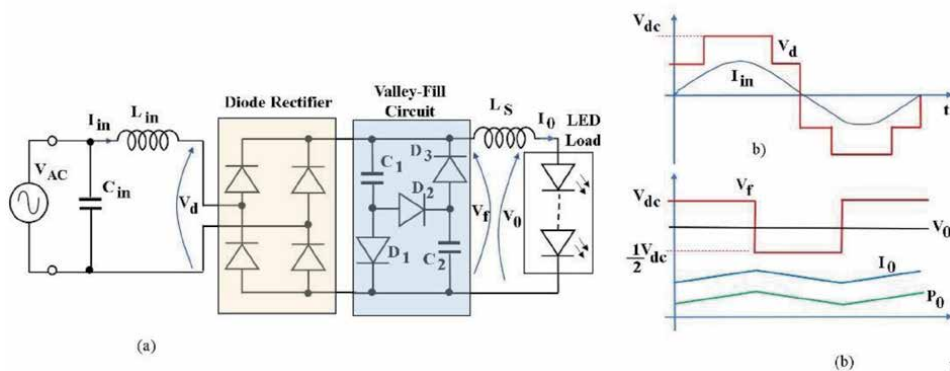
Figure 3.
(a) Passive driver circuit with valley-fill circuit. (b) Idealized waveforms of circuit operation.

voltage into a direct current source I_0 to drive the LED load. The input capacitor C_{in} is useful for further improvement of the input power factor. The use of a power factor correction capacitor C_{in} is a standard method used in the magnetic ballast in the case of fluorescent lamps [18].

A passive driver circuit using the Valley-fill topology is depicted in **Figure 3a**. The Valley-fill circuit has been widely used in ballast systems for powering gaseous discharge lamps. It allowed having a power factor of 95% without the need for additional control [19]. In the case of LED diode drivers, Valley-fill enhances the improvement of the ripple of the output voltage, maintaining an adequate quality of the current waveform at the input thanks also to the presence of the L_{in}. Also in the Valley-fill circuit the capacitors used are not electrolytic. The idealized waveforms of the main input and output voltages together with the power P_0 are shown in **Figure 3b**. The analysis of the presented waveforms is reported in detail in [20].

2.2 Active drive circuits

In low power applications, linear regulators are used extensively. As power increases due to losses, these regulators are replaced by current regulated switching converters. In many applications, the LED diodes in single or in string configuration are used as indicators (smart home devices, LED displays, rear lights, directional lights in the automotive sector, animated LED circuits, etc.) with linear regulators using dedicated integrated circuit (IC) devices.

The principle of operation of a linear regulator is shown in **Figure 4a**. the necessary constant current is established by means of feedback through a sensing resistor and a comparator circuit which compares a reference voltage with the actual voltage on the sensing resistor. The necessary LED current is established by the relation (2).

$$I_{LED} = \frac{V_{REF}}{R_S} \qquad (2)$$

This type of regulator is usually realized in an integrated way. The integrated solution is more attractive because reduces board space and component count, simplifying circuit and system designs [21]. In **Figure 4b** the application circuit of an integrated regulator (IC) with battery source (NUD4001 - On-Semiconductor) for driving up to 500 mA of a LED strings is shown [22].
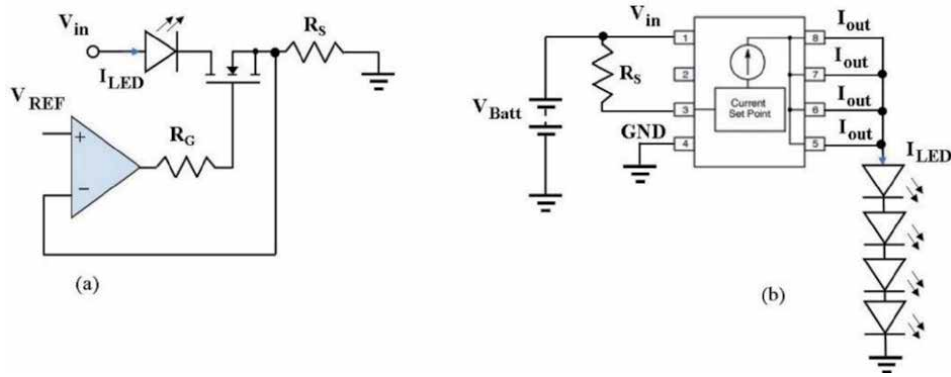
Figure 4.
(a) Operation principle of a linear regulator LED driver. (b) Schematic of actual IC (NUD4001) for a string LED driver applications.

Driver topology	Current control method	Advantage	Disadvantage
Passive	Resistor	• Easy design procedure • Low cost	• Not accurate current control • High power dissipation on the resistor for high power LED • Low Efficiency with increasing LED power request
Active Linear	Linear control loop	• Accurate current control • Capability of dimming by current control • do not require electromagnetic interference (EMI) filters	• High power dissipation with heat-sink need with increasing LED power request • Lower efficiency
Active switching	PWM current control	• High efficiency • Dimming capability by PWM control	• More complex design • Higher cost • EMI design constraint

Table 1.
Design constraint comparison for passive and active driver circuits.

The ever increasing demand for LED systems with high brightness and improved energy efficiency, especially for portable power applications, has led to the introduction of more and more advanced switching LED current control drivers with various features and better current matching/regulation. The use of power devices in switching operation allows to overcome the limits of linear regulators regarding efficiency [23]. Furthermore, the increasing switching frequency of the last generation power devices allows using inductor and high-frequency (HF) transformer with reduced core size featuring compact volume [24]. Several converter topologies are available depending on the power range and other characteristics such as galvanic isolation need, size and cost-effectiveness, easy dimming capability, modular approach availability and efficiency target. In switching converters, the current and voltage control is achieved by pulse width modulation (PWM) strategy. In a battery source, the switching LED driver is effective in the management of multiple LED strings and array in several kinds of application such as in automotive or in portable electronics devices [25]. The main design features of switching driver circuit with pros and cons compared with linear and passive solutions are reported in **Table 1**.
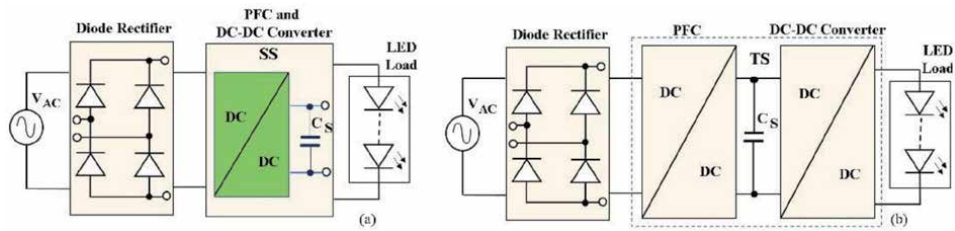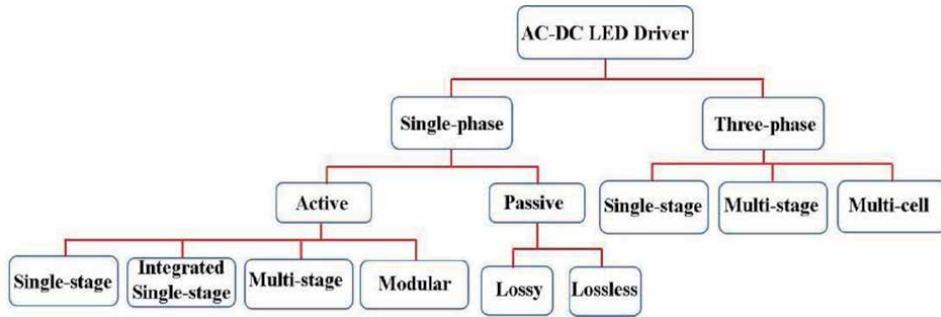
Figure 5.
(a) SS switching driver block schematic. (b) TS switching driver block schematic.

In the AC source the switching LED drivers are used specially in indoor application. For the topologies attached to the electricity grid, the power factor plays a crucial role. Two solutions are pursued. In the first solution, the PFC can be composed within a single stage together with the actual driving circuit. In this case, it is referred to as a single-stage driver (SS). The SS driver block schematic plus the filter capacitor C_S are reported in **Figure 5a**. In the SS driver circuit, the filter capacitor is usually connected after the DC-DC converter, which is on the high-frequency side to obtain a high PF [26, 27]. In the second approach, the driver topologies have a two stage (TS). The first stage is a front-end PFC converter and the second stage is a DC-DC converter which controls the requested current in a string of LED [28]. In **Figure 5b** the block schematic of a TS driver is depicted. In TS driver the filter capacitor is placed between the two semi-staged downstream from the PFC DC-DC converter to obtain high PF. SS drivers arrangement can significantly increase efficiency by dramatically reducing component cost and volume at the expense of more complex control. In the case of light bulbs of reduced power and small dimensions, single-stage topologies are certainly to be preferred. The TS solution provides accurate and flexible control also with dimming feature of the DC-DC converter separated by the PFC control design at the expense of additional circuitry and cost. Furthermore, with the second stage DC-DC converter, is possible the use of a not electrolytic capacitor. The second stage compensates the low-frequency ripple on the output voltage to achieve an AC-DC LED driver with a lifetime comparable to that of the LED devices. In the range of medium power, SS or TS topologies choice depending on the trade-off of the design constraints. Generally, TS approach is suitable in higher power applications.

In case of industrial environment and higher power request for high-brightness Light-Emitting Diodes (HB-LEDs), three-phase AC source can be supplied. In these applications three phase rectifier can be used to power the DC-DC converter. In three-phase AC source also a multi-cell converter solution may be used. In this topology approach, three single-phase converters in a star or delta connection to the three-phase power grid are arranged and linked in parallel connection at the output [29]. Finally, in **Figure 6a** block diagram classification of ac-dc LED drivers for both single-phase and three-phase AC source are summarized.

3. DC-DC converter topologies for LED driver circuits

The LED driver circuits topologies selection depending on three basic needs. The kind of energy sources (DC or AC), the power requirement and the galvanic isolation features. In the following, as the first study case, the converters for DC sources are investigated.

Figure 6.
Block diagram of AC-DC LED driver circuits classification.

3.1 DC-DC converter circuits

LED drivers often require step-up/step-down regulation DC/DC converters. The power converters supply constant current at a voltage from a not constant input voltage (actual battery source). The battery source voltage can be higher or lower than the load request. The converter output voltage can be regulated by the power switch duty ratio modulation strategy (PWM), taking into account a feedback adjustment by the output current [30]. Considering a single switch converter, a simple buck converter is a basic topology for the voltage and current control of the LED string (**Figure 7a**). It enables simple, efficient and cost-effective solutions for driving regular and high-brightness LEDs. In steady-state the duty cycle regulates the output voltage by the duty cycle (d) duration (3).

$$V_0 = d \bullet V_{in} \tag{3}$$

Multiple LEDs solution need an adequate voltage amount. Step-up (boost) LED drivers acting with a current control achieving a higher load voltage of the DC source available (**Figure 7b**). In this step-up converter, in steady-state conditions, the output voltage is higher than the input voltage as described by

$$V_0 = \frac{1}{1-d} V_{in} \tag{4}$$

In case of a wide input voltage range, a buck-boost topology is preferable. In the buck-boost converter, the output voltage is regulated by

$$V_0 = \left| \frac{d}{1-d} \right| \bullet V_{in} \tag{5}$$

In this converter the output voltage has an opposite polarity than the input voltage (**Figure 7c**). Furthermore, the diode D_S and C_0 in the output stage can provide an LED short circuit protection feature. This circuit property, for example, is very crucial in automotive applications.

An improving alternative is the Ćuk converter. It is composed of a boost converter followed by a buck converter. As the buck-boost, it is suitable in applications where an input voltage from a continuous source (e.g. battery) can be greater or less than the requested output voltage. It maintains the same regulation law at steady-state of the traditional buck-boost converter with inverted polarity in the output voltage. The Ćuk converter features some benefits compared with the buck-boost converter in the matching of the LED driver design constraint. The topology
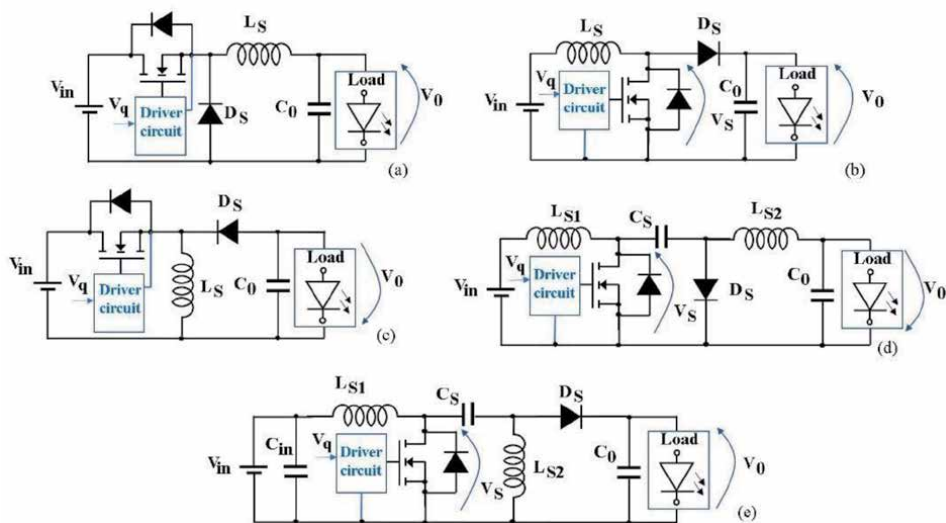
Figure 7.
Non isolated converter for LED driver circuits. (a) Buck converter (b) boost converter, (c) Buck- boost converter, (d) Ćuk converter, (d) SEPIC converter.

structure achieves low input and output current ripples [31]. The presence of an inductor in the input stage of the circuit allows a smoothed input current wave-forms. Furthermore, the LC filter in the output stage facilitates a smooth current waveform (**Figure 7d**). Moreover, this converter has four energy storage devices (two inductors and two capacitors) which can provide higher output power compared to other converters such as buck, boost and buck-boost of the same electrical characteristics. The disadvantage of this topology is a higher number of passive components and more complex control. Another interesting topology is the SEPIC converter [32]. It has the advantages of low input current ripple achievement due the presence of the LC filter in the input stage (**Figure 7e**). Furthermore, the output voltage is not inverted polarity. The drawbacks are as a Ćuk converter the higher number of passive components and more complex control due to fourth order dc-dc converter transfer function. Moreover, SEPIC converter has a higher voltage stresses on the power switch.

$$V_S = V_{in} + V_0 \tag{6}$$

To reduce the current ripple every converter described usually operated at constant current mode (CCM) and the power rate of these converter applications is up to about 150 W.

3.2 Current control in LED driver DC-DC converter circuits

A basic control system to reach the requested LED brightness a peak current control (PCC) is widely used for drive based on Buck, Boost and Buck-Boost converter topologies. In the following, for simplicity, the Buck converter control strategy is investigated, but the considerations that will be made can be easily extended for the other topologies already described. In the Buck converter, the current sensing resistor can be connected to the source of MOSFET devices (**Figure 8a**). In this way, the current is only sensed during the on-state of the MOSFET switch compared to the sensing resistance located in load side, reducing power losses. Generally, the Buck converter topology can be rearranged in a
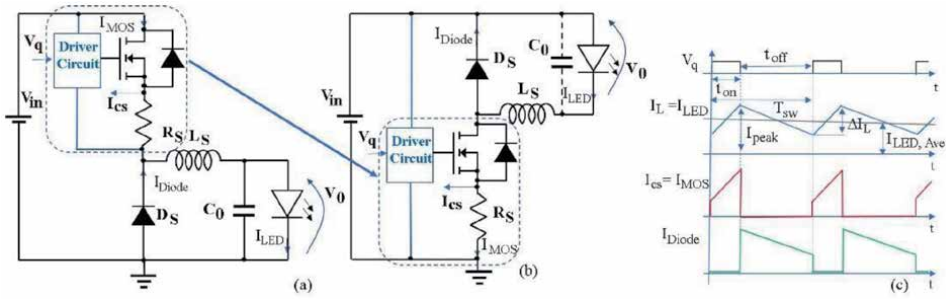
Figure 8.
Buck converter with MOSFET with the sensing resistance layout arrangement in the traditional in (a) high-side location and in (b) low-side position. (c) Switching waveforms of command signal V_q and the main converter currents.

different way to reduce the noise signal, positioning the sensing resistor with a pin to ground (**Figure 8b**). The capacitor C_0 in some industrial application, in low side MOSFET solution, is removed as highlighted in **Figure 8b** (LUMILED HB-LED arrangement) [33]. The main switching current waveforms and the gate control voltage V_q in steady state conditions are reported in **Figure 8c**.

The operating principle of the PCC control is shown in **Figure 9** in the condition with the low-side MOSFET and the sensing resistor between source and ground.

The current control works as follows. The clock signal leads the control signal V_q high and the current in the inductor ramps up. When the transduced MOSFET current I_{cs} reaches the reference I_{peak}, the comparator resets the command signal and at the next clock signal, the control cycle is repeated [34]. The schematic of the PCC control is depicted in **Figure 9a**. The main control waveforms and the LED current are reported in **Figure 9b**. From **Figure 9b** the current ripple, ΔI_L, is evaluated by:

$$\Delta I_L = \frac{V_{in} - V_0}{L_S} t_{on} = \frac{V_0}{L_S} t_{off} \tag{7}$$

The average LED current $I_{LED,Ave}$ can be calculated as

$$I_{LED,Ave} = I_{peak} - \frac{\Delta I_L}{2} = I_{peak} - \frac{V_0}{2L_S} t_{off} \tag{8}$$

$$I_{LED,Ave} = I_{peak} - \frac{V_0 T_{sw}}{2L_S}\left(1 - \frac{V_0}{V_{in}}\right) \tag{9}$$
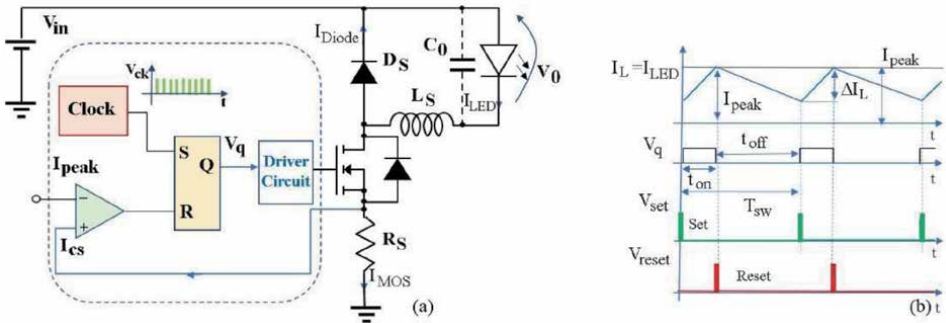
Figure 9.
Peak current control technique (a) circuit schematic of the control method and Buck in low side MOSFET solution. (b) Main control signal and led current behavior.

As demonstrated in (9) the LED current depends on V_{in}. A large variation of V_{in} affects the $I_{LED,Ave}$ losing control accuracy with respect to the I_{peak} reference.

A more accurate control should contain compensation for the variation of the input voltage V_{in} in order to keep the LED current closer to the reference value I_{peak}.

The CPM technique achieves the following advantages

- Simply control circuit implementation and robust;

- Constant switching frequency strategy, with constant switching losses.

- Intrinsic short circuit protection. MOSFET failure for over current can be controlled by limiting the maximum reference current;

- In converter application with isolating transformer, the saturation problems can be reduced;

- Easy LED driver module application capability. The modules can be connected in parallel with equal current sharing providing equal current control for each module.

As disadvantages have

- Susceptibility to noise;

- Sensitive to the wide V_{in} variation.

Finally, the current regulation of LED to obtain a dimming effect combine the PCC strategy and an adjustable PWM signal. A conventional circuit structure is shown in **Figure 10**.

To avoid inaccuracy in the controlled current a hysteresis-current control (HCC) technique can be implemented. In HCC strategy is necessary to control the on and off current value. The controlled current is always included within a defined hysteresis band [33]. In this control solution, the sensing resistor can be positioned in series to the LED, thus the high-side MOSFET buck layout may be used, as shown in **Figure 11a**, to allocate the sensing resistor with a grounded pin [35]. The sensing
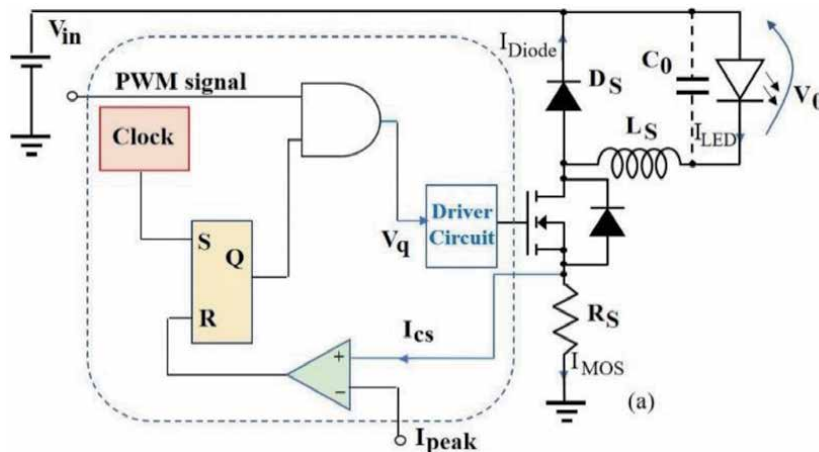
Figure 10.
Schematic of driver circuit with PCC strategy combined and PWM control signal to act the dimming effect.
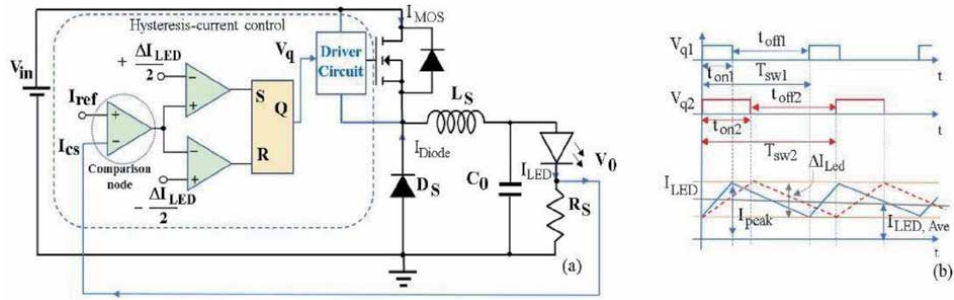
Figure 11.
(a) HCC control scheme in high-side MOSFET Buck converter. (b) The controlled current behavior with a fixed hysteresis band in two different cases of the control signal V_q.

current is compared with a reference current and the error is forward to a window detector with the band levels positive and negative requested. The controlled current behavior with a fixed hysteresis band in two different cases of the control signal V_q is reported in **Figure 11b**. The HCC technique is non-constant frequency control.

The advantages of this control strategy are

- Fixed band hysteresis control does not present stability problems

- low software requirements in digital form implementation,

- high reliability, and less tracking error.

The main disadvantage is the non-constant frequency control. It means a switching losses variable and generally higher compared with the previous control method. But with the new generation of wide-bandgap devices such as GaN, the switching losses are strongly reduced and this control method is more attractive [36].

A further hardware arrangement to achieve switches losses reduction in buck converter is the use of a MOSFET (or GaN) devices to replace the diode D_S working in a synchronous way with the high-side switch [36].

3.3 Higher power LED driver DC-DC converter and galvanic insolation feature

As the power required for driving LEDs increases, more complex topologies and galvanic isolation is required to isolate the DC source from the LED strings, increasing safety and protection against short circuits on the load side. In the field of medium power (up to about 100 W) the Flyback topology is usually the one most used for the reduced number of components, low cost, together with efficiency even above 90% (**Figure 12**). The increase in efficiency depends on the type of switch selected, whether pure silicon or wide-bandgap devices [37]. The presence of two inductances coupled to transfer energy between the primary side and the secondary side allows the galvanic isolation required in many applications. The Flyback converter is an isolated arrangement of the Buck-Boost converter. The output voltage depends on the ratio of the number of windings on the primary side and secondary side and maintains the Buck-Boost converter duty cycle dependence (10).

$$V_0 = \frac{N_s}{N_p} \cdot \frac{d}{1-d} \cdot V_{in} \tag{10}$$
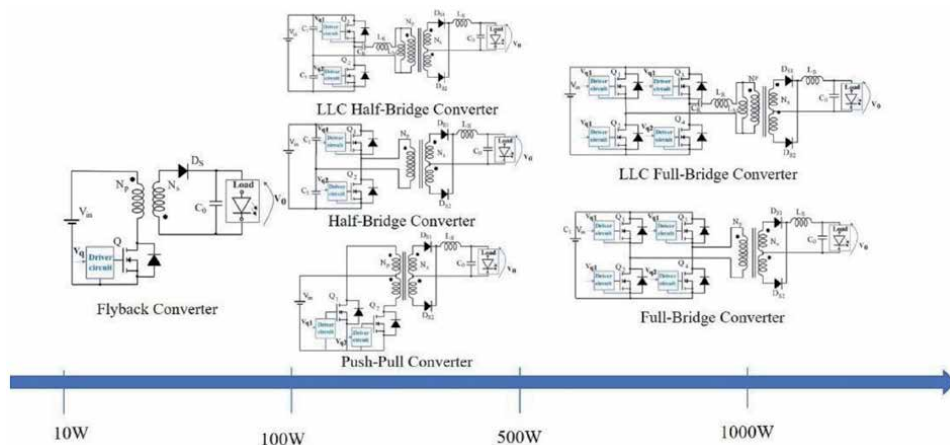
Figure 12.
A qualitative estimation of the isolated application versus the power rate.

It works with a DC power supply and therefore falls within the classification outlined. Usually, the Flyback converter is used attached to the grid to create single-stage AC/DC drivers, thus it will be more fully discussed in the next session.

In the Flyback converter, the single switch use limits the power rate. Furthermore, a single switch does not make the best exploitation of the magnetic hysteresis loop, producing losses in the magnetic core [38]. In the field of higher powers, topologies based on Half-Bridge, Push-Pull and Full-Bridge converter are applied to supply high current. These converters all have high-frequency transformers that allow galvanic isolation. The high switching frequencies used (around hundreds of kHz with wide-bandgap devices) achieve a transformer volume reduction. An additional advantage of the transformer is the availability to feature several secondary windings. Therefore, several LED strings can be supplied at the same time also with different strings arrangement. The Half-Bridge converter (**Figure 12**) has the following transfer function

$$\frac{V_0}{V_{in}} = \frac{N_s}{N_p} \bullet d \qquad (11)$$

To avoid devices cross conduction, the duty cycle must be d < 0.5. It has the following pro and cons.

Pro: better transformer utilization, best application up to 500 W, single winding primary, switch voltage limited stress (equal to V_{in}).

Cons: hard switching operation, floating driver circuit need for the high side MOSFET, high primary current stress.

The Push-Pull converter operates in hard switching at d < 0.5. It has the same transfer function of the Half-Bridge converter multiplied by 2. In the Push-Pull converter the MOSFETs driver circuits are more simple because there are two switches in low side position (**Figure 12**). Push-Pull topology features lower input ripple than the Half-Bridge. On the other hand, at turn-off the switches have higher voltage stress are ($2V_{in}$). Furthermore, in the primary side the transformer is center tapped [39].

The Full-Bridge structure is composed of four switches (see **Figure 12**). It has a twice transfer voltage ratio as the Half-Bridge topology and operating with d < 0.5. It features twice the power rate than the Half-Bridge solution with equal MOSFETs voltage stress (equal to V_{in}), but it has a more complex structure.

To reduce power losses with increasing efficiency, in higher power driver converter topologies, solutions with soft switching operation have been increasingly used. In these circuit types, the LLC resonant converter in half-bridge and full-bridge topologies are the most studied and applied [40]. The LLC resonant converter operation will be better discussed in the next section.

In **Figure 12** qualitative estimation of the isolated power converter topologies versus the output power rate are shown.

4. AC connected switching LED driver circuits

LED driver circuits connected to the grid must meet several requirements regarding the frequency and the quality of the waveforms that are linked to the grid. The power factor must be controlled by means of a dedicated PFC circuit. Furthermore, it is necessary to keep the levels of Electromagnetic Interference (EMI) contents introduced into the grid low. Also, the flicker limits for LEDs must be considered.

In the design of drivers connected to the electrical network, before finding the circuit solutions it is essential to know the regulations and recommendations that an LED driver must comply with. The following design rules and standards must be taken into consideration.

- the ENERGY STAR® program recommendations, with specific regulations and requirements for LED lighting equipment [41],

- the harmonic standard (i.e. IEC 61000–3-2),

- flicker rules and metrics [14].

To observe the design constraints, the driver circuit is composed of several modular blocks. Each block meets certain requirements. In **Figure 13**, the schematic of the LED driver for an AC lighting system is reported. From the line to the load (LED strings), there are the EMI filter, the diode rectifier, the PFC and the DC-DC converter. This schematization has been referred to as a dual-stage driver. If the power factor correction is integrated into the control in the DC-DC converter, then it is referred to as a single-stage driver.

4.1 Flyback single stage LED driver circuit

The single-stage LED driver is very attractive. On the other hand, it has to combine the control both the PF and the current to be supplied to the LEDs. The topology widely used in these applications is the Flyback converter especially at power rates below 100 W. The structure of the Flyback converter has the least
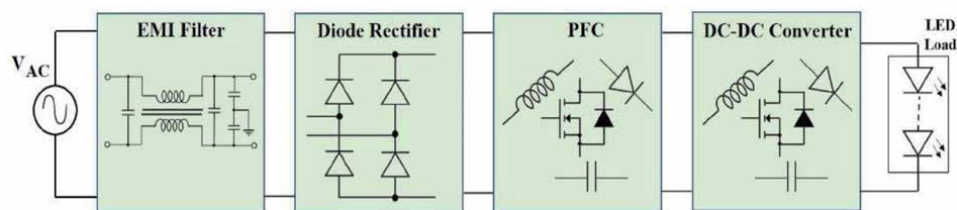
Figure 13.
*Blocks schematic of a AC source LEDs driver circuit.*

components compared with other isolated converters, and many studies have been conducted on the grid connection to obtain high PF and low THD [42, 43]. In the LED driver application, the operative conditions usually used is a critical conduction mode (CRM) or the discontinuous conduction mode (DCM) [44]. In DCM (or CRM) the switch turn-on can be driven when the transformer is completely demagnetized, thus transformer saturation is avoided. The efficiency of the Flyback converter can be increased using the soft-switching technique exploiting the parasitic components present in the structure of the converter and of the power switch (**Figure 14a**). The quasi-resonant (QR) mode is used in the Flyback application to reduce the switching losses despite the non-constant frequency operation. Moreover, the QR operation allows has an enhanced transient response in DCM operation and it features a smaller EMI filter [45].

In addition, the QR Flyback LED driver has higher safety properties under output short circuit conditions. In the QR operation, the MOSFET is not turned on until the primary windings are fully demagnetized. On the other hand, a high ripple output current and high output diode and switch conduction losses in comparison to the fixed frequency driver. A further drawback well know is the high voltage stress on the switch given by

$$V_{DS,peak} = V_{in} + \frac{N_p}{N_s}V_0 + V_{stray} = V_{in} + V_r + V_{stray} \tag{12}$$

Where V_r is the output voltage reflected in the primary side and V_{stray} is the peak voltage of the ringing at turn-off transient due to the equivalent primary inductance L_{ps} and the equivalent parasitic capacitance (C_{ps}) composed by the output MOSFET capacitor and the equivalent primary side stray capacitor (**Figure 14a** and **b**). The resonant frequency f_{rs} is

$$f_{rs} = \frac{1}{2\pi\sqrt{L_{ps} \bullet C_{ps}}} \tag{13}$$
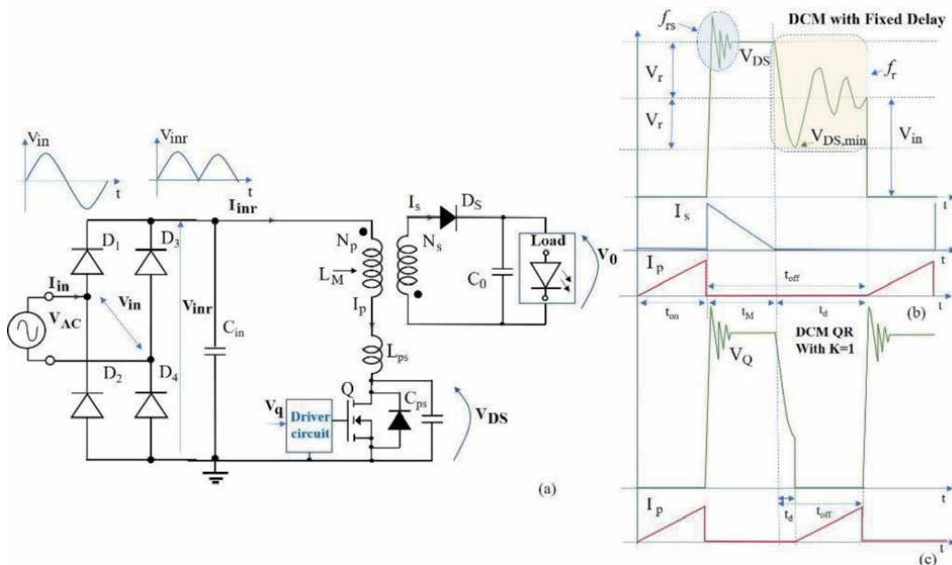
Figure 14.
(a) Schematic of Flyback converter with the stray inductance and capacitance reported on the primary side. (b) DCM operation at td constant. (c) DCM in QR operation with k = 1.

In a DCM traditional operation flyback converter, the gate driver acts with a constant switching frequency, while in a QR operation a variable frequency is featured [46]. To turn on the switch a demagnetization time t_M is necessary. After t_M, a natural oscillation typical of a second-order system appears. The resonant frequency f_r is lower than f_{rs} and is related to the equivalent primary inductance L_p composed by the magnetization inductance L_M and the equivalent stray inductance on the primary side L_{ps} with the equivalent parasitic capacitance.

$$f_r = \frac{1}{2\pi\sqrt{L_p \bullet C_{ps}}} \tag{14}$$

A simplified Flyback converter with the stray inductance and equivalent parasitic capacitor on the primary side linked to the AC source by a rectifier bridge is depicted in **Figure 14** a. In DCM operation at a constant frequency, a constant delay time t_d is added to t_M to compose the turn-off time. In QR operation a resonant valley detection achieved by the control circuit is provided to switching at lower power losses. **Figure 14b** depicts the drain-source voltage waveforms and the current both in the primary and secondary side in DCM with constant frequency operation and QR operation with the turn-off at the first valley (**Figure 14c**).

The switching period T_{sw} is

$$T_{sw} = t_{on} + t_M + t_{osc} \tag{15}$$

Where t_{osc} is the complete ringing time for the V_{DS}

$$t_{osc} = \frac{1}{2}[1 + 2(k-1)]\frac{1}{f_r} \tag{16}$$

As reduced load t_{on} is reduced yet. At light load, the switching frequency is higher. Also, the ringing time t_{osc} increase with the decrease of the load [47]. The quantitative k specifies the number of rings within t_{osc}. Even, the number k is inversely proportional to the load. The control strategy acts considering the k to detect the better valley point to turn-off. At light load, the controller can be operated considering k different from 1 because the losses are still reduced. At high load, the k usually considered is equal to 1 to reduce drastically the losses.

4.2 Control method to obtain high power factor

The market requirements are based on standard IEC61000–3-2. It defines some input current THD targets (e.g., <10% at full power) that are very difficult to achieve, especially when working with lighting equipment over 25 W.

As know, the distortion corresponding to the harmonics contents. The distortion power factor DPF in the hypothesis of a perfectly sinusoidal input voltage is

$$DPF = \frac{1}{\sqrt{1 + THD_i{}^2}} = \frac{I_{in1,rms}}{I_{in,rms}} \tag{17}$$

Where THD_i is the input current total harmonic distortion. The current $I_{in1,rms}$ is the baseband component of the current, while $I_{in,rms}$ is the total input current. The true Power Factor (TPF) in non-linear grid load such as the power converter is related to the Distortion Power Factor and the Displacement Power Factor.

The Displacement Power Factor is due to the phase shift between voltage and current at the fundamental line frequency. It is defined as the ratio between the real

power average P_{ave} and the apparent power in perfect sinusoidal waveforms the displacement power factor is equal to cosφ. Thus, in case of pure sinusoidal system, Displacement Power factor and True Power factor are equivalent.

In switching operative condition displacement power factor is established as

$$PF_{disp} = \frac{P_{avg}}{V_{in1,rms} \bullet I_{in1,rms}} \tag{18}$$

Where $V_{in1,rms}$ and $I_{in1,rms}$ are the first harmonic of the AC voltage and current respectively. The P_{avg} is defined as

$$P_{avg} = \sum_{i=1}^{\infty} V_{in(i),rms} \bullet I_{in(i),rms} \bullet \cos \varphi \tag{19}$$

Neglecting the Harmonic beyond the first one is valid the approximation of P_{avg1} related to the first harmonic quantities equal to P_{avg}, the true power factor can be established as the multiplication between the Distortion Power Factor and the Displacement Power Factor [48].

$$TPF = \frac{1}{\sqrt{1 + THD_i^2}} \bullet \frac{P_{avg1}}{V_{in1,rms} \bullet I_{in1,rms}} \tag{20}$$

In switching converter, to obtain a high TPF two target can be pursued: low THD_i and Displacement Power Factor very close to one. The control strategy target is to combine an input current quite close a sinusoidal waveform (high THD) with the same phase of the input voltage to reach high-PF. Furthermore, the common PFC control method is usually combined with a peak current control.

Indeed, several integrated control chips for Flyback converter are based on the peak current PFC control implementing also QR operation [49]. A basic function block diagram of the QR peak current mode IC is depicted in **Figure 15a**. In **Figure 15a**, V_{inr} is the rectified AC line voltage. V_{fb} is the signal feedback of the output voltage V_0. V_{ref} is the reference voltage. The output of the error amplifier 1 is a multiplier factor of a suitable reduced value of V_{inr} ($k_p{\cdot}V_{inr}$). The bandwidth of the error amplifier is quite low to have in a slow variation of the output error (low pass filter effect) with a low ripple. The output of the multiplier block is proportional to V_{inr}. The signal voltage V_{Rs} is related to the primary inductor peak current. If V_{Rs} reaches the output voltage of the multiplier V_{Mu} the pulse width modulation (PWM) signal is reset turning off the power switch Q. The turn-on is achieved by the valley detect circuit (VDC) obtaining the waveforms depicted in **Figure 15b** The VDC acts after the full demagnetization of
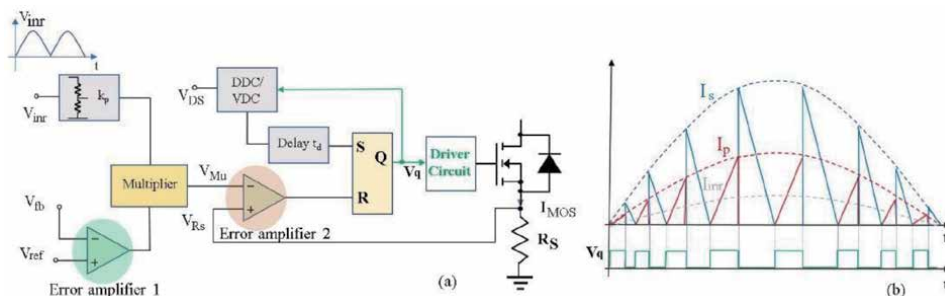
Figure 15.
(a) PFC control circuit simplified schematic. (b) Primary and secondary side current behavior and driver signal V_q.

the primary windings provided by an enable signal of a demagnetization detection circuit (DDC). The output signal of the VDC block set the delay time t_d. As shown in **Figure 15b** the current envelope both at the primary and secondary side is a half sinusoidal cycle. In particular, the inductor peak current will be a sine wave with the same phase as the input voltage, which can achieve a quite high-power factor. As above described, the control signal V_q has a non-constant frequency.

The controller can be used in the simple DCM operation without QR enhancement, replacing the VDC block with only the DDC and settling the delay time t_d at a constant value. In this last control approach, the driver signal V_q acts at constant frequency.

The control method investigation is based on the analysis detailed in [47, 50]. The control method quantities depending on the instantaneous line voltage. For simplicity of analysis in the following, the term $\theta = 2\pi f_{line}t$ is considered. Where f_{line} is the frequency of the grid line quantities. Furthermore, the analysis is based on the following hypothesis.

- The input voltage V_{in} is fully sinusoidal.

- The coupling between the inductors on the Flyback is ideal.

- The power switch and the diodes have conduction and switching losses negligible).

- The output voltage is constant in a line half-cycle.

- The Flyback converter operates in DCM and QR with k = 1

Based on the first assumption the voltage downstream the rectifier bridge is a rectified sinusoidal waveform.

$$V_{inr}(\theta) = V_{inr,pk} \bullet \sin\theta \qquad (21)$$

Where $V_{inr,peak}$ is the max peak amplitude of the rectified V_{inr}.

The current peak $I_{p,pk}$ at the primary side is enveloped by a rectified sinusoid as shown in **Figure 15b**. It is given by. It is given by

$$I_{p,pk}(\theta) = I_{p,PK} \bullet sin\theta \qquad (22)$$

Where $I_{p,PK}$ is the maximum peak amplitude of the enveloped current in the primary side. In the secondary side the $I_{s,pk}$ is proportional to the primary current.

$$I_{s,pk}(\theta) = n \bullet I_{p,pk} \qquad (23)$$

Where n is the transform ratio, n = N_p/N_s.

Considering the current I_p as a triangle form, as shown in **Figure 14b** and **c**, t_{on} is expressed by

$$t_{on} = \frac{L_M \bullet I_{p,pk}(\theta)}{V_{inr}(\theta)} \qquad (24)$$

At turn-off, t_{off} is

$$t_{off} = \frac{L_s \bullet I_{s,pk}(\theta)}{V_0} = \frac{L_M \bullet I_{p,pk(\theta)}}{n \bullet V_0} \qquad (25)$$

Considering the assumption of k = 1 and neglecting the t_d for simplicity (very close to the CRM operation). The switching time T_{sw} is given by

$$T_{sw} = t_{on} + t_{off} = \frac{L_M \bullet I_{p,PK}}{V_{inr,pk}} \bullet \left[1 + \frac{V_{inr,pk}}{V_r} \bullet |\sin\theta| \right] \qquad (26)$$

From (24) the minimum value of the stitching frequency $f_{sw,min}$ is achieved at $\sin\theta = 1$ (the peak of the rectified sinusoid).

$$f_{sw} = \frac{V_{inr,pk}}{L_M \bullet I_{p,PK}} \bullet \frac{1}{1 + \frac{V_{inr,peak}}{V_r}} \qquad (27)$$

The duty cycle is given by

$$d(\theta) = \frac{t_{on}}{T_{SW}} = \frac{1}{1 + \frac{V_{inr,peak}}{V_r} \sin\theta} \qquad (28)$$

The control strategy described above in **Figure 15b** leads to the envelope current on the primary stage following the sinusoid described by (22) and better specified as

$$I_{p,pk} = \frac{1}{L_M} \bullet \left(V_{inr,pk} \bullet \sin\theta \right) \bullet t_{on} \qquad (29)$$

The rectified input current $I_{inr}(\theta)$ can be established as the average value of the primary current in each triangle over a switching cycle (**Figure 15b**).

$$I_{inr}(\theta) = \frac{1}{2} \bullet I_{p,pk}(\theta) \bullet \frac{t_{on}(\theta)}{T_{sw}(\theta)} = \frac{1}{2L_M} \left(V_{inr,pk} \bullet \sin\theta \right) \bullet \frac{t_{on}^2(\theta)}{T_{sw}(\theta)} \qquad (30)$$

The constraint design condition for achieve a displacement power factor equal to 1 is

$$d^2(\theta) \bullet T_{SW}(\theta) = \left[\frac{t_{on}(\theta)}{T_{sw}(\theta)} \right]^2 \bullet T_{sw}(\theta) = \frac{t_{on}^2(\theta)}{T_{sw}(\theta)} = constant \qquad (31)$$

4.3 Two-stage LED driver circuits

The two-stage driver converter is more expensive in terms of components used but offering better immunity to line disturbances and greater flexibility because the power factor control is separated by the DC-DC current allowing more simple dimmable applications. Furthermore, the modular The wide solution for the PFC topology is a boost converter. In power converters such as the Boost (also the SEPIC and ĆuK converter, but with more numerous components than the Boost) the switch non directly disconnect the power source (see **Figure 7**). This causes a not complete interruption of the input current such as in the Buck or Buck-Boost topologies. Furthermore, the current ripple can be smoothly controlled from the converter, making the Boost topology very attractive for active PFC. To increase the power rate requested an interleaved solution can be adopted [51].

The second stage DC-DC converter topology depends on the power rate requested. Over the 100 W Half and Full Bridge topologies are implemented as described in **Figure 12**. Usually, an isolated resonant converter is considered to increase the efficiency and reduce the EMI contents. In the resonant topologies, the
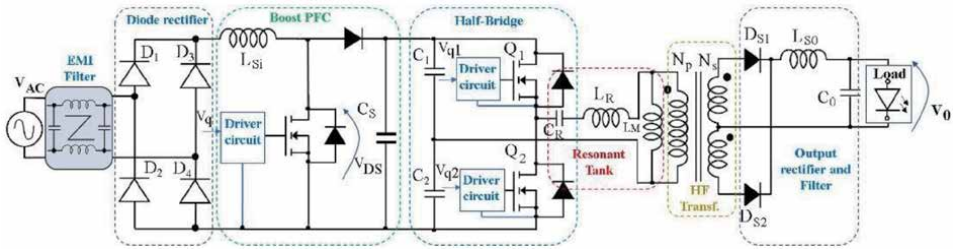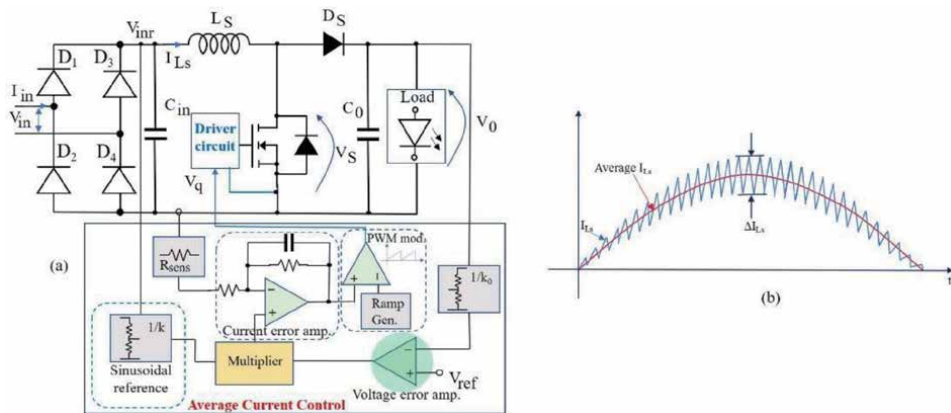
Figure 16.
Two stage LED driver circuit composed by PFC boost converter and half-bridge LLC converter.

LLC converter is mainly adopted in LED driver applications because of its soft-switching characteristic. The LLC converter features zero-voltage switching turn-on of the switches on the primary side and zero-current turn-off for the rectifier diodes on the secondary side. The soft-switching transients allow both low noises and reduced stress during the switches transients. In addition, the LLC converter regulates the output voltage in a wide-output voltage. Moreover, the isolated high-frequency transformer allows a multi-output driver circuit for the string LEDs solution. In **Figure 16** two stage LED driver composed by a Boost PFC converter and Half-Bridge LLC converter useful for load until 500 W is reported.

4.4 Boost PFC circuit evaluation

The Boost PFC converter has a simple topology. The switch driver circuit is referenced to the ground reducing the driver switching noises. Furthermore, it can guarantee a power factor close to one obtainable with several control techniques [52]. It allows an input current with low distortion and an output voltage with a very low ripple thanks to the presence of the capacitor C_s. On the other hand, the presence of the capacitor C_s produces high currents during converter switching on and has an intrinsic weakness in the short circuit as the output is connected directly to the input by means of the inductor L_s. At higher powers, it needs to run on CCM to ensure adequate power transfer. In this operation mode, the current in the inductor never reaches zero during the switching cycle. Usually, the most used controllers for these applications are based on the average current control that allows CCM operation. The Boost PFC scheme with the average current control is described in **Figure 17**.

Figure 17.
(a) Simplified block scheme of the boost PFC with average current control. (b) Inductor average and ripple currents.

The control loop to obtain the average current mode maintains the current proportional to the input voltage. While the voltage control loop regulates the output voltage to the boost value requested.

The advantages of the average current control are the following

- a constant switching frequency:

- little sensitivity to switching noises;

- the high quality of input current waveforms with reduced inductor current ripple

- the maximum peak current in the switching device is reduced

The disadvantages concern

- the need to sense the current in the inductor;

- the need to insert a compensation network in the current amplifier which takes into account the characteristics of the converter used and the duty point during the line voltage cycle.

In **Figure 17b** the inductor average current behavior and the inductor current ripple are shown. The value of ΔI_{Ls} is chosen during the design phase in the range from 20 to 25% of the peak of the input current I_{in}. The input peak current in the case of pure sinusoidal waveform is given by

$$I_{in,pk} = \frac{\sqrt{2} \bullet P_{in,max}}{V_{in,rms,min}} \tag{32}$$

Where $P_{in,max}$ is the input power at the maximum output power requested. It is given by

$$P_{in,max} = \frac{P_{0,max}}{\eta_{min}} \tag{33}$$

With η_{min} is the minimum converter efficiency.
The peak inductor current is

$$I_{Ls,pk} = I_{in,pk} + \frac{\Delta I_{Ls}}{2} \tag{34}$$

Where

$$\Delta I_{Ls} = K_{\Delta I} \bullet I_{in,pk} \tag{35}$$

Where $K_{\Delta I}$ is the inductor ripple factor (supposing 20% of the ΔI_L maximum, $K_{\Delta I} = 0.20$). To design the Boost inductance, the duty cycle at the peak of the minimum sinusoidal input voltage is considered. The value of the rectified voltage is obtained from

$$V_{in,pk,min} = \sqrt{2} \bullet V_{in,pk,min}(\theta) \tag{36}$$

The duty cycle at the minimum input voltage and considering the required output voltage (approximately it is a constant voltage) is calculated by

$$d = \frac{V_0 - V_{in,pk,min}}{V_0} \tag{37}$$

then, the inductance L_s is given by

$$L_s = \frac{V_{in,pk,min} \bullet d}{f_{sw} \bullet \Delta I_{L_s}} \tag{38}$$

The purpose of the output capacitor C_{in} in **Figure 17a** is to filter the high-frequency current component of the inductance.

The HF capacitor acts as an EMI filter minimizing the HF harmonic component (this HF current component are shorted by C_{in}) [53].

The HF capacitor design is a trade-off to minimize the noise injected into the line grid and the value that avoid zero-crossing line current distortion. C_{in} is given by

$$C_{in} = K_{\Delta I} \bullet \frac{I_{in,pk}}{2\pi \bullet f_{sw} \bullet r \bullet V_{in,pk,min}} \tag{39}$$

Where $K_{\Delta I}$ = 0.20 and r is input voltage ripple factor ($\Delta V_{in}/V_{in}$) settled usually in the range of 5–6%. An HF film capacitor with low ESL and high-voltage rating (630 V for European line voltage of 230 V). Usually, ceramic technology capacitor is selected for this converter application.

The output capacitor selection C_0 is related to the output voltage maximum ripple required (ΔV_0). C_0 is calculated by

$$C_0 \geq \frac{P_0}{2\pi \bullet f_{sw} \Delta V_0 \bullet V_0} \tag{40}$$

As the required power increases ($\geq$500 W), the PFC converter performances can be optimized by adopting an interleaved solution. The interleaved Boost topology is obtained connecting two or more single Boost legs as shown in **Figure 18**, controlling the switching of every MOSFET with a proper control strategy.

The command signals of the switches are supplied in out of phase mode according to

$$phaseshift = \frac{360°}{N_c} \tag{41}$$

where N_c is the number of legs in the interleaved boost circuit. Despite the increase in the number of components and a more complex control technique, in the interleaved topologies several advantages are shown.

- Reduced overall input current ripple.

- Reduced electromagnetic contents and consequently EMI filter.

- Reduction of the magnetics components size.

- RMS current rating decrease in the output capacitance.

- Use of the power semiconductor devices with a less current rate.

- Reduction of conduction diode and MOSFET losses thanks to the parallel structure.

In the interleaved topology the reduced current ripple allows to avoid the capacitor C_{in}. A complete design of 3 kW PFC based on an interleaved PFC Boost converter is reported in [54]. The control technique is based on Microcontroller Units (MCUs) or specialized Integrated Circuits (ICs). An example of the high-performance IC controller of common use is the FAN9673 (On-Semiconductor) [55]. It is an interleaved three−channel CCM PFC controller, implementing a channel management function. It enables a single cell at light load (less than one-third of the rated load) or two or three cells depending on power − level request. The interleaved cells management optimizes PFC efficiency. Three legs interleaved Boost PFC schematic linked to the line grid by a diode rectifier bridge and EMI filter is shown in **Figure 18**.

4.5 Half-bridge LLC converter notes

LLC resonant converter in its half-bridge implementation is more popular in LED driver circuit for the low switching noise and the capability to achieve a high-power density. An HF transformer is used to attain galvanic isolation. A compact volume is obtained by integrating part of the resonant tank into the HF transformer sizing. In this design approach, the transformer arrangement leads to satisfying the requirements on L_M and L_R, thus avoiding adding additional external components. Thus, the transformer inductive parameters and a series-connected capacitor C_R are used to make a resonant tank. The LLC solution allows Buck and Boost transfer characteristics in the soft-switching operative region. The switching devices Q_1 and Q_2 operate at a duty cycle of just under 50% to avoid cross conduction. The output voltage is regulated through a variation of the converter switching frequency. The converter features two resonant frequencies. The resonant frequency depends of the resonant tank components and the load conditions. The higher resonant
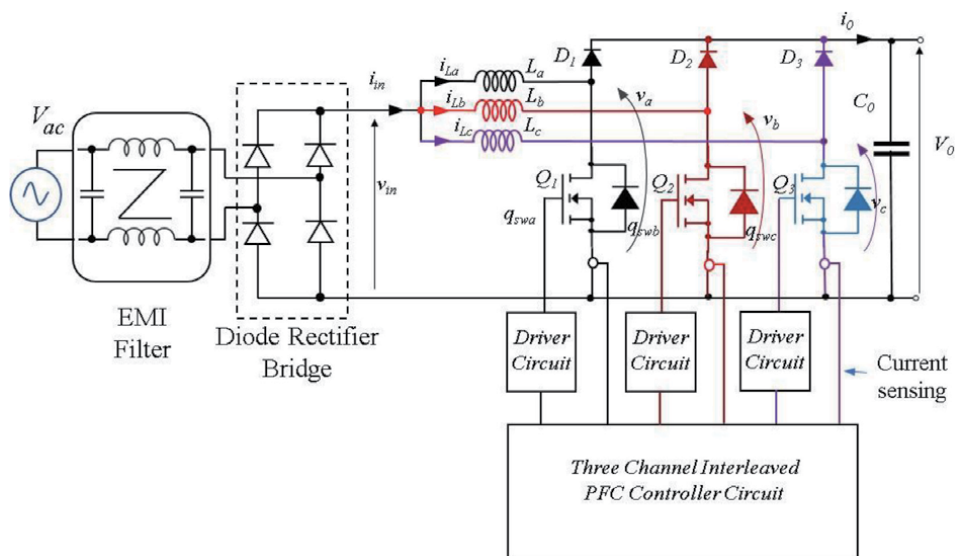
Figure 18.
Three channel boost PFC simplified electrical scheme.

frequency f_{R1} occurs considering the higher load conditions. In this case the L_M can be neglected and f_{R1} is given by

$$f_{r1} = \frac{1}{2\pi \bullet \sqrt{L_R \bullet C_R}} \qquad (42)$$

A lower resonant frequency f_{r2} appears at light load operation. In this operative condition, L_M must be considered. The resonant frequency consequently changes.

$$f_{r2} = \frac{1}{2\pi \bullet \sqrt{(L_R + L_M) \bullet C_R}} \qquad (43)$$

From (42) and (43) appears that $f_{r1} > f_{r2}$. The frequency f_{r2} is also called the second resonance frequency. The LLC converter can operate in several ways related to the input voltage and load current conditions. The difference between the two resonant frequencies depends on the relationship between L_M and L_R. Usually, the LLC converter operates at a constant duty cycle. The condition $f_{sw} < f_{r2}$ is not used in actual applications because an instability condition arises from the study of the transfer function of the converter [56]. In LLC converter there are three different operative conditions: $f_{r2} > f_{sw} > f_{r1}$, $f_{sw} = f_{r1}$ and, $f_{sw} > f_{r1}$. Referring to the LLC converter shown in **Figure 19a**, the resonant converter waveforms in the three operation modes are shown in **Figure 19b**.

At resonant frequency operation, at $f_{sw} = f_{r1}$, the resonant tank has unity gain and the best efficiency is reached. Primary-side and secondary-side RMS currents are the lowest values. In the primary-side switches, ZVS operation is achieved while on the secondary-side the diodes operate in zero current switching (ZCS). Furthermore, In the narrow neighborhood of f_{R1} the gain does not depend on the load conditions [57]. The analysis of the gain behavior depending on the electrical parameters of the resonant tank and load request. A detailed analysis is reported in [58].

At the f_{sw} above f_{r1}, the switching period is shorter than the resonant period. The resonant half cycle is not fully completed by the starting of the other half of the switching cycle, as shown in **Figure 19b**. In this case, on the secondary side, the rectifier diodes do not achieve the ZCS operating in hard switching. Also in this
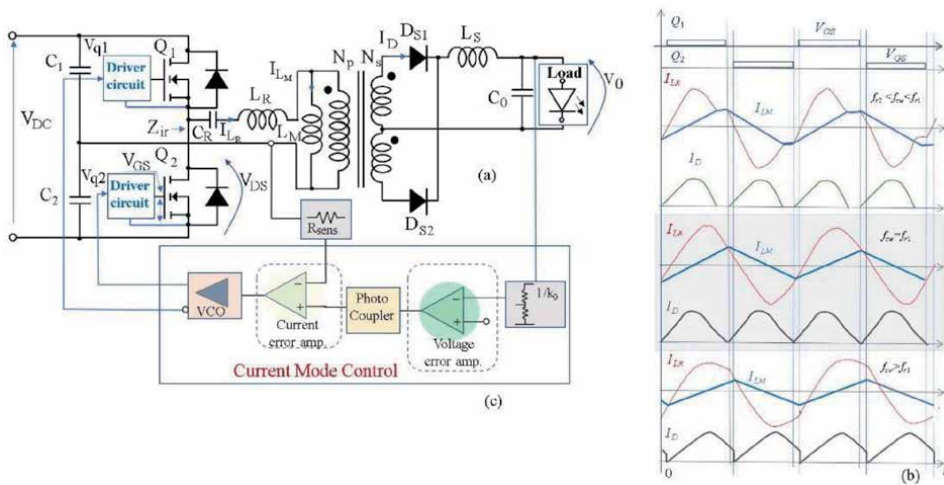
Figure 19.
(a) LLC converter schematic. (b) Main converter waveforms at $f_{r2} > f_{sw} > f_{r1}$, $f_{sw} = f_{r1}$ and, $f_{sw} > f_{r1}$.
(c) Simplified current mode controller with VCO.

operative condition, on the primary-side switches, the ZVS is reached. Finally, the resonant tank features a voltage gain lower than unity.

In the switching frequency between the two resonant frequencies ($f_{r2} > f_{sw} > f_{r1}$). The resonant tank gives a voltage gain higher than unity. The primary-side switches commutate in ZVS and in the secondary-side diodes achieve ZCS. In this operative condition, the peak value of the resonant current circulating through the L_M is larger leading to higher conduction losses through the converter. Based on the load the equivalent impedance connected to the half-bridge switching leg can be either inductive or capacitive at frequency variation. Usually, the LLC converter operates in the region where the input impedance of the resonant tank has an inductive behavior (i.e. it increases with f_{sw}) [59]. Furthermore, the ZVS mode on the primary-side is achieved only if the tank input impedance Z_{ir} is inductive. This operative condition can be controlled by changing the switching frequency. Higher output power is obtained by reducing the frequency and vice versa.

In the LED driver application, the output current must be controlled. In LLC the current mode controller is arranged with a voltage-controlled oscillator (VCO) that change the current control signal in variable switching frequency to drive the primary-side MOSFETs [60]. A simplified schematic of the current control with the VCO block is depicted in **Figure 19c**. The drawback of the LLC converter results from the difficulty in achieving consistent dynamic performance over wide-operating conditions. To reduce the switching losses on the secondary-side a synchronous rectifier solution may be arranged. In this case the diodes are replaced by low voltage MOSFETs driven in synchronous mode by a suitable control technique [61].

4.6 Multiple outputs LED driver circuits

Multi-channel LED structure is popularly implemented in some lighting systems such as indoor lighting and street lighting. Also, in display backlighting, advanced color-mixing and dimming LED systems the multi-channel LED driver solutions are used [62]. The multi-channel LED topologies connected to the line grid are usually composed of traditional five stages: the EMI filter, the bridge rectifier PFC stage, front-end DC/DC stage and multi-channel post-current-regulator stage. In multiple outputs LED driver independent output current control can be necessary. The post-current regulator can be performed in a linear mode current regulator or switch-mode converter.

A simplified block schematic of the multi-channel constant current LED driver is reported in **Figure 20a**.

In the isolated LED driver solutions, the Flyback converter is widely used in multiple-output Flyback LED driver to integrate DC-DC converter with PFC circuit. The constant current source of multiple channel LED can be supplied in linear mode as shown in **Figure 20b** or with switch-mode converter as depicted in **Figure 20c** [63]. In **Figure 20c** the current source for the LED string is achieved by a synchronous Buck current regulator to reduce the power losses.

In multi-channel applications there are also non-isolated LED driver circuits application. In this kind of LED driver, the single-inductor multiple-output (SIMO) structure is more attractive [64]. It is based on several Buck converters arrangement. In the SIMO solution LED strings current are regulated by switching Buck-type power converters. Furthermore, a main Buck converter is used to interface the rectified voltage performing the PFC functions [65]. The inductor of the main Buck converter is shared with the multi-channel Buck regulators. The simplified schematic of the SIMO structure is shown in **Figure 21**. The noticeable advantage of the SIMO technologies is their compact size the low cost and high-power efficiency especially at the increasing of LED strings.
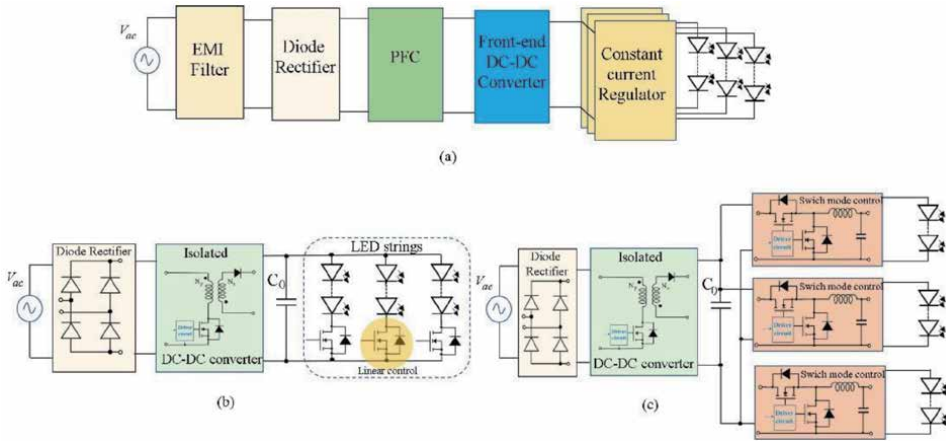
Figure 20.
Multi-channel LED driver circuits (a) block scheme of general AC LED driver system for multi-channel LED string. (b) Flyback converter solution with linear regulator on the secondary side. (c) Flyback converter solution with switching type synchronous Buck current regulator.
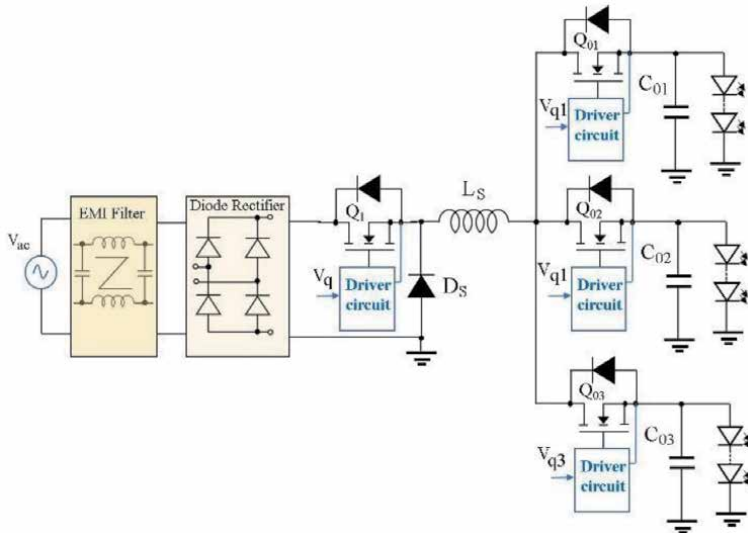
Figure 21.
Multi-channel LED driver circuits with single-inductor multiple-output solution.

For high current LED string the LLC converter with multiple-output secondary of the HF transformer can be considered [66]. In the secondary side as described in **Figure 20b** and **Figure 20c** a switching or linear type current regulator is added to drive the LED strings.

5. Conclusion

The LED driver circuits in several applications needs are investigated. The passive and active circuits are critically evaluated in terms of power request, topology simplicity, efficiency, reliability, and cost. The LED driver circuits are evaluated based on the different supply sources and power request. The DC-DC converters connected directly to a DC source such as battery are classified and pro and cons are

discussed. The main current control strategies are described, and the dimming features are also considered. Furthermore, the power converters connected to the AC line are explored considering the one-stage and two-stage converter solutions. In the one-stage LED driver a Flyback converter description is focused. The design issues and the control method to meet the output current regulation and the high-power factor request are explored. Afterwards, the two-stage driver converters for higher power applications are investigated. The first stage Boost converter PFC circuit design and control issues are exanimated, and the interleaved solution is introduced. The second stage LLC for a higher current LED driver is also considered providing basic information on the operation and the applications. Finally, multi-channel LED driver circuits in non-isolated and isolated conditions are presented and discussed.

Author details

Salvatore Musumeci
Department of Energy "G. Ferraris", Politecnico di Torino, Torino, Italy

*Address all correspondence to: salvatore.musumeci@polito.it

IntechOpen

References

[1] Wang Y Y, Alonso J M, Ruan X. A Review of LED Drivers and Related Technologies. IEEE Transactions on Industrial Electronics. 2017; 64 (7): 5754–5765. Doi: 10.1109/ TIE.2017.2677335.

[2] Zissig G, Bertoldi P. Status of LED-Lighting world market in 2017. European commission, JRC Technical Report, [Internet] 2018. Available from: https:// e3p.jrc.ec.europa.eu/publications/status-led-lighting-world-market-2017

[3] Arias M, Vázquez A, Sebastián J. An Overview of the AC-DC and DC-DC Converters for LED Lighting Applications. Automatika. 2012; 53 (2): 156–172. DOI: 10.7305/ automatika.53-2.154.

[4] Di Mauro S, Musumeci S, Raciti A. Analysis of electrical and photometric quantities of CFL and LED bulb lamp. In: Proceedings of the IEEE Industry Applications Society Annual Meeting. (IAS '17); 1–5 Oct. 2017; Cincinnati OH: IEEE; 2017. p. 1–8.

[5] Di Mauro S, Raciti A, Rizzo S A, Susinni G, Musumeci S. Effects of the aging time on CFL and LED lamps: experimental tests on the electrical and photometric quantities. In: Proceedings of the AEIT International Annual Conference (AEIT '18); 3–5 Oct. 2018; Bari. Italy: IEEE; 2018. p. 1–6.

[6] Uddin S, Shareef H, Mohamed A, Hannan M A, Mohamed K. LEDs as energy efficient lighting systems: A detail review. In: Proceedings of the IEEE Student Conference on Research and Development, 19–20 Dec. 2011; Cyberjaya. Malaysia: IEEE; 2011 p. 468–472.

[7] Ogunjuyigbe A S O, Ayodele T R, Idika V E, Ojo O. Effect of lamp technologies on the power quality of electrical distribution network. In:

Proceedings of the IEEE PES PowerAfrica, 27–30 June 2017; Accra. Ghana: IEEE; 2017. p. 159–163.

[8] Life-Cycle Assessment of Energy and Environmental Impacts of LED Lighting Products Part I: Review of the Life-Cycle Energy Consumption of Incandescent, Compact Fluorescent, and LED Lamps February 2012, Updated August 2012. [Internet]. 2012 Available from: https://www1.eere.energy.gov/buildings/publications/pdfs/ssl/2012_LED_Lifecycle_Report.pdf.

[9] Görbe P, Magyar A, Csuti P. Power Quality Management of LED Light Sources in Frequency Domain. Chemical Engineering Transactions, 2013; 35: 1309–1314. https://doi.org/10.3303/ CET1335218

[10] Di Mauro S, Raciti A, Rizzo S A, Susinni G, Musumeci S. Steady-state equivalent circuit of LED bulbs accounting for the current harmonics. In: Proceedings of the IEEE 44th Annual Conference of the IEEE Industrial Electronics Society (IECON '18), 21–23 Oct. 2018; Washington DC. USA: IEEE; 2018. p. 1513–1518.

[11] Luz P C V, Bolzan P E, Kirsten A L, do Prado R N. Isolated topologies family for street lighting using LED as source light. In: Proceedings of the IEEE 42nd Annual Conference of the IEEE Industrial Electronics Society (IECON '16); 10–16 Oct. 2016; Florence. Italy: IEEE; 2016. p. 3451–3457.

[12] Adam GK. DALI LED Driver Control System for Lighting Operations Based on Raspberry Pi and Kernel Modules. Electronics. 2019; 8(9):1021. https://doi.org/10.3390/ electronics8091021.

[13] Lehman B, Wilkins A J. Designing to Mitigate Effects of Flicker in LED Lighting: Reducing risks to health and

safety. IEEE Power Electronics Magazine. 2014; 1 (3): 18–26. Doi: 10.1109/MPEL.2014.2330442.

[14] Castro I, Vazquez A, Arias M, Lamar D G, Hernando M M, Sebastian J. A Review on Flicker-Free AC–DC LED Drivers for Single-Phase and Three-Phase AC Power Grids. IEEE Transactions on Power Electronics. 2019; 34 (10): 10035–10057. Doi: 10.1109/TPEL.2018.2890716.

[15] Li S, Tan S, Lee C K, Waffenschmidt E, Hui S Y, Tse C K. "A survey, classification, and critical review of light-emitting diode drivers," IEEE Transactions on Power Electronics. 2016; 31 (2): 1503–1516. Doi: 10.1109/TPEL.2015.2417563.

[16] Direct-AC, Linear LED Driver Topology: CCR Straight Circuit (120 VAC & 230 VAC). Design Note – DN05079/D. On-Semiconductor [Internet]. 2015. Available from https://www.onsemi.com/pub/Collateral/DN05079-D.PDF

[17] Chen W, Li S N, Hui S Y R. A comparative study on the circuit topologies for offline passive light-emitting diode (LED) drivers with long lifetime & high efficiency. In Proceedings of IEEE Energy Conversion Congress and Exposition (ECCE '10); 12–16 Sept. 2010; Atlanta, GA, USA: IEEE; 2010. p. 724–730.

[18] Tung NT, Tuyen ND, Huy NM, Phong NH, Cuong NC, Phuong LM. Design and Implementation of 150 W AC/DC LED Driver with Unity Power Factor, Low THD, and Dimming Capability. Electronics. 2020; 9(1):52. https://doi.org/10.3390/electronics9010052

[19] Li S, Tan S, Lee C K, Waffenschmidt E, Hui S Y, Tse C K. A survey, classification, and critical review of light-emitting diode drivers. IEEE Transactions on Power

Electronics. 2016; 31 (2): 1503–1516. Doi: 10.1109/TPEL.2015.2417563.

[20] Hui S Y, Li S N, Tao X H, Chen W, Ng W M. A Novel Passive Offline LED Driver with Long Lifetime. IEEE Transactions on Power Electronics. 2010; 25 (10): 2665–2672. Doi: 10.1109/TPEL.2010.2048436.

[21] Cosp-Vilella J, Martínez-García H. Design of an on-chip linear-assisted DC-DC voltage regulator. In: Proceedings of the IEEE 20th International Conference on Electronics, Circuits, and Systems (ICECS '13); Abu Dhabi. United Arab Emirates: IEEE; 2013. p. 353–356.

[22] NUD4001, ON-Semiconductor, Datasheet [Internet]. 2011. Available from: https://www.onsemi.com/pub/Collateral/NUD4001-D.PDF

[23] Chiu H, Lo Y, Chen J, Cheng S, Lin C, Mou S. A High-Efficiency Dimmable LED Driver for Low-Power Lighting Applications. IEEE Transactions on Industrial Electronics. 2010; 57 (2): 735–743. Doi: 10.1109/TIE.2009.2027251.

[24] Hurley W G, Wolfle W H, Breslin J G. Optimized transformer design: inclusive of high-frequency effects. IEEE Transactions on Power Electronics. 1998; 13 (4): 651–659. Doi: 10.1109/63.704133.

[25] Doshi M, Zane R. Digital Architecture for Driving Large LED Arrays with Dynamic Bus Voltage Regulation and Phase Shifted PWM. In: Proceedings of the IEEE Twenty-Second Annual Applied Power Electronics Conference and Exposition, (APEC '07); 25 Feb.-1 March 2007; Anaheim CA. USA: IEEE; 2007. p. 287–293.

[26] Lin W, Chen H, Ke S. Research on a single-stage Flyback/boost LED driver with lower output ripple. In: Proceedings of the IEEE 2nd Annual

Southern Power Electronics Conference (SPEC '16); 5–8 Dec. 2016; Auckland. New Zealand: IEEE; 2016. p. 1–5.

[27] Qiu Y, Wang L, Wang H, Liu Y, Sen P C. Bipolar Ripple Cancellation Method to Achieve Single-Stage Electrolytic-Capacitor-Less High-Power LED Driver. IEEE Journal of Emerging and Selected Topics in Power Electronics. 2015; 3 (3): 698–713. Doi: 10.1109/JESTPE.2015.2433918.

[28] Athalye P, Harris M, Negley G. A two-stage LED driver for high-performance high-voltage LED fixtures. In: Proceedings of the IEEE Twenty-Seventh Annual IEEE Applied Power Electronics Conference and Exposition (APEC '12); 5–9 Feb. 2012; Orlando. FL. USA: IEEE; 2012. p. 2385–2391.

[29] Castro I, Lamar D G, Arias M, Hernando M M, Sebastian J. Multicell Three-Phase AC–DC Driver for HB-LED Lighting Applications. IEEE Transactions on Industry Applications. 2017; 53 (4): 3803–3813. Doi: 10.1109/TIA.2017.2686802.

[30] Chen W, Cheng KWE, Shao J. Circuit Topology Analysis for LED Lighting and its Formulation Development. Energies. 2019; 12(21):4203. https://doi.org/10.3390/en12214203.

[31] Ferdous S M, Oninda M A M, Sarowar G, Islam K K, Hoque M A. Non-isolated single stage PFC based LED driver with THD minimization using Cúk converter. In: Proceedings of the IEEE 9th International Conference on Electrical and Computer Engineering (ICECE '16); 20–22 Dec. 2016; Dhaka. Bangladesh: IEEE; 2016. p. 471–474.

[32] Jha A, Singh B. SEPIC PFC converter fed LED driver. In: Proceedings of the IEEE 1st International Conference on Power Electronics, Intelligent Control and Energy Systems (ICPEICES '16), Delhi. India: IEEE 2016. p. 1–6.

[33] In-Hwan Oh. An analysis of current accuracies in peak and hysteretic current controlled power LED drivers. In: Proceedings of the IEEE Twenty-Third Annual IEEE Applied Power Electronics Conference and Exposition (APEC '08); 24–28 Feb. 2008; Austin. TX. USA: IEEE; 2008 p. 572–577.

[34] Shao J. Single Stage Offline LED Driver. In: Proceedings of the IEEE Twenty-Fourth Annual IEEE Applied Power Electronics Conference and Exposition (APEC '09); 15–19 Feb. 2009; Washington. DC. USA: IEEE; 2009. p. 582–586.

[35] Deng H, Shan L, Yin Y, Si G, Sun Y. Design of a LED constant-current driver using a novel hysteresis-current control method with adaptive off-time control. In: Proceedings of the IEEE 8th International Congress on Image and Signal Processing (CISP '15); 14–16 Oct. 2015; Shenyang. China: IEEE; 2015. p. 1551–1555.

[36] Faraci E, Seeman M, Gu B, Ramadass Y, Brohlin P. High efficiency and power density GaN-based LED driver. In: Proceedings of the IEEE Applied Power Electronics Conference and Exposition (APEC '16); 20–24 March 2016; Long Beach. CA. USA: IEEE; 2016. p. 838–842.

[37] Puukko J, Xu J; Liu L. Consideration of flyback converter using GaN devices. In: Proceedings of the IEEE 3rd Workshop on Wide Bandgap Power Devices and Applications (WiPDA '15); 2–4 Nov. 2015; Blacksburg. VA. USA: IEEE; 2015. p. 196–200.

[38] Zhang X, Liu H, Xu D. Analysis and design of the flyback transformer. In: Proceedings of the IEEE 29th Annual Conference of the IEEE Industrial Electronics Society (IECON'03); 2–6 Nov. 2003; Roanoke. VA. USA: IEEE; 2003. p. 715–719.

[39] Wang X, Tang J, Zhang X, Xie S, Mao X, Chen H. A High-Efficiency High

Power Driver Circuit for Joint Illumination and Communication System With Phase Shift Pre-Emphasis Technology. IEEE Access. 2020; 9: 6325–6333. Doi: 10.1109/ACCESS.2020.3048168.

[40] Zeng J, Zhang G, Yu S S, Zhang B, Zhang Y. LLC resonant converter topologies and industrial applications — A review. Chinese Journal of Electrical Engineering. 2020; 6 (3): 73–84. Doi: 10.23919/CJEE.2020.000021.

[41] ENERGY STAR Program Requirements for Solid State Lighting Luminaires, Eligibility Criteria - Version 1.1. [Internet]. 2008. Available from: http://www.energystar.gov/index.cfm?c=new_specs.ssl_luminaires

[42] Gritti G, Adragna C. Primary-controlled constant current LED driver with extremely low THD and optimized phase-cut dimming compatibility. In: Proceedings of the IEEE 17th European Conference on Power Electronics and Applications (EPE'15 ECCE-Europe); 8–10 Sept. 2015; Geneva. Switzerland: IEEE; 2015. p. 1–10.

[43] Hu Y, Huber L, Jovanovic M M. Single-Stage Flyback Power-Factor-Correction Front-End for HB LED Application. In: Proceedings of the IEEE Industry Applications Society Annual Meeting (IAS '09); 4–8 Oct. 2009; Houston. TX. USA: IEEE; 2009. p. 1–8.

[44] Al-Naemi F, Yang J, Zhang W. A Low Power Single-stage LED Driver Operating between Discontinuous Conduction Mode and Critical Conduction Mode. Elsevier, Energy Procedia. 2015; 74: 817–825. https://doi.org/10.1016/j.egypro.2015.07.817.

[45] Xu Y, Lin J, Xie X, Cai C. Design of a single-stage Flyback LED Constant current Driving Power Supply. Journal of Physics: Conference Series, IOP Publishing. 2019; 1288; 012086: 1–7. Doi: 10.1088/1742-6596/1288/1/012086.

[46] Wu S. Single-Stage High Power Factor Flyback for LED Lighting. Richtek, Application Note, AN012 [Internet]. 2014. Available from: https://www.richtek.com/Design%20Support/Technical%20Document/AN012

[47] Adragna C, Gritti G, Raciti A, Rizzo SA, Susinni G. Analysis of the Input Current Distortion and Guidelines for Designing High Power Factor Quasi-Resonant Flyback LED Drivers. Energies. 2020; 13(11):2989. https://doi.org/10.3390/en13112989.

[48] Mack Grady W, Gilleskie R J. Harmonics and How they Relate to Power Factor. In: Proceedings of the EPRI Power Quality Issues & Opportunities Conference (PQA'93); November 1993; San Diego. CA. pp 1–8.

[49] Adragna C, Gritti G. High-power-factor quasi-resonant flyback converters draw sinusoidal input current. In: Proceedings of the IEEE Applied Power Electronics Conference and Exposition (APEC '15); 15–19 March 2015; Charlotte. NC. USA: IEEE; 2015. p. 498–505.

[50] Gritti G. Adragna C. Analysis, design and performance evaluation of an LED driver with unity power factor and constant-current primary sensing regulation. AIMS Energy. 2019; 7 (5): 579–599. Doi: 10.3934/energy.2019.5.579.

[51] Cheng C, Cheng H, Chang C, Yang F, Chung T. A single-stage LED driver for street-lighting applications with interleaving PFC feature. In: Proceedings of the IEEE International Symposium on Next-Generation Electronics (ISNE '13); 25–26 Feb. 2013; Kaohsiung. Taiwan: IEEE; 2013. p. 150–152.

[52] Rossetto L, Spiazzi G, Tenti P. Control Techniques for Power Factor Correction Converters. In: Proceedings of the International Conference on

Power Electronics and Motion Control, September 1994; Warsaw. Poland. p. 1310-1318.

[53] Naraharisetti K, Green P B. Design of 200 W boost PFC plus HB LLC resonant converter with IR1155, IRS27952 and IR11688. Infineon Application Note, AN1907 PL88 1908 004522 [Internet]. 2020. Available from: https://www.infineon.com/dgd l/Infineon-LLC_Resonant_Converter_ IR1155_IRS27952_IR11688-Applica tionNotes-v02_02-EN.pdf?fileId=5546d 4626cb27db2016d003926ff1da3.

[54] Musumeci S, Bojoi R, Armando E, Borlo S, Mandrile F. Three-Legs Interleaved Boost Power Factor Corrector for High-Power LED Lighting Application. Energies. 2020; 13(7):1728. https://doi.org/10.3390/en13071728.

[55] Musumeci S, Bojoi R, Borlo S, Armando E. IGBT based Three Channel Interleaved PFC Boost Converter for Inverter Front-End Application. In: Proceedings of the IEEE AEIT International Annual Conference (AEIT 2019); 18–20 Sept. 2019; Florence. Italy: IEEE; 2019. p. 1–6.

[56] Musumeci S. Inductor Constraints on LLC Converter Design in Battery Charger Applications. In: Proceedings of the IEEE 5th International Forum on Research and Technology for Society and Industry (RTSI '19); 9–12 Sept. 2019; Florence. Italy: IEEE; 2019. p. 269–274.

[57] Musumeci S, Cristaldi D, Portoghese F. Super-junction power MOSFET in half bridge DC-DC zero-voltage converter for energy conversion management. In: Proceedings of the IEEE International Conference on Clean Electrical Power (ICCEP '15); 16–18 June 2015; Taormina. Italy: IEEE; 2015. p. 755–760.

[58] De Simone S, Adragna C, Spini C, Gattavari G. Design-oriented steady-state analysis of LLC resonant converters based on FHA. In: Proceedings of the IEEE International Symposium on Power Electronics, Electrical Drives, Automation and Motion (SPEEDAM '06); 23–26 May 2006; Taormina. Italy: IEEE; 2006. p. 200–207.

[59] Han J-H, Lim Y-C. Design of an LLC Resonant Converter for Driving Multiple LED Lights Using Current Balancing of Capacitor and Transformer. Energies. 2015; 8(3):2125–2144. https://doi.org/10.3390/ en8032125.

[60] Jang J, Pidaparthy SK, Choi B. Current Mode Control for LLC Series Resonant DC-to-DC Converters. Energies. 2015; 8(6):6098–6113. https:// doi.org/10.3390/en8066098.

[61] Di Mauro S, Musumeci S, Raciti A, Fusillo F, Scrimizzi F, Scollo R. Synchronous rectification with low voltage MOSFETs in LLC converters. In: Proceedings of the IEEE AEIT International Annual Conference (AEIT '17); 20–22 Sept. 2017; Cagliari. Italy: IEEE; 2017. p. 1–6.

[62] Wu H, Ji S, Lee F C, Wu X. Multi-channel constant current (MC3) LLC resonant LED driver. In: Proceedings of the IEEE Energy Conversion Congress and Exposition, Phoenix (ECCE '11); 17–22 Sept. 2011; Phoenix. AZ. USA: IEEE; 2011. p. 2568–2575.

[63] Guo Y, Li S, Lee A T L, Tan S, Lee C K, Hui S Y R. Single-Stage AC/DC Single-Inductor Multiple-Output LED Drivers. IEEE Transactions on Power Electronics. 2016. 31 (8): 5837–5850. Doi: 10.1109/TPEL.2015.2496247.

[64] H. Chen, Y. Zhang and D. Ma, "A SIMO Parallel-String Driver IC for Dimmable LED Backlighting With Local Bus Voltage Optimization and Single Time-Shared Regulation Loop," in IEEE Transactions on Power Electronics, vol.

27, no. 1, pp. 452–462, Jan. 2012, doi: 10.1109/TPEL.2011.2160404.

[65] Li S, Guo Y, Tan S, Hui S Y. An Off-line Single-Inductor Multiple-Output LED Driver with High Dimming Precision and Full Dimming Range. IEEE Transactions on Power Electronics. 2017; vol. 32; no. 6; p. 4716–4727. Doi: 10.1109/TPEL.2016.2597237.

[66] Yi KH. High Voltage, Low Current High-Power Multichannel LEDs LLC Driver by Stacking Single-Ended Rectifiers with Balancing Capacitors. Electronics. 2020; 9(3):529. https://doi.org/10.3390/electronics9030529.

Section 2

Photodetectors

Chapter 4

Near-Infrared Schottky Silicon Photodetectors Based on Two Dimensional Materials

Teresa Crisci, Luigi Moretti, Mariano Gioffrè and Maurizio Casalino

Abstract

Since its discovery in 2004, graphene has attracted the interest of the scientific community due to its excellent properties of high carrier mobility, flexibility, strong light-matter interaction and broadband absorption. Despite of its weak light optical absorption and zero band gap, graphene has demonstrated impressive results as active material for optoelectronic devices. This success pushed towards the investigation of new two-dimensional (2D) materials to be employed in a next generation of optoelectronic devices with particular reference to the photodetectors. Indeed, most of 2D materials can be transferred on many substrates, including silicon, opening the path to the development of Schottky junctions to be used for the infrared detection. Although Schottky near-infrared silicon photodetectors based on metals are not a new concept in literature the employment of two-dimensional materials instead of metals is relatively new and it is leading to silicon-based photodetectors with unprecedented performance in the infrared regime. This chapter aims, first to elucidate the physical effect and the working principles of these devices, then to describe the main structures reported in literature, finally to discuss the most significant results obtained in recent years.

Keywords: graphene, silicon, photodetector, Schottky diode, near-infrared

1. Introduction

In the last few decades, the enormous evolution of social networks and the progress of the Internet of Things (IoT) has made necessary the management of a huge amount of data. For this reason, industry and scientific research has been focused on the development of new technologies to support and to manage the data traffic increase.

Silicon photonics (SP) fits perfectly into this scenario, since it combines the advantages of the mature silicon technology developed in microelectronics with the possibility to further reduce costs simultaneously increasing the transmission speed thanks to the use of light. Hence, SP is currently emerging as an appealing market promising to reach $4 billion in 2025 (**Figure 1**) [1]. Nowadays, Intel and Luxtera play leadership roles in the SP industry, bringing products to market that can support 100Gb/s of communication throughput.

Silicon photonics is by now a widely consolidated field originating from the pioneering work of Soref et al. [2, 3] and from the manufacture of silicon on insulator (SOI) substrates particularly suitable to the realization of guiding

Figure 1.
Silicon photonics 2019–2025 market forecast [1].

structures, both in the 1980s. Thus, the possibility to build optoelectronic devices by using CMOS facilities, would allow not only the low costs advocated by telecommunications industry but also the possibility to integrated both electronic and photonic functionalities on the same chip.

In this context silicon-based photodetectors (Si PDs) are a key component able to establish a connection between the world of electronics and photonics. Si PDs working in the visible spectrum can be easily found on the market, however the telecommunications industry requires components operating in the infrared regime, where, unfortunately, silicon has a negligible absorption due to its indirect bandgap of 1.12 eV.

To overcome this drawback the most common approach is based on the integration of germanium (Ge) on silicon. Nonetheless, the performances of these devices are often limited by a relatively high leakage current caused by the lattice mismatch with silicon of 4,3%. This effect can be mitigated by growing a Ge buffer layer on Si by a two steps epitaxial method giving rise to problems of thermal budget and planarity that limit the monolithic Ge integration on Si.

For all these reasons, an all-silicon approach is preferable, and the exploitation of the absorption phenomena based on the internal photoemission effect (IPE) in a Schottky diode is among the most promising and innovative.

In a Schottky diode configuration, the photons incident on a Metal-Si interface, with an energy below the silicon bandgap, can cause the generation of photoexcited carriers in the metal with energy higher than Schottky barrier. This "hot" carriers are injected into the silicon, accelerated by the electric field in the depletion region of the junction and collected as a photocurrent [4–7].

In literature, several examples of IR charged coupled devices (CCDs) based on a Schottky diode can be easily found. The most common example of this family of PDs is based on Pd_2Si/Si and $PtSi/Si$ Schottky junctions used for aerospace applications. The main problem with these photodetectors, however, is the requirement of cryogenic temperatures to minimize the noise current due to the low Schottky barrier (SBH) necessary to achieve a reasonable device efficiency [8–13].

Consequently, to exploit the IPE at room temperature, new classes of devices characterized by higher values of SBH, have been proposed. Obviously, this approach leads to a worsening of the performances of PDs and, therefore, different solutions

have been investigated. Some devices use a Fabry-Perot type resonant geometry for compensating the reduction in efficiency [14, 15], others use nanometric metallic structures such as Si nanoparticles (NP) [16], gratings [17] and antennas [18]. Lastly, PDs based on the IPE at room temperature have also been realized by taking advantage of surface plasmonic polaritons on metal strips of nanometric scale (SPP) [19, 20]. Despite of these efforts, however, it was possible to obtain a maximum responsivity of only 30 mA/W for PDs integrated in waveguide configuration [16].

To increase these low responsivity values, deriving from the small probability of the photo-excited carriers of overcoming the Schottky barrier, the reduction of the metal thickness has stood out as a good strategy [21, 22], influencing the research towards the integration of 2D materials with Si. In particular, 2D layered materials have emerged thanks to their exceptional optical and electronic properties, low cost and simple fabrication process.

In literature it is possible to find various graphene/Si PDs based on FET structures [23, 24]; however, such kind of devices suffer of a high dark current needing of interdigitated electrodes because the electric field in graphene is formed in a small region within 200 nm from the contact. On the other hand, by taking advantage of an IPE approach, it is possible to minimize the dark current thanks to the rectifying nature of Schottky diodes that do not need of interdigitated structures.

Graphene has opened the way for the investigation of other 2D layered materials. Notable attention has been given to transition-metal dichalcogenides (TMDCs) since their very naturally abundant and possess a tunable bandgap in addition to most of graphene properties [25–27]. Recently, several heterostructures TMDCs/Si have been investigated: the formation of a potential barrier at the interface between the two materials has allowed the exploitation of the IPE to realize high detectivity and ultrafast NIR PDs [28–31].

In this chapter the topic of NIR PDs based on 2D materials/silicon junctions is discussed. In the first section the theoretical background behind the behavior of junctions based on 2D materials with particular reference to graphene will be explored and compared to the classical theory describing the Schottky junctions using 3D metals. In the second part, several examples of NIR PDs exploiting 2D materials/silicon junctions reported in literature will be presented and discussed.

2. Theoretical background

The responsivity R of a photodetector can be defined as the ratio between the photogenerated current (I_{ph}) to the incident optical power (P_{inc}). It is very important for the quantification of the PD performance since it is strictly related to the efficiency of the device. This relation is explicated by the following formula:

$$R = \frac{I_{ph}}{P_{inc}} = \frac{\lambda[nm]}{1242} \bullet \eta_{ext} \qquad (1)$$

where η_{ext} is the external quantum efficiency, that represents the number of charged carriers generated for each incident photon. The external quantum efficiency depends on the internal quantum efficiency by the equation $\eta_{ext} = A\eta_{int}$, where η_{int} is the ratio of the number of charged carriers generated to the number of absorbed photons and A is the active material absorption.

The first theoretical model of photoemission from metal to vacuum was published by Fowler in 1931 [32]. Afterwards, in the 60s, the Fowler's theory was extended to the photoemission in the semiconductor by Cohen, Vims and Archer [33] and Elabd and Kosonocky [21].

By following the Elabd approach, it is possible to obtain the expression of η_{int} by starting with the consideration of the number of excited carriers N_T is:

$$N_T = \int_0^{hv} D(E)dE \tag{2}$$

where hv is the incident photon energy, E is the carriers energy referred to Fermi level and the argument function of the integral $D(E)$ is the absorber material density of state (DOS). On the other hand, not all the excited carriers can be emitted from the metal into semiconductor, indeed only those localized to energies higher than Schottky barrier have a certain probability of being emitted. Therefore, the number of states occupied by charge carriers that have a probability $P(E)$ of being emitted in the silicon can be written as:

$$N = \int_{q\phi_{B0}}^{hv} D(E)P(E)dE \tag{3}$$

where $P(E)$ is the charge carrier emission probability.

Elabd and Kosonocky formulated, with the zero-temperature approximation, the internal quantum efficiency in junctions involving 3D materials (metals) by the following [21]:

$$\eta_{int}^{3D} = \frac{N}{N_T} = \frac{1}{8q\phi_{Bo}} \bullet \frac{(hv - q\phi_{B0})^2}{hv} \tag{4}$$

being ϕ_{B0} the Schottky barrier height (SBH) at zero bias, $hv = 1242/\lambda_0$ [nm] the photon energy (λ_0 is the wavelength in vacuum condition) and q the electron charge. Very often a generic factor C (named quantum efficiency coefficient) replaces the factor $1/8q\phi_{B0}$ in order to achieve a better agreement between the theory and the experimental data. In order to achieve the expression (4) it is necessary to take $P(E) = (1 - \cos\vartheta)/2$, where ϑ is named carrier escape angle [21]. Elabd and Kosonocky in their work outline also as the diminishing of the thickness of the metal causes an enhancement of the efficiency due to the increased emission probability $P(E)$.

The 3D apex in the Elabd and Kosonocky Eq. (4) indicates the internal quantum efficiency for a metal-based junction, i.e. for a 3D material, but this equation fails to correctly describe the behavior of a junction based on 2D materials [34, 35] due to the different expressions to use for both the density of state $D(E)$ and the emission probability $P(E)$.

This issue has been discussed in detail for graphene [34, 36]. Graphene has a band structure characterized by valence and conduction bands which touch in six points of the Brillouin zone. These points are termed Dirac points and represent the zero level of energy. In the graphic representation of the band diagram of a graphene/n-Si Schottky junction (**Figure 2**) one of these Dirac points is represented with a conical surface [37].

Unlike metals, Graphene shows a density-of-state function $D(E)$ linearly dependent on the energy according to the formula: $D(E) = \frac{2|E|}{n\hbar^2 v_F^2}$ [38], where $\hbar$ is the reduced Plank constant and v_F is the Fermi velocity. On the other hand, as discussed in Ref. [27], the emission probability $P(E)$ simply can be taken equal to 1/2 because the graphene π orbital are always perpendicular to graphene/Si interface and therefore the momenta of the photo-excited carriers can only have two directions: towards the Si semiconductor or in the opposite direction [34].
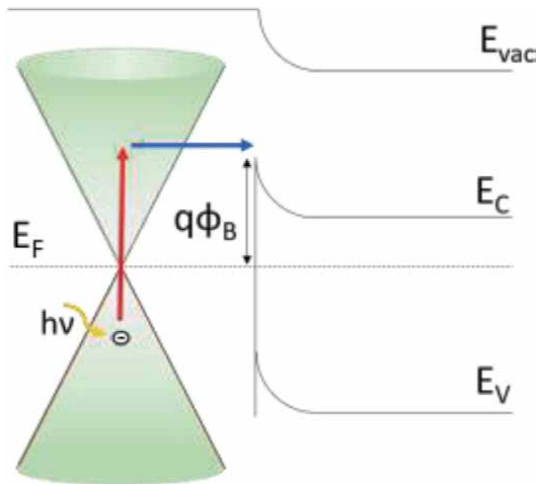
Figure 2.
Energy band diagram of a graphene/n-Si Schottky junction with the conical representation of a Dirac point. E_V (E_C): Silicon valence (conduction) band; E_F: Metal Fermi level; $q\Phi_B$: Schottky barrier.

Downstream of all these considerations and taking advantage of Eqs. (2–3), the graphene quantum efficiency can be written:

$$\eta_{int}^{2D} = \frac{N}{N_T} = \frac{1}{2} \bullet \frac{(h\nu)^2 - (q\phi_{B0})^2}{(h\nu)^2} \tag{5}$$

where the apex 2D indicates that the formula is referred to a bi-dimensional material [34, 35].

From the plot of the (5) and (4) it is evident that the IPE effect is enhanced by using graphene material, as showed in the **Figure 3** where the trend of the internal quantum efficiency versus the wavelength is reported for three different SBHs.
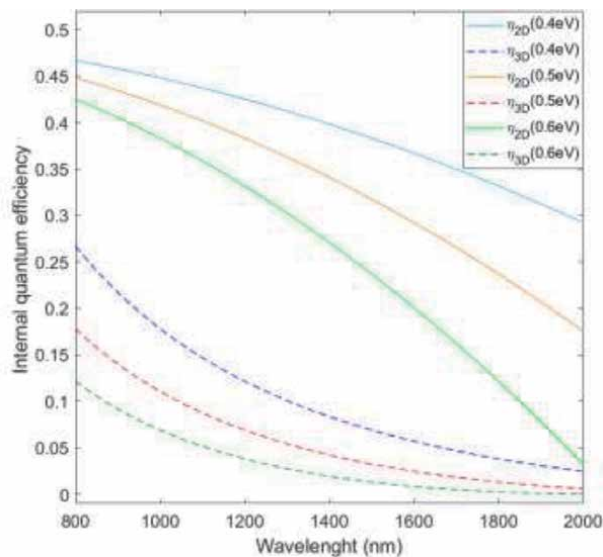
Figure 3.
Comparison between η_{int}^{3D} and η_{int}^{2D} at vary wavelengths for three different value of Schottky barriers: 0.4, 0.5 and 0.6 eV.

3. Schottky silicon photodetectors based on 2D materials

In last years, graphene has revolutionized the world of photonics and electronics thanks to its exceptional properties. Since its discovery, many researchers have concentrated their efforts on the possibility to integrate the graphene into opto-electronic devices. Notably, its zero direct bandgap make it very attractive for photodetection on a wide range from UV to IR. In particular, the demonstration of the graphene/silicon Schottky junction [39] has opened the path to realize more efficient NIR photodetectors exploiting the IPE.

In 2013, Amirmazlaghani et al. investigated a NIR PD based on exfoliated graphite on the top of a silicon substrate [34]. The Schottky barrier at the interface between the two materials resulted 0.44–0.47 eV and the ideality factor was 1.3–2.1. When a reverse bias of 16 V was applied, the device exhibited a dark current of the order of μA and, under a 1.55 μm illumination, a maximum responsivity of 9.9 mAW^{-1}. This value, higher than the one predicted by the Eq. (4), was explained by the authors as a consequence of the of the linear dispersion in graphene that requires a correction of the modified Fowler theory. By taking into account the two-dimensional nature of the graphene they derived the Eq. (5) able to provide a better agreement with the experimental data. This issue was confirmed by Goykhman et al. who in 2016 demonstrated an increase in efficiency of 7% with respect to the values predicted by the Eq. (4). The device investigated in [4] is a 5 μm silicon waveguide covered by a layer of graphene. The plasmonic enhancement was obtained thanks to a film of Au on the top of the graphene. At 1 V reverse bias the authors reported a responsivity of 85mAW^{-1}, that could grow up to 0.37AW^{-1} at a reverse voltage of -3 V. This happens thanks to an avalanche multiplication effect that unfortunately caused an abrupt increment of the dark current from 20 nA to 3 μA. Recently, Levy et al. [36] have proposed a phenomenological theory to explain the enhancement of internal photoemission in gold/graphene/silicon plasmonic structures.

In 2017 Casalino et al. realized vertically illuminated resonant cavity enhanced PDs exploiting the IPE through a CVD grown Single Layer Graphene (SLG) placed on top of a silicon substrate provided of a gold mirror on the back which acted as an optical cavity (**Figure 4a**) [40]. This optical microcavity allowed to trap the radiation increasing the light round-trips in the cavity and enhancing the SLG optical absorption. A wavelength-dependent photoresponse was achieved (**Figure 4b**)
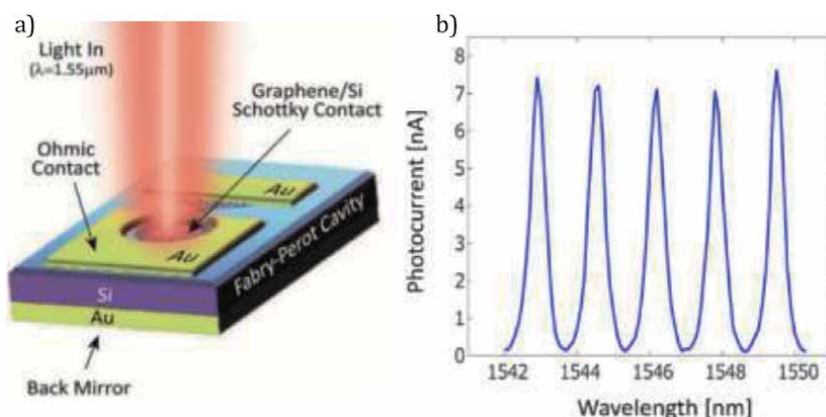
Figure 4.
Sketch (a) and PDs spectral photoresponse (b) of the resonant cavity enhanced PDs investigated by Casalino et al. [40]. Reprinted with permission from ACS Nano 2017, 11, 11, 10955–10963. Copyright 2017 American Chemical Society.

with a peak value of the responsivity at 1.55 μm of 20mAW^{-1}at -10 V applied voltage. At such bias the dark current was 147 μA. The authors also evaluated the NEP and the bandwidth of the devices, that resulted 3.5 x 10^{-10} WHz^{-1} and 120 MHz, respectively. Furthermore, it is worth noting that the Fabry-Perot cavity with a finesse of 5.4 determined a high spectral selectivity that could be easily tuned by changing the length of the resonant structure. The same author has devised another device, theoretically investigated in [41, 42], where the SLG was situated in the centre of c-Si/a-Si:H optical cavity. The photodetection mechanism is based on IPE through the SLG/c-Si junction. The resonant structure, embedded between two high reflectivity dielectric mirrors, enabled an increased number of round-trips of the radiation that crossed multiple times the graphene layer strongly increasing its absorption. This not only provides a 100% maximum SLG absorption but also a responsivity and a finesse of 0.43 A/W and 172 in a correctly designed PD. Further, in this work the bandwidth and the noise of the device were discussed. In addition, a similar device taking advantage of a double silicon on insulator substrate working as a high-reflectivity mirror has been recently proposed and theoretically discussed [43].

In 2016 Chen et al. [44] demonstrated graphene short-wave SWIR PDs with a very high responsivity of 83A/W at 1.55 μm thanks to the combination of two different mechanisms that allow the improvement of the performances of their devices. Indeed, they overcome the problems of the low optical absorption and the short lifetime of the photogenerated charge carriers by exploiting plasmonic effects and a vertical built-in field at the graphene/silicon interface. The exploitation of the plasmonic effects occurs through a gold nanoparticles (Au NPs) array on the graphene channel (**Figure 5a**). By tuning their shape and size, the gold NPs traps and absorbs the light at the resonance wavelength, resulting in a very high absorption that allows a greater photogeneration of charge carriers in the graphene (**Figure 5b**). Then, the vertical built-in potential at the interface between the graphene and the silicon induces a sort of carrier-trapping effect, by guiding the electrons away of the graphene and thus by generating holes with a consequent longer carrier lifetime. Indeed, the extension of the built- in field along all the large heterojunction produces a diminishing of the carrier recombination. This work shows how the Schottky junctions can play a relevant role in the field of SP in the context of NIR detection and demonstrates the need to exploit new structures to enhance the graphene absorption.

Recently, it has been proved that graphene/Si PDs based on the IPE can operate also at wavelengths greater than 1.55um. In [40] Casalino et al. reported the first
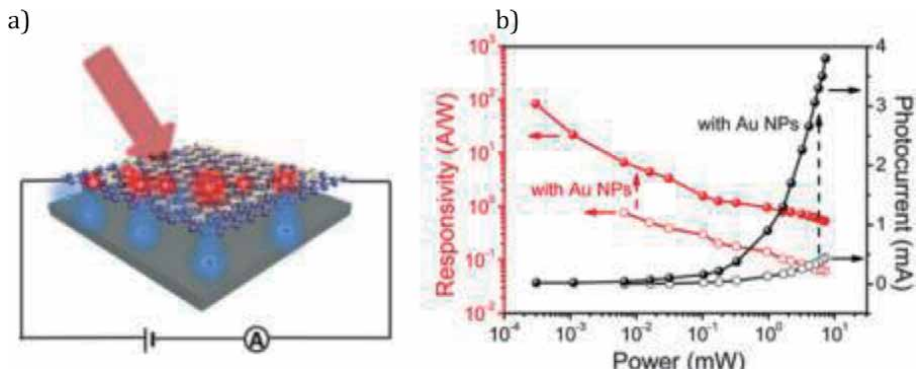
Figure 5.
a) Schematic illustration of the graphene SWIR PD reported in [44]. In b) the comparison between the photoresponse of the devices with and without gold nanoparticles at vary illumination powers. Reprinted with permission from ACS Nano 2017, 11, 1, 430–437. Copyright 2017 American Chemical Society.

demonstration of free-space vertically-illuminated PDs operating under a 2 µm radiation. Through an electrical analysis in a range of temperature from 280 to 315°C, they extracted the value of the SBH resulted to be 0.62 eV at 300 K. From the analysis it emerged a temperature dependence of the SBH which has been ascribed to the presence of defect at the interface between graphene and silicon. The proposed devices show at zero bias an internal responsivity of 10.3 mA/W, corresponding to an external one of 0.16 mA/W, accordingly to the theorical predictions.

In last years, there has been increasing interest in others 2D layered materials. In particular, TMDCs have emerged thanks to the attractive possibility to tune their bandgaps through the quantity of layers as well as their exceptional electronic and optical properties.

Molybdenum disulfide (MoS2) is characterized by an indirect bandgap of about 1.3 eV that increases up to 1.8 eV and changes into a direct one in the monolayer.

In 2015, Wang et al. presented a MoS_2/Si heterojunction based on vertically standing layered configuration for the realization of ultrafast photodetectors [28]. The deposition of MoS_2 via sputtering allowed the growth of a policrystalline film with a vertical structure, from the p-silicon substrate up to the Ag electrode, enabling the exploitation of the high in-plane mobility of the MoS_2. The electrical analysis of the junctions showed a potential barrier at the interface between the two materials of 0.33 eV while the good quality of the junction was proved by an ideality factor of 1.83 and a rectification ratio of about 5000. The PD worked over a broadband spectrum, from visible to near infrared, with a maximum responsivity of $300 mAW^{-1}$ at 808 nm. The low dark current of the junction ensured a high detectivity up to 10^{13} Jones and a fast response of 2 µs. Furthermore, the PD exhibited a photovoltaic behavior by producing a photovoltage and a photocurrent of 210 mV and 100 µA, respectively, at open circuit and zero bias.

Subsequently, Kim et al. have proposed a similar PD based on a tungsten disulphite active layer [29]. Thanks to a bottom-up approach, by using a magnetron sputtering, they were able to grow vertical WS_2 layers onto a p-Si wafer at different temperatures **Figure 6a**. Through the X-Rays Diffraction (XRD) analysis they found a highly crystalline structure in the layers deposited at 400°C.

The I-V curves demonstrated the formation of the heterojunction and the rectifying behavior within ±2 V where the rectification ratio was about 20000. The ideality factor and the dark saturation current I_S were estimated to be 1.43 and 0.1 µA, respectively. The WS_2/Si junction exhibited a zero-bias photoresponse and
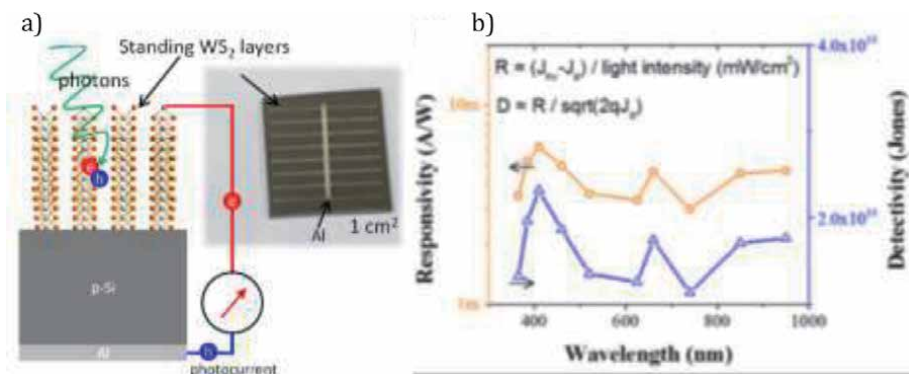
Figure 6.
a) Sketch and photograph of the WS_2/p-Si based PD investigated by [29] et al. and b) spectral photoresponse of the device. Reprinted with permission from ACS Appl. Mater. Interfaces 2018, 10, 4, 3964–3974. Copyright 2018 American Chemical Society.

an open-circuit voltage of 210 mV together with a remarkable signal-to-noise ratio greater than 9000 for an incident radiation of 850 nm.

As shown in **Figure 6b**, the photoresponse of the device spanned the range of wavelengths from UV to NIR with peak responsivity values of 5-6mAW^{-1} at 420, 680, 800 and 1000 nm suggesting a an excitonic absorption of the WS$_2$. In addition, Kim et al. analyzed the transient photocurrent at various wavelengths allowing to evaluate the photoresponse speed of the photodetectors that results to be about 1.1 μs for a 10 kHz modulated signal, very higher than the conventional Si UV photodetectors. This impressive performance can be attributed to the large in-plane charge WS$_2$ carrier mobility.

Very interestingly, in 2019 Ahmad et al. reported a photodetector based on a WS$_2$ monolayer/Si junction [30]. The WS$_2$ monolayer was characterized by a lower bandgap with respect to the bulk material enabling higher responsivity of 10.46 mAW^{-1} at 785 nm. On the other hand, such configuration did not permit to take advantage of the in-plane conductivity of the absorber medium, resulting in a slower response of 186.7 ms for a 20 kHz modulated signal.

Another emerging 2D TMDC is the platinum diselenide (PtSe$_2$). Its bandgap, ranging from zero in the monolayer to 1.2 eV in the bulk, make it very promising for the NIR photodetection. Recently, Xie et al. investigated PDs exploiting a multilayered PtSe$_2$/silicon heterojunction [31]. In their work a thermally assisted conversion was used in order to have the *in situ* preparation of the PtSe$_2$ on the silicon substrate. Such technique permitted to realize interfaces with a small number of defects that would trap the photogenerated carriers. The XRD patterns displayed a policrystalline structure with nanometer-sized crystalline domains. The as-deposited 14.5 nm-thick film, corresponding to about 17 layers of PtS$_2$, can be accordingly considered as a semimetal. The I-V curves confirmed the rectifying nature of the heterojunction in the range within ±5 V and the ideality factor was estimated to be about 1.64. The PDs could operate in a wide spectrum ranging from 200 to 1550 nm with a maximum responsivity of 520mAW^{-1} at 808 nm. This device showed also the capability to detect the telecommunication wavelengths of 1310 and 1550 nm with a responsivity of 33.25 and 0.57mAW^{-1}, respectively. Such results were attributed to the high NIR radiation optical absorption of the PtSe$_2$ layer. It is worth mentioning that these PDs showed a fast response, indeed, the rise time and fall time were 55.3 and 170.5 μs, respectively. The clean interfaces obtained thanks to the *in situ* preparation strongly influenced the performance of the device that exhibited a response speed comparable to the above mentioned works on TMDC PDs based on vertical structure.

4. Conclusions

In this chapter the physical principles of NIR Schottky PDs based on 2D materials have been elucidated and the main devices reported in literature have been discussed. In particular, PDs exploiting the IPE among 2D layered materials and silicon are deepened since to date they represent the most promising approach for the realization of high performances Si-based PDs. Devices discussed along this chapter have been summarized in **Table 1** to allow an immediate comparison of their performance. It emerges that the low absorption coefficient of the graphene makes indispensable the use of structures enabling the light trapping for enhancing the light-matter interaction. Indeed, devices exploiting resonant cavities, waveguides and plasmonic effects result to have best performances in terms of responsivity. These structures show performance comparable with the well-established germanium technology adding the potentialities to detect wavelength

Ref.	Type	R	λ(μm)	I_d	SBH (eV)	Config.
[34]	Exfoliated graphite/ p-Si	9.9mAW^{-1} at -16 V	1550	~2.4 μA at -16 V	0.44–0.46	Free-space
[4]	SLG/p-Si	370mAW^{-1} at −3 V	1550	~3 μA at −3 V	0.34	WG
[40]	SLG/p-Si	20mAW^{-1} at −10 V	1550	~147 μA at −10 V	0.46	Free-space
[41]*	SLG/p-Si	0.43AW^{-1} at 0 V	1550	561 nA if SLG radius < 15 μm	0.45	Free-space
[44]	SLG/n-Si	83AW^{-1}	1550	~0.1 μA at -1.5 V	0.5	Free-space
[35]	SLG/p-Si	0.16mAW^{-1} at 0 V	2000	~3 μA at −6 V	0.62	Free-space
[28]	MoS_2/p-Si	300mAW^{-1}	808	—	0.33	Free-space
[29]	n-WS_2/p-Si	5-6mAW^{-1}	420, 680, 800, 1000	0.1 μA (saturation current)	—	Free-space
[30]	WS_2/n-Si	10.46mAW^{-1}	785	0.1 μA at −6 V	—	Free-space
[31]	$PtSe_2$/p-Si	520mAW^{-1}/ 0.57mAW^{-1}	808/ 1550	1.1 nA at -1 V	—	Free-space

Theoretical work.

Table 1.
Comparison of the main electrical and optical parameters of the 2D materials/Si NIR PDs reported in this chapter.

longer than 1550 nm. Although most of the Schottky PDs are based on graphene, more recently others 2D materials have stood out showing promising outcomes in the NIR spectrum.

Thanks to the easy fabrication processes and the low cost of production, this new family of PDs represents a breakthrough, opening the way towards the commercial integration of silicon in photonics.

Author details

Teresa Crisci[1,2], Luigi Moretti[1], Mariano Gioffrè[2] and Maurizio Casalino[2]*

1 Department of Mathematics and Physics (DMF), University of Campania "Luigi Vanvitelli", Naples, Italy

2 Institute of Applied Science and Intelligent Systems (ISASI), National Research Council (CNR), Naples, Italy

*Address all correspondence to: maurizio.casalino@na.isasi.cnr.it

IntechOpen

References

[1] Yole Dèvelop. [Internet]. 2020 Available from: http://www.yole.fr/Si_Photonics_Datacom_Sensing.aspx

[2] Soref, R. A., and J. P. Lorenzo: Single-crystal silicon: a new material for 1.3 and 1.6 µm integrated-optical components. Electronics Letters 21.21 1985; 953-954

[3] Soref, R.A.; Lorenzo, J.P. IEEE J. Quantum Electron. 1986, 22, 873–879

[4] Goykhman, I., Sassi, U., Desiatov, B., Mazurski, N., Milana, S., De Fazio, D., ... & Ferrari, A. C.: On-chip integrated, silicon–graphene plasmonic Schottky photodetector with high responsivity and avalanche photogain. Nano letters. 2016; 16.5: 3005-3013. DOI: 10.1021/acs.nanolett.5b05216

[5] Alavirad, M., Roy, L., & Berini, P.: Surface plasmon enhanced photodetectors based on internal photoemission. Journal of Photonics for Energy, 2016; 6.4: 042511

[6] Casalino, M.: Internal photoemission theory: Comments and theoretical limitations on the performance of near-infrared silicon Schottky photodetectors. IEEE Journal of Quantum Electronics, 2016; 52.4: 1-10

[7] Scales, C.; Berini, P.: Thin-Film Schottky Barrier Photodetector Models. IEEE J. Quantum Electron. 2010; 46, 633–643

[8] Elabd, H.; Villani, T.; Kosonocky, W. F.: Palladium-Silicide Schottky-Barrier IR-CCD for SWIR Applications at Intermediate Temperatures. IEEE ED Lett. 1982; 3, 89

[9] Elabd, H.; Villani, T.S.; Tower, J.R.: High density Schottky-barrier IRCCD sensors for SWIR applications at intermediated temperature. In Proceedings of the SPIE's Technical Symposium East, Arlington, VA, USA, 3–7 May 1982

[10] Kosonocky, W.F., Elabd, H., Erhardt, H.G., Shallcross, F.V., Villani, T., Meray, G., Cantella, M.J., Klein, J., Roberts, N. 64 → 128-Elements High-Performance PtSi IR-CCD Image Sensor. In Proceedings of the 1981 International Electron Devices Meeting, Washington, DC, USA, 7–9 December 1981

[11] Kosonocky, W.F., Elabd, H., Erhardt, H.G., Shallcross, F.V., Meray, G.M., Villani, T.S., Groppe, J.V., Miller, R., Frantz, V.L., Cantella, M.J., et al. Design and performance of 64 → 128-element PtSi Schottky-barrier IR-CCD focal plane array. In: Proceedings of the SPIE's Technical Symposium East, Arlington, VA, USA, 3–7 May 1982

[12] Wang, W. L., Winzenread, R., Nguyen, B., Murrin, J.J. High fill factor 512 x 512 PtSi focal plane array. In: Proceedings of the SPIE's 33rd Annual Technical Symposium, San Diego, CA, USA, 22 December 1989

[13] Crisci, T.; Moretti, L.; Casalino, M.: Theoretical Investigation of Responsivity/NEP Trade-off in NIR Graphene/Semiconductor Schottky Photodetectors Operating at Room Temperature. Applied Sciences, 2011; 11, 3398.

[14] Casalino, M.; Sirleto, L.; Moretti, L.; Della Corte, F.; Rendina, I.: Design of a silicon resonant cavity enhanced photodetector based on the internal photoemission effect at 1.55 µm. Journal of Optics A: Pure and applied optics, 2006; 8.10: 909

[15] Casalino, M.; Sirleto, L.; Moretti, L.; Gioffrè, M.; Coppola, G.; Rendina, I.: Silicon resonant cavity enhanced photodetector based on the internal photoemission e↵ect at 1.55 micron:

Fabrication and characterization. Appl. Phys. Lett. 2008; 92, 251104

[16] Zhu, S.; Chu, H.S.; Lo, G.Q.; Bai, P.; Kwong, D.L.: Waveguide-integrated near-infrared detector with self-assembled metal silicide nanoparticles embedded in a silicon p-n junction. Appl. Phys. Lett. 2012; 100, 61109

[17] Sobhani, A.; Knight, M.W.; Wang, Y.; Zheng, B.; King, N.S.; Brown, L.V.; Fang, Z.; Nordlander, P.; Halas, N.J.: Narrowband photodetection in the near-infrared with a plasmon-induced hot electron device. Nat. Commun. 2013; 4, 1643

[18] Knight, M.W.; Sobhani, H.; Nordlander, P.; Halas, N.J.: Photodetection with active optical antennas. Science 2011; 332, 702–704

[19] Berini,P.; Olivieri,A.; Chen,C.: Thin Au surface plasmon waveguide Schottky detectors on p-Si. Nanotechnology 2012; 23, 444011

[20] Akbari, A.; Tait, R.N.; Berini, P.: Surface plasmon waveguide Schottky detector. Opt. Express 2010; 18, 8505–8514

[21] Elabd, H.; Kosonocky, W.F.: Theory and measurements of photoresponse of thin film Pd2Si and PtSi Schottky-barrier detectors with optical cavity. RCA Rev. 1982; 43, 569

[22] Vickers, V.E.: Model of Schottky barrier hot-electron-mode photodetection. Appl. Opt. 1971; 10, 2190

[23] Wang, X.; Gan, X.: Graphene integrated photodetectors and opto-electronic devices—A review. Chin. Phys. B 2017; 26, 34201

[24] Koppens, F.H.L.; Mueller, T.; Avouris, P.; Ferrari, A.C.; Vitiello, M.S.; Polini, M.: Photodetectors based on graphene, other two-dimensional materials and hybrid systems. Nat. Nanotechnol. 2014; 9, 780–793

[25] Wang, Q. H., Kalantar-Zadeh, K., Kis, A., Coleman, J. N., & Strano, M. S.: Electronics and optoelectronics of two-dimensional transition metal dichalcogenides. Nature nanotechnology, 2012; 7.11: 699-712.

[26] Tang, Y., & Mak, K. F.: 2D materials for silicon photonics. Nature nanotechnology, 2017; 12.12: 1121-1122.

[27] Novoselov, K. S., Mishchenko, O. A., Carvalho, O. A., & Neto, A. C.: 2D materials and van der Waals heterostructures. Science; 2016, 353.6298.

[28] Wang, L., Jie, J., Shao, Z., Zhang, Q., Zhang, X., Wang, Y., ... & Lee, S. T: MoS2/Si heterojunction with vertically standing layered structure for ultrafast, high-detectivity, self-driven visible–near infrared photodetectors. Advanced Functional Materials, 2015; 25.19: 2910-2919

[29] Kim, H. S., Patel, M., Kim, J., & Jeong, M. S.: Growth of wafer-scale standing layers of WS2 for self-biased high-speed UV–Visible–NIR optoelectronic devices. ACS applied materials & interfaces, 2018; 10.4: 3964-3974

[30] Ahmad, H., Rashid, H., Ismail, M. F., & Thambiratnam, K.: Fabrication and characterization of tungsten disulphide/silicon heterojunction photodetector for near infrared illumination. Optik, 2019; 185: 819-826

[31] Xie, C., Zeng, L., Zhang, Z., Tsang, Y. H., Luo, L., & Lee, J. H.: High-performance broadband heterojunction photodetectors based on multilayered PtSe2 directly grown on a Si substrate. Nanoscale, 2018; 10.32: 15285-15293

[32] Fowler, R.H.: The analysis of photoelectric sensitivity curves for clean

metals at various temperatures. Phys. Rev. 1931; 38, 45–56

[33] Cohen, J.; Vilms, J.; Archer, R.J.: Investigation of Semiconductor Schottky Barriers for Optical Detection and Cathodic Emission; Report No. 68-0651; Air Force Cambridge Research Labs: Force Base, OH, USA, 1968; p. 133

[34] Amirmazlaghani, M.; Raissi, F.; Habibpour, O.; Vukusic, J.; Stake, J.: Graphene-Si Schottky IR detector. IEEE J. Quant. Elect. 2013; 49, 2589

[35] Casalino, M., Russo, R., Russo, C., Ciajolo, A., Di Gennaro, E., Iodice, M., & Coppola, G.: Free-space Schottky graphene/silicon photodetectors operating at 2 μm. ACS Photonics, 2018; 5.11: 4577-4585

[36] Levy, U., Grajower, M., Goncalves, P. A. D., Mortensen, N. A., & Khurgin, J. B.: Plasmonic silicon Schottky photodetectors: The physics behind graphene enhanced internal photoemission. Apl Photonics, 2017; 2.2: 026103

[37] Goncalves, P.A.D.; Peres, N.M.R.: Electromagnetic properties of solids in a nutshell. In An Introduction to Graphene Plasmonics; World Scientific: Singapore, 2016; pp. 17–24. ISBN 978-981-4749-97-8

[38] Van Tuan, D. Electronic and Transport Properties of Graphene. In Charge and Spin Transport: in Disordered Graphene-Based Materials; Springer: Cham, Switzerland, 2016; p. 10

[39] Chen, C. C., Aykol, M., Chang, C. C., Levi, A. F. J., & Cronin, S. B.: Graphene-silicon Schottky diodes. Nano letters, 2011; 11.5: 1863-1867

[40] Casalino, M., Sassi, U., Goykhman, I., Eiden, A., Lidorikis, E., Milana, S., ... & Ferrari, A. C.: Vertically illuminated, resonant cavity enhanced, graphene–silicon Schottky photodetectors. ACS nano, 2017; 11.11: 10955-10963

[41] Casalino, M.: Design of resonant cavity-enhanced schottky graphene/silicon photodetectors at 1550 nm. Journal of Lightwave Technology, 2018; 36.9: 1766-1774

[42] Casalino, M., Crisci, T., Moretti, L., Gioffrè, M., Iodice, M., Coppola, G., ... & Morandi, V.: Silicon Meet Graphene for a New Family of Near-Infrared Resonant Cavity Enhanced Photodetectors. In: 2020 22nd International Conference on Transparent Optical Networks (ICTON); 19-23 July; Bari, Italy: IEEE; 2020. p. 1-4

[43] Casalino, M.: Theoretical Investigation of Near-Infrared Fabry–Pérot Microcavity Graphene/Silicon Schottky Photodetectors Based on Double Silicon on Insulator Substrates. Micromachines, 2020; 11.8: 708

[44] Chen, Z., Li, X., Wang, J., Tao, L., Long, M., Liang, S. J., ... & Xu, J. B.: Synergistic effects of plasmonics and electron trapping in graphene short-wave infrared photodetectors with ultrahigh responsivity. ACS nano, 2017; 11.1: 430-437

Chapter 5

Photo-Detectors Based on Two Dimensional Materials

Mubashir A. Kharadi, Gul Faroz A. Malik
and Farooq A. Khanday

Abstract

2D materials like transition metal dichalcogenides, black phosphorous, silicene, graphene are at the forefront of being the most potent 2D materials for optoelectronic applications because of their exceptional properties. Several application-specific photodetectors based on 2D materials have been designed and manufactured due to a wide range and layer-dependent bandgaps. Different 2D materials stacked together give rise to many surprising electronic and optoelectronic phenomena of the junctions based on 2D materials. This has resulted in a lot of popularity of 2D heterostructures as compared to the original 2D materials. This chapter presents the progress of optoelectronic devices (photodetectors) based on 2D materials and their heterostructures.

1. Introduction

Photodetectors are devices that sense the light and convert it into an electric current. Photodetectors are essential components of many devices that are a part of our day to day life [1–5]. Primarily, silicon (Si) has been a material of choice for photodetector applications. Such photodetectors are readily integrated with complementary metal oxide semiconductor (CMOS) technology. The aggressive scaling has reduced the cost of Si-based devices and expanded their range of applications. Though Si photodetectors have evolved and developed over the years. But their performance is limited by the indirect nature of the bandgap of Si. The absorption of Si is limited to the visible and near-infrared parts of the electromagnetic spectrum. Also, the indirect nature of Si's bandgap leads to phonon generation to conserve the momentum during the light assisted transition of carriers from lower energy to higher energy. These phonons lead to scattering of the carriers and thereby reduce the efficiency of Si photodetectors. Also, Si as a material is not a good absorber of light in bulk form, further degrading Si photodetectors' efficiency. These limitations of Si photodetectors have prompted a quest in the research community for alternate materials. Two dimensional (2D) materials, among the class of novel materials for optoelectronic applications, have shown favorable characteristics. Features like direct nature and wide range of bandgap, atomically thin nature, efficient light-matter interaction, and heterostructures forming are interesting. The class of 2D materials encompasses materials like graphene,

transition metal-di-chalcogenides (TMDCs), Xenes etc. 2d materials are artificially derived materials. These materials are derived from layered van der Waals solids. In van der Waals solids, the atomic arrangement is such that the constituent atoms are held together by covalent or ionic bonds giving rise to atomic layers, whereas these atomic layers are held together by van der Waals interactions. The weak nature of van der Waals forces makes it possible to cleave individual layers from these materials. It is possible to obtain a free-standing single atomic or few atomic layers via mechanical exfoliation [6, 7] or liquid phase exfoliation [8, 9]. Graphene, which is a single layer of carbon atoms arranged in a hexagonal manner, is regarded as the original 2D material. Over the years, it has been revealed that graphene possesses many appealing electronic, mechanical, optical and thermal properties. [10–12]. Interaction of light with graphene occurs over a broad bandwidth range (terahertz to ultraviolet wavelengths) because of semi-metallic/gapless nature. This makes graphene a candidate for wide spectral range photodetectors. The atomically thin nature of graphene limits its absorption coefficient [13–15]. Graphene absorbs only 2.3% of incident light (visible and ultraviolet), making this a primary limitation of graphene for photodetector applications. A high absorption coefficient is desirable for an optimum magnitude of photocurrent [16–18]. For the efficient operation of a photodetector, a longer lifetime of the photo exited carriers is desired. Graphene's gapless nature results in a shortened lifetime of photo-excited carriers, which further limits graphene photodetectors' performance. Beyond graphene, TMDCs have also attracted a lot of attention for optoelectronic applications over the past decade. One advantage of TMDCs over graphene is their semiconducting nature. TMDCs possess varied bandgaps, thus making them applicable for broadband photodetection. TMDCs can be represented by the general formula of MX2, where M represents a transition metal and X represents a chalcogenide atom. The arrangement of atoms in MX2 is such that the metal atom is sandwiched between the two chalcogenide atoms, as shown in **Figure 1**. TMDCs detect light at different wavelengths because of layer dependent bandgap [19–21]. Most of the TMDCs have a direct

(a)

(b)
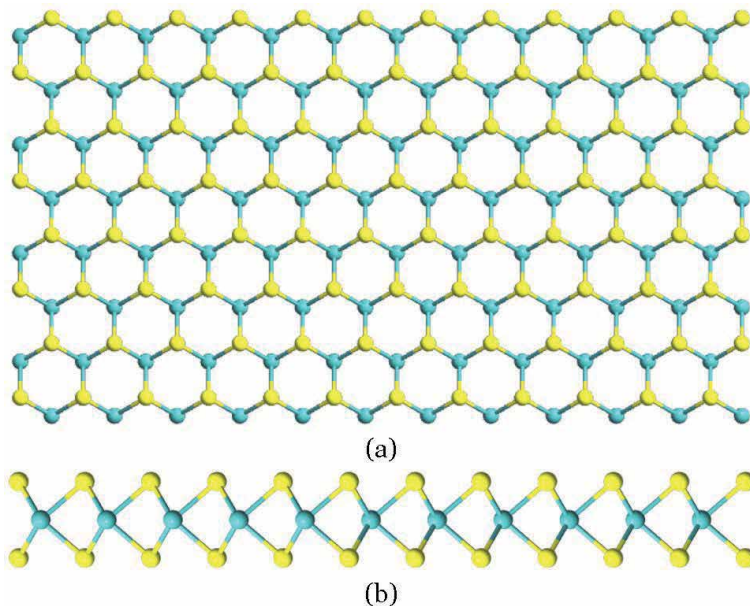
Figure 1.
Structural arrangement of TMDCs (MoS$_2$). (a) Top view and (b) side view. Cyan and Yellow balls are Molybdenum and Sulfur atoms respectively.

nature of the bandgap, limiting the phonon scattering in TMDCs photodetectors, which leads to better efficiency [22]. 2D materials have localized electronic bands, leading to sharp peaks in the density of states (DOS) called Van Hove singularities at specific energies [22]. Generally, in 2D materials like TMDCs, these singularities reside near conduction and valence bands. This leads to an increased probability of electron–hole pair generation upon excitation with light [22, 23]. TMDCs photodetectors show excellent light to current conversion with high responsivity [22]. Although TMDCs based photodetectors have shown an appealing development in their performance over the years, these devices are limited by slow response speed. Furthermore, TMDCs photodetectors are still behind the absorption efficiency of bulk Si photodetectors. Apart from these 2D materials, materials like silicene, phosphorene etc., have shown promising theoretical results as far as optoelectronic applications are considered.

Though the field of 2D materials is still developing, the early results of optoelectronic devices based on these materials are very promising. The unique properties of 2D materials have ushered in a lot of theoretical and experimental research for optoelectronic applications over the past decade or so. This has led to the proposal of numerous photodetectors based on 2D materials both theoretically and experimentally. This chapter aims at presenting an insight into the novel photodetectors based on 2D materials. Section 2 offers a discussion on photodetectionchanisms in 2D materials. Section 3 presents a discussion on photodetectors based on 2D materials and their heterostructures; Section 4 presents a brief summary of the chapter and future scope of 2D materials for photodetector applications.

2. Photodetection mechanisms in 2D materials

Generally, photocurrent generation mechanisms are divided into three categories, viz. photovoltaic effect, photo-thermoelectric effect, and photo-bolometric effect. In the photovoltaic effect, a built-in electric field results in the separation of the electrons and holes. This built-in electric field may be generated due to a Schottky barrier at the metal–semiconductor interface. Photodetectors working under this mechanism are called photodiodes. In the photo-thermoelectric effect, a non-uniform light source is used. This light source leads to non-uniform heating of the channel, resulting in a temperature gradient within the channel. Due to this temperature gradient, carriers move from the high-temperature region to the low-temperature region. The migration of the carriers leads to their accumulation in the low-temperature region, which results in a potential. The photo-bolometric effect is based on uniform heating of the material under illumination. This uniform heating results in a change in the resistivity of the material. This effect is directly proportional to the variation of the material's conductivity and the increment in temperature caused by light irradiation. In contrast to the photo-thermoelectric effect, the photo-bolometric effect does not drive the current but only changes the intensity of the current under external bias and illumination.Another unique mechanism observed in optoelectronic devices like photodetectors is internal photoemission (IPE). IPE involves photoinjection of electrons from an emitter/source (metal or semiconductor) into the conduction band of a collector/drain (semiconductor or insulator) in a BJT/FET. The holes are photoinjected into the valence band of the collector/drain and is called as hole photoemission [24]. In IPE, an optical excitation of electrons in the metal to an energy above the Schottky barrier is involved. These excited electrons are then transported to the conduction band of the semiconductor. The Initial theory of IPE was proposed by Fowler [25, 26]. However, this theory does not take the thickness of the Schottky

metal layer into consideration. Over the years the original theory of IPE has been refined largely resulting in much better assessment of the performance of the devices based on this effect [27, 28].

3. Photodetectors based on 2D materials

3.1 Graphene photodetectors

Graphene is regarded as the original 2D material and has a hexagonal arrangement of atoms. Graphene has a planar geometry contrary to some other 2D materials like Xenes (silicene, germanene stanene etc.). The Xenes, in general, have a buckled geometry wherein the two sub lattices of the hexagonal lattice are slightly displaced with respect to each other. Graphene can absorb light with a wavelength ranging from ultraviolet to mid-infrared [29, 30]. Graphene has small optical absorption due to its atomically thin nature, limiting the photoresponsivity of the photodetectors based on it. A graphene photodetector exhibited a bandwidth of 500 GHz and a photoresponsivity of 0.5 mAW^{-1} [31]. A metal-graphene-metal (MGM) photodetector having asymmetric electrodes has been investigated for extended operating frequency. This device shows an external photoresponsivity of 6.1 mAW^{-1}.

Some of the essential advantages of graphene photodetectors are high speed, ultra-broadband frequency range, and compatibility to circuits [32]. Compared to conventional semiconductors, graphene photodetectors show low photoresponsivity, which proves to be a significant drawback of such photodetectors. To overcome this and the other drawbacks, some techniques have been proposed to improve graphene photodetectors' optical absorption. For example, the use of nanostructured plasmonics leads to enhanced light concentration in the device via plasmonics resonance [33, 34]. This helps in improving the local electric field [33, 34]. Apart from enhancing the quantum efficiency, the plasmonics can also help in achieving multicolor detection [35]. A graphene photodetector possessing plasmonics nanoantennas sandwiched between two graphene layers shows a quantum efficiency of up to 20%. Though this method may offer quantum efficiency improvements, it reduces the device's operational bandwidth as the nanostructures' resonance determines the working wavelength in these systems.

Another method to improve graphene photodetectors' photoresponsivity is to integrate quantum dots with graphene [36]. The photoresponsivity and photodetection gain of such a device are 10^7 AW^{-1} and 10^8, respectively. The presence of quantum dots in this device helps the photo-excited carriers (electrons or holes) to reach the graphene sheet while trapping the opposite type of carriers (holes or electrons). This leads to a phenomenon known as field-effect doping. Graphene photodetectors using PbS quantum dots have also been fabricated [37]. The device portrays a photoresponsivity of 10^7 AW^{-1}. Graphene-quantum dot photodetectors are limited by factors like low operational speed and low operating bandwidth.

Another method to improve the photoresponse in graphene photodetectors is to use micro-cavities [38–42]. Such photodetectors are characterized by high speed, high efficiency, ultra-wide bandwidth and high photoresponsivity. The disadvantage of using micro-cavities is that the device's dimensions are relatively large compared to traditional photodetectors [41].

3.2 Molybdenum disulfide (MoS$_2$) photodetectors

MoS$_2$ in its monolayer form has exciting properties like high carrier mobility 200 cm^{2}V^{-1} s^{-1} [8, 43, 44], direct bandgap of $\approx$1.8 eV [43, 45], high On/Off ratio of

current [45], strong light-matter interaction [8, 44], mechanical flexibility, chemical stability and ease of processing etc. Such exciting features of MoS_2 in its monolayer and few-layer forms make it the most widely studied 2D semiconductor for optoelectronic applications. A photodetector having a typical field-effect transistor (FET) configuration was first reported by Yin et al. [46]. The device comprises of a mechanically exfoliated monolayer of MoS_2 monolayer nanosheet as the effective region. The device shows a unique response with a cut-off wavelength of 670 nm. The cut-off wavelength is consistent with the bandgap of MoS_2 in its monolayer form (1.8 eV). The maximum responsivity of this device is 7.5 mAW^{-1} along with a response speed of 50 ms. A similar photodetector/phototransistor was reported by Lopez-Sanchez et al. [47]. Again, this device is based on an exfoliated MoS_2 monolayer but has an improved responsivity of 800 mAW^{-1} and a cut-off wavelength of 680 nm [47]. The model of the device is shown in **Figure 2**. The improvement in the device performance is attributed to improved mobility of the carriers, quality of the contacts and positioning technique. Apart from improved responsivity, the device portrays a low noise equivalent power (NEP) of 1.5×10^{-15} $WHz^{-1/2}$. Such a low value of NEP is associated with a low value of dark current.

Furthermore, the dark current in this device is limited by the bandgap of MoS_2, which reduces the role of thermally excited carriers. However, the device is relatively slow in its response time, which is of the order of several seconds. Though the response time can be reduced (to 0.6 s) by using short pulses on the gate terminal to remove trapped charges, the response time is still considerable compared to other devices [46]. The photodetector reported by Lopez-Sanchez et al. shows a sublinear dependence of photocurrent on the intensity of the light. Such behavior and the surrounding dependent response speed of MoS_2 indicate that charge trapping in MoS_2 and/or at the MoS_2-SiO_2 interface plays a vital role in the sensing process.

Some of the properties and qualities of MoS_2 depend on the number of layers; accordingly, the performance of the photodetectors varies with the number of layers of MoS_2 [43, 45, 48]. For example, in bulk form, MoS_2 is an indirect bandgap semiconductor and is not suitable for optoelectronic applications, whereas, in its monolayer form, it is a direct bandgap semiconductor, making it suitable for optoelectronic applications. The lifetime of the photoexcited carriers is also dependent on the number of layers. Lee et al. have fabricated phototransistors, having single, double and triple layer MoS_2 as the effective region. The optical bandgap of monolayer MoS_2 is 1.82 eV, whereas, for double and triple layer MoS_2, it is 1.65 eV and 1.35 eV, respectively. Based on the observations, it is seen that triple layer MoS_2 photodetector shows good detection for the red light, whereas double and monolayer MoS_2 photodetectors show good detection for the green light. The layer dependent bandgap in MoS_2 allows for its use in wavelength range up to near-infrared (NIR) [49]. Multilayer MoS_2
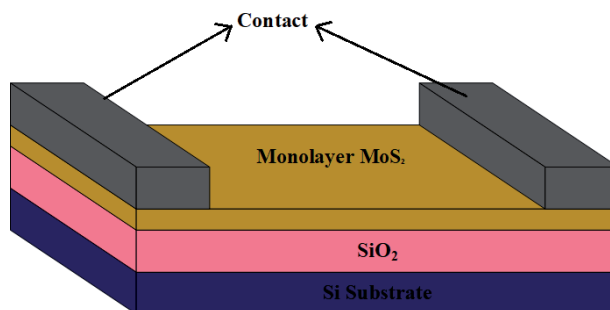
Figure 2.
Model of the exfoliated single layer MoS_2 phototransistor [47].

phototransistors show a degraded responsivity value of 100 mAW^{-1}. Khan et al. have also demonstrated that parameters like responsivity and response speed show a high dependence on the number of MoS$_2$ layers [50].

The properties of 2D MoS$_2$ are distinctly dependent on the method of preparation. Zheng et al. reported a phototransistor based on chemical vapor deposition (CVD) grown MoS$_2$ [51]. This device has a maximum responsivity of 2200 AW^{-1} in vacuum operating at a wavelength of 532 nm. The same device shows a responsivity of 780 AW^{-1} in air. The cause for such a decrease in responsivity is the adsorbates. Due to the large surface-to-volume ratio of MoS$_2$, many adsorbates migrate from ambient air to the surface of MoS$_2$ and the MoS$_2$/substrate interface. These adsorbents act as p-type dopants, leading to carrier scattering and degraded carrier mobility and responsivity in air. The photoresponse could also get affected (decreased) as the adsorbents may act as recombination centers for photoexcited carriers [52].

Perea-Lopez et al. have also fabricated a photodetector based on CVD-grown MoS$_2$ monolayer [53]. The reported device shows a relatively lower responsivity of 1.1 mAW^{-1} at an illuminating wavelength of 514.5 nm [53]. Such a considerable variation in the two devices' responsivity shows the significant role of contact resistance in these devices. Another study has put CVD-grown few-layer MoS$_2$ to use for a photodetector [54]. The performance of the device has been evaluated under harsh conditions with a wavelength of 532 nm [54]. Even at 200°C, the device portrays a photocurrent to dark current ratio of 10. Photodetectors based on MoS$_2$ employing other methods of synthesis like liquid exfoliation [55], solution synthesis [56] and magnetron sputtering [57] have also been reported. As compared to mechanically exfoliated and CVD grown MoS$_2$ based devices, these devices show degraded values of responsivities.

In photodetectors, based on monolayer and bilayer MoS$_2$, both photoconductive and photogating effects were observed to contribute to the photocurrent [58]. Different response times were observed for the two effects, respectively, making it possible to identify their independent contribution to the photocurrent. The photogating effect shows an obvious dependence on the gate voltage and is a slow process. The slowness of this effect comes from the longer lifetime of the trapped charges at the MoS$_2$-SiO$_2$ interface. In contrast, the photoconductive effect has a negligible dependence on the gate voltage and is a fast process. The fast response of the photoconductive effect arises from the mid-gap states due to structural defects in MoS$_2$. The photoconductive response can be studied independently by varying the illuminating light faster than the photo-gating effect.

In view of the average performance of MoS$_2$ photodetectors, several techniques have been proposed to improve their performance [59–66]. One such technique proposed by Leu et al. involves micro-patterning and localized modification of the MoS$_2$ layer [59]. The device is operated at an illuminating wavelength of 532 nm. The local modification is achieved by surface oxidation and oxygen doping. A photodetector based on such a modified MoS$_2$ layer shows improved photoresponse with a responsivity increase of several folds [59]. Kwon et al. proposed a photodetector based on multilayer MoS$_2$ with a bottom gate configuration [60]. As compared to previously reported global gate counterparts, the device shows much-improved photocurrent [49, 60, 67]. The purpose of a bottom gate in such a device is to impose a large tunnel barrier at ungated channel regions, which helps accumulate holes, thereby reducing the potential barrier for free electrons. Once the potential barrier is reduced, there is an increase in the electron depletion region's thermionic current. Furthermore, photocurrent improvement in the accumulation region arises due to decreased tunnel barrier for photoexcited holes. Also, the dark current is suppressed because of the series resistance from ungated areas.

Consequently, the responsivity shows huge improvements and attains a value of $342.6 AW^{-1}$. Kufer et al. fabricated a MoS_2 photodetector, wherein HfO_2 encapsulates the MoS_2 layer. Upon encapsulation, it was seen that the electronic and optoelectronic properties of multilayer MoS_2 photodetector improved [61]. The encapsulated MoS_2, along with negligible hysteresis in the transfer characteristics, showed an enhanced n-type behavior. Encapsulation decreases the number of surface adsorbents, which eventually leads to improved performance. Encapsulation results in an increase in the mobility of carriers and a decrease in the contact resistance. These two effects, in combination, give rise to an increased response speed and responsivity. The device's responsivity can be tuned by the gate voltage and ranges from 10 to $10^4 AW^{-1}$.

3.3 Other TMDCs photodetectors

Apart from MoS_2, other TMDCs have been utilized for photodetector applications. These include $MoSe_2$, WS_2, WSe_2, $MoTe_2$, ReS_2 and $ReSe_2$. This section presents photodetectors based on these materials.

Like MoS_2, monolayer $MoSe_2$ has several alluring properties, such as a direct bandgap of 1.5 eV [68], enhanced photoluminescence (PL) [69] and considerable binding energy of excitons [70]. Improvements in the synthesis of $MoSe_2$ via mechanical exfoliation [71, 72] and CVD methods [73–75] have widened their scope of photodetector applications. Chang et al. and Xi et al. have reported monolayer $MoSe_2$ phototransistors [76, 77]. $MoSe_2$ monolayers for the phototransistors were prepared via CVD methods. The responsivities of the phototransistors are of the order of mAW^{-1}, which is lower than the CVD-grown MoS_2 monolayer counterparts by a few orders [51]. However, if the density of the charge impurities and defects are reduced, an improved photoresponse of the order of tens of milliseconds is expected. The responsivity of $MoSe_2$ based devices can be improved by using a CVD-grown multilayer $MoSe_2$ [78]. But the improvement comes at the cost of degraded response speed [78]. A phototransistor based on a few-layer $MoSe_2$ has been fabricated by Abderrehmane et al. [72]. $MoSe_2$ layers were obtained by mechanical exfoliation methods [72]. This device has a response time of tens of milliseconds and a responsivity of $97.1 AW^{-1}$ operating at a wavelength of 532 nm.

Photodetectors based on monolayer and few-layer WS_2 obtained via different synthesis methods have been reported [79, 80]. The photoresponse of CVD-grown few-layer WS_2 has been studied by Parea-Lopez et al. [81]. The photoresponse reportedly shows a high dependence on photon energy [81]. The responsivity and response speed of the device are reported to be $92 \mu AW^{-1}$ and 5 ms, respectively at a wavelength of 457-647 nm. The dependence of multilayer WS_2 devices' responsivity was observed to depend on the surrounding gaseous environment by Huo et al. [82]. The responsivity shows an increase when the environment changes from vacuum (tens of AW^{-1}) to NH_3 ($884 AW^{-1}$) at a wavelength of 633 nm. The increased responsivity is a consequence of the charge transfer between the NH_3 gas molecule and WS_2. The doping level of WS_2 gets modified by the charge transfer, which eventually increases the lifetime of photoexcited carriers and hence the responsivity. Another study conducted by Lan et al. showed a similar surrounding dependent performance of WS_2 devices [83]. The device showed a decrease in its responsivity from $18.8 mAW^{-1}$ in vacuum to $0.2 \mu AW^{-1}$ in air.

Monolayer and few-layer WSe_2 has also been studied for photodetector applications. Zheng et al. have fabricated photodetectors using CVD-grown WSe_2 monolayer [84]. The effect of metal contacts having different work functions on the device's photoresponse is studied [84]. The device exhibits the maximum ($1.8 \times 10^5 AW^{-1}$) and minimum responsivity with Pd and Ti contacts at a wavelength of

650 nm. However, the device with Ti contacts shows a much smaller response time (23 ms) than the device with Pt contacts. The variation in the device's performance results from the considerable difference in Schottky barriers between WSe_2 and different materials, highlighting the significant role of metal contacts in these devices. Pradhan et al. have demonstrated a photodetector based on a trilayer WSe_2 [85]. The device exhibits the responsivity and response speed of $7AW^{-1}$ and 10 μs, respectively at an illuminating wavelength of 532 nm. Other reports involving graphene contacts and doping of a few-layer WSe_2 have been observed to improve the performance of WSe_2 photodetectors [66, 86, 87].

A newly introduced 2D material, $MoTe_2$ has excellent electronic and optoelectronic properties, due to which it has received a lot of attention recently [88–90]. Yin et al. have reported a phototransistor based on exfoliated few-layer $MoTe_2$ [91]. A study of the effect of different metal contacts on the electrical properties of the $MoTe_2$ phototransistor is presented. The device attains a responsivity of 2.56×10^3 under optimum conditions under an illumination of 473 nm laser.

Re-dichalcogenides are different from the majority of other layered TMDCs due to their high crystal symmetry. ReS_2 and $ReSe_2$, in their distorted 1 T in-plane structure are anisotropic semiconductors [92]. The electrical, mechanical, and optical properties of these materials are extremely anisotropic, rendering these materials interesting for optoelectronic and electronic applications. The bandgap and carrier mobility of $ReSe_2$ was found to be dependent on the layer thickness by Yang et al. [93]. This allows modification of the electronic and optoelectronic properties of ReS_2 devices. A monolayer $ReSe_2$ phototransistor has an exceptional photoresponse with responsivity and response time of $95\ AW^{-1}$ and tens of milliseconds, respectively [93]. The operating wavelength for the device is chosen to be 633 nm. Just like MoS_2 and WS_2 devices, the photoresponse of $ReSe_2$ devices is also found to be dependent on the surroundings [50, 51, 82, 83, 94]. The charge transfer between the surrounding gas and $ReSe_2$ consequently affects the device performance. This charge transfer alters the doping in $ReSe_2$ along with the carrier lifetime [94]. One way to avoid this dependence of performance on surroundings is to use encapsulation or passivation. Though the $ReSe_2$ photodetectors/phototransistors show promising results but an obvious disadvantage of these devices is that the current after removing the illuminating light can not return to dark current levels. This disadvantage is a consequence of the slow recombination rate of the photoexcited carriers. However, this issue may be solved by applying short pulses at the gate terminal to reset the device [36].

Because of the anisotropic crystal structure, ReS_2, in particular, can be utilized to detect polarized light [95]. The model of one such photodetector is shown in **Figure 3**. The responsivity of ReS_2 photodetectors can be largely improved up to the levels of 3.97×10^3 to 1.18×10^6 by electron doping [96] under illumiation of a 1064 nm laser. Besides improved responsivity, the device portrays a broad range of wavelength detection and fast response speed of the order of tens of milliseconds. Significant enhancement in both the electronic and optoelectronic properties of ReS_2 via O_2 plasma treatment was observed by Shin et al. [97]. The device exhibits a high responsivity of $2.5 \times 10^7\ AW^{-1}$ at a laser illumination of 405 nm, which is the highest obtained for a 2D semiconductor based back gated photodetector. Such a high responsivity is a consequence of large thickness (30 nm) and direct bandgap of ReS_2 layers. The response time is observed to be inversely proportional to the plasma treatment duration. Prolonged plasma treatment leads to the formation of trap states within the bandgap of ReS_2. Such trap states result in enhanced recombination rates of photoexcited carriers, which consequently reduce the response time.

In summary, TMDCs photodetectors/phototransistors show a widely varying performance. Responsivities and the response times range from $10^{-7}\ AW^{-1}$ to 10^7
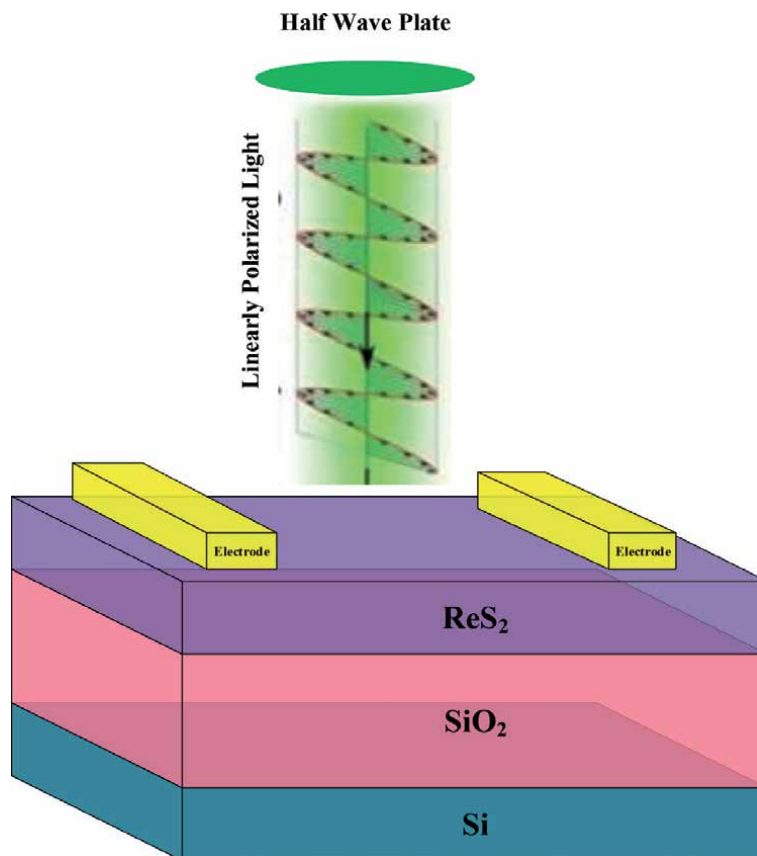
Figure 3.
Model of ReS₂ photodetector [95].

and 10^{-5} to 10^3, respectively. Generally, trap states affect the performance of TMDCs photodetectors. An increase in responsivities is observed at the existence of the trap states in TMDCs and/or at TMDC-dielectric interfaces. However, the response speed is found to decrease because of these trap states. Other factors that affect the TMDCs photodetectors/phototransistors are synthesis methods, number of layers, contact resistance and surrounding environment.

3.4 Black phosphorous photodetectors

Phosphorous, in its elemental nature, can exist in many forms. One such form of phosphorous is called black phosphorous (BP). With a formation energy of -395 $KJmol^{-1-}$ black phosphorous is a thermodynamically stable form of phosphorous at room temperature. Black phosphorous is similar to graphite in its appearance, properties and structure. Black phosphorous sheets have a puckered geometry [98]. Black phosphorous was first successfully exfoliated in 2014 and has received a lot of attention since then [99, 100]. In its monolayer form, the phosphorous atoms form covalent bonds with three adjacent atoms, which results in a wrinkled honeycomb structure. The corresponding layers are held together by van der Waals forces [101]. Unlike graphene, black phosphorous is a semiconductor with a direct bandgap. Due to its strong anisotropic interaction with electrons and photons, black phosphorous is a strong candidate for electronic and optoelectronic applications.

The bandgap's direct nature in black phosphorous makes it easy for the carriers to transit to excited states, as there are negligible chances of phonon scattering [102]. The

photoelectric characteristics of a black phosphorous FET were studied by Buscema et al. [103]. **Figure 4** shows the model of the device. The device operates at a wavelength ranging from visble to NIR part of the spectrum. The device shows an On/Off ratio of 10 along with an electron mobility of 0.5 cm^{2}V^{-1} s^{-1}. Wavelength ranging from visible to NIR results in a photocurrent generation in the proposed device. The responsivity exhibits a typical increase with a decreasing wavelength and attains a maximum value of 4.8 mAW^{-1}. Chen et al. used a sandwich of hBN-BP-hBN to demonstrate a photodetector with a widely tuneable infrared wavelength range [104]. The device shows an absorption of 3% at a wavelength of 3.4 μm, and the absorption of the device was observed to decrease with increasing wavelength. Furthermore, it was observed that the light absorption decreases with an increase in vertical electrical bias. Due to the vertical bias, the bandgap shrinks, giving rise to an increase in carrier concentration. The high carrier concentration results in decreased photo-carrier lifetime and degraded performance of the device. The hBN layer aims to prevent the black phosphorous from oxidation and provide a clean interface.

One of the primitive methods to improve the performance of TMDC photodetectors is to use doping. Accordingly, Keng et al. demonstrated an n-type and p-type black phosphorous photodetectors [105]. The concentration of the dopants was found to be dependent on the thickness of the black phosphorous layer. The device shows a responsivity of 1.4×10^4 AW^{-1} for a device with a black phosphorous thickness of 10 nm [105].

Using a transparent substrate opens up the possibility of novel device designs. Miao et al. have fabricated a photodetector based on multilayer black phosphorous on polyimide film substrate [106]. The device shows a responsivity of 53 AW^{-1}. It is observed that when the device is illuminated by infrared light, enhanced scattering of the carriers with the phonons occurs, which eventually degrades the carrier mobility and the performance of the device. However, such behavior is not observed when a SiO$_2$/Si substrate is used instead of polyimide film.

3.5 Photodetectors based on 2D-heterostructures

The ever-growing evolution and development of 2D materials have led to the formulation of 2D van der Waals heterostructures. Based on these heterostructures, several photodetectors have been reported recently. Apart from their high degree of integration, these devices exhibit excellent performance. The electronic structure and properties induced between these 2D heterostructures' layers show promising characteristics as far as electronic and optoelectronic applications are concerned. 2D heterostructures/heterojunctions are essential building blocks of modern
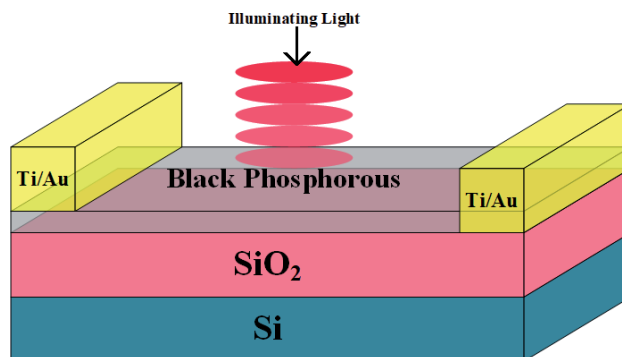
Figure 4.
Model of the few layer black phosphorous photodetector [103].

electronic devices [107]. The band structures of the constituent 2D materials of these heterostructures undergo considerable changes due to electrostatic interactions. Xue et al. have fabricated a MoS_2/WS_2 vertical heterostructures based photodetector [108]. Mo, S and WO_3 were used to prepare the MoS_2/WS_2 heterojunction. The device shows a high rectification along with a considerable responsivity of 2.3 AW^{-1}. The characteristics of the device are evaluated at an illuminatring light of 450 nm. The interfacial built-in electric field prompts the separation of the photo-generated carriers [109]. On transferring the heterojunction to the polydimethyl-siloxane (PMDS) substrate, a decrease in photocurrent is observed due to trapping states between the heterojunction and the substrate [47]. Duan et al. demonstrated a heterojunction diode based on WSe_2/MoS_2 heterojunction [110]. The heterojunction was obtained by transferring the exfoliate MoS_2 to a physical vapor deposition (PVD) grown WSe_2 monolayer. A significant rectification ratio, along with high external quantum efficiency (EQE), was observed at an operating wavelength of 514 nm. It is noteworthy to mention that the EQE of the device is much higher than what is achieved in a lateral doped WSe_2 p-n homojunction [111]. Such a behavior is a consequence of the much better charge separation at the vertically stacked junction interface. Peng et al. have also reported a heterojunction between MoS_2 and WSe_2 [112]. The MoS_2/WSe_2 heterojunction is obtained by mechanical exfoliation and transfer methods. A high charge transfer of 99% from WSe_2 to MoS_2 is observed in a very short time of 470 fs [112]. The device shows promising characteristics for sub-picosecond applications.

Apart from the semiconducting materials based heterostructures, graphene has also been utilized for heterostructures formation. Graphene may not be suitable for photodetector applications independently due to its zero bandgap and high light transmittance. Yu et al. formulated a photodetector based on $MoTe_2$/graphene heterostructures [113] as shown in **Figure 5**. $MoTe_2$ multilayer serves as a light active material in the said heterostructure, and graphene monolayer serves as an efficient transport path for photo-excited carriers. The heterostructure shows better performance as compared to individual graphene and $MoTe_2$ based devices. $MoTe_2$/graphene photodetectors work on the principle of photogating effect. Due to this photogating effect, electrons are trapped in localized states of $MoTe_2$ and holes are shifted towards the graphene layer. The high carrier mobility of graphene allows for a quick extraction of the holes injected into the graphene layer. This results in an enhanced photocurrent in the device. The device shows exceptional values of photoconductive gain and responsivity.

Britnell et al. demonstrated a photodetector based on the heterostructures of a few-layer TMDCs and graphene [114]. The device's performance depends on the encapsulation of one or more layers of TMDC sheets with graphene. The device has a sandwich structure wherein the TMDC photoactive layer is encapsulated between the top and bottom graphene electrodes. Because of the transparency of graphene, the illuminating light can reach efficiently to the TMDC layer. An appreciable photocurrent is observed when the illuminating light impinges on the overlapped regions of graphene and TMDC. The direction of the photocurrent aligns with the direction of the built-in electric field resulting from the gate voltage. This allows to modulate the photocurrent through gate voltage. Due to graphene, the extraction of charges is swift, thus reducing the recombination rate of photo-excited carriers. A similar structure is reported by Duan et al. as well [115]. The device consists of a vertical sandwich of graphene-MoS_2-graphene heterojunction. Similar to the device reported by Britnell et al. [114], the top and bottom layers of graphene act as electrodes, whereas the middle MoS_2 layer acts as the barrier layer. Upon illuminating the MoS_2 layer, the electron–hole pairs get separated asymmetric potentials at the graphene/MoS_2 interface, which leads to

an appreciable photocurrent [115]. A graphene-WSe$_2$-graphene heterostructure based photodetector is reported by Massicotte et al. [116]. The heterostructure is packaged with hBN layers. The device exhibits an ultra-fast response time of 5.5 ps.

Apart from graphene, another novel material called silicene has received a lot of attention in recent years. Silicene, regarded as the 'silicon version of graphene,' also has a hexagonal structure [117–119]. Silicene is the single-layer version of graphene, having the constituent Si atoms arranged in a hexagonal form via covalent bonds [22, 23]. Silicene shares many properties of graphene, like zero bandgap, high mobility of carriers and the presence of a Dirac cone in its band structure. Apart from these excellent electronic properties, one advantage of silicene over graphene is its expected integration with the present state of the art Si-based technology. Kharadi et al. have proposed a photodetector based on silicene/MoS$_2$
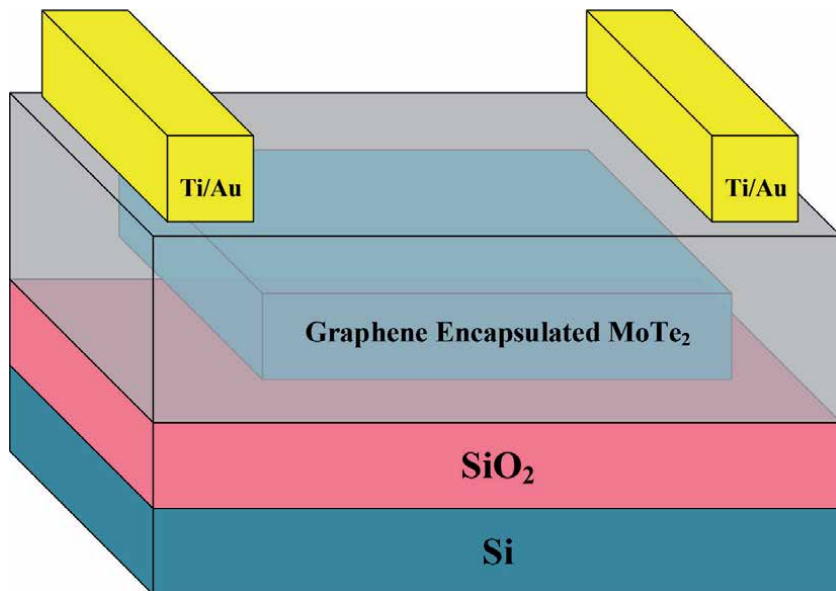
Figure 5.
Photodetector based on MoTe$_2$/graphene heterostructure [113].
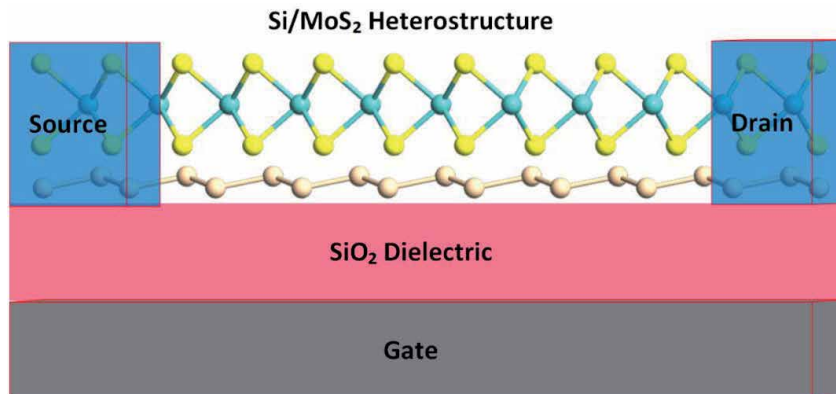
Figure 6.
Model of Si/MoS$_2$ heterostructure based photodetector [22].

Device Type	Wavelength	Responsivity	Response Speed	NEP/Detectivity
Single-Layer MoS_2 Phototransistor [46]	670 nm	7.5 mAW^{-1}	50 ms	—
Ultra-Sensitive Monolayer MoS_2 Photodetector [47]	680 nm	800 mAW^{-1}	0.6 s	1.5×10^{15} $WHz^{-1/2}$
High-detectivity multilayer MoS_2 phototransistors [49]	Up to NIR	100 mAW^{-1}	—	—
High-gain CVD-grown MoS_2 monolayer phototransistor [51]	532 nm	2.2×10^3 AW^{-1} in Vacuum 780 AW^{-1} in Air	—	—
High photosensitivity few-layered $MoSe_2$ back-gated field-effect phototransistor [72]	532 nm	97.1 AW^{-1}	~10 ms	—
Few Layer WS_2 Phototransistor [81]	457-647 nm	92 μAW^{-1}	5 ms	—
Multilayer WS_2 Nano-flakes Photo responsive FET [82]	633 nm	5.7 AW^{-1} in Vacuum 884 AW^{-1} in NH3 Environment	< 20 ms	—
WSe_2 Monolayer Phototransistor [84]	650 nm	1.8×10^5 AW^{-1}	< 23 ms	10^{14} Jones
High Photo responsive Few-layered WSe_2 Transistor[85]	532 nm	7 AW^{-1}	10 μs	—
$ReSe_2$ nanosheet transistor [93]	633 nm	95 AW^{-1}	~ 10 ms	—
Few-layer Black Phosphorus FET [103]	Visible-NIR	48 mAW^{-1}	—	—
Silicene/MoS_2 heterostructure [22]	650 nm	5.66×10^5 AW^{-1}	—	4.76×10^{10} Jones

Table 1.
Characteristics of photodetectors and phototransistors based on different 2D materials.

heterostructure [22]. The model of the device is shown in **Figure 6**. Due to the high mobility of carriers in silicene, it is used as a high-velocity transport path for the photo-excited carriers. Illuminating the device's active region with a light of 650 nm results in the electron–hole pair generation. The electron–hole pairs are separated at the silicene/MoS_2 heterostructure interface due to the built-in electric field generated by a combined effect of charge transfer between silicene and MoS_2 and the gate voltage. Apart from an appreciable photoconductive gain of 2.5×10^{11}, the device exhibits considerable values of responsivity (5.66×10^5 AW^{-1}) and detectivity (4.76×10^{10} Jones).

Table 1. presents the characteristics of the optoelectronic devices based on different 2D materials. In general it can be seen that the light sensitive devices based on 2D materials have shown a steady increase in the performance over the years. Depending on the bandgap of the material used, the photosensitive device can be used in different wavelength regions of the electromagnetic spectrum.

4. Summary

This chapter has summarized the present advances of the photodetectors based on 2D materials. With the ongoing research on 2D materials and their heterostructures, the class of 2D materials may mature to a large extent as far as electronic applications in general and optoelectronic applications, in particular, are concerned. Despite the promising results, certain gaps need to be bridged for the swift development of 2D material-based devices. First, convenient and cost-effective methods for the synthesis of high-quality 2D materials should be explored and developed. Second, several new properties of 2D materials are yet to be fully explored and understood. An exhaustive effort should be focused on exploring and understanding these properties. Third, more effort should be made to formulate the application-specific heterostructures of 2D materials. The electronic and optoelectronic applications may receive a heavy push upon concurrent improvements in material growth processes and fabrication methods.

The future applications of 2D materials depend on effective integration with the present Si-based technology. Materials like silicene, germanene etc., have brought a fresh breath to 2D materials' integration with Si-based technology. Though high-performance optoelectronic applications of 2D materials have been realized, there is still a lot of room for improvement. In general, one may not be surprised if wide-spread 2D material based applications are seen in the commercial market in the near future.

Author details

Mubashir A. Kharadi*, Gul Faroz A. Malik and Farooq A. Khanday
University of Kashmir, Srinagar, J&K, India

*Address all correspondence to: kharadimubashir@gmail.com

IntechOpen

References

[1] Y. Gu, E. S. Kwak, J. L. Lensch, J. E. Allen, T. W. Odom, and L. J. Lauhon, "Near-field scanning photocurrent microscopy of a nanowire photodetector," Appl. Phys. Lett., vol. 87, no. 4, 2005, doi:10.1063/1.1996851.

[2] L. Tang *et al.*, "Nanometre-scale germanium photodetector enhanced by a near-infrared dipole antenna," Nat. Photonics, vol. 2, no. 4, pp. 226-229, 2008, doi: 10.1038/nphoton.2008.30.

[3] H. C. Liu, C. Y. Song, A. J. SpringThorpe, and J. C. Cao, "Terahertz quantum-well photodetector," Appl. Phys. Lett., vol. 84, no. 20, pp. 4068-4070, 2004, doi: 10.1063/1.1751620.

[4] J. B. K. Law and J. T. L. Thong, "Simple fabrication of a ZnO nanowire photodetector with a fast photoresponse time," Appl. Phys. Lett., vol. 88, no. 13, pp. 1-4, 2006, doi: 10.1063/1.2190459.

[5] S. Assefa, F. Xia, and Y. A. Vlasov, "Reinventing germanium avalanche photodetector for nanophotonic on-chip optical interconnects," Nature, vol. 464, no. 7285, pp. 80-84, 2010, doi: 10.1038/nature08813.

[6] H. Li, J. Wu, Z. Yin, and H. Zhang, "Preparation and applications of mechanically exfoliated single-layer and multilayer MoS2 and WSe2 nanosheets," Acc. Chem. Res., 2014, doi: 10.1021/ar4002312.

[7] M. Chhowalla, H. S. Shin, G. Eda, L. J. Li, K. P. Loh, and H. Zhang, "The chemistry of two-dimensional layered transition metal dichalcogenide nanosheets," Nature Chemistry. 2013, doi: 10.1038/nchem.1589.

[8] G. Eda, H. Yamaguchi, D. Voiry, T. Fujita, M. Chen, and M. Chhowalla, "Photoluminescence from chemically exfoliated MoS 2," Nano Lett., 2011, doi: 10.1021/nl201874w.

[9] J. N. Coleman *et al.*, "Two-dimensional nanosheets produced by liquid exfoliation of layered materials," *Science (80-.).*, 2011, doi: 10.1126/science.1194975.

[10] M. J. Allen, V. C. Tung, and R. B. Kaner, "Honeycomb carbon: A review of graphene," Chem. Rev., 2010, doi: 10.1021/cr900070d.

[11] K. S. Novoselov, V. I. Fal'Ko, L. Colombo, P. R. Gellert, M. G. Schwab, and K. Kim, "A roadmap for graphene," Nature. 2012, doi: 10.1038/nature11458.

[12] E. J. H. Lee, K. Balasubramanian, R. T. Weitz, M. Burghard, and K. Kern, "Contact and edge effects in graphene devices," Nat. Nanotechnol., 2008, doi: 10.1038/nnano.2008.172.

[13] Z. Sun and H. Chang, "Graphene and graphene-like two-dimensional materials in photodetection: Mechanisms and methodology," ACS Nano. 2014, doi: 10.1021/nn500508c.

[14] F. H. L. Koppens, T. Mueller, P. Avouris, A. C. Ferrari, M. S. Vitiello, and M. Polini, "Photodetectors based on graphene, other two-dimensional materials and hybrid systems," Nature Nanotechnology. 2014, doi: 10.1038/nnano.2014.215.

[15] J. Li, L. Niu, Z. Zheng, and F. Yan, "Photosensitive graphene transistors," *Advanced Materials*. 2014, doi: 10.1002/adma.201400349.

[16] F. Bonaccorso, Z. Sun, T. Hasan, and A. C. Ferrari, "Graphene photonics and optoelectronics," Nat. Photonics, vol. 4, no. 9, pp. 611-622, 2010, doi: 10.1038/nphoton.2010.186.

[17] F. Xia, T. Mueller, Y. M. Lin, A. Valdes-Garcia, and P. Avouris, "Ultrafast graphene photodetector,"

Nat. Nanotechnol., 2009, doi: 10.1038/nnano.2009.292.

[18] W. Bao *et al.*, "Stacking-dependent band gap and quantum transport in trilayer graphene," Nat. Phys., 2011, doi: 10.1038/NPHYS2103.

[19] A. Castellanos-Gomez, M. Poot, G. A. Steele, H. S. J. Van Der Zant, N. Agraït, and G. Rubio-Bollinger, "Elastic properties of freely suspended MoS2 nanosheets," Adv. Mater., 2012, doi: 10.1002/adma.201103965.

[20] K. He, C. Poole, K. F. Mak, and J. Shan, "Experimental demonstration of continuous electronic structure tuning via strain in atomically thin MoS2," Nano Lett., 2013, doi: 10.1021/nl4013166.

[21] H. J. Conley, B. Wang, J. I. Ziegler, R. F. Haglund, S. T. Pantelides, and K. I. Bolotin, "Bandgap engineering of strained monolayer and bilayer MoS2," Nano Lett., 2013, doi: 10.1021/nl4014748.

[22] M. A. Kharadi, G. F. A. Malik, F. A. Khanday, and K. A. Shah, "Silicene/MoS₂ Heterojunction for High-Performance Photodetector," IEEE Trans. Electron Devices, pp. 1-6, 2020, doi: 10.1109/TED.2020.3037285.

[23] M. A. Kharadi, G. F. A. Malik, K. A. Shah, and F. A. Khanday, "Performance analysis of functionalized silicene nanoribbon-based photodetector," Int. J. Numer. Model. Electron. Networks, Devices Fields, 2020, doi: 10.1002/jnm.2809.

[24] J. S. Helman and F. Sánchez-Sinencio, "Theory of Internal Photoemission," Phys. Rev. B, vol. 7, no. 8, pp. 3702-3706, Apr. 1973, doi: 10.1103/PhysRevB.7.3702.

[25] R. H. Fowler, "The Analysis of Photoelectric Sensitivity Curves for Clean Metals at Various Temperatures," Phys. Rev., vol. 38, no. 1, pp. 45-56, Jul. 1931, doi: 10.1103/PhysRev.38.45.

[26] I. Goykhman *et al.*, "On-Chip Integrated, Silicon–Graphene Plasmonic Schottky Photodetector with High Responsivity and Avalanche Photogain," Nano Lett., vol. 16, no. 5, pp. 3005-3013, May 2016, doi: 10.1021/acs.nanolett.5b05216.

[27] M. Casalino, "Silicon Photodetectors Based on Internal Photoemission Effect: The Challenge of Detecting Near-Infrared Light," L. Sirleto, Ed. Rijeka: IntechOpen, 2012, p. Ch. 3.

[28] M. Casalino, L. Sirleto, L. Moretti, and I. Rendina, "A silicon compatible resonant cavity enhanced photodetector working at 1.55 $\mathrm{\mu}$m," Semicond. Sci. Technol., vol. 23, no. 7, p. 75001, May 2008, doi: 10.1088/0268-1242/23/7/075001.

[29] R. R. Nair *et al.*, "Fine structure constant defines visual transparency of graphene," *Science (80-.).*, 2008, doi: 10.1126/science.1156965.

[30] K. F. Mak, L. Ju, F. Wang, and T. F. Heinz, "Optical spectroscopy of graphene: From the far infrared to the ultraviolet," Solid State Commun., 2012, doi: 10.1016/j.ssc.2012.04.064.

[31] T. Mueller, F. Xia, and P. Avouris, "Graphene photodetectors for high-speed optical communications," Nat. Photonics, 2010, doi: 10.1038/nphoton.2010.40.

[32] L. Zheng, L. Zhongzhu, and S. Guozhen, "Photodetectors based on two dimensional materials," J. Semicond., vol. 37, no. 9, 2016, doi: 10.1088/1674-4926/37/9/091001.

[33] T. J. Echtermeyer *et al.*, "Strong plasmonic enhancement of photovoltage in graphene," Nat. Commun., 2011, doi: 10.1038/ncomms1464.

[34] S. F. Shi, X. Xu, D. C. Ralph, and P. L. McEuen, "Plasmon resonance in individual nanogap electrodes studied using graphene nanoconstrictions as photodetectors," Nano Lett., 2011, doi: 10.1021/nl200522t.

[35] Y. Liu *et al.*, "Plasmon resonance enhanced multicolour photodetection by graphene," Nat. Commun., 2011, doi: 10.1038/ncomms1589.

[36] G. Konstantatos *et al.*, "Hybrid grapheneĝquantum dot phototransistors with ultrahigh gain," Nat. Nanotechnol., 2012, doi: 10.1038/nnano.2012.60.

[37] Z. Sun, Z. Liu, J. Li, G. A. Tai, S. P. Lau, and F. Yan, "Infrared photodetectors based on CVD-grown graphene and PbS quantum dots with ultrahigh responsivity," Adv. Mater., 2012, doi: 10.1002/adma.201202220.

[38] X. Gan *et al.*, "Chip-integrated ultrafast graphene photodetector with high responsivity," Nat. Photonics, 2013, doi: 10.1038/nphoton.2013.253.

[39] X. Wang, Z. Cheng, K. Xu, H. K. Tsang, and J.-B. Xu, "High-responsivity graphene/silicon-heterostructure waveguide photodetectors," Nat. Photonics, vol. 7, no. 11, pp. 888-891, 2013, doi: 10.1038/nphoton.2013.241.

[40] X. Zhu, W. Yan, N. A. Mortensen, and S. Xiao, "Bends and splitters in graphene nanoribbon waveguides," Opt. Express, 2013, doi: 10.1364/oe.21.003486.

[41] K. Kim, J. Y. Choi, T. Kim, S. H. Cho, and H. J. Chung, "A role for graphene in silicon-based semiconductor devices," Nature. 2011, doi: 10.1038/nature10680.

[42] N. Youngblood, Y. Anugrah, R. Ma, S. J. Koester, and M. Li, "Multifunctional graphene optical modulator and photodetector integrated on silicon waveguides," Nano Lett., 2014, doi: 10.1021/nl500712u.

[43] K. F. Mak, C. Lee, J. Hone, J. Shan, and T. F. Heinz, "Atomically Thin MoS_2 : A New Direct-Gap Semiconductor," *Phys. Rev. Lett.*, 2010.

[44] A. Splendiani *et al.*, "Emerging photoluminescence in monolayer MoS2," Nano Lett., 2010, doi: 10.1021/nl903868w.

[45] B. Radisavljevic, A. Radenovic, J. Brivio, V. Giacometti, and A. Kis, "Single-layer MoS2 transistors," Nat. Nanotechnol., 2011, doi: 10.1038/nnano.2010.279.

[46] Z. Yin *et al.*, "Single-Layer MoS2 Phototransistors," ACS Nano, vol. 6, no. 1, pp. 74-80, Jan. 2012, doi: 10.1021/nn2024557.

[47] O. Lopez-Sanchez, D. Lembke, M. Kayci, A. Radenovic, and A. Kis, "Ultrasensitive photodetectors based on monolayer MoS 2," Nat. Nanotechnol., 2013, doi: 10.1038/nnano.2013.100.

[48] W. Jin *et al.*, "Direct measurement of the thickness-dependent electronic band structure of MoS2 using angle-resolved photoemission spectroscopy," Phys. Rev. Lett., 2013, doi: 10.1103/PhysRevLett.111.106801.

[49] W. Choi *et al.*, "High-detectivity multilayer MoS2 phototransistors with spectral response from ultraviolet to infrared," *Adv. Mater.*, vol. 24, no. 43, pp. 5832-5836, 2012, doi: 10.1002/adma.201201909.

[50] M. F. Khan, M. W. Iqbal, M. Z. Iqbal, M. A. Shehzad, Y. Seo, and J. Eom, "Photocurrent response of MoS2 field-effect transistor by deep ultraviolet light in atmospheric and N2 gas environments," ACS Appl. Mater. Interfaces, 2014, doi: 10.1021/am506716a.

[51] W. Zhang, J. K. Huang, C. H. Chen, Y. H. Chang, Y. J. Cheng, and L. J. Li,

"High-gain phototransistors based on a CVD MoS2 monolayer," Adv. Mater., 2013, doi: 10.1002/adma.201301244.

[52] C. Xie, C. Mak, X. Tao, and F. Yan, "Photodetectors Based on Two-Dimensional Layered Materials Beyond Graphene," Adv. Funct. Mater., vol. 27, no. 19, 2017, doi: 10.1002/adfm.201603886.

[53] P.-L. Néstor *et al.*, "CVD-grown monolayered MoS 2 as an effective photosensor operating at low-voltage," 2D Mater., 2014.

[54] D. S. Tsai *et al.*, "Few-layer MoS2 with high broadband photogain and fast optical switching for use in harsh environments," ACS Nano, 2013, doi: 10.1021/nn305301b.

[55] J. Li, M. M. Naiini, S. Vaziri, M. C. Lemme, and M. Östling, "Inkjet printing of MoS2," Adv. Funct. Mater., 2014, doi: 10.1002/adfm.201400984.

[56] G. Cunningham *et al.*, "Photoconductivity of solution-processed MoS2 films," *J. Mater. Chem. C*, 2013, doi: 10.1039/c3tc31402b.

[57] Z. P. Ling *et al.*, "Large-scale two-dimensional MoS_2 photodetectors by magnetron sputtering," Opt. Express, 2015, doi: 10.1364/oe.23.013580.

[58] M. M. Furchi, D. K. Polyushkin, A. Pospischil, and T. Mueller, "Mechanisms of photoconductivity in atomically thin MoS2," Nano Lett., 2014, doi: 10.1021/nl502339q.

[59] J. Lu *et al.*, "Improved photoelectrical properties of MoS2 films after laser micromachining," ACS Nano, 2014, doi: 10.1021/nn501821z.

[60] J. Kwon *et al.*, "Giant Photoamplification in Indirect-Bandgap Multilayer MoS2 Phototransistors with Local Bottom-Gate Structures,"

Adv. Mater., 2015, doi: 10.1002/adma.201404367.

[61] D. Kufer and G. Konstantatos, "Highly Sensitive, Encapsulated MoS2 Photodetector with Gate Controllable Gain and Speed," Nano Lett., 2015, doi: 10.1021/acs.nanolett.5b02559.

[62] X. Wang *et al.*, "Ultrasensitive and Broadband MoS2 Photodetector Driven by Ferroelectrics," *Adv. Mater.*, vol. 27, no. 42, pp. 6575-6581, 2015, doi: 10.1002/adma.201503340.

[63] H. S. Lee *et al.*, "Metal Semiconductor Field-Effect Transistor with MoS2/Conducting NiO(x) van der Waals Schottky Interface for Intrinsic High Mobility and Photoswitching Speed.," ACS Nano, vol. 9, no. 8, pp. 8312-8320, Aug. 2015, doi: 10.1021/acsnano.5b02785.

[64] Y. Pang *et al.*, "Tribotronic enhanced photoresponsivity of a MOS2 phototransistor," Adv. Sci., 2015, doi: 10.1002/advs.201500419.

[65] J. D. Lin *et al.*, "Electron-doping-enhanced trion formation in monolayer molybdenum disulfide functionalized with cesium carbonate," ACS Nano, 2014, doi: 10.1021/nn501580c.

[66] D. H. Kang *et al.*, "High-Performance Transition Metal Dichalcogenide Photodetectors Enhanced by Self-Assembled Monolayer Doping," *Adv. Funct. Mater.*, 2015, doi: 10.1002/adfm.201501170.

[67] H. S. Lee *et al.*, "MoS 2 nanosheet phototransistors with thickness-modulated optical energy gap," Nano Lett., 2012, doi: 10.1021/nl301485q.

[68] Y. Zhang *et al.*, "Direct observation of the transition from indirect to direct bandgap in atomically thin epitaxial MoSe2," Nat. Nanotechnol., 2014, doi: 10.1038/nnano.2013.277.

[69] S. Tongay *et al.*, "Thermally driven crossover from indirect toward direct bandgap in 2D Semiconductors: MoSe2 versus MoS2," *Nano Lett.*, 2012, doi: 10.1021/nl302584w.

[70] J. S. Ross *et al.*, "Electrical control of neutral and charged excitons in a monolayer semiconductor," Nat. Commun., 2013, doi: 10.1038/ncomms2498.

[71] S. Larentis, B. Fallahazad, and E. Tutuc, "Field-effect transistors and intrinsic mobility in ultra-thin MoSe 2 layers," Appl. Phys. Lett., 2012, doi: 10.1063/1.4768218.

[72] A. Abderrahmane, P. J. Ko, T. V. Thu, S. Ishizawa, T. Takamura, and A. Sandhu, "High photosensitivity few-layered MoSe2 back-gated field-effect phototransistors," Nanotechnology, 2014, doi: 10.1088/0957-4484/25/36/365202.

[73] X. Lu *et al.*, "Large-area synthesis of monolayer and few-layer MoSe2 films on SiO2 substrates," Nano Lett., 2014, doi: 10.1021/nl5000906.

[74] X. Wang *et al.*, "Chemical vapor deposition growth of crystalline monolayer MoSe2," ACS Nano, 2014, doi: 10.1021/nn501175k.

[75] G. W. Shim *et al.*, "Large-area single-layer MoSe2 and its van der Waals heterostructures," ACS Nano, 2014, doi: 10.1021/nn405685j.

[76] Y. H. Chang *et al.*, "Monolayer MoSe2 grown by chemical vapor deposition for fast photodetection," ACS Nano, 2014, doi: 10.1021/nn503287m.

[77] J. Xia *et al.*, "CVD synthesis of large-area, highly crystalline MoSe2 atomic layers on diverse substrates and application to photodetectors," Nanoscale, 2014, doi: 10.1039/c4nr02311k.

[78] C. Jung *et al.*, "Highly Crystalline CVD-grown Multilayer MoSe2 Thin Film Transistor for Fast Photodetector," Sci. Rep., 2015, doi: 10.1038/srep15313.

[79] W. Sik Hwang *et al.*, "Transistors with chemically synthesized layered semiconductor WS 2 exhibiting 10 5 room temperature modulation and ambipolar behavior," Appl. Phys. Lett., 2012, doi: 10.1063/1.4732522.

[80] S. Hwan Lee, D. Lee, W. Sik Hwang, E. Hwang, D. Jena, and W. Jong Yoo, "High-performance photocurrent generation from two-dimensional WS 2 field-effect transistors," Appl. Phys. Lett., 2014, doi: 10.1063/1.4878335.

[81] N. Perea-Lõpez *et al.*, "Photosensor device based on few-layered WS2 films," *Adv. Funct. Mater.*, 2013, doi: 10.1002/adfm.201300760.

[82] N. Huo, S. Yang, Z. Wei, S. S. Li, J. B. Xia, and J. Li, "Photoresponsive and Gas Sensing Field-Effect Transistors based on Multilayer WS 2 Nanoflakes," Sci. Rep., 2014, doi: 10.1038/srep05209.

[83] C. Lan, C. Li, Y. Yin, and Y. Liu, "Large-area synthesis of monolayer WS2 and its ambient-sensitive photo-detecting performance," Nanoscale, 2015, doi: 10.1039/c5nr01205h.

[84] W. Zhang, M. H. Chiu, C. H. Chen, W. Chen, L. J. Li, and A. T. S. Wee, "Role of metal contacts in high-performance phototransistors based on WSe2 monolayers," ACS Nano, 2014, doi: 10.1021/nn503521c.

[85] N. R. Pradhan *et al.*, "High Photoresponsivity and Short Photoresponse Times in Few-Layered WSe2 Transistors," ACS Appl. Mater. Interfaces, 2015, doi: 10.1021/acsami.5b02264.

[86] J. Chen *et al.*, "Chemical Vapor Deposition of Large-Sized Hexagonal

WSe2 Crystals on Dielectric Substrates," *Adv. Mater.*, 2015, doi: 10.1002/adma.201503446.

[87] S.-H. Jo *et al.*, "A High-Performance WSe2 /h-BN Photodetector using a Triphenylphosphine (PPh3)-Based n-Doping Technique.," Adv. Mater., vol. 28, no. 24, pp. 4824-4831, Jun. 2016, doi: 10.1002/adma.201600032.

[88] Y. F. Lin *et al.*, "Ambipolar MoTe2 transistors and their applications in logic circuits," *Adv. Mater.*, 2014, doi: 10.1002/adma.201305845.

[89] C. Ruppert, O. B. Aslan, and T. F. Heinz, "Optical properties and band gap of single- and few-layer MoTe2 crystals," Nano Lett., 2014, doi: 10.1021/nl502557g.

[90] N. R. Pradhan *et al.*, "Field-effect transistors based on few-layered α-MoTe2," ACS Nano, 2014, doi: 10.1021/nn501013c.

[91] L. Yin *et al.*, "Ultrahigh sensitive MoTe2 phototransistors driven by carrier tunneling," Appl. Phys. Lett., 2016, doi: 10.1063/1.4941001.

[92] J. A. Wilson and A. D. Yoffe, "The transition metal dichalcogenides discussion and interpretation of the observed optical, electrical and structural properties," Adv. Phys., 1969, doi: 10.1080/00018736900101307.

[93] S. Yang *et al.*, "Layer-dependent electrical and optoelectronic responses of ReSe2 nanosheet transistors," Nanoscale, 2014, doi: 10.1039/c4nr01741b.

[94] S. Yang, S. Tongay, Q. Yue, Y. Li, B. Li, and F. Lu, "High-performance few-layer Mo-doped ReSe 2 nanosheet photodetectors," Sci. Rep., 2014, doi: 10.1038/srep05442.

[95] F. Liu *et al.*, "Highly Sensitive Detection of Polarized Light

Using Anisotropic 2D ReS2," Adv. Funct. Mater., 2016, doi: 10.1002/adfm.201504546.

[96] S. H. Jo *et al.*, "Broad Detection Range Rhenium Diselenide Photodetector Enhanced by (3-Aminopropyl)Triethoxysilane and Triphenylphosphine Treatment," *Adv. Mater.*, 2016, doi: 10.1002/adma.201601248.

[97] J. Shim *et al.*, "High-Performance 2D Rhenium Disulfide (ReS2) Transistors and Photodetectors by Oxygen Plasma Treatment," Adv. Mater., 2016, doi: 10.1002/adma.201601002.

[98] V. V. Korolkov *et al.*, "Supramolecular networks stabilise and functionalise black phosphorus," *Nat. Commun.*, 2017, doi: 10.1038/s41467-017-01797-6.

[99] J. Miao *et al.*, "Single Pixel Black Phosphorus Photodetector for Near-Infrared Imaging," *Small*, 2018, doi: 10.1002/smll.201702082.

[100] F. Xia, H. Wang, and Y. Jia, "Rediscovering black phosphorus as an anisotropic layered material for optoelectronics and electronics," Nat. Commun., 2014, doi: 10.1038/ncomms5458.

[101] Y. Cai, G. Zhang, and Y. W. Zhang, "Layer-dependent band alignment and work function of few-layer phosphorene," Sci. Rep., 2014, doi: 10.1038/srep06677.

[102] A. N. Rudenko, S. Yuan, and M. I. Katsnelson, "Toward a realistic description of multilayer black phosphorus: From GW approximation to large-scale tight-binding simulations," *Phys. Rev. B - Condens. Matter Mater. Phys.*, 2015, doi: 10.1103/PhysRevB.92.085419.

[103] M. Buscema, D. J. Groenendijk, S. I. Blanter, G. A. Steele, H. S. J. Van

Der Zant, and A. Castellanos-Gomez, "Fast and broadband photoresponse of few-layer black phosphorus field-effect transistors," Nano Lett., 2014, doi: 10.1021/nl5008085.

[104] X. Chen *et al.*, "Widely tunable black phosphorus mid-infrared photodetector," Nat. Commun., 2017, doi: 10.1038/s41467-017-01978-3.

[105] D.-H. Kang *et al.*, "Self-Assembled Layer (SAL)-Based Doping on Black Phosphorus (BP) Transistor and Photodetector," *ACS Photonics*, vol. 4, no. 7, pp. 1822-1830, Jul. 2017, doi: 10.1021/acsphotonics.7b00398.

[106] J. Miao *et al.*, "Photothermal Effect Induced Negative Photoconductivity and High Responsivity in Flexible Black Phosphorus Transistors," ACS Nano, 2017, doi: 10.1021/acsnano.7b01999.

[107] S. J. Haigh *et al.*, "Cross-sectional imaging of individual layers and buried interfaces of graphene-based heterostructures and superlattices," Nat. Mater., 2012, doi: 10.1038/nmat3386.

[108] Y. Xue *et al.*, "Scalable Production of a Few-Layer MoS2/WS2 Vertical Heterojunction Array and Its Application for Photodetectors.," ACS Nano, vol. 10, no. 1, pp. 573-580, Jan. 2016, doi: 10.1021/acsnano.5b05596.

[109] X. Hong *et al.*, "Ultrafast charge transfer in atomically thin MoS2/WS2 heterostructures," Nat. Nanotechnol., vol. 9, no. 9, pp. 682-686, 2014, doi: 10.1038/nnano.2014.167.

[110] R. Cheng *et al.*, "Electroluminescence and photocurrent generation from atomically sharp WSe2/MoS2 heterojunction p-n diodes.," Nano Lett., vol. 14, no. 10, pp. 5590-5597, Oct. 2014, doi: 10.1021/nl502075n.

[111] A. Pospischil, M. M. Furchi, and T. Mueller, "Solar-energy conversion and light emission in an atomic monolayer p-n diode," Nat. Nanotechnol., 2014, doi: 10.1038/nnano.2014.14.

[112] B. Peng *et al.*, "Ultrafast charge transfer in {MoS} 2 /{WSe} 2 p{\textendash}n Heterojunction," *2D Mater.*, vol. 3, no. 2, p. 25020, May 2016, doi: 10.1088/2053-1583/3/2/025020.

[113] W. Yu *et al.*, "Near-Infrared Photodetectors Based on MoTe2/Graphene Heterostructure with High Responsivity and Flexibility," Small, vol. 13, no. 24, p. 1700268, 2017, doi: https://doi.org/10.1002/smll.201700268.

[114] L. Britnell *et al.*, "Strong light-matter interactions in heterostructures of atomically thin films," *Science (80-.).*, 2013, doi: 10.1126/science.1235547.

[115] W. J. Yu *et al.*, "Highly efficient gate-tunable photocurrent generation in vertical heterostructures of layered materials," Nat. Nanotechnol., 2013, doi: 10.1038/nnano.2013.219.

[116] M. Massicotte *et al.*, "Picosecond photoresponse in van der Waals heterostructures," Nat. Nanotechnol., 2016, doi: 10.1038/nnano.2015.227.

[117] M. A. Kharadi, G. F. A. Malik, F. A. KHANDAY, K. Shah, S. Mittal, and B. K. Kaushik, "Review—Silicene: From Material to Device Applications," ECS J. Solid State Sci. Technol., Dec. 2020, doi: 10.1149/2162-8777/abd09a.

[118] M. A. Kharadi, G. F. A. Malik, K. A. Shah, and F. A. Khanday, "Sub-10-nm Silicene Nanoribbon Field Effect Transistor," IEEE Trans. Electron Devices, 2019, doi: 10.1109/TED.2019.2942396.

[119] M. A. Kharadi, G. F. A. Malik, F. A. Khanday, and K. A. Shah, "Hydrogenated silicene based magnetic junction with improved tunneling magnetoresistance and spin-filtering efficiency," Phys. Lett. A, vol. 384, no. 32, p. 126826, 2020, doi: https://doi.org/10.1016/j.physleta.2020.126826.

Two-Dimensional Group-10 Noble-Transition-Metal Dichalcogenides Photodetector

Haoran Mu, Jian Yuan and Shenghuang Lin

Abstract

2D Transition-Metal Dichalcogenides (TMDs) have been widely considered as a promising material for future optoelectronics due to the strong light-matter interaction, fantastic electronic properties and environmental stability. However, the relatively large bandgap and low mobility of conventional TMDs (such as MoS_2 and WS_2) limit their applications in infra optoelectronics and high-speed photodetection. In this chapter, we introduce a new type of group-10 noble TMDs (NTMDs), which exhibit outstanding properties such as unique structural phase, widely tunable energy gap and high mobility. Till now, various NTMDs-based photodetectors have been realized with ultrabroad detection waveband (200 nm to 10.6 μm), fast response time, high responsivity and detectivity, and polarization sensitivity. NTMDs have been excellent potential candidates for next-generation photodetection devices with high-performance, wafer-scalability and flexibility.

Keywords: noble-transition-metal dichalcogenides, 2D materials, photodetectors, optoelectronics, van der Waals

1. Introduction

Photodetectors, which can capture, identify and visualize the optical signals, have been indispensable devices in modern integrated electronics and communication technology [1–5]. Nowadays, various photosensitive materials have been investigated as the functional materials in photodetectors. For example, gallium nitride (GaN) is commercially for ultraviolet light detection (UV, <400 nm), Si for visible–near-infra (NIR, 400–1100 nm), InGaAs for NIR–mid-IR (MIR, 1–5 μm), and HgCdTe for MIR–far-IR detection (FIR, >5 μm) [2]. However, the ultra-miniaturization and integration of photodetectors with multi-materials are challenging, which require complex nanomanufacturing process and exorbitant production costs. In addition, there are some inherent disadvantages. For example, poor flexibility is a common problem in these conventional semiconductor materials, which restricts their application potential in flexible and wearable electronics. Some specific materials (*e.g.,* HgCdTe) are environment toxic and cannot operated at room temperature [1]. The development trend for high-performance detection and different application scenarios prompts scientists to continue to pursue new materials with novel physical properties.

Two-dimensional (2D) materials have attracted tremendous attention in the past few decades [6–12]. Among them, 2D Transition-Metal Dichalcogenides (TMDs) are considered to be promising for next-generation optoelectronics due to the strong light-matter interaction, weak interlayer van der Waals (vdW) interaction, flexible characteristics and the ease of integration with current silicon-based optical electronics [13–17]. Group-10 noble TMDs (NTMDs) are outstanding representatives in the TMDs family [18–20]. The reintroduced new materials are generalized formulated by Group-10 noble elements (Pt, Pd, and so on.) and chalcogens (S, Se, or Te). Unlike traditional TMDs, the d-electrons in NTMDs are fully occupied their d-orbitals resulting in the highly hybridized P_z orbits and strong interlayer interactions [21, 22]. Therefore, NTMDs exhibit relatively small and widely tunable bandgaps compared with traditional TMDs (such as MoS_2 and WS_2). For example, PtS_2 shows a layer-dependent bandgap from 1.6 to 0.25 eV [21], while $PtSe_2$ changes from a typical semiconductor state (1.2 eV in 1 L $PtSe_2$) to semi-metal state when the thickness increases to over 5 layers [23]. Combining with the high mobility (>1000 $cm^2V^{-1}S^{-1}$, larger than most other TMDs and comparable for that of BP) and environmental stability, NTMDs has great potential in photodetectors applications [21, 23–25]. Moreover, the unique puckered pentagonal structure of PdS_2 and $PdSe_2$ inherently provides them with anisotropic properties [26–28] and may promote the development of polarized photodetectors.

In this chapter, we first discuss the structural, electronic and optical properties of NTMDs. Then we focus on the NTMDs based photodetectors. Wafer-scale NTMDs films with high-quality and large-scale monocrystalline NTMDs nanosheets have been fabricated, which are appropriate for optoelectronic applications. NTMDs and their heterostructure based photodetectors show many advantages such as high-performance, ultrawide spectra detection, long-term environment stability, and anisotropic characteristics. NTMDs have great potential for large-scale imaging and flexible devices, which could be the next-generation optoelectronic core materials.

2. Structural and electronic properties of 2D NTMDs

The atomic coordination of monolayer TMD usually is either trigonal prismatic phase (2H or D_{3h}) or octahedral phase (1 T or D_{3d}), as shown in schematics in **Figure 1a** and **b** [22, 29, 32]. In 2H phase, the d orbitals in transition metal centers split into three degenerated d orbitals (d_{z^2} , $d_{x^2-y^2,xy}$ and $d_{xz,yz}$) and there is usually an energy bandgap (~1 eV in TMDs) between the first two degenerated d orbitals. While in 1 T phase, the centers of transition metal have two degenerated d orbitals (d_{z^2,x^2-y^2} and $d_{xz,yz,xy}$) [22, 29, 32]. Therefore, the thermodynamically favored phase is highly influenced by d electrons count in the transition metals. For NTMDs, the noble metal atoms have abundant d electronics and the d^2sp^3 hybridization is preferred, which lead to the full-filled d-bands. Most NTMDs have thermo-dynamically favored 1 T phase, such as $PtSe_2$, PtS_2, $PtTe_2$ and $PdTe_2$ (See **Figure 1c**) [30]. The strong interlayer hybridization of adjacent chalcogen atoms makes the widely tunable electronic energy band structure with the layer numbers. Here we use PtS_2 and $PtSe_2$ as examples. Both of them are 1 T favored phase, where the bandgap is about 1.17 and 1.6 eV in monolayer $PtSe_2$ and PtS_2, respectively (**Figure 1e** and **f**) [21]. With the increase of stacked layers, the interlayer hybridization would be stronger, with lead to the rapidly decrease of energy gap. According to theoretical calculations, the energy gap in bi-layer $PtSe_2$ is only 0.3 eV, while the stacked layered increase beyond 4 layers, the energy level of valence band
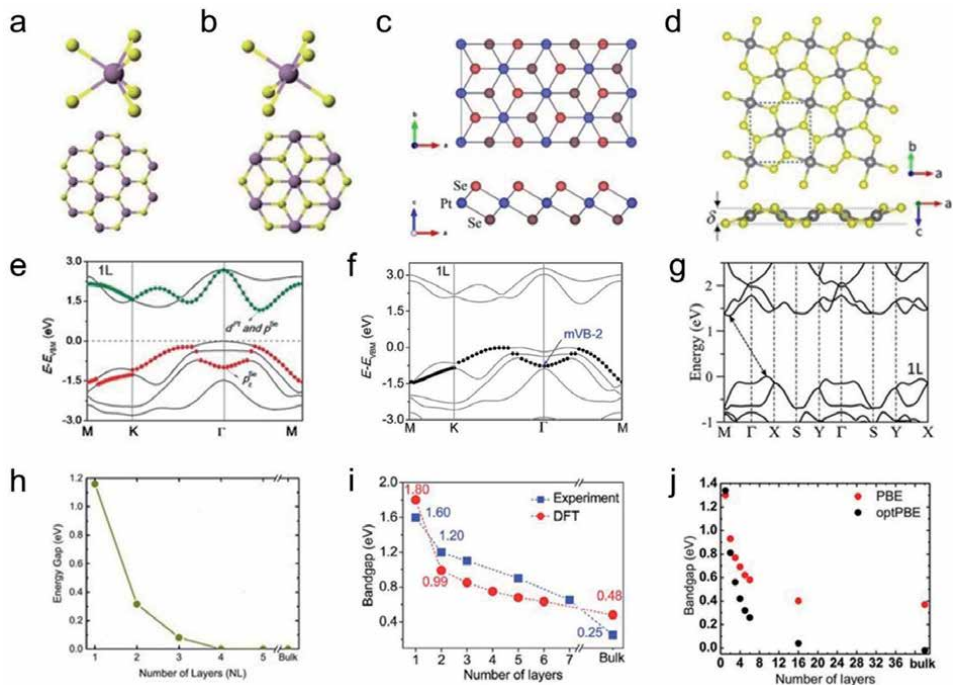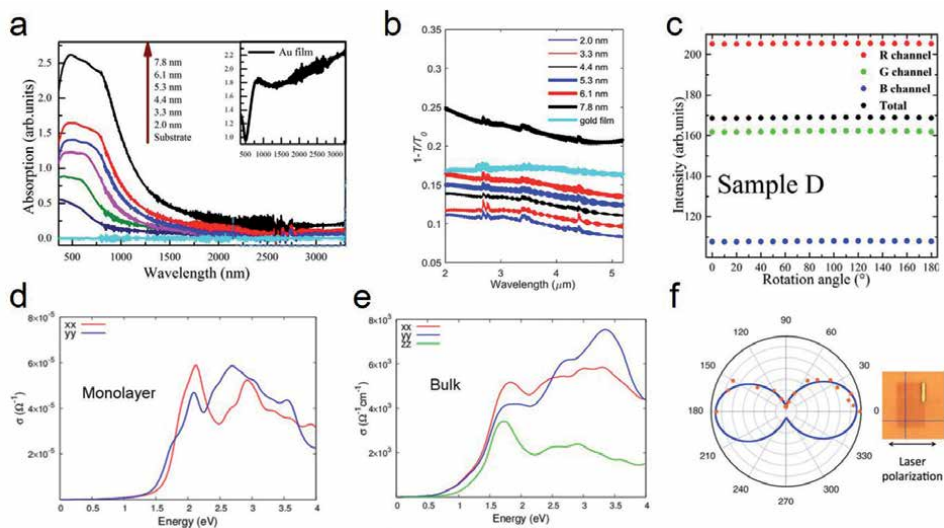
Figure 1.
Crystal and electronic structure of NTMDs. (a) and (b) schematic images of 2H and 1 T lattice phase in TMDs, reproduced with permission [29]. (c) Thermodynamically favored 1 T-phase structural schematic of PtSe₂, reproduced with permission [30]. (d) Puckered pentagonal structure of PdSe₂, reproduced with permission [26]. (e) Energy band structure of monolayer PtSe₂, reproduced with permission [23]. (f) Energy band structure of monolayer PtS₂, where bands mVB-2 were highlighted spanning the Brillouin zone by black dots. (g) Calculated electronic band structures of monolayer PdSe₂ by the optPBE method. (h)-(j) evolution of energy bandgap as a function of the number of layers of PtSe₂(h), PtS₂(i) and PdSe₂(j). (h) Is reproduced with permission [31]. (f) and (i) are reproduced with permission [21]. (g) and (j) are reproduced with permission [26].

maximum (VBM) will exceed that of conduction band minimum (CBM) and PtSe₂ undergoes a transition from semiconductor to metallic state (**Figure 1h**) [31]. Similarly, as shown in **Figure 1i**, the energy bandgap in bulk PtS₂ decreases to 0.25 eV from 1.6 eV.

Apart from conventional TMDs materials with hexagonal structures, PdS₂ and PdSe₂ consist of pentagonal rings with the puckered vertical conformation (**Figure 1d**) [26]. In each layer, a Pd atom binds to four chalcogen atoms other than six chalcogen atoms, while every two neighbor chalcogen atoms bind each other with a covalent bond. The unique pentagonal structure not only provides the materials with anisotropic properties, but also can realize the transition of topological quantum phase and the spin-orbit coupling enhancement. In 2017, Akinola O., et al. experimentally and theoretically prove that monolayer PtSe₂ has 1.3 eV indirect band gap and semi-metal state in the bulk (**Figure 1g** and **j**) [26].

3. Optical properties of 2D NTMDs

The widely tunable electronic energy gap of NTMDs make them layer-dependent optical absorption [31]. As shown in **Figure 2a**, PtSe₂ samples with thickness from 2.2 nm to 7.8 nm show broadband light absorption from 450 nm to over 3000 nm. The absorption peaks have significant red-shift with the increase

Figure 2.
Optical properties of NTMDs. (a)-(b) Vis-near-IR and mid-IR absorption spectra of $PtSe_2$ with different thickness. The substrates are sapphires and the (a) inset is optical absorption spectrum of 5 nm thick Au film as reference. (c) Reflective intensity of RGB channels as the function of rotational incident angle, which reflect the in-plane isotropic absorption of $PtSe_2$. (a)-(c) are reproduced with permission [33]. (d)and (e) calculated optical conductivity spectra of 1 L and bulk $PdSe_2$, reproduced with permission [34]. (f) Integrated SHG intensity diagram with different rotation angle of line-polarized laser, reproduced with permission [35].

of thickness, which is originates from the narrower energy gap in thicker samples. In particular, the semi-metal nature in thick $PtSe_2$ samples allows them absorb mid-NIR and even far-NIR light. In **Figure 2b**, all of these samples have broadband absorption in the range from 2 to 5 μm, which is different from tradition TMDs materials. The optical polarization properties of $PtSe_2$ were studied by polarized light imaging experiments. The optical responses of 2D $PtSe_2$ film almost unchanged under the incident channel with different rotation angle, which indicate the in-plane isotropic absorption of $PtSe_2$ (**Figure 2c**).

On contrary, due to the unique orthorhombic pentagonal structure, $PdSe_2$ shows anisotropic optical response in the van der Waals plane [34]. From the calculated optical conductivity spectra in **Figure 2d** and **e**, the cut-off energy in bulk $PdSe_2$ is lower than that in 1 L $PdSe_2$, and the conductivity curves in xx and yy direction in both bulk and 2D $PdSe_2$ perform very different characteristics. The anisotropic phenomenon appears at ~1.5 and 1.25 eV in bulk and 2D structure, respectively. The large anisotropy also be predicted at ~2 eV in monolayer $PdSe_2$. Second harmonic generation (SHG) polarization diagram is also performed for observing the anisotropic properties [35]. When the polarization direction of incident light and the crystal orientation are parallel (position of 0° and 180° in **Figure 2f**), the intensity achieves the maximum, while at the position of 0° and 180°, the SHG signal shows significantly decrease.

4. Synthesize of 2D NTMDs

In order to realizing the practical applications of the new kind of TMDs materials, the effective synthesis methods are essential to prepare particular samples with high crystallinity quality, desirable thickness and large lateral size. Up to now, various of synthesis strategies have been conducted to a variety of high-quality NTMDs. Here we do a general review on the different fabrication methods for NTMDs. Chemical vapor transport (CVT) and chemical vapor deposition (CVD) techniques

are most two important methods for NTMDs which are applied to the following photodetector applications.

CVT method is a traditional crystal growth method, which is recently reintroduced for the direct synthesis of TMDs with high crystal quality [36–38]. The synthesis setup is as shown in **Figure 3a** [39]. Pt and Se powders with strict ratio are loaded in the quartz ampoule. After the vapor reactions with the help of a gaseous reactant under high temperature and vacuum, PtSe$_2$ crystals are formed and deposited elsewhere. By carefully adjusting the amounts of reactants and transport, Hu et al. successfully obtained triangular-shaped PtSe$_2$ flakes with 10–50 μm and good controllability [41]. From **Figure 3d**, the optical images exhibit that PtSe$_2$ nanoflakes have controlled layer numbers from 1-layer (1 L) to 20 layers (~20 L) and the atomic force microscope (AFM) images in insets provide the thickness information. The as-grown nanoplates with monocrystalline structure, controllable thickness and large lateral size are very suitable for electronic and photonic devices. Due to the ease of growing bulk crystals by CVT, people also use this method to grow high quality single-crystalline bulk NTMDs and obtain one- to few-layer 2D flakes by peeled from the bulk NTMDs crystal.

CVD is a very common synthesis method in which a large number of 2D materials with scalable size, controllable thickness and high-quality crystal structure have been prepared such as graphene, TMDs, Xene, MXene, boron nitride and so on [44–46]. Recently, the CVD method also be adopted for large-scale NTMDs fabrication. **Figure 3b** shows a CVD selenization method for scalable PtSe$_2$ films. The Pt film as seed were deposited on the substrate (usually the SiO$_2$ or Si wafer) at first and placed in the center of CVD furnace. The Se powder is at the upstream
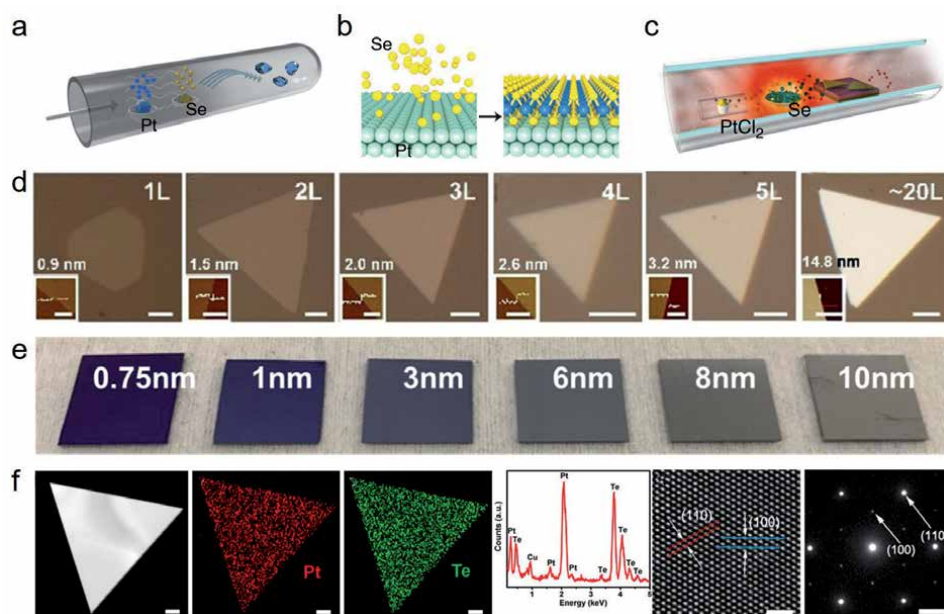
Figure 3.
Materials fabrication for large-scale films and monocrystalline nanosheets. (a) Schematic of CVT method for PtSe$_2$ with controllable thickness, reproduced with permission [39]. (b) Schematic of CVD selenization method for scalable PtSe$_2$ films, reproduced with permission [40]. (c) Schematic of CVD method for the controlled synthesis of NTMDs nanosheets, reproduced with permission [39]. (d) Optical images of PVT-grown PtSe$_2$ flakes with 10–50 μm and controlled layer numbers from 1 L to ~20 L, reproduced with permission [41]. (e) Photographs of CVD-grown 2D PtSe$_2$ polycrystal films from 0.75 to 10 nm, reproduced with permission [42]. (f) Material characterizations for PtSe$_2$ single crystal nanosheets by CVD method, including HAADF-STEM, EDS, Raman, HRTEM and SEAD techniques, reproduced with permission [43].

side. Then the direct selenization of the Pt film happens under high temperature, low pressure and argon gas protection. In 2015, Wang et al. firstly synthesized monolayer $PtSe_2$ nanosheets [40]. Then Han et al. obtained large area $PtSe_2$ film (> a few cm^2) with controllable thickness [42]. **Figure 3e** shows the photographs of as-grown 2D $PtSe_2$ polycrystal films from 0.75 to 10 nm (corresponding to the layer numbers from 1 L to ~15 L). In 2018, Yuan et al. successfully fabricated $PtSe_2$-PtS_2 heterostructure film with wafer-scale and successfully achieved the wafer-scale photodetector application [47]. Besides, CVD method can also synthesize high-quality 2D NTMDs nanocrystals. **Figure 3c** exhibits a schematic of growing 2D nanosheets and through the method, Ma et al. successfully fabricated 2D $PtTe_2$ nanoplates with tunable thickness and a large lateral size up to 80 μm [43]. From **Figure 3f**, the high-angle annular darkfield scanning-TEM (HAADF-STEM) image as well as the EDS mapping analysis shows the well-faceted triangular geometry and the uniformly spatial distribution of Pt and Te elements. The Raman spectrum and High-resolution TEM (HRTEM) furtherly show the high quality of nanosheets and the 6-fold symmetry SEAD pattern shows the hexagonal crystal structure. Type-II Dirac fermions are observed in the high-quality nanocrystal platform. Another advantage of the grown method is that 2D materials can be grown on arbitrary substrates, because both the pre-deposition and post-selenization process do not have strict requirements to the substrate. Till now, 2D NTMDs have been fabricated on different substrates including Si, SiO_2, Sapphire, gallium nitride (GaN), fused quartz, and flexible polyimide.

There are some other synthesize ways for atomic TMDs. Mechanical exfoliation (ME) is one of the most extensively adopted approaches for 2D nanoflakes from their bulk counterparts [13]. Therefore, the as-prepared 2D flakes can maintain the intrinsic structure. Nowadays, most of mechanically exfoliated NTMDs thin flakes are from bulk crystals grown by CVT [48] and self-flux method [26, 49]. These typical nanosheets show the extraordinary electronic properties, but their small lateral size and uncontrollability during the fabrication process limit their application potential in practical devices. Molecular beam epitaxy (MBE) has also been applied for 2D NTMDs, including $PtSe_2$ [50], $PdTe_2$ [51] and $PdSe_2$ [52], which shows the merits of large-size monocrystalline, and controllable thickness on different substrates. For example, the high-quality $PtSe_2$ atomic film was epitaxial grown on bi-layer graphene/6H-SiC substrate through MBE method [50]. The as-grown film had controllable thickness from single-layer to over 22 layers, which shows extraordinary thickness-dependent electronic properties and tunable bandgaps.

5. 2D NTMDs for photodetection

So far, various NTMDs based photodetectors with diverse constructions and high-performance have been reported [53]. **Table 1** summarizes their characteristic parameters. The strong optical absorption capability and large carrier mobility of NTMDs provide high responsivity (R) and detectivity (D^*) for these photodetectors, while the narrow bandgaps of atomic layered PtS_2, $PtSe_2$ and $PdSe_2$ make them inherently suitable for NIR detection. For multi-layer NTMDs (over 5 L for $PtSe_2$), which can be regarded as semimetal materials, they can be combined with other semiconductor materials and construct Schottky heterostructures. By choosing a suitable semiconductor functional layer with a particular bandgap (such as n-Si, III − V, 2D perovskite, 2D MoS_2, and so on), the photodetector can work efficiently at a specific wavelength. In addition, owing to the majority-carrier-dominant current-flow mechanism, photodetectors based on NTMDs heterostructures have advantages in high-speed applications. Combined with other electronic

Device structure	Material grown methods	R (AW^{-1})	τ_r/τ_f	D* (Jones)	Measurement conditions	Spectral range	Ref.
Few-layer PtSe$_2$	CVT	0.01	—	—	$\lambda = 500$ nm, $V_g = -80$ V	Visible-NIR	[23]
Bilayer PtSe$_2$	CVT + ME	4.5	1.1/1.2 ms	7×10^8	$\lambda = 10$ μm, $V_b = 0.1$ V	Visible-MIR	[39]
Few-layer PtS$_2$	CVT	1.56×10^3	460/460 ms	2.9×10^{11}	$\lambda = 500$ nm, $V_b = 0.1$ V	Visible	[48]
Few-layer PdSe$_2$	ME	708	—	1.31×10^9	$\lambda = 1064$ nm, $V_g = 30$ V	Visible-MIR	[54]
PtSe$_2$/Si	TAC	0.52	55.3/170.5 μs	3.26×10^{13}	$\lambda = 808$ nm, $V_b = 0$ V	Visible-NIR	[55]
PtSe$_2$/n-Si	TAC	0.49	—	—	$\lambda = 808$ nm, $V_b = -2$ V	UV-NIR	[56]
PtSe$_2$/Ge	CVD	0.602	742/16.71 μs	6.31×10^{11}	$\lambda = 1550$ nm, $V_b = 0$ V	Visible-NIR	[57]
PtSe$_2$GaAs	CVD	0.262	5.5/6.5 μs	$\sim 10^2$	$\lambda = 808$ nm, $V_b = 0$ V	DUV-NIR	[58]
PtSe$_2$/GaN	CVD	0.193	45/102 μ	3.8×10^{14}	$\lambda = 265$ nm, $V_b = 0$ V	DUV	[59]
PtSe$_2$/CdTe	CVD	0.51	8.1/43 μs	4.2×10^{11}	$\lambda = 780$ nm, $V_b = 0$ V	DUV-NIR	[60]
PtSe$_2$/FA$_{0.85}$Cs$_{0.15}$PbI$_3$	CVD	0.118	78/60 ns	2.9×10^{12}	$\lambda = 808$ nm, $V_b = 0$ V	UV-NIR	[61]
PtS$_2$/PtSe$_2$	CVD	0.361	66/75 ms	—	$\lambda = 532$ nm, $V_b = 0$ V	Visible-NIR	[47]
PdSe$_2$/n-Si	CVD	0.3	—	$\sim 10^{13}$	$\lambda = 780$ nm, $V_b = 0$ V	UV-NIR	[62]
G/PdSe$_2$/Ge	CVD	0.69	6.4/92.5 μs	1.73×10^{13}	$\lambda = 265$ nm, $V_b = 0$ V	DUV-MIR	[63]
PdSe$_2$/FA$_{0.85}$Cs$_{0.15}$PbI$_3$	CVD	0.313	3.5/4 μs	$\sim 10^{13}$	$\lambda = 265$ nm, $V_b = 0$ V	DUV-NIR	[64]
PdSe$_2$/MoS$_2$	CVT	42.1	—	8.21×10^9	$\lambda = 10.6$ μm, $V_b = 1$ V	Visible-MIR	[65]

*The detectivity D of a photodetector is a figure of merit, defined as the inverse of the noise-equivalent power (NEP). The larger the detectivity of a photodetector, the more it is suitable for detecting week signals which compete with the detector noise. But the specific detectivity D* is the detectivity normalized to a unit detector area and detection bandwidth; one can calculate it by multiplying the detectivity with the square root of the product of detector area (in square centimeters) and the detector bandwidth (in Hz). That term is useful for comparing the performance of different detector technologies.

Table 1.
Summary of characteristic parameters for NTMDs based photodetectors.

characteristics, different photodetectors with wide-spectral, fast-speed, self-powered and anisotropic have been realized. NTMDs based wafer-scalable and flexible photodetectors arrays could be the future development trend. We will comprehensively discuss them in this section.

5.1 2D NTMDs photodetectors

Due to the great electronic transport and optical properties of NTMDs, various of NTMDs based phototransistors have been studied [23, 39, 48, 54]. Here we illustrate a typical PtS_2 phototransistor as an instance [48]. The device schematic is as shown in **Figure 4a**, in which few-layer PtS_2 as the channel material on h-BN substrate. The device shows a high field-effect mobility of ~13 $cm^2V^{-1}S^{-1}$ and the high on/off ratio of 10^5. Then the photo-response ability under light illumination at visible wavelength (500 nm) is studied. Both photogenerated conductive and photo-gating effects are observed in the device. **Figure 4b** is the 3D diagram which shows the combined photocurrent with incident light intensity and gate voltage (V_g). By calculation, the detectivity and responsivity are obtained with the function of V_g (**Figure 4c**). when V_g is zero, the responsivity is highly at 1560 AW^{-1}, which shows 10^6 times higher than that of graphene and 10^3 times higher than that of BP detectors (~0.5 and 657 mAW^{-1}, respectively). Similarly, the detectivity (D^*), as the inverse of the noise-equivalent power and the key parameter related to the signal-to-noise rate of the device, reaches 2.9×10^{11} Jones, which is also higher than that of other 2D-based devices (**Figure 4c**). The photo-gain is about 2×10^6 at 30 V of V_g, which could be the highest gain in 2D-based photodetectors. The few-Layered PtS_2 phototransistor shows that NTMDs is outstanding candidate in photodetection area at visible wavelength range.

Mid-IR optoelectronics is fantastic and important because there is an optical transparent window at Mid-IR in the atmosphere. However, in traditional TMDs
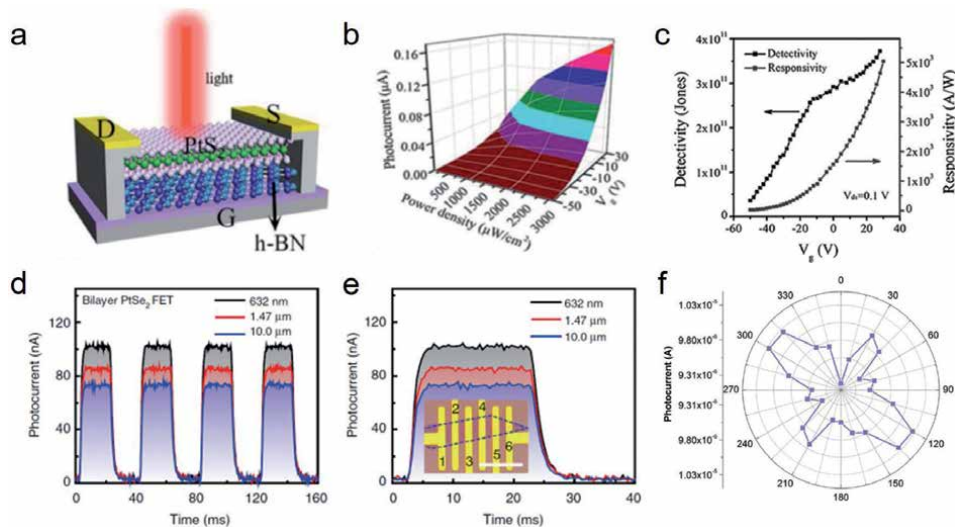
Figure 4.
2D NTMDs phototransistors. (a)-(c) PtS₂ on h-BN for photodetection. (a) Schematic of the device structure. (b) 3D view of photocurrent mapping. (c) the responsivity and detectivity as a function of vg measured at V_ds = 0.1 V. (a)-(c) are reproduced with permission [48]. (d)-(f) bilayer PtSe₂ for ultrawide spectra photodetection. (d) and (e) time-resolved photo-response curve at the wavelength of 0.63, 1.47 and 10 μm. (d)-(e) are reproduced with permission [39]. (f) Polarized plot diagram which shows the photocurrent of the device as a function of linear polarization rotation. The gate bias is 50 V and the wavelength is 532 nm, reproduced with permission [54].

based photodetectors, it is very difficult to realize the effective detection at Mid-IR. NTMDs can overcome the difficulty due to the narrow bandgap. Yu et al. fabricated a bi-layer $PtSe_2$ based phototransistor, which can realize wide-spectral and sensitive detection from 632 nm to 10 μm [39]. As shown in **Figure 4d** and **e**, the time-resolved photo-response results are obtained at 632 nm, 1.47 μm and 10 μm, with photo-responsivity of 6.25 AW^{-1}, 5.5 AW^{-1} and 4.5 AW^{-1}, respectively. The achieved photo-current responsivity at 10 μm is 3 orders of magnitude higher than that of graphene and comparable to commercial mid-IR detectors. The rise and fall time are also better than other TMDs based photodetectors owing to the high mobility of $PtSe_2$. Overall, bilayer $PtSe_2$ shows promising potential in mid-IR optoelectronic applications.

For anisotropic detector applications, Liang et al. adopted $PdSe_2$ as the photo-sensitive material [54]. The photodetector shows effective photo-response covering from 532 nm to 4.05 μm. The responsivity is 708 AW^{-1}, which is five orders larger than graphene and two orders larger than commercial InGaAs near-IR photodetectors. Furthermore, with the unique pentagonal structure of $PdSe_2$, the detector shows anisotropic photo-response for the linear-polarized light with varying polarization angle. In **Figure 4f**, when the increase of rotation angle with the step of 15° from 0° to 360°, the photocurrent clearly shows periodical variation and reaches the maximum value at 120° and 300°, which is coincident with the angle-resolved polarized Raman response results, furtherly showing the lattice effects. The aniso-tropic detectors as linear dichroism media have potential in optical communication and structural chemistry analysis.

Overall, with the first realization of $PtSe_2$ photodetectors in 2016 [23], Various of NTMDs and their photodetection abilities are studied, which show great per-formance. Till now, NTMDs based photodetectors exhibit higher responsivity and photo-gain than that of graphene, conventional TMDs and other 2D photodetec-tors. The work wavelength has been extended to 10 μm and the anisotropic detec-tion has also been realized. With the development of NTMDs synthesis technique, the optimization of device structure, and the study of NTMDs photo-current mechanism, the narrow bandgap material will be the excellent candidate in the field of photodetection.

5.2 2D NTMDs heterostructures for photodetection

NTMDs with widely tunable energy gaps and high carrier mobility have broad prospects in developing high-performance photodetectors. However, the ultrathin thickness nature makes 2D NTMDs relatively low light absorption. Constructing NTMDs based heterostructures can not only enhance the light absorption, but accelerate the separation and transmission of carriers, and invent the high-speed photodetectors. Therefore, different NTMDs heterostructures have been studied for fast, broadband, self-powered and polarization-sensitive photodetectors.

Due to the atomic thickness, NTMDs is very convenient to from heterostructures with conventional semiconductors such as Si [55], n-Si [56, 62], Ge [57, 63], GaAs [58], GaN [59] and CdTe [60]. Few-layer $PtSe_2$ is semimetal state. By choosing p-doped bulk semiconductors with appropriate work function and bandgaps and contacting them with Few-layer $PtSe_2$ layer, the Schottky junction will be formed. The detection wavelength is determined by the bulk semiconductor. Zeng et al. fab-ricated the $PtSe_2$-GaAs vertical heterostructure detector [58]. The device schematic and the photocurrent generation mechanism are depicted in **Figure 5a**. Under the light illumination, the electron–hole pairs forms at the interface of the heterojunc-tion, then separates with the function of in-built electric field. The photocurrent generates and gathered by two electrodes. The device shows the broadband work wavelength from200 to 1200 nm and a large photo-response at visible wavelength
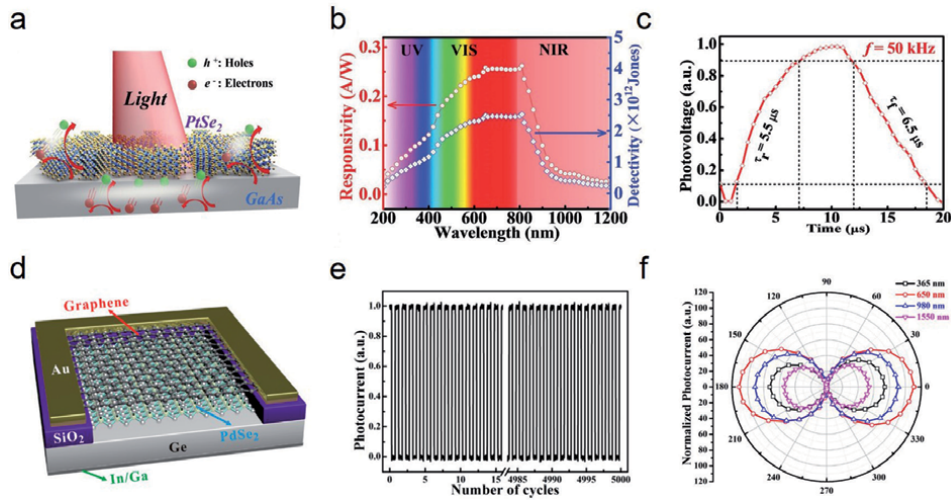
Figure 5.
(a) Device schematic and the photocurrent generation mechanism of the PtSe$_2$-GaAs photodetector. (b) Wavelength-dependent specific detectivity and responsivity of PtSe$_2$-GaAs photodetector. (c) Fast photo-response with the rise/fall time of 5.5/6.5 μs. (a)-(c) are reproduced with permission [58]. (d) Schematic diagram of graphene-PdSe$_2$-Ge based photodetectors. (e) the long-term stability measurement results, where the device still remains stable with continuedly working over 5000 cycles. (f) Normalized photocurrent graphs which obtained by changing illumination polarization angle of linearly polarized light with wavelengths of 365, 650, 980 and 1550 nm. (d)-(f) are reproduced with permission [63].

(**Figure 5b**). The responsivity and specific detectivity reach to 708 mAW^{-1} and 2.9 × 10^{12} Jones at 808 nm, respectively. Moreover, the device achieves the fast response speed, in which the rise and fall time are only 5.5 and 6.5 μs (**Figure 5c**). By choosing the semiconductor layer with relatively large energy gap, *e.g.,* GaN, the deep-UV photodetectors can be realized [59]. The self-powered PtSe$_2$-GaN pho-totransistor has the responsivity of 193 mAW^{-1}, an ultra-high specific detectivity of 3.8 × 10^{14} Jones and a fast response time of 45.2/102.3 μs at zero gate voltage. In particular, the calculated linear dynamic range (LDR) exceeds 155 dB, which much higher than all reported 2D based detectors and commercial photodetectors. For infra-wavelength application, Wang et al. designed a near-infrared light photovol-taic detector by constructing few-layer PtSe$_2$-Ge heterostructure [57]. Since the device works at photovoltaic region, the self-start operation can be realized without any external power supply. The device also has high responsivity (602 mAW^{-1} at 1550 nm, closed to that of commercial device) and long environment stability. Then Wu and the co-workers designed the improved graphene-PdSe$_2$-Ge heterostructure (**Figure 5d**) [63]. With graphene as a transport and protector layer, the device has great stability and can realize the imaging application. In particular, with contin-uedly working over 5000 cycles, the photo-response still remains stable, showing the practical application potential (**Figure 5e**). Due to the particularity of PdSe$_2$, the device can achieve the dipole anisotropic operation (see **Figure 5f**).

Perovskite is also an emerging material with a large absorption coefficient, long diffusion length and low trapping density, which has aroused extensive research interest in optoelectronics. Zhang et al. reported a new type of detector based on few-layer PtSe$_2$ and FACsPbI$_3$ perovskite heterostructure [61]. The device has broad spectra response from 300 to 1200 nm, with the responsivity of 117.7 mAW^{-1}, high I$_{light}$/I$_{dark}$ ratio of 5.7 × 10^3 and considerable specific detectivity of 2.6 × 10^{12} Jones. Especially, due to the extraordinary electronic properties of PtSe$_2$ and the perovskite and the well-designed built-in electric field at Schottky junction inter-face, the response time is only 78/60 ns, which is one of the fastest reported values

in mixed-dimensional 2D-3D van der Waals heterostructures. Zeng and the co-workers chose $PtSe_2$ to construct heterojunction with $FA_{1-x}Cs_xPbI_3$ perovskite film, which can realize the self-powered detection operation from 200 to 1550 nm [64]. The device demonstrates high responsivity, large on/off ratio, a good polarization sensitivity over 10^4, and reliable imaging application at 808 nm.

The heterostructure between NTMDs with other 2D materials is also fantastic. Here we use $PdSe_2$-MoS_2 heterostructure as an example [65]. Both of $PdSe_2$ and MoS_2 are multilayer flakes with thickness of ~10 nm. The ultra-thin device can not only a ultrawide spectra working range from 532 nm to 10.6 μm, but contributes an ultrahigh responsivity of 42.1 AW^{-1} at 10.6 μm.

5.3 Perspective of 2D NTMDs in photodetectors

Due to the industrial demand and the inherent advantages of 2D materials, the development trend of 2D optoelectronics is scalability and flexibility. Yuan et al. has realized the fabrication of wafer-scale PtS_2- $PtSe_2$ heterojunctions and devices [47]. They pre-deposited 0.8 nm Pt films as arrays of periodic square, then directly grew PtS_2 and $PtSe_2$ 2D thin films by CVD method. **Figure 6a** is the photograph and **Figure 6b** shows the schematic illustration of one single device. The photodetector array can work from 405 nm to 2200 nm. The ultrathin device has a large external quantum efficiency (EQE) (1.2% at 1064 nm, 0.2% at 1550 nm, and 0.05% at 2200 nm). The response time is several milliseconds. If the quality of thin film is improved, the response time could be faster. The scalable devices can be adopted for high-resolution imaging, as shown in **Figure 6c**.

For the study of NTMDs flexible devices, Su and the co-workers did the pioneer work [66]. $PtSe_2$ thin films with 2.5 nm thickness (~3 L) on flexible polyimide substrate were directly grown by plasma-assisted selenization process, which show p-doped semiconductor behaviors and the average field effect mobility of
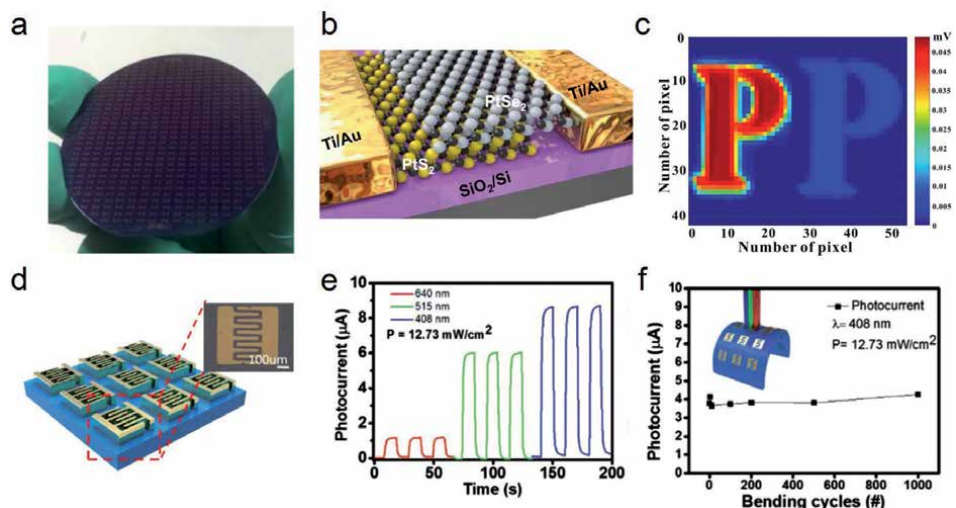
Figure 6.
(a)-(c) Wafer-scale NTMDs photodetection and imaging. (a) Photograph of PtS_2- $PtSe_2$ photodetectors array on a SiO_2/Si wafer. (b) Schematic illustration of the photodetector device. (a)-(b) are reproduced with permission [47]. (c) high-resolution imaging by NTMDs based photodetectors, reproduced with permission [63]. (d)-(f) Flexible photodetection based on $PtSe_2$. (d) illustration of the $PtSe_2$ thin film based Flexible photodetector. (e) Time-resolved photo-response curve at the wavelength of 408, 515 and 640 nm. (f) Mechanic stability measurement, in which the photocurrent is recorded as a function of bending cycles. (e)-(f) are reproduced with permission [66].

0.7 cm^{2}V^{-1}S^{-1}. **Figure 6d** shows the array of devices with the finger-type electrode structure. The flexible photodetector shows good photoresponse with responsivity of 0.4, 0.25 and 0.1AW^{-1} at 408, 515 and 640 nm, respectively (**Figure 6e**). Moreover, the great mechanic stability is exhibited. Under large bending with different radius over 1000 cycles, the device can still generate stable photocurrent with almost no degradation, which is depicted in **Figure 6f**.

6. Conclusions

In this chapter, we focus on 2D NTMDs and their applications in the field of photodetectors. 2D NTMDs exhibit extraordinary structural, electronic and optical properties. Unlike conventional TMD materials, the emerging NTMDs with abundant d-electrons and strong interlayer electronic hybridization have broadband optical absorption and ultra-high mobility, which are promising in optoelectronics. Then we have discussed efficient and controllable synthesis methods for 2D NTMDs with high crystal quality and large scalability. Various NTMDs based photodetectors have been developed till now. We have witnessed their outstanding performance, including wide-spectral range, ultrafast response, self-power and anisotropy. With the development of the materials technology and device manufacturing technology, NTMDs will have great potential in practical optoelectronic applications.

Acknowledgements

Conflict of interest

The authors declare no conflict of interest.

Author details

Haoran Mu[1,2], Jian Yuan[3] and Shenghuang Lin[1*]

1 Songshan Lake Materials Laboratory, Dongguan, China

2 Department of Materials Science and Engineering and ARC Centre of Excellence in Future Low-Energy Electronics Technologies (FLEET), Monash University, Clayton, Victoria, Australia

3 School of Physics and Electronic Information, Huaibei Normal University Huaibei, Anhui, P.R. China

*Address all correspondence to: linshenghuang@sslab.org.cn

IntechOpen

References

[1] Arquer FPG, Armin A, Meredith P, Sargent EH. Solution-processed semiconductors for next-generation photodetectors. Nature Reviews Materials. 2017;2(3): 1-17.

[2] Donati S. Photodetectors: Prentice Hall PTR; 1999.

[3] Zhai T, Fang X, Liao M, Xu X, Zeng H, Yoshio B, et al. A comprehensive review of one-dimensional metal-oxide nanostructure photodetectors. Sensors. 2009;9(8):6504-29.

[4] Sang L, Liao M, Sumiya M. A comprehensive review of semiconductor ultraviolet photodetectors: from thin film to one-dimensional nanostructures. Sensors. 2013;13(8):10482-518.

[5] Zhong Y, Malagari SD, Hamilton T, Wasserman DM. Review of mid-infrared plasmonic materials. Journal of Nanophotonics. 2015;9(1):093791.

[6] Champness NR. Two-dimensional materials: Crystallized creations in 2D. Nature Chemistry. 2014;6(9):757-9.

[7] Xia F, Wang H, Xiao D, Dubey M, Ramasubramaniam A. Two-dimensional material nanophotonics. Nature Photonics. 2014;8(12):899-907.

[8] Burch KS, Mandrus D, Park J-G. Magnetism in two-dimensional van der Waals materials. Nature. 2018;563(7729):47-52.

[9] Low T, Chaves A, Caldwell JD, Kumar A, Fang NX, Avouris P, et al. Polaritons in layered two-dimensional materials. Nature Materials. 2017;16(2):182-94.

[10] Ferrari AC, Bonaccorso F, Fal'Ko V, Novoselov KS, Roche S, Boggild P, et al. Science and technology roadmap for graphene, related two-dimensional crystals, and hybrid systems. Nanoscale. 2015;7(11):4598-810.

[11] Ponraj JS, Xu Z-Q, Dhanabalan SC, Mu H, Wang Y, Yuan J, et al. Photonics and optoelectronics of two-dimensional materials beyond graphene. Nanotechnology. 2016;27(46):462001.

[12] Tan C, Cao X, Wu X-J, He Q, Yang J, Zhang X, et al. Recent advances in ultrathin two-dimensional nanomaterials. Chemical Reviews. 2017;117(9):6225-331.

[13] Wang QH, Kalantar-Zadeh K, Kis A, Coleman JN, Strano MS. Electronics and optoelectronics of two-dimensional transition metal dichalcogenides. Nature Nanotechnology. 2012;7(11):699-712.

[14] Hu Z, Wu Z, Han C, He J, Ni Z, Chen W. Two-dimensional transition metal dichalcogenides: interface and defect engineering. Chemical Society Reviews. 2018;47(9):3100-28.

[15] Choi W, Choudhary N, Han GH, Park J, Akinwande D, Lee YH. Recent development of two-dimensional transition metal dichalcogenides and their applications. Materials Today. 2017;20(3):116-30.

[16] Jariwala D, Sangwan VK, Lauhon LJ, Marks TJ, Hersam MC. Emerging device applications for semiconducting two-dimensional transition metal dichalcogenides. ACS Nano. 2014;8(2):1102-20.

[17] Tian X, Kim DS, Yang S, Ciccarino CJ, Gong Y, Yang Y, et al. Correlating the three-dimensional atomic defects and electronic properties of two-dimensional transition metal dichalcogenides. Nature Materials. 2020:1-7.

[18] Pi L, Li L, Liu K, Zhang Q, Li H, Zhai T. Recent Progress

on 2D Noble-Transition-Metal Dichalcogenides. Advanced Functional Materials. 2019;29(51):1904932.

[19] Chen E, Xu W, Chen J, Warner J. 2D layered noble metal dichalcogenides (Pt, Pd, Se, S) for electronics and energy applications. Materials Today Advances. 2020;7:100076.

[20] Gong Y, Lin Z, Chen Y-X, Khan Q, Wang C, Zhang B, et al. Two-Dimensional Platinum Diselenide: Synthesis, Emerging Applications, and Future Challenges. Nano-Micro Letters. 2020;12(1):1-34.

[21] Zhao Y, Qiao J, Yu P, Hu Z, Lin Z, Lau SP, et al. Extraordinarily strong interlayer interaction in 2D layered PtS_2. Advanced Materials. 2016;28(12):2399-407.

[22] Yang H, Kim SW, Chhowalla M, Lee YH. Structural and quantum-state phase transitions in van der Waals layered materials. Nature Physics. 2017;13(10):931-7.

[23] Zhao Y, Qiao J, Yu Z, Yu P, Xu K, Lau SP, et al. High-electron-mobility and air-stable 2D layered $PtSe_2$ FETs. Advanced Materials. 2017;29(5):1604230.

[24] Wang Z, Li Q, Besenbacher F, Dong M. Facile synthesis of single crystal $PtSe_2$ nanosheets for nanoscale electronics. Advanced Materials. 2016;28(46):10224-9.

[25] Li G, Zhang Y-Y, Guo H, Huang L, Lu H, Lin X, et al. Epitaxial growth and physical properties of 2D materials beyond graphene: from monatomic materials to binary compounds. Chemical Society Reviews. 2018;47(16):6073-100.

[26] Oyedele AD, Yang S, Liang L, Puretzky AA, Wang K, Zhang J, et al. $PdSe_2$: pentagonal two-dimensional layers with high air stability

for electronics. Journal of the American Chemical Society. 2017;139(40):14090-7.

[27] Wang Y, Li Y, Chen Z. Not your familiar two dimensional transition metal disulfide: structural and electronic properties of the PdS_2 monolayer. Journal of Materials Chemistry C. 2015;3(37):9603-8.

[28] Chow WL, Yu P, Liu F, Hong J, Wang X, Zeng Q, et al. High mobility 2D palladium diselenide field-effect transistors with tunable ambipolar characteristics. Advanced Materials. 2017;29(21):1602969.

[29] Kappera R, Voiry D, Yalcin SE, Branch B, Gupta G, Mohite AD, et al. Phase-engineered low-resistance contacts for ultrathin MoS_2 transistors. Nature Materials. 2014;13(12):1128-34.

[30] Huang H, Fan X, Singh DJ, Zheng W. Modulation of Hydrogen Evolution Catalytic Activity of Basal Plane in Monolayer Platinum and Palladium Dichalcogenides. ACS Omega. 2018;3(8):10058-65.

[31] Setiyawati I, Chiang K-R, Ho H-M, Tang Y-H. Distinct electronic and transport properties between $1T$-$HfSe_2$ and $1T$-$PtSe_2$. Chinese Journal of Physics. 2019;62:151-60.

[32] Chhowalla M, Shin HS, Eda G, Li L-J, Loh KP, Zhang H. The chemistry of two-dimensional layered transition metal dichalcogenide nanosheets. Nature Chemistry. 2013;5(4):263-75.

[33] Xie J, Zhang D, Yan X-Q, Ren M, Zhao X, Liu F, et al. Optical properties of chemical vapor deposition-grown $PtSe_2$ characterized by spectroscopic ellipsometry. 2D Materials. 2019;6(3):035011.

[34] Sun J, Shi H, Siegrist T, Singh DJ. Electronic, transport, and optical properties of bulk and mono-layer

PdSe$_2$. Applied Physics Letters. 2015;107(15):153902.

[35] Puretzky AA, Oyedele AD, Xiao K, Haglund AV, Sumpter BG, Mandrus D, et al. Anomalous interlayer vibrations in strongly coupled layered PdSe$_2$. 2D Materials. 2018;5(3):035016.

[36] Hu D, Xu G, Xing L, Yan X, Wang J, Zheng J, et al. Two-dimensional semiconductors grown by chemical vapor transport. Angewandte Chemie International Edition. 2017;56(13):3611-5.

[37] Wang J, Zheng H, Xu G, Sun L, Hu D, Lu Z, et al. Controlled Synthesis of Two-Dimensional 1T-TiSe$_2$ with Charge Density Wave Transition by Chemical Vapor Transport. Journal of the American Chemical Society. 2016;138(50):16216-9.

[38] Du Z, Zhang C, Wang M, Zhang X, Ning J, Lv X, et al. Synthesis of WS$_{1.76}$Te$_{0.24}$ alloy through chemical vapor transport and its high-performance saturable absorption. Scientific Reports. 2019;9(1):1-9.

[39] Yu X, Yu P, Wu D, Singh B, Zeng Q, Lin H, et al. Atomically thin noble metal dichalcogenide: a broadband mid-infrared semiconductor. Nature Communications. 2018;9(1):1-9.

[40] Wang Y, Li L, Yao W, Song S, Sun J, Pan J, et al. Monolayer PtSe$_2$, a new semiconducting transition-metal-dichalcogenide, epitaxially grown by direct selenization of Pt. Nano letters. 2015;15(6):4013-8.

[41] Hu D, Zhao T, Ping X, Zheng H, Xing L, Liu X, et al. Unveiling the layer-dependent catalytic activity of PtSe$_2$ atomic crystals for the hydrogen evolution reaction. Angewandte Chemie. 2019;131(21):7051-5.

[42] Han SS, Kim JH, Noh C, Kim JH, Ji E, Kwon J, et al. Horizontal-to-vertical

transition of 2D layer orientation in low-temperature chemical vapor deposition-grown PtSe$_2$ and its influences on electrical properties and device applications. ACS Applied Materials & Interfaces. 2019;11(14):13598-607.

[43] Ma H, Chen P, Li B, Li J, Ai R, Zhang Z, et al. Thickness-tunable synthesis of ultrathin type-II Dirac semimetal PtTe$_2$ single crystals and their thickness-dependent electronic properties. Nano Letters. 2018;18(6):3523-9.

[44] Li X, Cai W, An J, Kim S, Nah J, Yang D, et al. Large-area synthesis of high-quality and uniform graphene films on copper foils. Science. 2009;324(5932):1312-4.

[45] Najmaei S, Liu Z, Zhou W, Zou X, Shi G, Lei S, et al. Vapour phase growth and grain boundary structure of molybdenum disulphide atomic layers. Nature Materials. 2013;12(8):754-9.

[46] Sun J, Lu C, Song Y, Ji Q, Song X, Li Q, et al. Recent progress in the tailored growth of two-dimensional hexagonal boron nitride via chemical vapour deposition. Chemical Society Reviews. 2018;47(12):4242-57.

[47] Yuan J, Sun T, Hu Z, Yu W, Ma W, Zhang K, et al. Wafer-scale fabrication of two-dimensional PtS$_2$/PtSe$_2$ heterojunctions for efficient and broad band photodetection. ACS Applied Materials & Interfaces. 2018;10(47):40614-22.

[48] Li L, Wang W, Chai Y, Li H, Tian M, Zhai T. Few-layered PtS$_2$ phototransistor on h-BN with high gain. Advanced Functional Materials. 2017;27(27):1701011.

[49] Shawkat MS, Chung H-S, Dev D, Das S, Roy T, Jung Y. Two-dimensional/three-dimensional Schottky junction photovoltaic devices realized by the direct CVD growth of vdw 2D PtSe$_2$

layers on silicon. ACS Applied Materials & Interfaces. 2019;11(30):27251-8.

[50] Zhou J, Kong X, Sekhar MC, Lin J, Le Goualher F, Xu R, et al. Epitaxial Synthesis of Monolayer PtSe$_2$ Single Crystal on MoSe2 with Strong Interlayer Coupling. ACS Nano. 2019;13(10):10929-38.

[51] Li E, Zhang R-Z, Li H, Liu C, Li G, Wang J-O, et al. High quality PdTe$_2$ thin films grown by molecular beam epitaxy. Chinese Physics B. 2018;27(8):086804.

[52] Li E, Wang D, Fan P, Zhang R, Zhang Y-Y, Li G, et al. Construction of bilayer PdSe$_2$ on epitaxial graphene. Nano Research. 2018;11(11):5858-65.

[53] Yao J, Yang G. 2D material broadband photodetectors. Nanoscale. 2020;12(2):454-76.

[54] Liang Q, Wang Q, Zhang Q, Wei J, Lim SX, Zhu R, et al. High-Performance, Room Temperature, Ultra-Broadband Photodetectors Based on Air-Stable PdSe$_2$. Advanced Materials. 2019;31(24):1807609.

[55] Xie C, Zeng L, Zhang Z, Tsang Y-H, Luo L, Lee J-H. High-performance broadband heterojunction photodetectors based on multilayered PtSe$_2$ directly grown on a Si substrate. Nanoscale. 2018;10(32):15285-93.

[56] Yim C, McEvoy N, Riazimehr S, Schneider DS, Gity F, Monaghan S, et al. Wide spectral photoresponse of layered platinum diselenide-based photodiodes. Nano Letters. 2018;18(3):1794-800.

[57] Wang L, Li J-J, Fan Q, Huang Z-F, Lu Y-C, Xie C, et al. A high-performance near-infrared light photovoltaic detector based on a multilayered PtSe$_2$/Ge heterojunction. Journal of Materials Chemistry C. 2019;7(17):5019-27.

[58] Zeng LH, Lin SH, Li ZJ, Zhang ZX, Zhang TF, Xie C, et al. Fast, self-driven, air-Stable, and broadband photodetector based on vertically aligned PtSe$_2$/GaAs heterojunction. Advanced Functional Materials. 2018;28(16):1705970.

[59] Zhuo R, Zeng L, Yuan H, Wu D, Wang Y, Shi Z, et al. In-situ fabrication of PtSe$_2$/GaN heterojunction for self-powered deep ultraviolet photodetector with ultrahigh current on/off ratio and detectivity. Nano Research. 2019;12(1):183-9.

[60] Wu D, Wang Y, Zeng L, Jia C, Wu E, Xu T, et al. Design of 2D layered PtSe$_2$ heterojunction for the high-performance, room-temperature, broadband, infrared photodetector. ACS Photonics. 2018;5(9):3820-7.

[61] Zhang Z-X, Zeng L-H, Tong X-W, Gao Y, Xie C, Tsang YH, et al. Ultrafast, self-driven, and air-stable photodetectors based on multilayer PtSe$_2$/perovskite heterojunctions. The Journal of Physical Chemistry Letters. 2018;9(6):1185-94.

[62] Zeng LH, Wu D, Lin SH, Xie C, Yuan HY, Lu W, et al. Controlled synthesis of 2D palladium diselenide for sensitive photodetector applications. Advanced Functional Materials. 2019;29(1):1806878.

[63] Wu D, Guo J, Du J, Xia C, Zeng L, Tian Y, et al. Highly polarization-sensitive, broadband, self-powered photodetector based on graphene/PdSe$_2$/germanium heterojunction. ACS Nano. 2019;13(9):9907-17.

[64] Zeng LH, Chen QM, Zhang ZX, Wu D, Yuan H, Li YY, et al. Multilayered PdSe$_2$/Perovskite Schottky Junction for Fast, Self-Powered, Polarization-Sensitive, Broadband Photodetectors, and Image Sensor Application. Advanced Science. 2019;6(19):1901134.

[65] Long M, Wang Y, Wang P, Zhou X, Xia H, Luo C, et al. Palladium diselenide

long-wavelength infrared photodetector with high sensitivity and stability. ACS Nano. 2019;13(2):2511-9.

[66] Su TY, Medina H, Chen YZ, Wang SW, Lee SS, Shih YC, et al. Phase-engineered PtSe$_2$-layered films by a plasma-assisted selenization process toward all PtSe$_2$-based field effect transistor to highly sensitive, flexible, and wide-spectrum photoresponse photodetectors. Small. 2018;14(19):1800032.

Group III-Nitrides and Their Hybrid Structures for Next-Generation Photodetectors

Deependra Kumar Singh, Basanta Kumar Roul,
Karuna Kar Nanda and Saluru Baba Krupanidhi

Abstract

In the last few decades, there has been a phenomenal rise and evolution in the field of III–Nitride semiconductors for optoelectronic applications such as lasers, sensors and detectors. However, certain hurdles still remain in the path of designing high-performance photodetectors (PDs) based on III-Nitride semiconductors considering their device performance. Recently, a lot of progress has been achieved in devices based on the high quality epilayers grown by molecular beam epitaxy (MBE). Being an ultra-high vacuum environment based-technique, MBE has enabled the realization of high-quality and highly efficient PDs which have exhibited competitive figures of merit to that of the commercial PDs. Moreover, by combining the novel properties of 2D materials with MBE-grown III-Nitrides, devices with enhanced functionalities have been realized which would pave a way towards the next-generation photonics. In the current chapter, the basic concepts about photodetection have been presented in detail, followed by a discussion on the basic properties of the III-Nitride semiconductors, and the recent advancements in the field of MBE-grown III-Nitrides-based PDs, with an emphasis on their hybrid structures. Finally, an outlook has been provided highlighting the present shortcomings as well as the unresolved issues associated with the present-day devices in this emerging field of research.

Keywords: group III-nitrides, molecular beam epitaxy, photodetectors, hybrid structures, next-generation photonic devices

1. Introduction

Photodetectors (PDs) are the photonic devices that convert an incoming light signal into an output electrical signal. High-performance PDs are crucial for the advancements in the industrial and scientific communities, and these are being extensively used in areas such as video imaging, space and optical communications, flame detection, photovoltaic applications, environmental monitoring, and so on [1–5]. Some of the most extensively employed inorganic semiconductors for the development of PDs are zinc oxide (ZnO) [6], gallium arsenide (GaAs) [7], indium gallium antimonide (InGaSb) [8], germanium silicide (GeSi) [9] and gallium oxide (Ga_2O_3) [10], due to their excellent electronic properties like high charge carrier mobility and high light absorption coefficients. However, large exciton binding energies, low values of responsivity, slower response and narrow-band detection are some

of the major downsides associated with these materials [11]. Moreover, the synthesis as well as post-processing steps in the fabrication of antimony and arsenic-based devices involves toxic precursors as well as products, which are extremely hazardous for human health and for the environment as well. Thus, the quest is on for the development of high-performance PDs consisting of environment-friendly constituents.

The recent developments in the III-Nitride semiconductors-based devices have made a tremendous impact upon a number of technological areas such as information storage, lighting and full color displays, underwater and space communications, high-power and high-frequency electronic devices, photovoltaics, sensors and detectors, and so on [12–15]. The wurtzite polytypes of indium nitride (InN), aluminum nitride (AlN), and gallium nitride (GaN) have proved to be excellent semiconductors for band gap engineering, due to formation of continuous range of alloys with direct and tunable band gaps in the range of 0.7 to 6.2 eV [16]. Therefore, their intrinsic physical and chemical properties along with intense technological efforts have made the realization of versatile and reliable detectors in the entire ultraviolet (UV)-visible–near infrared (NIR) spectrum.

In spite of the significant progresses, the growth of epitaxial group III-Nitride thin films for practical devices, having low defect densities, has always been a challenge due to the lack of availability of lattice matched substrates. As of now, among various epitaxial growth techniques for III-Nitrides, plasma assisted molecular beam epitaxy (PAMBE) has emerged as the most versatile and environment-friendly synthesis technique, involving low growth temperature, controlled growth rates which result into the formation of heterostructures with sharp interfaces, and non-hazardous precursors and by-products. Since pristine III-Nitride substrates are immensely costly and therefore, not yet available for research and industrial purposes, the development of this family of semiconductors proceeds entirely by the heteroepitaxial growth on various foreign substrates such as sapphire, Si (111) and 6H-SiC [16–18], and one has to often compromise with the device performance. It may be noted here that hybrid structures of III-Nitrides with other semiconductors such as ZnO, perovskites, and two-dimensional (2D) layered materials such as MoS_2 are expected to deliver competitive device performance as compared to the commercial PDs ([19–21]. In the forthcoming sections, we discuss about the figures of merit involved in the evaluation of a PD, followed by a brief overview of III-Nitrides and their properties. Then, a detailed analysis about the recent advancements in the MBE-grown III-Nitrides for photodetection application has been presented and finally, we wind up by discussing the unresolved difficulties and propose an outlook in this developing field of optoelectronics.

2. Basic concepts about photodetection

A PD is a sensor that detects an incoming electromagnetic radiation. Whenever light waves of energy greater than or equal to the band gap of a semiconductor are absorbed, there is an overall change in the conductivity of the semiconductor. Thus, PD is a device developed on the principle of this photoconducting effect and it quantifies the speed and the amplitude of the change in the conductivity, in respect of incoming electromagnetic radiations.

2.1 Important figures of merit of a PD

Several figures of merit and parameters are used for the evaluation of a PD, and these performance metrics allow us to compare various devices. Mostly, the output

electrical signal is recorded from the device and realized in the form of an output photocurrent, and thus, all the key figures of merit are defined in terms of this output photocurrent. The output photocurrent (I_P) is defined [11] as

$$I_P = I_{Illuminated} - I_{Dark} \qquad (1)$$

where $I_{Illuminated}$ is the output current detected upon light illumination and I_{Dark} is the dark current in the device (i.e. without any light illumination). Photocurrent can be enhanced by reducing the probability of recombination of photogenerated electrons and holes, and this can be achieved by fabricating high-quality and defect-free devices, using heterojunctions with type-II band alignment which result into the effective separation of charge carriers. Devices utilizing p-n junctions which operate in reverse bias, usually show a large photocurrent due to the enhanced carrier separation as well as lower dark current.

2.1.1 Responsivity

Responsivity (R_λ) is defined as the ratio of the photocurrent generated and the incident optical power of a specific wavelength on a predefined device area. It is given [11] by the following mathematical formula

$$R_\lambda = \frac{I_P}{P \times A} \qquad (2)$$

where P is the incident power density of light and A is the device area where light is being illuminated. Its units are AW^{-1}. It quantifies the extent of achievable electrical signal in a PD when illuminated by a light of certain power density. Thus, a larger responsivity signifies a larger electrical output signal for a specific optical excitation power. Replacing a single material-based or homojunction-based device with heterojunction-based devices with type-II band alignment is an effective way to enhance the responsivity due to minimized recombination of photogenerated electrons and holes [22]. Another approach is to promote devices which possess a strong built-in potential that supports the external electric field to enhance the carrier separation and transport [15]. Growth of high-quality crystals reduces the defect density present in the system, thereby suppressing the scattering and recombination of the charge carriers which enhances the responsivity of the device. Manohar et al. [6] recently demonstrated a highly cost effective and an elegant method to immensely enhance the photoresponsivity of a PD by suppressing the carrier recombination through coatings of different materials which facilitate either electron or hole transfer to the metal contacts.

2.1.2 Specific detectivity

A fundamental performance parameter for a PD is its specific detectivity, that measures the ability of a PD to detect weak light signals. For a PD, this metric can be defined in terms of the noise equivalent power (NEP). The NEP of a PD is proportional to the ratio of the square root of the dark current (I_{Dark}) to the responsivity (R_λ) of the PD at a given wavelength. It can be defined by the following relation:

$$NEP = \frac{\sqrt{(2 * e * I_{Dark})}}{R_\lambda} \qquad (3)$$

where e is the electronic charge. The specific detectivity (D^*) of a PD is defined as the ratio of the square root of the active area (A) to its NEP [4], and is given by the following equation

$$D^* = \frac{\sqrt{A}}{NEP} \tag{4}$$

It is measured in Jones. Higher detectivity of a PD indicates that even a very weak signal can be detected. It may be noted that lower is the dark current, higher is the detectivity. PDs based on p-n junctions operated in the reverse bias generally exhibit very high specific detectivities because of low values of dark current.

2.1.3 Internal gain

The internal gain (G) of a PD refers to the number of electrons collected at the electrodes per incident photon. It can be determined [4] by the following relation

$$G = \frac{hc * R_\lambda}{\eta e \lambda} \tag{5}$$

where h, c, η and λ are the Planck's constant, the velocity of light in vacuum, the EQE of the device and the illumination wavelength, respectively.

In other words, internal gain is the ratio of the hole carrier lifetime to the electron transit time and is given [4, 10] by

$$G = \tau/t \tag{6}$$

where τ is the mean hole carrier lifetime and t is the electron transit time. So, high internal gains can be achieved by fabricating devices which exhibit high responsivities. Another approach to enhance gain is by trapping one kind of charge carrier (generally holes), so as to prevent it from recombination. Thus, the carrier lifetime of the holes increases and in turn gain increases.

2.1.4 Sensitivity

Sensitivity (S) of a PD is defined [23] as the ratio of the photocurrent to the dark current.

$$S = \frac{I_P}{I_{Dark}} \tag{7}$$

Hence, sensitivity can be improved by either enhancing the value of photocurrent or lowering the dark current. The enhanced photocurrent can be achieved by fabricating high quality and defect-free interfaces and devices, thus, reducing the scattering effects of the photogenerated electrons and holes, and leading to higher photocurrents. Devices consisting of p-n junctions show ultralow values of dark currents exhibiting higher sensitivities.

2.1.5 Response/recovery time

An important aspect of a PD is how fast it detects the incident light, and how fast it comes back to its initial state once the incident light is removed. This is quantified by estimating the response/recovery times of the PD. Lower the values of

these time constants, faster is the detection process. Mukhokosi et al. [23] have demonstrated that the response times of a PD are controlled by the carrier mobilities of the constituent semiconductors of the PD. The transit time ($\tau_{transit}$) of a p-n heterojunction is given [23] by the following relation

$$\tau_{transit} = \frac{W}{v_{drift}} = \frac{W}{\mu_{drift} E_o} \qquad (8)$$

where W is the depletion region width, μ_{drift} is the carrier mobility and E_o is the built-in electric field at the junction. Therefore, high-quality substrates with high carrier mobilities such as p-Si, usually result into very small response time. The depletion width can be narrowed down by fabricating highly doped p-n junctions, which in turn decreases the transit time in accordance with Eq. (8).

Other parameters that affect the response speed of a PD are the junction capacitance (C) and the series load resistance (R), and thus, the corresponding RC time constant. The rise time of a PD with an RC circuit is given by:

$$\tau_r \cong 2.2RC \qquad (9)$$

Therefore, decreasing the junction capacitance can further improve the response time. The junction capacitance depends on the width of the depletion layer, and smaller depletion widths increase the capacitance. Therefore, the width of the depletion region should be optimum to minimize the carrier transit time.

In addition, defect-free semiconductors exhibit faster response times, because of reduced recombination of the photogenerated carriers. For the case of linear devices, high-quality photosensitive materials as well as defect-free semiconductor/electrode interfaces are required to minimize the carrier scattering and recombination processes, and result into the lowering of the carrier transit time.

2.1.6 Power consumption

One of the most critical parameters associated with a PD is its power consumption. Generally, PDs require an external power source as the driving force to separate the photogenerated electrons and holes efficiently. Thus, a lot of external energy is required in a system that consists of several such detectors. Therefore, it is a big concern in the present energy scenario. Hence, a lot of research is being focussed these days on achieving self-powered or zero-biased PDs [24, 25], which utilize a built-in electric potential for the effective charge carrier separation. The extensively used technique for fabricating self-powered PDs is by utilizing a p-n junction, where a strong electric field is created at the interface, and therefore, the device can operate in zero-bias mode.

2.1.7 Spectral range

Another crucial aspect of PDs is their detection range. PDs are generally classified into two categories based on their spectral range of detection: broad-band (which shows a considerable detection to a wide range of wavelengths) and narrow-band or wavelength-selective (whose detection range is very limited) PDs. The most common way to fabricate a wavelength-selective PD is by using a single semiconductor (of desired band gap) as the active material in the device. Another way to achieve wavelength selectivity is by integrating an optical microcavity within the PD. This optical microcavity consists of distributed Bragg reflectors (DBR), which allow multiple reflections of a specific wavelength. These reflections interfere

constructively, leading to increased light-matter interactions and result into the enhancement of photocurrent. This occurs only at the design wavelength of the cavity, whereas all the off-resonance wavelengths incident on the PD are rejected by the cavity. On the other hand, broad-band photodetection can be realized by making heterojunctions-based devices consisting of different semiconductors of appropriate band gaps, as demonstrated by Singh et al. [26] by making a hybrid device based on SnS_2/p-Si heterojunction, which shows a broad-band response in the entire ultraviolet to near infrared range. Usually, conventional PDs suffer from the trade-off between selective and broad-band detection. Recently, a few devices have been reported to exhibit a unique feature wavelength-selectivity in a broad-band spectral response, through the phenomenon of polarity switching [27, 28].

2.2 Different mechanisms of photodetection

PDs rely on distinct sensing mechanisms depending upon the intrinsic properties of the photosensitive materials used as well as the architecture of the device structures. We now briefly discuss the most commonly adopted sensing mechanisms.

2.2.1 Photoconductive and photogating effects

The photoconductive effect involves photogeneration of excess free carriers in a semiconductor material, when photons with energy higher than the band gap of the semiconductor are absorbed, which eventually leads to a change in its electrical conductivity. The photoconductive effect is the most primitive form of photodetection, where two Ohmic contacts are deposited on the semiconductor surface to form a metal–semiconductor–metal (MSM) type linear device configuration [29]. The schematic of a PD depicting the process of photoconduction is shown in **Figure 1(a)**. It is important to note that this change in conductivity is a result of the change in the free charge carrier concentration due to the photogeneration process. Thus, the effective spectral range of photoconductive PDs is limited by the band gap of the semiconducting material or the photoactive layer. Additionally, a photoconductive PD usually requires an externally applied voltage for the effective separation and the directional propagation of the photogenerated carriers. This generally results in relatively larger values of the dark current, which leads to a lower on/off ratio and higher energy consumption. Additionally, conventional photodiodes (non-linear devices) also work in the photoconductive mode when operated in the reverse bias condition.
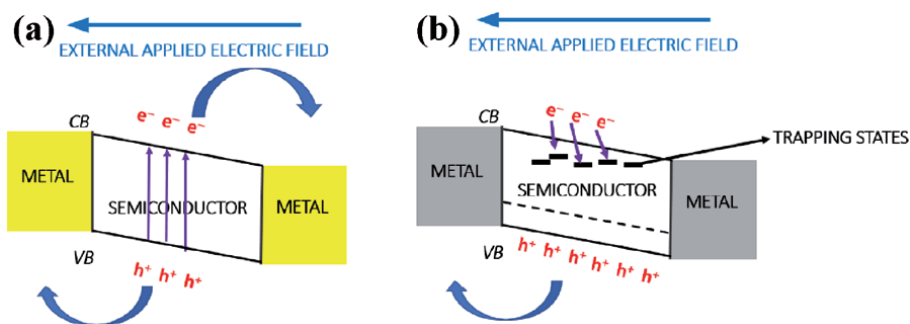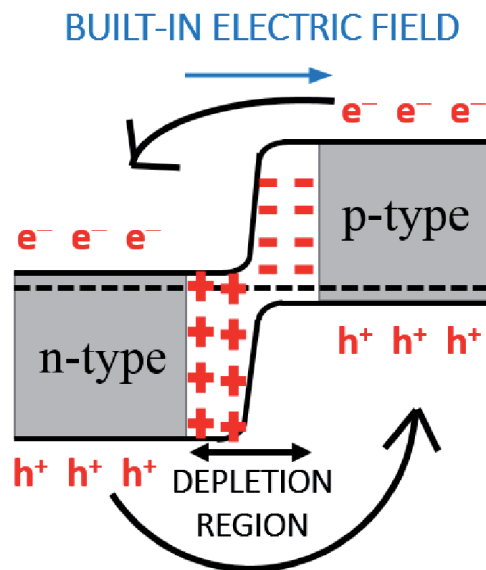

Figure 1.
Schematic view of (a) a photoconductor depicting the process of electron–hole pairs generation and their transport and (b) a PD based on the photogating effect under illumination. The defect states capture electrons which eventually modulates the conductivity of the material.

Photogating effect is a type of photoconducting effect, wherein certain localized states such as defects or surface states exist within the forbidden gap of the semiconductor. The effect normally originates when the photogenerated charge carriers are captured by the localized trapping states present within the system [30] as depicted in **Figure 1(b)**. This effect is pronounced in low-dimensional material systems such as 2D layered materials and quantum dots, which have very large surface-to-volume ratio and less screening in the z-direction. Since one type of charge carriers are trapped, it leads to prolonged carrier lifetimes, and therefore, PDs which exhibit the photogating effect usually show higher photogains. In addition, faster transit times and enhanced photocurrent is observed due to suppressed carrier recombination.

2.2.2 Photovoltaic effect

Photovoltaic effect is the phenomenon of spontaneous generation of a photocurrent upon light illumination in a PD. This effect is generally realized in p-n junction-based devices, where a built-in electric potential exists at the interface [31]. Upon light illumination, electrons and holes are created near the semiconductor interface. Under the influence of the existing built-in voltage, these electrons and holes get separated, thereby, causing a photocurrent to flow along the direction of this built-in potential (**Figure 2**). The photovoltaic effect is closely related to the photoelectric effect and therefore, the effective wavelength range is usually limited by the band gap of the constituent photosensitive material. However, in the case of p-n heterojunctions, due to the intimate energy band coupling that enables interband transition between different semiconductors, the effective detection range can be modulated beyond the limitation of the band gaps. The biggest advantage associated with PDs based on the photovoltaic effect is that due to the intrinsic built-in electric potential, the PDs do not require any external power for their operation [11]. Furthermore, the photovoltaic PDs possess low dark current under the zero-biased working mode, which is beneficial for the detector.

Figure 2.
Schematic depicting the photovoltaic effect.

2.2.3 Photothermoelectric effect

The origin of photothermoelectric (PTE) effect is the temperature gradient (ΔT) developed due to the thermal effects of the light illumination. Subsequently, a potential gradient (ΔV_{PTE}) is created that serves as the driving force for the transport of the photocurrent through the device (**Figure 3**). The thermoelectric voltage generated is given [32] by

$$\Delta V_{PTE} = S\Delta T \qquad (10)$$

where S is Seebeck coefficient of the material [33]. PTE effect-based PDs can operate without external power, i.e. they are self-powered in nature. However, the thermoelectric potential created is very low, generally in the range of millivolts (mV) and microvolts (μV), which seriously limits the popularization and hence, wide scale applications of PTE-based PDs.

2.2.4 Piezophototronic effect

The devices that make use of the piezo-potential of the constituent materials for controlling the carrier generation and transport, for improving the overall performance of the opto-electronic devices are referred to as piezophototronic [32]. The basic requirement of such devices is a piezo-electric material such as ZnO, GaN, etc. which can produce an electric potential upon variations in the applied stress. The operational mechanism of a piezophototronic device is based upon the fundamental principles of the conventional Schottky contacts and p–n junctions. Ionic charges are introduced by the effect of piezoelectric polarization, which tune the charge transport at the junction. The effect of piezophototronicity on a p-n junction (GaN/MoS_2 in this case) under compressive strain is shown in **Figure 4(a).** When the [0001]-oriented GaN film is under a compressive strain, negative piezopotential is produced inside GaN. This results into the lowering of the junction barrier. Therefore, more photogenerated charge carriers can cross the junction [34]. Hence, the photoresponsivity gets enhanced. An opposite effect (positive piezopotetial in GaN film, which increases the junction barrier) is observed in the case of applied tensile stress.

2.2.5 Photobolometric effect

Photobolometric effect is the alteration in the electrical resistance of a material, which is induced by the heating effect of uniform light illumination [32]. Typically, the active material layer absorbs the incident photons and then converts them into
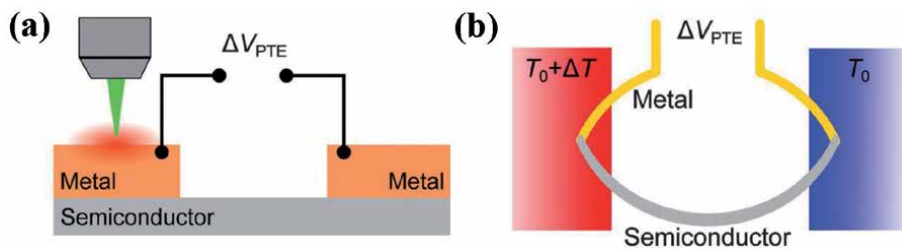
Figure 3.
(a) Schematic of a PTE based device illuminated locally by focused light. An open circuit voltage which is equal to the thermoelectric voltage ΔV_{PTE} gets developed across the electrodes. (b) Thermal circuit equivalent to the device depicted in (a). Figure is reproduced with permission from Ref. [33].
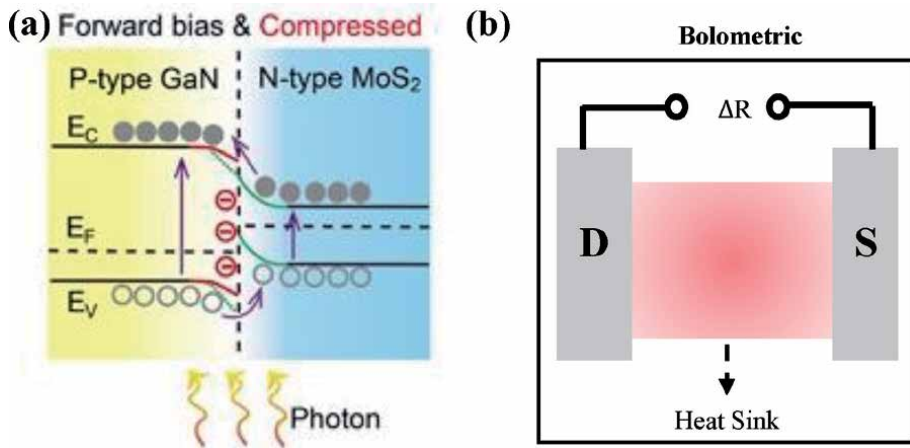
Figure 4.
(a) Piezophototronic enhancement observed in p-GaN/n-MoS₂ heterojunction. When the [0001]-oriented GaN film is compressed, negative piezoelectric charges develop in the GaN film near the interface, and the junction barrier gets lowered. This allows a greater number of carriers to pass through the junction. Figure is reproduced with permission from Ref. [34]. (b) Schematic depicting bolometric effect. The red shaded region indicates elevated temperature with the temperature gradient (ΔT) and ΔR denotes the resistance change across the channel. Figure is adapted from Ref. [35].

heat energy. The extent of this effect is proportional to the conductance change in the photoactive material with temperature (dG/dT) as well as the homogeneous temperature change (ΔT) induced by light illumination (**Figure 4(b)**). The change in conductance is influenced by change in the charge carrier mobility of the material because of the induced temperature change. Photobolometric effect generally occurs in the wavelength range of mid-infrared to far-infrared. Additionally, similar to PDs based on photoconductive effect, photobolometric PDs also require an external power source, which differentiates them from the PTE-based PDs.

3. Group III-Nitride semiconductors

From the early decades, silicon has been considered as one of the major components in the semiconductor industry because of its unique properties. Later, III-V materials, particularly the arsenic based compounds, gained much attention because of their superior properties such as high electron mobility, direct and tunable band gap, etc. The group III-Nitrides came into the picture around 1960s, and active research on this material system started with the development of blue light emitting diodes. Over the time, much of the attention of the researchers and scientists has been diverted on different classes of materials. However, group III-Nitride semiconductors continue to maintain their stronghold due to the exceptional properties and the unique advantages they offer.

3.1 Crystal structure and optical properties of group III-Nitrides

Group III-Nitride semiconductors, mainly comprising of AlN, GaN and InN, exist in three different crystal structures, namely, wurtzite, zincblende and rocksalt. Among these, the most stable and the lowest energy structure is the wurtzite system [36]. The wurtzite structure has a hexagonal unit cell and contains six atoms of each type, with space group P63mc. The wurtzite polytype is made up of two interpenetrating hexagonal close-packed unit cells, each containing one type

of atom, and with an offset along the c-axis by 5/8 of the cell height. The stacking sequence in the hexagonal structure consists of alternating hexagonal planes of group III and N atom, with a stacking sequence of ABAB [36]. A stick-and-ball model-based diagram of the hexagonal unit cell of III-Nitride semiconductors is shown in **Figure 5**. The group III semiconductors and the nitrogen atoms have been shown in different colors [37]. The polytypes of the III-Nitrides having wurtzite structure, form a continuous alloy system, with direct band gaps ranging from 0.7 eV for InN, 3.4 eV for GaN, and to 6.2 eV for AlN [16]. Therefore, the III-Nitrides are potential candidates for fabrication of optical devices which are active at wavelengths ranging from the NIR to the UV.

3.2 Growth of group III-Nitride semiconductors

The first successful synthesis of GaN dates back to as early as 1930s. In 1969, Maruska and Tietjen [38] synthesized single crystalline GaN layers on sapphire substrates by using the technique of hydride vapor phase epitaxy (HVPE). Although most of the III-Nitride semiconductors, especially for industrial-scale production, are usually synthesized via metal–organic chemical vapor deposition (MOCVD), metal–organic vapor phase epitaxy (MOVPE) and HVPE, however, these techniques have some serious drawbacks associated with them. These fabrication methods are generally characterized by quite high growth temperatures (>900°C). Thus, the sample is subjected to a high level of stress when cooled down to the room temperature from such high temperatures. Moreover, the inevitability of such high temperatures has hindered the growth of high-quality InN and its alloys, which are potential candidates for IR and terahertz (THz) optoelectronic applications, due to the dissociation of InN at such high temperatures [16]. There are also various other less-known techniques used for the synthesis of the group III-Nitrides, which are derivatives of the above three methods. However, all these processes involve the treatment and usage of toxic precursors as by-products, and therefore, making
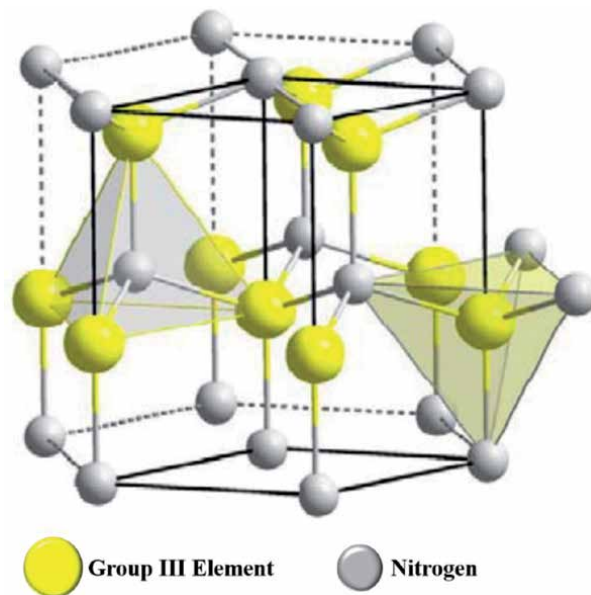
Figure 5.
The wurtzite crystal structure of III-nitrides. Nitrogen and group III atoms are represented by gray and yellow spheres, respectively. Figure has been reproduced with permission from Ref. [37].

these techniques less environment-friendly and hazardous to human health, which has become a major concern at the global level.

PAMBE, on the other hand, is a much cleaner synthesis technique and offers the advantage of fabrication of better-quality samples, along with a very important benefit of growth at much lower substrate temperatures when compared with most of its counterparts. MBE is an epitaxial and layer-by-layer growth technique involving precise control of the supply of thermally evaporated atomic species (**Figure 6(a)**). This results into construction of 2D layers on a substrate by means of lattice matching (**Figure 6(b)**). The major advantages of MBE are that it is clean, scalable and highly controlled with a high product quality. The involvement of ultra-high vacuum growth environment and the use of ultra-high purity elements as the source materials, minimize the inclusion of contaminants and impurities in the grown structures. Additionally, with the advent of higher growth rate RF-plasma
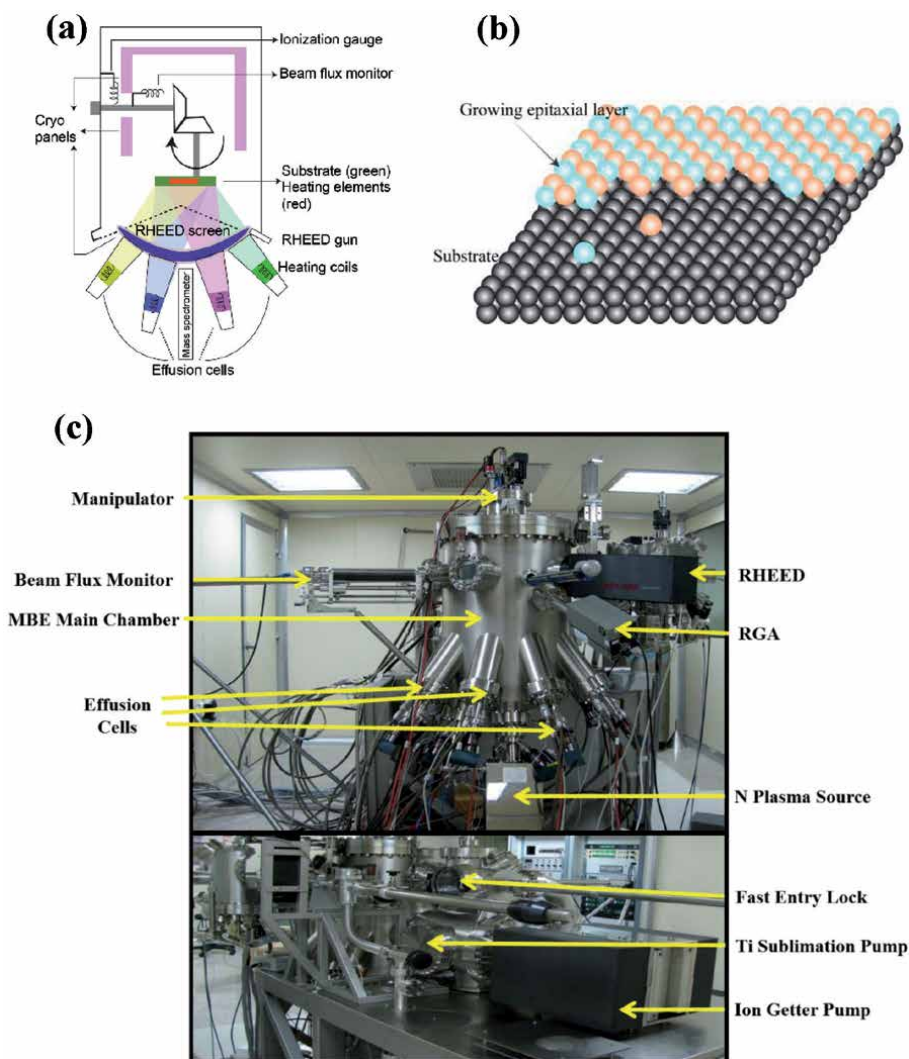
Figure 6.
(a) Schematic of a typical MBE system, showing various components. Figure has been adapted with permission from Ref. [40]. (b) Schematic depicting epitaxial growth of a material on a substrate. (c) MBE system located in materials research Centre, Indian Institute of Science, Bangalore, India.

sources, the synthesis times have been significantly reduced without compromising in the structural quality. One of the earliest works demonstrating growth of GaN by MBE was reported by Yoshida et al. [39] in 1983, wherein they successfully synthesized high electrical and optical quality GaN thin films on sapphire, with an AlN buffer layer via reactive MBE using ammonia as nitrogen source. **Figure 6(c)** shows the MBE setup located in Materials Research Centre, Indian Institute of Science, Bangalore, India.

3.3 Approaches to improve device performance of group III-Nitride semiconductors-based PDs

Researchers across the world have employed various approaches to improve the performance of the III-Nitrides-based devices. These include improvement in growth quality by the employment of different growth techniques, adopting novel growth methods like epitaxial lateral overgrowth (ELO), using different materials as buffer layers such as AlN, and by fabricating improved structures to reduce defects. Another way to improve the growth quality of III-Nitrides is to find the alternatives to conventional silicon and sapphire substrates. In this regard, transition metal dichalcogenides, having a small lattice mismatch with III-Nitrides, can be used as potential substrates. Engineering the device structures can also result into the improvement of the device performance, and this can be achieved by making quantum confinement architectures, and by making hybrid structures using 2D materials like graphene and MoS$_2$.

4. Recent advancements in the MBE grown III-Nitrides-based PDs

In the preceding sections, we have focused on the important figures of merit of PDs along with the different mechanisms of photodetection, and the properties and growth methods for group III-Nitride-based devices. Numerous reports exist which demonstrate the photodetection properties of III-Nitrides-based PDs. The recent state-of-the-art III-Nitride-based PDs have been discussed wherein a special emphasis on self-powered photodetection has been given.

4.1 III-Nitrides-based devices

Some early accomplishments in the field of GaN-based PDs grown by MBE have been achieved by several researchers such as Van Hove et al. [41], Son et al. [42], Torvik et al. [43], Osinsky et al. [44], Xu et al. [45], and so on. In 2005, Calarco et al. [46] reported the electrical transport of GaN nanowhiskers grown by MBE, in dark and under UV illumination. The photoresponse has been found to be sensitively dependent on the column diameter of the nanowhiskers and this effect has been quantitatively described through a mechanism of size dependent surface recombination. Jain et al. [47] have shown the effect of symmetric and asymmetric contact electrodes on *c*-GaN/sapphire based UV PD. In 2018, Goswami et al. [48] reported the growth of self-assembled GaN nanostructures on Si(111) for applications in UV photodetection (**Figure 7**). The device exhibited a responsivity of 5.7 mAW^{-1} at a bias of 1 V. Numerous other reports exist demonstrating the photodetection properties of GaN-based PDs.

In the meantime, researchers have also started exploring InN-based devices. One such work has been carried out by Shetty et al. [49]. They have grown InN quantum dots of varying densities on Si substrates using MBE. The device shows a strong response towards infrared illumination. The photoresponse studies revealed that
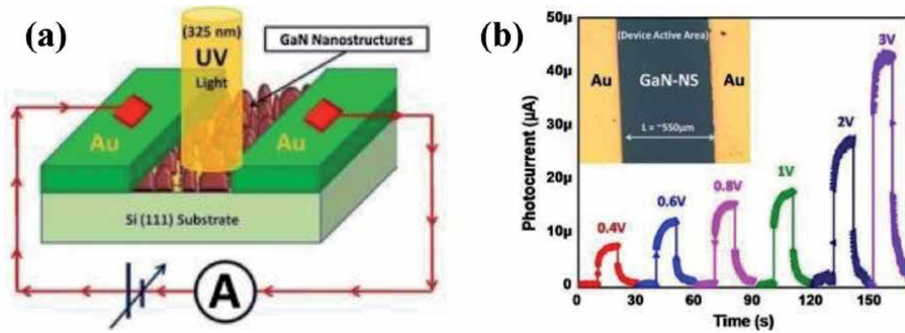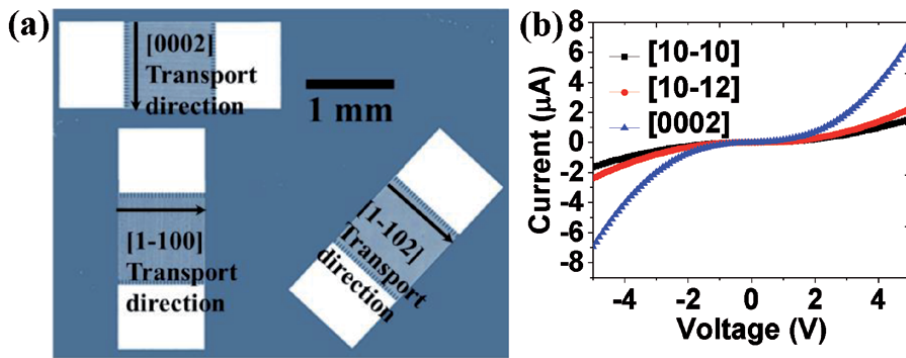
Figure 7.
(a) Schematic of the fabricated MSM device and (b) trend of photocurrent variation with respect to the applied bias. Inset shows the optical image of the actual PD. Figure has been reprinted with permission from Ref. [48].

the increasing dot density results in the improvement in the sensitivity of the PD. The increase in the photocurrent with the density of the quantum dots has been attributed to the increase in the number of photogenerated carriers in InN, which add up with the carriers generated in Si upon light illumination. The results have also been validated using simulations and it has been observed that the experimental as well as theoretical results have sufficient agreement between them.

However, the epitaxial growth of high-quality III-Nitrides has been always hindered by the lack of lattice-matched substrates, that hinders the development of high-performance devices. In all the above-mentioned reports, the growth has been accomplished on substrates (c-plane sapphire, Si(111), etc) which promote the c-plane oriented growth of the III-Nitrides i.e., in the polar direction. Moreover, the structures grown along the polar c-axis exhibit larger internal electric fields at the heterostructure interfaces, affecting the radiative recombination rates. To overcome these issues, non-polar III-Nitrides are being extensively explored now-a-days because of their several benefits over the polar III-Nitrides. Epitaxial growth of GaN in the non-polar (a-plane) direction seems to be a feasible way for the growth of high-quality films as the lattice mismatch between a-plane [11–20] GaN and the r-plane [1–102] sapphire is the least (1.19%) along one of the azimuth directions. Additionally, the absence of internal polarization fields in non-polar structures may enhance the photodetection performance. Mukundan et al. [50] in 2015 have shown improvement in the performance of non-polar GaN in comparison to that of the polar GaN in terms of figures of merit as well as the device stability.

In 2018, the mechanism of the higher device performance parameters of the non-polar GaN has been explained by Pant et al. [18] by performing azimuth angle-dependent photodetection. They have shown the non-uniformity in the defects present along the different azimuth directions. This is a consequence of the asymmetry in the strain between the substrate and film, as the lattice mismatch is asymmetric along various in-plane crystal directions. The mismatch in the lattice constants along the [0002] direction is ~1% whereas, along the [1–100] direction, it is ~13%. This induces a large number of defects along the [1–100] direction as compared to the [0002] azimuth direction. **Figure 8(a)** shows the a-GaN-based device used in this study. Furthermore, it has been shown in **Figure 8(b)** that the overall photocurrent in the UV region is also dependent on the different azimuth angles. A maximum responsivity of ~1.9 AW^{-1} and ~ 13.0 AW^{-1} have been obtained at a bias of 1 V and 5 V, respectively. These results underlined the importance of aligning the contact electrodes along the favorable azimuth direction in order to restrict the transport of the charge carriers. In a subsequent work, Pant et al. [51] have further shown

Figure 8.
(a) Fabrication of contact electrodes in different directions and (b) I–V characteristics of the device taken along different azimuth directions. Figure has been reprinted with permission from Ref. [18].

improvements in the photodetection properties of the non-polar GaN by optimizing the growth parameters and therefore, improving the overall quality of the thin film. A maximum responsivity of 25 AW^{-1} has been achieved at a low bias of 1 V and is among the highest reported responsivities at such low voltages.

Another approach to overcome the problem of lattice mismatch is by using AlN as a buffer layer. Wang et al. [52] in 2007 exhibited a Schottky-based metal–semi-conductor–metal PD, fabricated on 1 μm-thick and crack-free GaN on Si(111), utilizing an optimized $Al_xGa_{1-x}N$/AlN complex buffer layer. The device showed a high photoresponsivity of 4600 AW^{-1} at 1 V bias (366 nm) and this superior performance has been attributed to both the crack-free GaN film as well as the high internal gain. In another report, the growth of GaN p-n junction on AlN/Si(111) and the effects of thermal annealing of the Ni/Ag contact electrodes on the photo-detector applications have been explored by Yusoff et al. [14]. Recently, Ravikiran et al. [53] have demonstrated GaN UV PDs grown on AlN/Si(111) which exhibited a peak responsivity of 0.183 AW^{-1} at 15 V.

4.2 III-Nitride heterostructures-based devices

In the reports discussed above, various methods leading to enhancement in the responsivity have been highlighted. However, the responsivities and the transit times (in the order of a ms) of most of these PDs still remain inferior to that of the state-of-the-art detectors, and therefore, hamper their usage for the design and development of practical devices. The most elegant way to enhance the device performance is by utilizing a heterojunction with high-quality materials. There are many reports demonstrating PDs based on the heterojunctions of III-Nitrides with other III-Nitride semiconductors, ZnO, perovskites, 2D materials, and so forth.

In 2010, Rigutti et al. [54] have shown a single-nanowire PD relying on the charge carrier generation in the GaN/AlN quantum discs (QDs). The photolumi-nescence studies have shown that the emission energy of the QDs is lesser than the band gap of GaN, which is a consequence of the quantum confined Stark effect. The QD-based PDs exhibited a strong reduction in the dark current with responsivity (300 nm, −1 V) as high as 2×10^3 AW^{-1}. Yusoff et al. [55] have demonstrated AlN/ GaN/AlN heterostructures grown via PAMBE on Si substrates. The photoresponse shows promising results towards applications in UV detection. Pandey et al. [21] have reported the fabrication of a $BaTiO_3$/GaN (BTO/GaN)-based Schottky junc-tion PD on *c*-plane sapphire and its selective UV photodetection in temperature range of 313–423 K. The responsivity increased with increase in the temperature till

393 K and then it decreased. Such behavior has been explained by the enhancement in the device's dark current with increase in the temperature, which is also evident from the ideal diode equation. The device shows potential to be used as an UV PD in high-temperature applications.

In another report, Roul et al. [13] have demonstrated hybrid ZnO/AlN/Si-based UV PDs with infrared- and visible-blind photoresponse. The heterostructures have been formed by depositing ZnO films on Si(111) substrate with an introduction of AlN as an intermediate layer. The AlN layer helps in improving the crystallinity of the ZnO films and results in excellent optical properties. The vertical transport characteristics of the ZnO/AlN/Si heterojunction-based device under light illumination and in the dark demonstrate an intrinsic infrared- and visible-blind response, with excellent UV responsivity of 14.5 AW^{-1}. The AlN layer acts as an electron blocking layer and allows the holes to get transported across the heterojunction in the reverse biasing condition.

In the past few years, loads of efforts have been made in the field of III-Nitrides/2D materials-based heterostructures for high-performance optoelectronic devices. These 2D materials such as graphene, MoS_2, etc. are characterized by weak inter-layer van der Waals (vdW) forces, which lead to exceptional electronic properties, and can offer an open platform to design high-performance electronic devices. Moreover, the absence of surface dangling bonds in 2D materials results in high-quality heterointerfaces. Such an integration has been recently demonstrated by Goel et al. [20], wherein they have shown a high responsivity UV PD based on 2D/3D heterojunction, which has been formed by depositing few-layer of MoS_2 on GaN thin film. The superior light absorption properties of MoS_2 resulted in high performance MoS_2/GaN-based PD. The device shows a high responsivity of 3×10^3 AW^{-1} and detectivity of $\sim 10^{11}$ Jones (at a wavelength of 365 nm) at an applied reverse bias of 1 V under a light intensity of 12 $mWcm^{-2}$. The rise and the decay times of the PD were 5.3 and 5.6 ms, respectively.

Until now, all the reported devices discussed above require an external applied bias for achieving significant photodetection. In recent times, a lot of efforts are being made towards energy storage and energy producing devices due to the current situation of energy crisis [56–61]. Therefore, PDs that do not consume any external power are gaining a lot of attention. These self-powered devices depend upon the built-in potential at the interface, which enables the effective separation of the photogenerated charge carriers. Additionally, the built-in electric potential lowers the dark current, which is another advantage of such PDs. Thus, these self-powered nanodevices have a great outlook for the next-generation optoelectronic devices.

4.3 III-Nitrides and their heterostructures for self-driven photodetection

Off late, as mentioned above, there has been a tremendous focus on the self-powered PDs. In this section, we emphasize on the various methods unveiled to achieve self-driven photodetection with III-Nitrides-based PDs.

Prakash et al. [62] in 2016 have demonstrated a simple approach to fabricate a self-powered PD utilizing reduced graphene oxide (rGO) asymmetrical electrodes on MBE-grown GaN thin film as shown in **Figure 9(a)**. This integration of the transparent rGO contact electrodes on GaN has been realized through a simple drop-casting method, leading to a simple fabrication process as well as reduced processing time and cost. The hybrid shows a low photoresponsivity of 1.5 μAW^{-1} towards UV light at zero bias (**Figure 9(b)**), with fast response and recovery times of ~60 and ~267 ms, respectively. The difference in the work functions of rGO and GaN leads to formation of depletion regions at the two rGO/GaN interfaces. The drop casted contact electrodes are inhomogeneous in nature, which results into two
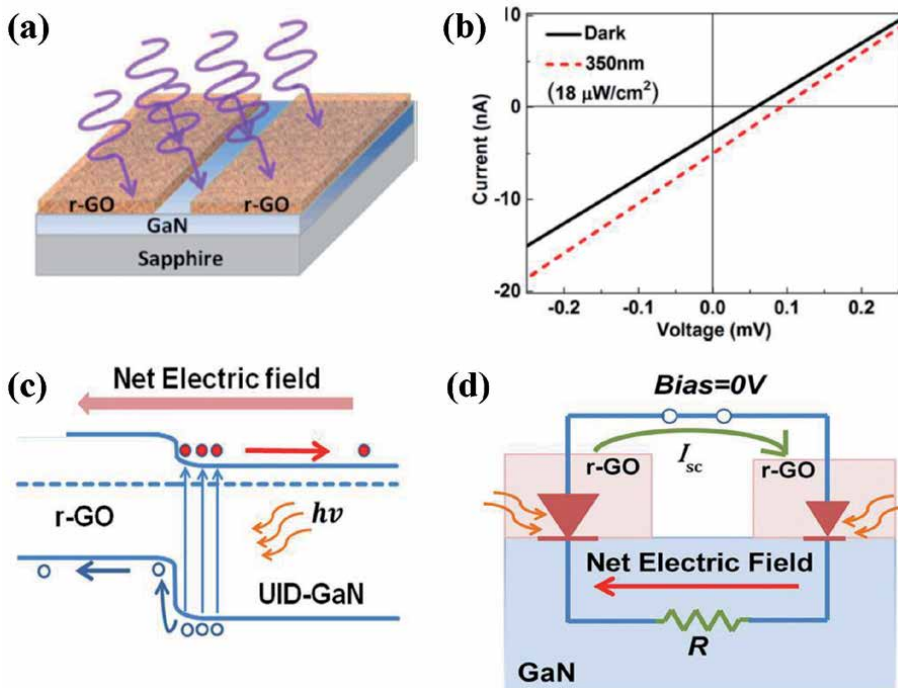
Figure 9.
(a) GaN-based device with rGO electrodes, (b) I-V characteristics of the PD, (c) energy band diagram and (d) mechanism for self-powered photodetection. Figure has been reproduced with permission from Ref. [62].

unlike built-in fields at these interfaces. Therefore, a net internal electric field is developed, leading to the self-powered detection (**Figure 9(c, d)**).

Using the same approach as described above, Pant et al. [63] have reported a self-driven a-GaN-based UV-A PDs showing a responsivity and detectivity of ~4.67 mAW^{-1} and 3.0 × 10^{13} Jones, respectively at a wavelength of 364 nm. In another work, Aggarwal et al. [64] have shown a UV PD based on GaN nanoflowers grown via MBE on Si(111) substrate. Under self-biased condition, the PD exhibits a very low dark current in the range of ≈nA, with a high responsivity of 132 mAW^{-1} and fast rise/fall times of 63/27 ms. In another report, Chowdhury et al. [25] have reported self-powered photodetection of an InN/AlN/Si semiconductor–insulator–semiconductor-based PD (λ = 1550 nm), where a photoresponsivity of ~3.36 μAW^{-1} has been observed with response/recovery times in milliseconds.

The major shortcoming of such devices lies with the obtained responsivities, which is entirely reliant on the degree of inhomogeneity or asymmetry between the electrodes, hence, limiting the PD's performance. One of the most effective ways for realizing self-driven PDs is by fabricating heterojunctions and utilizing the built-in potential at the heterointerface. Heterojunctions of III-Nitrides with several semiconductors such as Si, ZnO, Ga$_2$O$_3$, and so on have been explored and promising results have been achieved. In 2015, the advances in the high growth quality of epitaxial InGaN films on Si substrates synthesized via MBE along with the maturity in the Si-based technology have resulted in the demonstration of highly efficient PDs, as shown by Chandan et al. [65]. A self-powered n-InGaN/n-Si isotype heterojunction-based PD has been reported. The device shows a non-linear behavior and a responsivity of 0.094 AW^{-1}, with rise/fall times less than 100 ms. The mechanism of self-powered photodetection has been explained based on the presence of interfacial internal electric field.

Recently, a high-performance PD based on the p-GaN/n-ZnMgO heterojunction has been demonstrated [24]. The PD shows a clear rectifying *I–V* behavior characterized with a turn-on voltage of ~2.5 V. At zero-bias condition, the device exhibits a responsivity of 196 mAW^{-1} at a wavelength of 362 nm. The rise and the decay times of the PD are as short as 1.7 and 3.3 ms, respectively. This high performance of the device has been attributed to the excellent crystalline quality and electrical properties of p-GaN epilayer.

In another work, a simple approach has been reported [66] to fabricate a GaN/rGO: Ag nanoparticles (NPs) p–n heterojunction-based PD, integrated with a network of transparent Au nanowires (NWs) as the top contact electrode. The device demonstrates an excellent rectification ratio of ~105 with a broad-band photoresponse due to the presence of both the GaN layer (UV region) and the silver-loaded reduced graphene oxide (visible to infrared region). Furthermore, the reducing effect of the Ag NPs to graphene oxide in addition to the localized surface plasmon resonance has been utilized to improve the photoresponse in the NIR and the visible regions. The transparent Au NWs network efficiently collects the charge, ensuing high photoresponsivity and fast switching behavior. The heterojunction exhibits a responsivity of ~266 mAW^{-1} and detectivity of ~2.62 × 10^{11} Jones, under illumination of 360 nm light. Owing to the high built-in electric potential at the heterointerface, the self-powered operation is demonstrated under the entire excitation wavelength range (360–980 nm).

Exploiting the criterion of the difference between the electron affinities of the constituent semiconductors to create an internal field, an improvisation in the InGaN/Si-based structure has been demonstrated by Chowdhury et al. [15], where introduction of an AlN layer in between InGaN and Si leads to the formation of a semiconductor–insulator–semiconductor type structure, resulting in the multi-fold enhancement in the device performance. The n^+-InGaN/AlN/n-Si(111) hybrid structure has been realized by growing an n^+-InGaN thin film on a commercially obtained AlN/n-Si template using MBE. The device exhibits an exceptional self-powered and broad-band photorespnse under the illumination of UV–visible light (300–800 nm). The self-powered PD exhibits a high responsivity of 9.64 AW^{-1} at light illumination of 580 nm, with an ultrafast response/recovery time of ~20/21 μs, respectively. The maximum response at 580 nm is believed to be because of the deep donor defect states present in the InGaN epilayer.
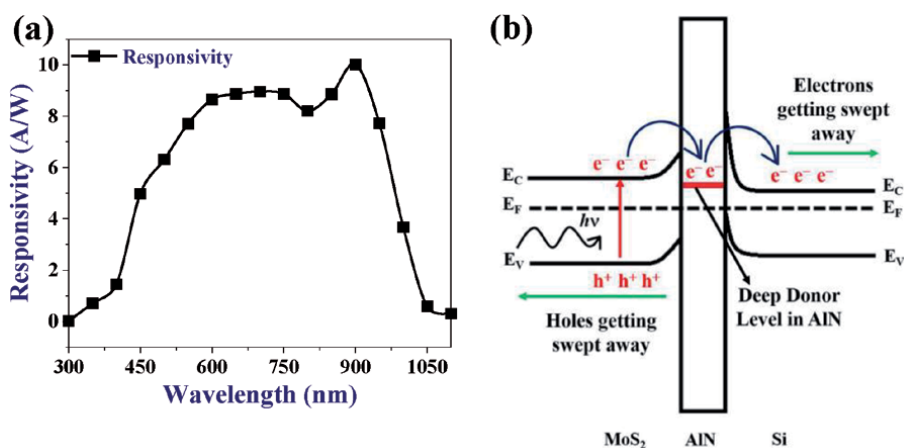
Figure 10.
(a) Spectral response of the MoS$_2$/AlN/Si-based PD. (b) Schematic of the deep defect states-modulated carrier transport in MoS$_2$/AlN/Si-based device. Figures have been reproduced with permission from Ref. [4].

In a recent work, Singh et al. [4] have fabricated an MoS_2/AlN/Si-based PD, combining the mature technologies of III-Nitride and Si with the unique properties of MoS_2. Additionally, due to the large difference between the work functions of these semiconducting materials, the band bending at the heterointerfaces resulted into the self-driven behavior. The vertical transport behavior of the device shows a broad-band photoresponse (300–1100 nm) with maximum responsivity of ~10 AW^{-1} under self-biased condition as shown in **Figure 10(a)**. The device also shows an ultrafast detection speeds (response/recovery times: ~13/15 μs). The importance of sandwiching the AlN layer has been shown as the MoS_2/Si-based PD shows a responsivity ~5 times less in the zero-bias mode. The authors have confirmed through transmission electron microscopy and X-ray photoelectron spectroscopy that oxygen defects exist throughout the AlN layer. These impurities form deep donor levels in AlN and moderate the charge transport, which leads to the enhanced device performance (**Figure 10(b)**).

5. Summary

The last two decades have indisputably witnessed incredible advances in the MBE growth of III-Nitrides and their applications in the area of photodetection. In this chapter, the important concepts about PDs, including the fundamental evaluation parameters and the various sensing mechanisms have been discussed. These mechanisms usually depend on the type of the photoactive material used to fabricate the device. Next, the basic properties of III-Nitrides and the common synthesis techniques used for their production have been reviewed briefly. Finally, a progressive discussion about the PDs based on the III-Nitrides fabricated through MBE has been given and summarized in **Table 1**. These extensive achievements have indisputably established MBE as one of the most reliable methods for fabricating high-quality III-Nitrides and these devices certainly have a lot of potential for the development of the advanced III-Nitrides-based PDs in future.

PD	Bias (V)	Responsivity (mAW^{-1})	Detectivity (Jones)	Rise/Fall Times (ms)
Ag-GaN-Pt [47]	5	633 @ 325 nm (4 mW)	—	—
GaN NS/Si [48]	1	5.7 @ 325 nm (13 mW)	—	—
InN QDs [49]	3	—	—	$1.43×10^3$/ $1.22×10^3$
a-GaN [50]	2	155 @ 360 nm (0.3 mW/cm^2)	—	$6×10^3$/ $15×10^3$
a-GaN [18]	1	$1.9×10^3$ @ 360 nm (0.3 mW/cm^2)	—	210/ $1.2×10^3$
a-GaN [51]	1	$2.5×10^4$ @ 360 nm (0.3 mW/cm^2)	—	222/ $2.1×10^3$
GaN [52]	1	$4.6×10^6$ @ 366 nm	—	—
GaN [53]	15	183 @ 362 nm (0.8 W/m^2)	—	—
GaN/AlN QDs [54]	-1	$2×10^6$ @ 300 nm	—	—
BTO/GaN [21]	5	$4.5×10^4$ @ 350 nm (413 K)	$2.57×10^{12}$	320/220

PD	Bias (V)	Responsivity (mAW^{-1})	Detectivity (Jones)	Rise/Fall Times (ms)
ZnO/AlN/Si [13]	−4	1.45×10^4 @ 365 nm (0.3 mW/cm^2)	—	1.12×10^4/ 7.65×10^4
MoS$_2$/GaN [20]	1	3×10^6 @ 365 nm (12 mW/cm^2)	~10^{11}	5.3/5.6
rGO/GaN [62]	0	1.54 @ 350 nm (18 μW/cm^2)	1.45×10^{10}	60/267
a-GaN [63]	0	4.67 @ 364 nm (0.06 mW/cm^2)	3×10^{13}	50/120
GaN Nanoflowers [64]	0	132 @ 325 nm (13 mW)	2.4×10^{10}	63/27
InN/AlN/Si [25]	0	3.36×10^{-3} @ 1550 nm (106.2 mW/cm^2)	—	10/18
n-InGaN/n-Si [65]	0	94.2 @ 310–380 nm (0.3 mW/cm^2)	—	20/33
p-GaN/n-ZnMgO [24]	0	196 @ 362 nm	—	1.7/3.3
GaN/rGO: Ag NP [66]	0	266 @ 360 nm (0.14 mW/cm^2)	2.62×10^{11}	680/700
InGaN/AlN/Si [15]	0	9.64×10^3 @ 580 nm (0.1 mW/cm^2)	1.93×10^{13}	19.9×10^{-3}/ 21.4×10^{-3}
MoS$_2$/AlN/Si [4]	0	10×10^3 @ 900 nm (0.05 mW/cm^2)	9.39×10^{12}	12.5×10^{-3}/ 14.9×10^{-3}

Table 1.
Comparison of the device performance parameters of various PDs discussed.

6. Outlook

Based upon the analysis of the reported devices in this field, a perspective regarding the future of III-Nitrides-based devices and the related follow-up work have been summarized below:

- The use of transition metal dichalcogenides (TMDCs) as substrates for epitaxial growth of III-Nitrides has been unexplored. TMDCs have a very small lattice mismatch with the III-Nitrides [67], and therefore, high-quality growth can be expected which would result into better device performance.

- The use of 2D transparent materials like graphene, graphene derivatives and 1T phase of TMDCs (semi-metallic), can be used as contact electrodes instead of the conventional metals, as the area for the light absorption gets maximized along with the outstanding electronic properties of these 2D semiconductors.

- Another interesting possibility would be combining non-polar nitrides with layered materials. The absence of the internal polarization field would provide a band to band transition, which is usually absent in the polar devices because of the quantum confined Stark effect at the interfaces. This property is very important for effective photodetection and has been evident from some of the very early works reported on the nonpolar *a*-GaN. Additionally, the presence of anisotropy in electrical conductivity as well as mobility can be helpful in tuning the optoelectronic and electronic properties of the PD.

- Till now, scientists across the world have generally exploited heterojunctions of III-Nitrides with 2D materials in the form of thin films. Heterojunctions based upon the one-dimensional (1D) nanostructures can provide new ways for the development of high-performance optoelectronic devices. The nanorods-based heterointerfaces of the III-Nitrides with 2D materials (growth along these nanorods or a core-shell structure) would enable a much higher aspect ratio and therefore, a much larger area for light absorption as well as a larger active interface, therefore, an enhancement in the optoelectronic performance.

Overall, the excellent properties of the III-Nitride semiconductors make them promising candidates for the applications in photodetection, and these PDs have exhibited outstanding device performance that competes with those available commercially. Thus, III-Nitrides and their heterojunctions-based PDs can be used for the development of futuristic self-biased and ultrafast PDs.

Acknowledgements

Author details

Deependra Kumar Singh[1], Basanta Kumar Roul[1,2], Karuna Kar Nanda[1]
and Saluru Baba Krupanidhi[1*]

1 Materials Research Centre, Indian Institute of Science, Bangalore, India

2 Central Research Laboratory, Bharat Electronics, Bangalore, India

*Address all correspondence to: sbkrupanidhi@gmail.com

IntechOpen

References

[1] Wu W, Zhang Q, Zhou X, Li L, Su J, Wang F, et al. Self-powered photovoltaic photodetector established on lateral monolayer MoS$_2$-WS$_2$ heterostructures. Nano Energy. 2018;**51**:45-53

[2] Singh RK, Kumar J, Kumar A, Kumar V, Kant R, Singh R. Poly(3-hexylthiophene): Functionalized single-walled carbon nanotubes: (6,6)-phenyl-C61-butyric acid methyl ester composites for photovoltaic cell at ambient condition. Solar Energy Materials and Solar Cells. 2010;94(12):2386-94.

[3] Khan MA, Nanda KK, Krupanidhi SB. Mechanistic view on efficient photodetection by solvothermally reduced graphene oxide. Journal of Material Science: Material in Electronics. 2017;28(19):14818-26.

[4] Singh DK, Pant R, Chowdhury AM, Roul B, Nanda KK, Krupanidhi SB. Defect-Mediated Transport in Self-Powered, Broadband, and Ultrafast Photoresponse of a MoS$_2$/AlN/Si-Based Photodetector. ACS Applied Electronic Materials. 2020;2(4):944-53.

[5] Mehew JD, Unal S, Torres Alonso E, Jones GF, Fadhil Ramadhan S, Craciun MF, et al. Fast and Highly Sensitive Ionic-Polymer-Gated WS$_2$-Graphene Photodetectors. Advanced Material. 2017;29:1700222.

[6] Sai Manohar GV, Krupanidhi SB, Nanda KK. Giant enhancement in photoresponse via engineering of photo-induced charge (electron and hole) transfer in linear and non-linear devices. Sensors and Actuators A: Physical. 2020;304:111842.

[7] Ilegems M, Schwartz B, Koszi LA, Miller RC. Integrated multijunction GaAs photodetector with high output voltage. Applied Physics Letters. 1978;33(7):629.

[8] Refaat TF, Abedin MN, Bhagwat V, Bhat IB, Dutta PS, Singh UN. InGaSb photodetectors using an InGaSb substrate for 2μm applications. Applied Physics Letters. 2004;85(11):1874.

[9] Murtaza SS, Campbell JC, Bean JC, Peticolas LJ. Asymmetric dual GeSi/Si Bragg mirror and photodetector operating at 632 and 780 nm. Applied Physics Letters. 1994;65(7):795.

[10] Arora K, Goel N, Kumar M, Kumar M. Ultrahigh performance of self-powered β-Ga$_2$O$_3$ thin film solar-blind photodetector grown on cost-effective Si substrate using high-temperature seed layer. ACS Photonics. 2018;5(6):2391-401.

[11] Yao JD, Zheng ZQ, Yang GW. Production of large-area 2D materials for high-performance photodetectors by pulsed-laser deposition. Progress in Materials Science. 2019;106:100573.

[12] Moustakas TD, Iliopoulos E, Sampath AV, Ng HM, Doppalapudi D, Misra M, et al. Growth and device applications of III-nitrides by MBE. Journal of Crystal Growth. 2001;227-228:13-20.

[13] Roul B, Pant R, Chowdhury AM, Chandan G, Singh DK, Chirakkara S, et al. Highly Responsive ZnO/AlN/Si Heterostructure-Based Infrared- and Visible-Blind Ultraviolet Photodetectors With High Rejection Ratio. IEEE Transactions on Electron Devices. 2019;66(3):1345-52.

[14] Mohd Yusoff MZ, Baharin A, Hassan Z, Abu Hassan H, Abdullah MJ. MBE growth of GaN pn-junction photodetector on AlN/Si(111) substrate with Ni/Ag as ohmic contact. Superlattices and Microstructures. 2013;56:35-44.

[15] Chowdhury AM, Chandan G, Pant R, Roul B, Singh DK, Nanda KK,

et al. Self-Powered, Broad Band, and Ultrafast InGaN-Based Photodetector. ACS Applied Material & Interfaces. 2019;11(10):10418-25.

[16] Singh DK, Roul B, Pant R, Chowdhury AM, Nanda KK, Krupanidhi SB. Different types of band alignment at MoS_2/(Al, Ga, In)N heterointerfaces. Applied Physics Letters. 2020;116(25):252102.

[17] Sasaki T, Matsuoka T. Substrate-polarity dependence of metal-organic vapor-phase epitaxy-grown GaN on SiC. Journal of Applied Physics. 1988;64(9):4531-5.

[18] Pant R, Shetty A, Chandan G, Roul B, Nanda KK, Krupanidhi SB. In-plane anisotropic photoconduction in nonpolar epitaxial a-plane GaN. ACS Applied Materials & Interfaces. 2018;10(19):16918-23.

[19] Zhang L, Zhao F, Wang C, Wang F, Huang R, Li Q. Optoelectronic characteristics of UV photodetector based on GaN/ZnO nanorods p-i-n heterostructures. Electronic Materials Letters. 2015;11(4):682-6.

[20] Goel N, Kumar R, Roul B, Kumar M, Krupanidhi SB. Wafer-scale synthesis of a uniform film of few-layer MoS_2 on GaN for 2D heterojunction ultraviolet photodetector. Journal of Physics D: Applied Physics. 2018;51(37):374003.

[21] Pandey BK, Bhat TN, Roul B, Nanda KK, Krupanidhi SB. BTO/GaN heterostructure based on Schottky junction for high-temperature selective ultra-violet photo detection. Journal of Physics D: Applied Physics. 2018;51(4):045104.

[22] Yang W, Hu K, Teng F, Weng J, Zhang Y, Fang X. High-Performance Silicon-Compatible Large-Area UV-to-Visible Broadband Photodetector Based on Integrated Lattice-Matched Type II

Se/n-Si Heterojunctions. Nano Letters. 2018;18(8):4697-703.

[23] Mukhokosi EP, Roul B, Krupanidhi SB, Nanda KK. Toward a fast and highly responsive $SnSe_2$-based photodiode by exploiting the mobility of the counter semiconductor. ACS Applied Materials & Interfaces. 2019;11(6):6184-94.

[24] Zhu Y, Liu K, Ai Q, Hou Q, Chen X, Zhang Z, et al. A high performance self-powered ultraviolet photodetector based on a p-GaN/n-ZnMgO heterojunction. Journal of Materials Chemistry C. 2020;8(8):2719-24.

[25] Chowdhury AM, Pant R, Roul B, Singh DK, Nanda KK, Krupanidhi SB. Double Gaussian distribution of barrier heights and self-powered infrared photoresponse of InN/AlN/Si (111) heterostructure. Journal of Applied Physics. 2019;126(2):025301.

[26] Singh DK, Pant R, Roul B, Chowdhury AM, Nanda KK, Krupanidhi SB. Temperature-Dependent Electrical Transport and Optoelectronic Properties of SnS_2/p-Si Heterojunction. ACS Applied Electronic Materials. 2020;2(7):2155-63.

[27] Gao L, Chen C, Zeng K, Ge C, Yang D, Song H, et al. Broadband, sensitive and spectrally distinctive SnS_2 nanosheet/PbS colloidal quantum dot hybrid photodetector. Light: Science and Applications. 2016;5(7):e16126–e16126.

[28] Ouyang B, Zhao H, Wang ZL, Yang Y. Dual-polarity response in self-powered ZnO NWs/Sb_2Se_3 film heterojunction photodetector array for optical communication. Nano Energy. 2020;68:104312.

[29] Hou Y, Mei Z, Du X. Semiconductor ultraviolet photodetectors based on ZnO and $Mg_xZn_{1-x}O$. Journal of Physics D: Applied Physics. 2014;47(28):283001.

[30] Shkir Mohd, Khan MT, Ashraf IM, Almohammedi A, Dieguez E, AlFaify S. High-performance visible light photodetectors based on inorganic CZT and InCZT single crystals. Scientific Reports. 2019;9(1):12436.

[31] Zhuo R, Wang Y, Wu D, Lou Z, Shi Z, Xu T, et al. High-performance self-powered deep ultraviolet photodetector based on MoS_2/GaN p–n heterojunction. Journal of Materials Chemistry C. 2018;6(2):299-303.

[32] Mukhokosi EP, Manohar GVS, Nagao T, Krupanidhi SB, Nanda KK. Device Architecture for Visible and Near-Infrared Photodetectors Based on Two-Dimensional $SnSe_2$ and MoS_2: A Review. Micromachines. 2020;11(8):750.

[33] Buscema M, Island JO, Groenendijk DJ, Blanter SI, Steele GA, van der Zant HSJ, et al. Photocurrent generation with two-dimensional van der Waals semiconductors. Chemical Society Reviews. 2015;44(11):3691-718.

[34] Xue F, Yang L, Chen M, Chen J, Yang X, Wang L, et al. Enhanced photoresponsivity of the MoS_2-GaN heterojunction diode via the piezo-phototronic effect. NPG Asia Materials. 2017;9(8):e418–e418.

[35] Koppens FHL, Mueller T, Avouris Ph, Ferrari AC, Vitiello MS, Polini M. Photodetectors based on graphene, other two-dimensional materials and hybrid systems. Nature Nanotech. 2014 Oct;9(10):780-93.

[36] Morkoç H. Handbook of nitride semiconductors and devices, Materials Properties, Physics and Growth. John Wiley & Sons; 2009.

[37] Hill, A. Growth, Characterization, and Thermodynamics of III-Nitride Semiconductors. PhD thesis. Arizona State University; 2011.

[38] Maruska HP, Tietjen JJ. The preparation and properties of vapor-deposited single-crystal-line GaN. Applied Physics Letters. 1969;15(10):327-9.

[39] Yoshida S, Misawa S, Gonda S. Improvements on the electrical and luminescent properties of reactive molecular beam epitaxially grown GaN films by using AlN-coated sapphire substrates. Applied Physics Letters. 1983;42(5):427-9.

[40] Pant R, Singh DK, Chowdhury AM, Roul B, Nanda KK, Krupanidhi SB. Next-generation self-powered and ultrafast photodetectors based on III-nitride hybrid structures. APL Materials. 2020;8(2):020907.

[41] Van Hove JM, Hickman R, Klaassen JJ, Chow PP, Ruden PP. Ultraviolet-sensitive, visible-blind GaN photodiodes fabricated by molecular beam epitaxy. Applied Physics Letters. 1997;70(17):2282-4.

[42] Son MS, Im SI, Park YS, Park CM, Kang TW, Yoo K-H. Ultraviolet photodetector based on single GaN nanorod p–n junctions. Materials Science and Engineering: C. 2006;26(5-7):886-8.

[43] Torvik JT, Pankove JI, Van Zeghbroeck BJ. Comparison of GaN and 6H-SiC p-i-n photodetectors with excellent ultraviolet sensitivity and selectivity. IEEE Transactions on Electron Devices. 1999;46(7):1326-31.

[44] Osinsky A, Gangopadhyay S, Yang JW, Gaska R, Kuksenkov D, Temkin H, et al. Visible-blind GaN Schottky barrier detectors grown on Si(111). Applied Physics Letters. 1998;72(5):551-3.

[45] Xu HZ, Wang ZG, Kawabe M, Harrison I, Ansell BJ, Foxon CT. Fabrication and characterization of metal–

semiconductor–metal (MSM) ultraviolet photodetectors on undoped GaN/sapphire grown by MBE. Journal of Crystal Growth. 2000;218(1):1-6.

[46] Calarco R, Marso M, Richter T, Aykanat AI, Meijers R, vd Hart A, Stoica T, Lüth H. Size-dependent photoconductivity in MBE-grown GaN— nanowires. Nano Letters. 2005;5(5):981-4.

[47] Jain SK, Krishna S, Aggarwal N, Kumar R, Gundimeda A, Husale SC, et al. Effect of Metal Contacts on a GaN/Sapphire-Based MSM Ultraviolet Photodetector. Journal of Electronic Materials. 2018;47(10):6086-90.

[48] Goswami L, Pandey R, Gupta G. Epitaxial growth of GaN nanostructure by PA-MBE for UV detection application. Applied Surface Science. 2018;449:186-92.

[49] Shetty A, Kumar M, Roul B, Vinoy KJ, Krupanidhi SB. InN Quantum Dot Based Infra-Red Photodetectors. Journal of Nanoscience and Nanotechnology. 2016;16(1):709-14.

[50] Mukundan S, Roul B, Shetty A, Chandan G, Mohan L, Krupanidhi SB. Enhanced UV detection by non-polar epitaxial GaN films. AIP Advances. 2015;5(12):127208.

[51] Pant RK, Singh DK, Roul B, Chowdhury AM, Chandan G, Nanda KK, et al. Photodetection Properties of Nonpolar a-Plane GaN Grown by Three Approaches Using Plasma-Assisted Molecular Beam Epitaxy. Physica Status Solidi A. 2019;216(18):1900171.

[52] Wang X, Wang X, Wang B, Xiao H, Liu H, Wang J, et al. High responsivity ultraviolet photodetector based on crack-free GaN on Si (111). Physica Status Solidi A. 2007;4(5):1613-6.

[53] Ravikiran L, Radhakrishnan K, Dharmarasu N, Agrawal M,

Wang Z, Bruno A, et al. GaN Schottky Metal–Semiconductor–Metal UV Photodetectors on Si(111) Grown by Ammonia-MBE. IEEE Sensors Journal. 2017;17(1):72-7.

[54] Rigutti L, Tchernycheva M, De Luna Bugallo A, Jacopin G, Julien FH, Zagonel LF, et al. Ultraviolet Photodetector Based on GaN/AlN Quantum Disks in a Single Nanowire. Nano Letters. 2010;10(8):2939-43.

[55] Mohd Yusoff MZ, Mahyuddin A, Hassan Z, Abu Hassan H, Abdullah MJ, Rusop M, et al. AlN/GaN/AlN heterostructures grown on Si substrate by plasma-assisted MBE for MSM UV photodetector applications. Materials Science in Semiconductor Processing. 2015;29:231-7.

[56] Wu Y, Yu Y. 2D material as anode for sodium ion batteries: Recent progress and perspectives. Energy Storage Materials. 2019;16:323-43.

[57] Li X, Wu J, Mao N, Zhang J, Lei Z, Liu Z, et al. A self-powered graphene–MoS_2 hybrid phototransistor with fast response rate and high on–off ratio. Carbon. 2015;92:126-32.

[58] Kumar A, Singh RK, Singh HK, Srivastava P, Singh R. Enhanced capacitance and stability of p-toluenesulfonate doped polypyrrole/carbon composite for electrode application in electrochemical capacitors. Journal of Power Sources. 2014;246:800-7.

[59] Kumar A, Singh HK, Singh RK, Singh R, Srivastava P. P-toluenesulfonate doped polypyrrole/carbon composite electrode and a process for the preparation thereof. United States patent US 10,074,453. 2018.

[60] Rambabu A, Singh DK, Pant R, Nanda KK, Krupanidhi SB. Self-powered, ultrasensitive, room

temperature humidity sensors using SnS$_2$ nanofilms. Scientific Reports. 2020;10(1):14611.

[61] Kumar S, Faraz M, Khare N. Enhanced thermoelectric properties of Sb$_2$Te$_3$-graphene nanocomposite. Materials Research Express. 2019;6(8):085079.

[62] Prakash N, Singh M, Kumar G, Barvat A, Anand K, Pal P, et al. Ultrasensitive self-powered large area planar GaN UV-photodetector using reduced graphene oxide electrodes. Applied Physics Letters. 2016;109(24):242102.

[63] Pant R, Singh DK, Chowdhury AM, Roul B, Nanda KK, Krupanidhi SB. Highly Responsive, Self-Powered *a*-GaN Based UV-A Photodetectors Driven by Unintentional Asymmetrical Electrodes. ACS Appl Electronic Materials. 2020;2(3):769-79.

[64] Aggarwal N, Krishna S, Sharma A, Goswami L, Kumar D, Husale S, et al. A Highly Responsive Self-Driven UV Photodetector Using GaN Nanoflowers. Advanced Electronic Materials. 2017;3(5):1700036.

[65] Chandan G, Mukundan S, Mohan L, Roul B, Krupanidhi SB. Trap modulated photoresponse of InGaN/Si isotype heterojunction at zero-bias. Journal of Applied Physics. 2015;118(2):024503.

[66] Sarkar K, Hossain M, Devi P, Rao KDM, Kumar P. Self-Powered and Broadband Photodetectors with GaN: Layered rGO Hybrid Heterojunction. Advanced Materials Interfaces. 2019;6(20):1900923.

[67] Gupta P, Rahman AA, Subramanian S, Gupta S, Thamizhavel A, Orlova T, et al. Layered transition metal dichalcogenides: promising near-lattice-matched substrates for GaN growth. Scientific Reports. 2016;6(1):23708.

Studying a LW-VCSEL-Based Resonant Cavity Enhanced Photodetector and Its Application in Microwave Photonics Circuits

Mikhail E. Belkin, Leonid I. Zhukov, Dmitriy A. Fofanov, Mikhail G. Vasil'ev and Alexander S. Sigov

Abstract

A detailed comparative experimental study was carried out to pursue advanced performances corresponding to the key parameters of two photodetectors based on vertical cavity surface emitting laser (VCSEL) operating in free-running or optically injection locked mode, as well as an inherent pin-photodetector. During the preliminary study, the key static and dynamic parameters were quantitatively determined and the optimal operating modes were derived for the both versions of VCSEL-based photodetectors as separate microwave-photonics circuit elements. Based on them, a final experiment was conducted to evaluate the processing quality, when one of the versions of VCSEL-based photodetectors or a inherent pin-photodetector is implemented as an optical-to-electrical converter for a typical microwave-photonics circuit that processes 120-Mbps 16-position quadrature amplitude modulated signal on the radio frequency carrier of 1–6 GHz. As a result, it was confirmed that better processing quality, i.e. Error Vector Magnitude value of less than 4%, could be obtained by using the free-running VCSEL-based photodetector version.

Keywords: resonant cavity enhanced photodetector, long-wavelength vertical cavity surface emitting laser, optically injection locking, microwave photonics, optoelectronic processing

1. Introduction

As well known, a pin-structured semiconductor photodetector (PD) is the most important active element of world-spread fiber-optics communication systems (FOCS) [1], where it performs the functions of an effective optical-electric converter (OEC) in the receiver unit located at the far end of a telecom link. Additionally, in the last decade, this device has found wide application in the intensively developing radio electronic systems (RES) for civil and military purposes based on microwave photonics (MWP) technology [2, 3]. In these systems, the MWP circuitry also contains two more requisite units that carry out electrical-optic conversion (EOC) and processing of radio-frequency (RF) signals in the optical domain [4]. Therein, the EOC operation is realized either by direct

modulation of a semiconductor laser's injection current or by external modulation of an optical modulator pumped by a laser source power. After optical processing such as transmission, amplifying, filtering, time delay, etc., an OEC operation must be performed, for the implementation of which a pin-photodetector is used. Thus, unlike traditional FOCSs, both a laser and a photodetector must be present in a common MWP circuit, which paves the way for its simplifying and, therefore, reducing the cost of the device by combining EOC and OEC functions.

The study of the structures and constructions of modern photodiode and widespread edge emitting laser showed that the former cannot operate in the lasing mode, since there is no amplification layer and optical resonators that provide positive feedback. In addition, the latter is not suitable for operation in a photo-detector mode, in principle, since it has a completely different design and even a very small reverse biasing leads to its failure. However, there is a semiconductor laser of a different design: a vertical cavity surface-emitting laser (VCSEL) with an epitaxial structure similar to a photodetector [5, 6], and its long-wavelength version (LW-VCSEL) has a great potential for the application in modern and prospective FOCSs [7] as well as in MWP circuits [8].

In general, a resonant cavity enhanced (RCE) PD based on a pin-photodiode or a Schottky-barrier photodiode is a long-time known optoelectronic device that overcomes the fundamental drawback of an inherent photodetector associated with a compromise between bandwidth and sensitivity [9, 10]. Its design with an active depletion region between two multilayer mirrors of a Fabry-Perot resonator is similar to a VCSEL. Modern development follows the path of researching and fabricating both individual RCE-PD chips in the short-wavelength or long-wavelength telecom spectral range [11, 12], as well as monolithically integrated chips containing on one substrate an optoelectronic pair based on a VCSEL and a RCE-PD [13]. So that, during a literature search, a publication was found [14] reporting the results of an experimental study of RCE photodiode based on a short-wavelength VCSEL with a quantum-well active region operating in the photovoltaic mode or in reverse bias mode. This technological study was carried out in order to determine the conditions for ensuring the maximum quantum efficiency of the OEC, which was regulated by sequentially etching the layers of the upper mirror, as well as the conditions for ensuring the maximum width of the frequency characteristic at the output. The latter was controlled by adjusting the diameter of the active layer.

The motivation for our recent investigation in this direction [15] was to measure the static and dynamic characteristics of the particular LW-VCSEL sample without any structural changes. For this goal, we simply reversed the DC bias polarity to assess the efficiency of its use as part of an optoelectronic coupler based on two identical LW-VCSEL chips, one of which worked as a laser source, and the other as a photodetector. An additional goal was to demonstrate the effective operation of a LW-VCSEL-based RCE photodetector (VCSEL-PD) in an economical photore-ceiver for the currently widespread digital FOCS with dense wavelength division multiplexing (DWDM), due to the absence of a spectral demultiplexer needed for a standard DWDM FOCS. Leveraging this concept, two other applications combining LW-VCSEL in the laser and photodetector modes have recently been investigated including the uses in a high-speed optoelectronic switch device for integrated photonics-based optical beamforming network [16] and in cost-efficient optoelectronic frequency-converting transceiver for a base station of 5G cellular communication network [17].

To date, there is one more version of LW-VCSEL-based photodetector [18, 19], where a new concept using such an effective laser technique, especially for low-power VCSEL, as optical injection locking (OIL) [20, 21], was proposed and preliminary investigated. From the operational point of view, an obvious advantage

of this approach compared to our one is the possibility of full-duplex operation in a combined EOC/OEC without switching the polarity of the power supply. In the cited papers, an integrated consideration is used that addresses the effect of expanding the bandwidth of an OIL VCSEL-based photodetector (OIL-VCSEL-PD) and experimental study of the signal quality (bit error rate) in a FOCS, when digital signals at a speed of 12 Gbps are transmitted. However, the key parameters of the OIL-VCSEL-PD itself, such as responsivity, the level of introduced noise, etc., have not been studied at all.

As a result, in present scientific publications there is no clear answer to the question of selecting the optimal photodetector for the application in micro-wave- photonics circuits. Eliminating it, this Chapter addresses a comparative experimental study reviewing the known, updated, and newer results to pursue advanced performances corresponding to the key OEC parameters of an inherent pin-photodetector as well as the two VCSEL-based photodetectors in free-running or OIL mode and their applications in the last generation of key MWP circuits for prospective photonics and radio-electronics systems. In particular, pursuing the goal to discovery optimal operation regimes for the VCSEL-based RCE photodetector, Section 2 reviews key features of the C-band (1530–1565 nm) free-running LW-VCSEL as the object for investigation. In addition, Section 3 presents the updated and newer results of measuring static and dynamic characteristics for the LW-VCSEL-based RCE photodetector under study in the above-mentioned operating modes. The results of design and comparative experimental research using a typical MWP circuit that includes OEC based on an inherent pin-photodetector or two versions of VCSEL-based RCE photodetectors under study are demonstrated in Section 4. Finally, Section 5 concludes the Chapter.

2. The object for investigation

For today, several technologies yielding LW-VCSEL with acceptable perfor-mances have been developed. Among them, wafer-fused LW-VCSELs under research (**Figure 1**) employing strained InP/InAlGaAs quantum well (QWs) active region, tunnel junction (TJ) for carrier and optical confinement, and distributed Bragg reflectors (DBR), have also reached the industrial production stage and proven reliability [8]. A particular preference of these LW-VCSELs is in covering the full ITU-T spectral range from O-band to U-band. Concerning MWP approach, an outstanding feature of LW-VCSELs is their compatibility with future large-scale silicon-based heterogeneous photonics integrated circuits [22], which should
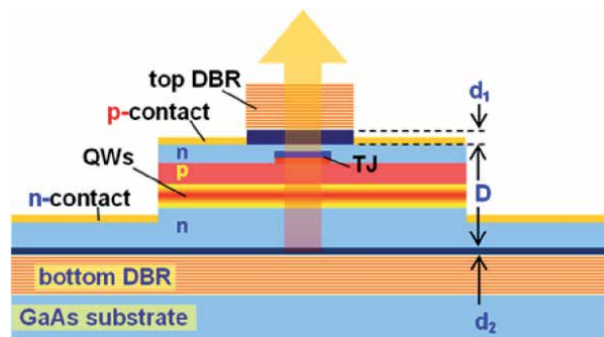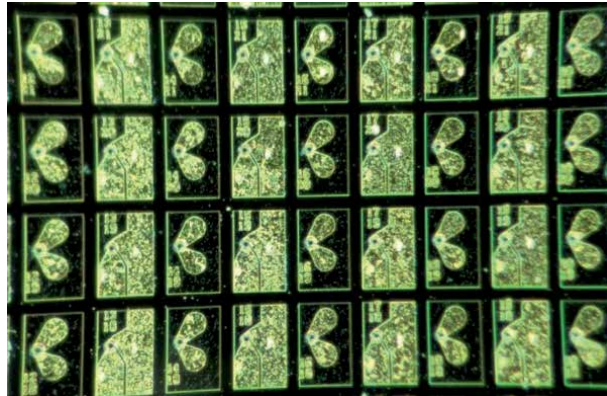

Figure 1.
Schematic of wafer-fused LW-VCSEL from beam express LLC, Switzerland.

provide many advantages when implementing MWP devices and techniques. The processing of the double-fused VCSEL wafer includes reactive ion etching in top DBR, selective chemical etching in the InAlGaAs/InP active cavity region, dielectric deposition, dry etching, and e-beam deposition of metals for contacts [8]. The much smaller size of the active region (D) in comparison with the edge emitting laser requires several times higher reflection coefficients of the upper and lower mirrors to generate lasing conditions, which is provided due to high-Q DBRs based on 30 or more intermittent layers of GaAs/AlGaAs. These mirrors are fused to top and bottom parts of an each active region before dicing [23].

Figure 2 shows a microscope view of a tiny piece of a laser wafer with formed electrical pads. As seen, the processed VCSEL wafer offers on-wafer testing possibility that decreases manufacturing cost as compared to edge emitting lasers. Moreover, a pattern of the full wafer-electroplated anode and cathode pads is designed in such a way to ensure the correct testing using a standard microwave probe of GS-type.

All further measurements will carry out on the Probe Station (PS) EP6 from Cascade Microtech. The workbench including thermo-electrical cooler for temperature controlling, coplanar RF probe (on the left), and fiber-optics probe (on the right) is shown in **Figure 3**.

Figure 2.
A microscope view of the VCSEL wafer under study.

Figure 3.
The workbench for VCSEL chip's study.

Below we, using widespread techniques and procedures, will present typical static and needed for MWP characterization dynamic characteristics of the LW-VCSEL under test in free-running mode of its operation [8, 23] that will use further for examination of the same device in RCE photodetector modes. The testbed (see **Figure 4**) operates in three ranges: direct current (DC), RF, and C-band (1530–1565 nm) optical ones. Besides the VCSEL under test, it contains a set of accessories such as optical coupler (Opneti, CP10/90–1550), reference photodiode (Finisar, BPDV2150, 43-GHz bandwidth, 0.6-A/W responsivity), bias-T (Pasternack, PE1BT-1002, 40-GHz bandwidth) as well as corresponding DC power suppliers and measuring tools including optical spectrum analyzer (Yenista OSA20), optical power meter (EXFO PM-1100), RF vector network analyzer (Agilent E8363B).

Figure 5(a) depicts a PS-assisted light-current characteristic (LCC) of the LW-VCSEL under test emitting in the fundamental wavelength of 1560.95 nm at the room temperature. For the device under test, the threshold current is near 2.3 mA and a quasi-linear dependence of coupled optical power vs. current was observed up to 9 mA. To estimate the losses introduced by the optical probe, **Figure 5(b)** shows typical LCCs and a voltage–current characteristic of a C-band LW-VCSEL chip when registering its complete output power [8].
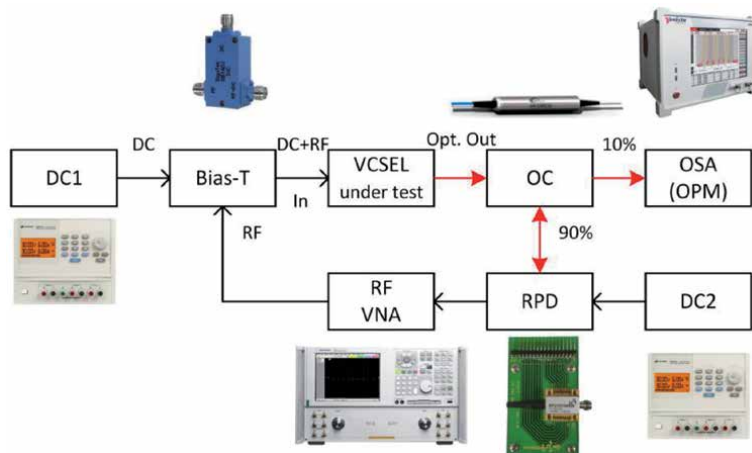
Figure 4.
Common testbed for measuring static and dynamic characteristics of the object for investigation, where OC, RPD, OSA, OPM, and RF VNA stand for optical coupler, reference photodiode, optical spectrum analyzer, optical power meter, and RF vector network analyzer, respectively. (optical connections are painted in red, electrical connections – in black).
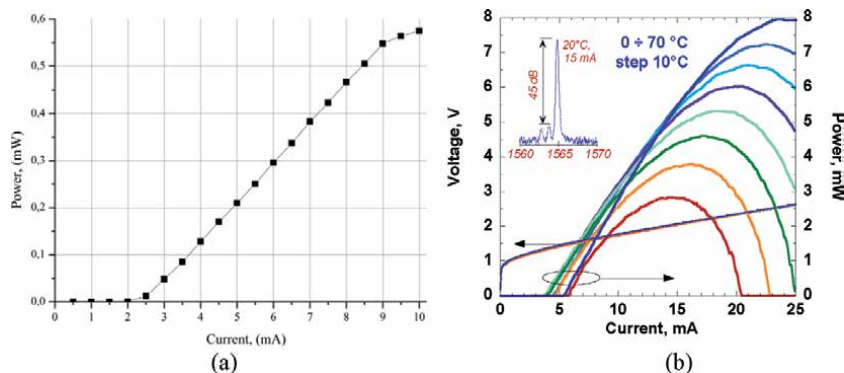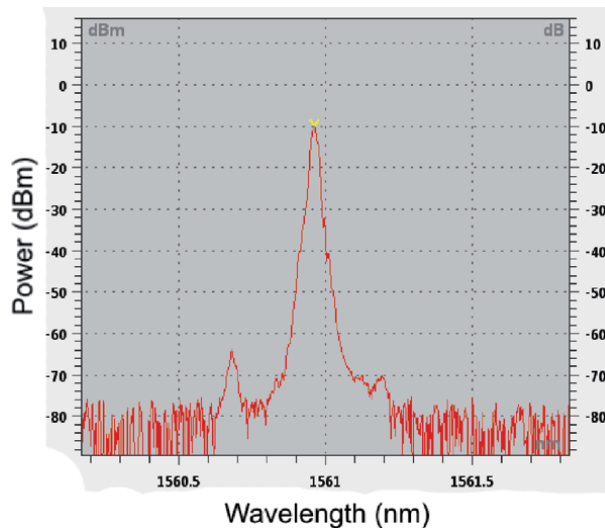

Figure 5.
Light-current characteristics of the VCSEL chip under study: (a) Probe station-assisted; (b) Registering its complete output power [8].

Figure 6 shows an example of a PS-assisted spectral characteristic of the LW-VCSEL under test at the current of 6 mA, where a fundamental mode with the coupled power of −10 dBm at the wavelength of 1560.95 nm and a side-mode suppression ratio of 52 dB are observed.

In addition, **Figure 7** presents the spectral evolution of VCSEL emission with currents and temperature.

Figure 8 presents the small-signal transmission gain (TG) of an optoelectronic pair comprising the LW-VCSEL under test and RPD (see **Figure 4**). As one can see, at lower modulation frequencies the TG value is −30 dB and the -3 dB bandwidth of the LW-VCSEL under test is 3.7 GHz at 3-mA and more than 9 GHz at 10-mA bias current.

For the sake of completeness, we will end this section with a couple of examples characterizing the VCSEL under study in an optically injection locked mode.

Figure 6.
Example of a spectral characteristic of the LW-VCSEL under test.
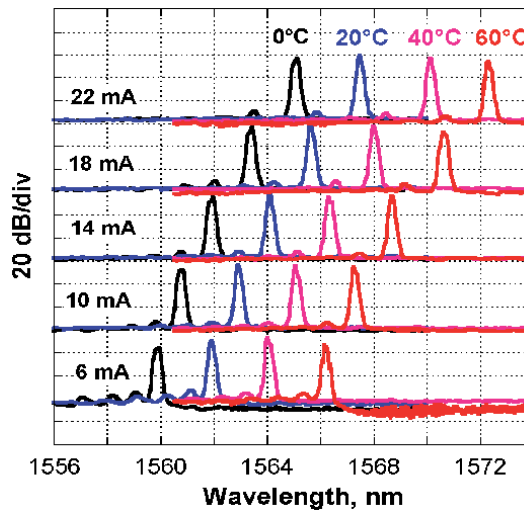
Figure 7.
Spectral evolution of the tested VCSEL emission with current and temperature.
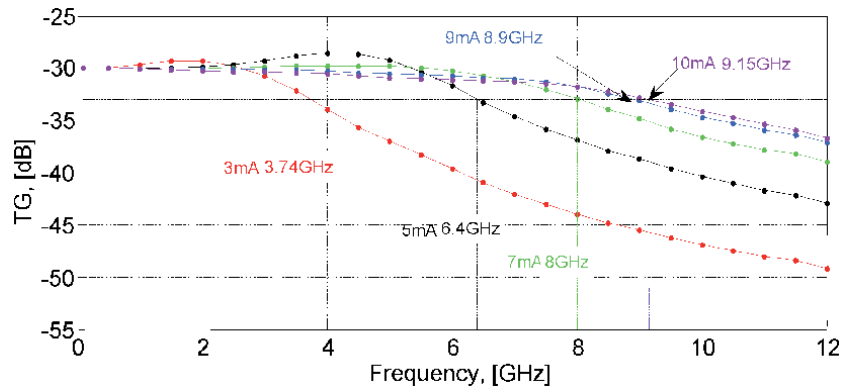
Figure 8.
Small-signal transmission gain characteristics of the wafer-fused LW-VCSEL under test.

The measurements will be made using the testbed of **Figure 4** by replacing the block "VCSEL under test" with the block-diagram shown in **Figure 9**.

Figures **10** and **11** exemplify an optical spectrum and small-signal modulation characteristics of tested VCSEL in OIL mode.

The following outcomes for the further study can be drawn from this section.

- Comparison of LCC (**Figure 5(a)**) with the previously obtained measurement results for a similar characteristic of a VCSEL chip when registering a complete output power (see **Figure 5(b)**) allows us to assess the probe-assisted coupled factor at a level of 19% (losses of about 7.2 dB), which will be taken into account in further estimates.

- As follows from a comparison of the spectral characteristics for VCSEL in free-running (**Figure 6**) and OIL (**Figure 10**) modes, the effect of optical injection locking leads to a more than 10-dB increase in emitted power and to a pure single-frequency spectrum with almost 10-dB gain in side-mode suppression ratio.

- As it can be observed from **Figure 7**, combinations of temperature and driving current allow tuning the emission wavelength inside 12 nm with the separate current tuning of near 0.25 nm/mA and temperature tuning of near 0.1 nm/°C.

- As follows from a comparison of the small-signal modulation characteristics for VCSEL in free-running mode (**Figure 8**) at current of 8 mA and in OIL mode (**Figure 11**), effect of optical injection locking leads to more than 4-fold modulation bandwidth.
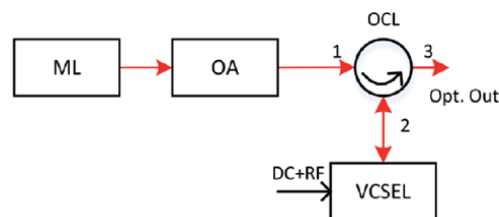
Figure 9.
Conceptual block-diagram of OIL-VCSEL, where ML, OA, and OCL stand for master laser, optical amplifier, and optical circulator, respectively. (optical connections are painted in red, electrical connections – in black).
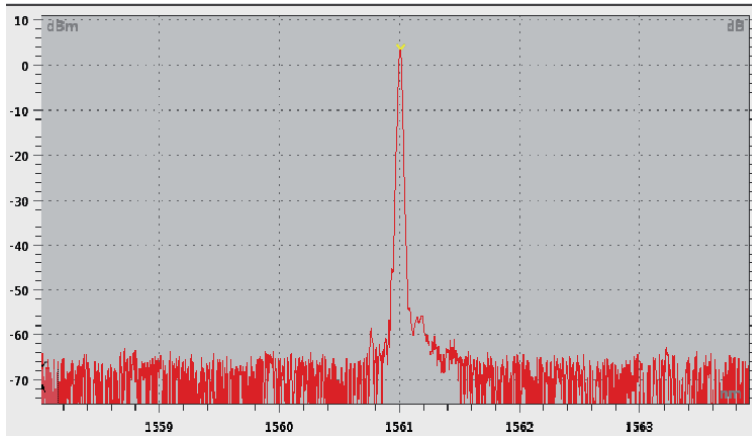
Figure 10.
*Optical spectrum of the OIL-VCSEL under test.*
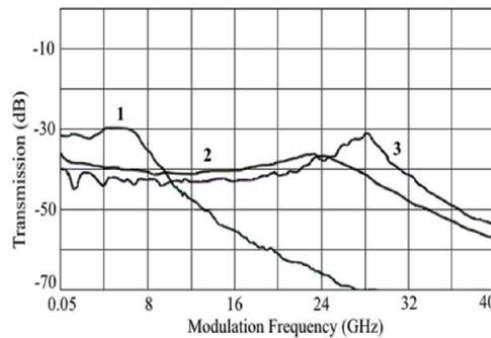
Figure 11.
Small-signal modulation characteristics of OIL-VCSEL under test in free-running mode (1), and in OIL mode when the power of the ML is 5 dBm (2) or 8 dBm (3).

3. VCSEL-based photodetector (VCSEL-PD)

Following the detailed analysis of the object for investigation carried out in Section 2, in this section we will conduct a comparative study of the typical characteristics of an inherent pin-photodetector and a photodetector based on a LW-VCSEL in two modes of its operation: in free-running mode and in OIL mode.

3.1 Reverse-biased free-running mode

Figure 12 depicts a common testbed for measuring static and dynamic characteristics of the VCSEL-PD using typical in photodetector's characterizing techniques and procedures [1, 3]. The testbed, besides the VCSEL-PD under test, contains a set of accessories such as optical circulator (Opneti, CIR-3-1550), master laser (PurePhotonics PPCL300, 1530–1565-nm wavelength range, 6–13.5-dBm power range), optical amplifier (Ericsson PGE 60830, 1540–1560-wavelength range, up to 20-dB gain, 13-dBm maximum output power), optical modulator (ThorLabs LN05S-FG, 1525–1605-nm wavelength range, 5-dB insertion loss, 35-GHz bandwidth), bias-T (Pasternack, PE1BT-1002, 40-GHz bandwidth) as well as corresponding DC power suppliers, digital multi-meter (INSTEK GDM-8245), and measuring tools including the same apparatuses as in **Figure 4**.
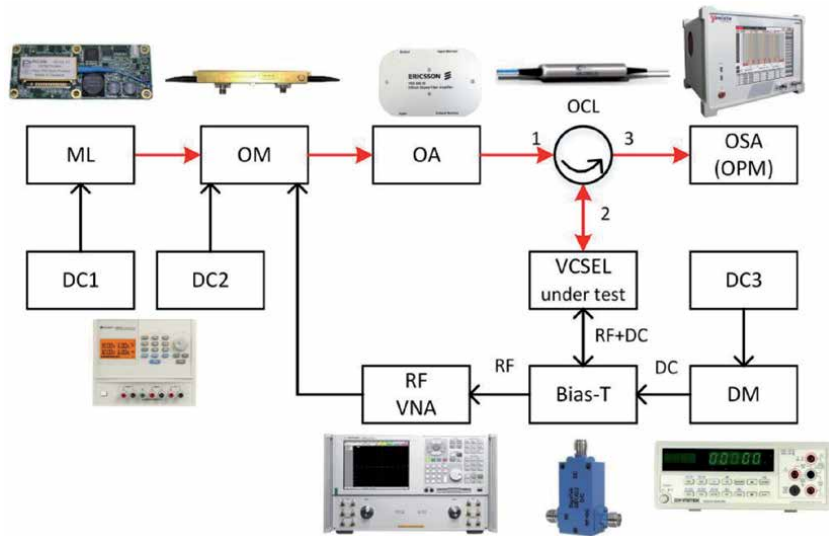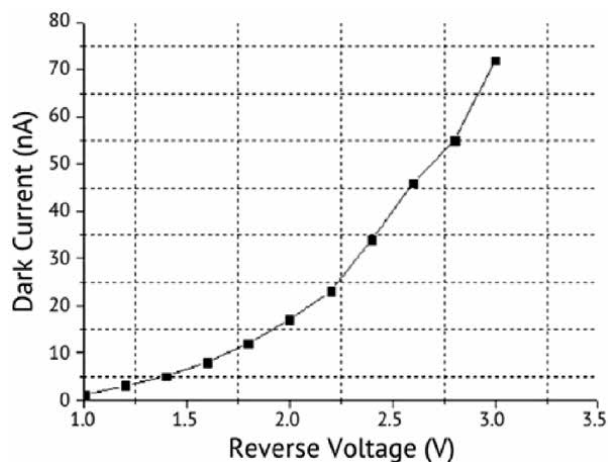
Figure 12.
Common testbed for measuring static and dynamic characteristics of the VCSEL-PD under test, where ML, OM, OA, OCL, DC, DM, OSA, OPM, and RF VNA stand for master laser, optical modulator, optical amplifier, optical circulator, DC source, digital multi-meter, optical spectrum analyzer, optical power meter, and RF vector network analyzer, respectively. (optical connections are painted in red, electrical connections – in black).

Figures below demonstrate the results of measuring the key static and dynamic characteristics of the free-running VCSEL-PD using reverse DC bias from DC3. First, **Figure 13** presents dark current vs. reverse voltage characteristic. For the device under test, dark current value is not more than 70 nA at a reverse voltage up to 3 V.

Figure 14 presents the effect of reverse bias voltage on photocurrent of the VCSEL-PD under test at the 1560.95-nm incident optical powers of 1, 2, and 3 mW.
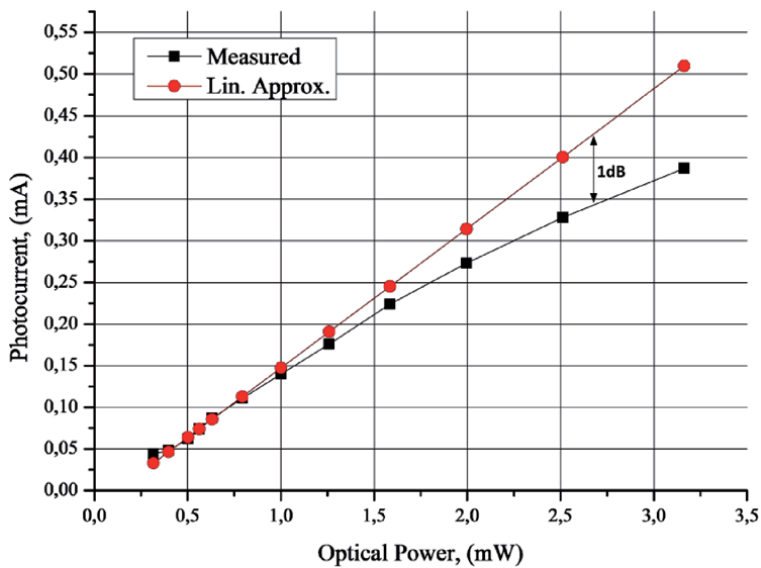
Figure 15 characterizes photocurrent vs. incident optical power of 1560.95-nm wavelength for the VCSEL-PD under test at reverse voltage of 1 V. As one can see from the Figure, the current responsivity at the initial segment of the characteristic is about 0.2 A/W, and the threshold of its linearity at a level of −1 dB is approximately 2.6 mW.

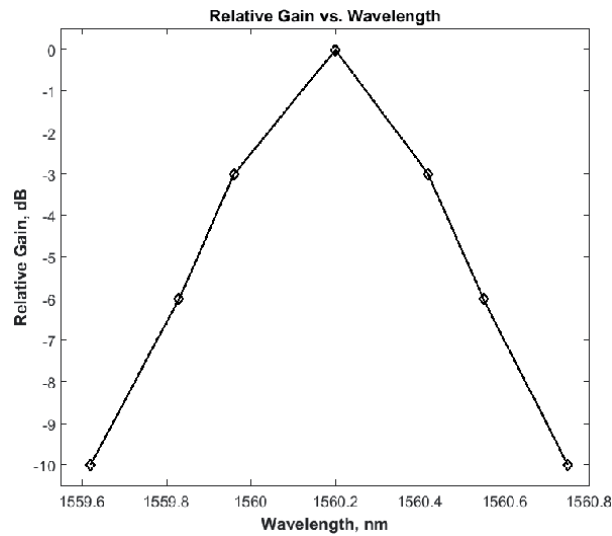**Figure 13.**
Dark current vs. reverse voltage characteristic.
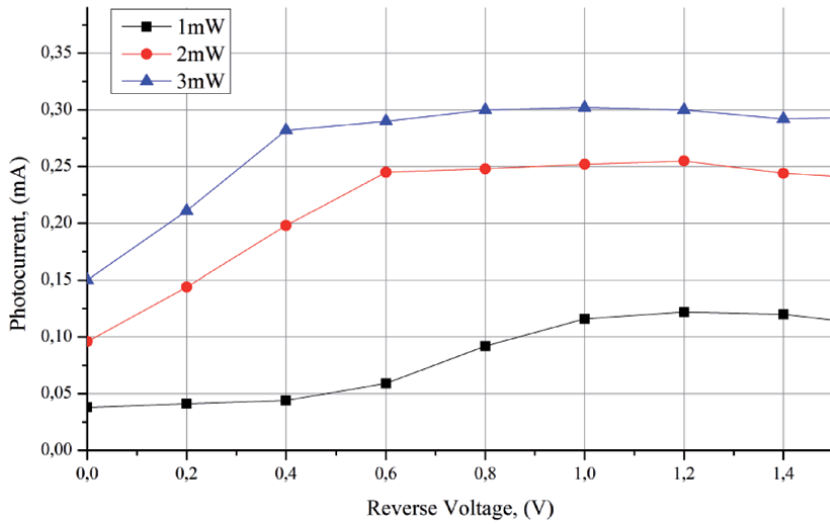
Figure 14.
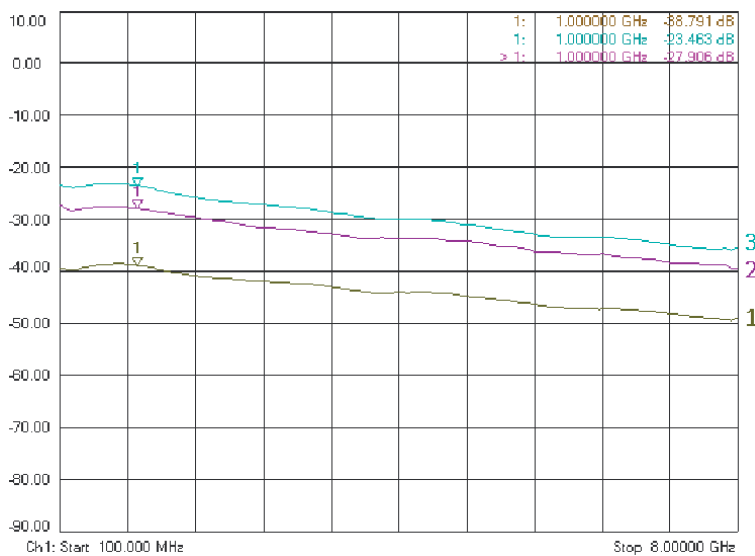*Photocurrent vs. reverse voltage and incident optical powers for the free-running VCSEL-PD under test.*

Figure 15.
Photocurrent vs. incident optical power of the VCSEL-PD under test.

Figure 16 demonstrates a fine optical spectral characteristic for the VCSEL-PD under test at reverse voltage of 1 V. As one can see, due to the built-in optical cavity, the characteristic has clear resonance properties with a full bandwidth at half level of about 70 GHz.

Finally, **Figure 17** demonstrates small-signal frequency characteristic of the free-running VCSEL-PD under test at the modulating RF power of −5 dBm and the reverse voltage of 1 V. As one can see from the Figure, the total gain for EOC + OEC at the modulating frequency of 1 GHz is −38 dB at the optical power of 1 mW (brown curve 1), −28 dB at the power of 2 mW (pink curve 2), and − 23.5 dB at the power of 3 mW (blue curve 3). Moreover, for all the powers, −3-dB bandwidth is near 3.5 GHz and − 5-dB bandwidth is near 5 GHz.

Figure 16.
Resonance features of the VCSEL-PD under test.

Figure 17.
Small-signal RF characteristic of the free-running VCSEL-PD under test.

The following outcomes can be drawn from this sub-section.

- The results of measuring the dark current (**Figure 13**) showed their comparability with the specifications of the inherent pin-photodetector of model BPDV2150 (5–200 nA) used in the further study.

- The study of the photocurrent vs. reverse voltage and optical powers (**Figure 14**) made it possible to determine their significant influence. In this case, the photocurrent value increases with the optical power, which corresponds to theory and practice for inherent InP-based pin-photodiodes [24]. Also, the minimum value of an operating reverse voltage is 1 V, which was taken into account in the course of further research.

- The results of measuring the dependence of the photocurrent on the incident power (**Figure 15**) showed that the current responsivity of the VCSEL-PD under test is approximately 3 times less than that of existing pin-photodetectors operating in the microwave band. However, the VCSEL-PD has a comparable level of linearity.

- An important distinction of the VCSEL-PD is the resonance properties (**Figure 16**) arising from the presence of a built-in optical cavity, which must be taken into account in further measurements.

- Measurement of the low-signal frequency response of the VCSEL-PD under study (**Figure 17**) confirms the effect of incident optical power on RF gain as predicted in **Figure 14**, which corresponds to inherent InP pin-photodiodes [24].

3.2 Forward-biased optically injection locked mode

In this sub-section, based on the results of the Section 2 associated with the improving single-frequency regime and broadening the modulation bandwidth under OIL, as well as on the work of other authors [18–21], we will investigate the static and dynamic characteristics of the OIL-VCSEL-PD as a separate device. The measurements will be carry out using the testbed of **Figure 12** by replacing the block "VCSEL-PD under test" with the block-diagram shown in **Figure 9**.

Figure 18 addresses a photocurrent offset of the OIL-VCSEL-PD under test vs. incident OIL power at the free-running injection currents of 4, 5, and 6 mA, which according to voltage–current characteristic of **Figure 5(b)** corresponds to the forward DC voltages of 1.35, 1.5, and 1.67 V, respectively. As one can see from the Figure, the values of photocurrent offset depend on both the DC bias voltage that is in analogy with VCSEL-PD (see **Figure 14**) as well as on the incident optical power. In the result, the average photocurrent responsivity is varied from 0.03 A/W at +1.67 V to 0.04 A/W at +1.5 V.
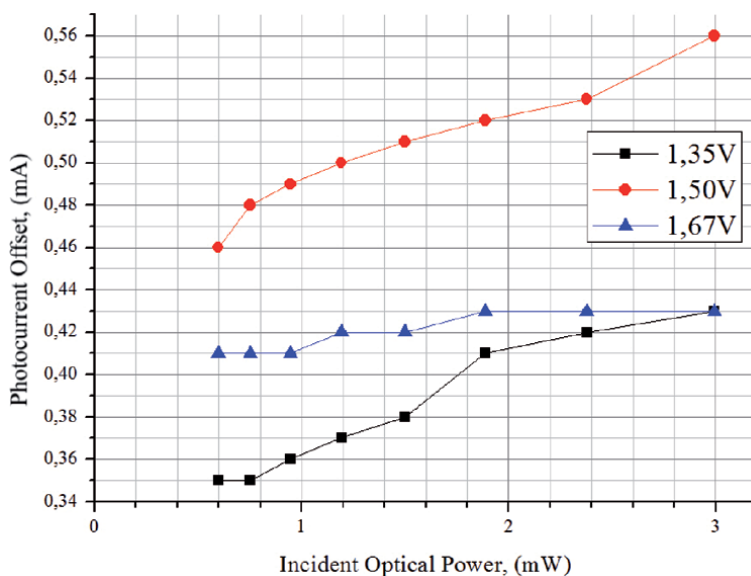
Figure 18.
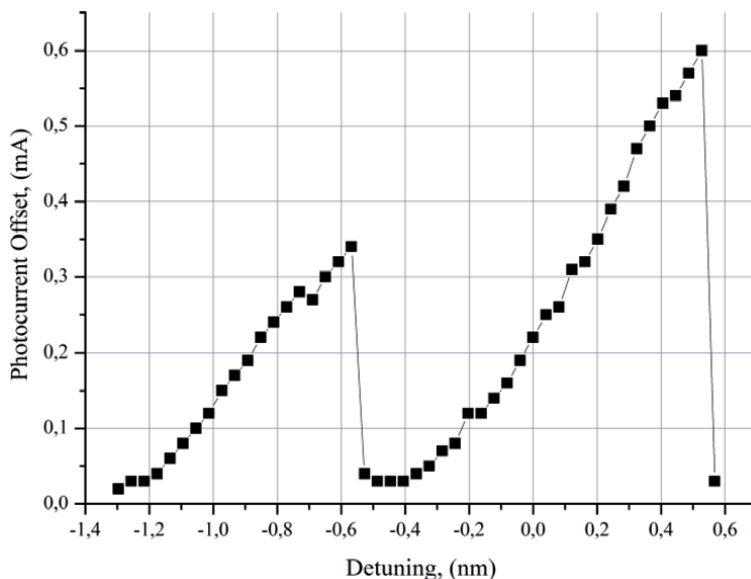*Photocurrent offset of the OIL-VCSEL-PD under test vs. incident OIL power.*

Figure 19 presents photocurrent offset of the OIL-VCSEL-PD under test vs. detuning between the wavelengths of VCSEL-PD in OIL mode and VCSEL in free-running mode (see **Figures 6** and **10**) at incident OIL power of 2 mW and forward bias voltage of 1.5 V. A sharp drop at the detuning near +0.55 nm means that the synchronization is lost. On the other hand, a sharp peak at the offset near −0.55 nm means a hop of locking from VCSEL's fundamental mode to the side mode (see **Figure 6**).

Finally, **Figure 20** presents small-signal frequency characteristic of the OIL-VCSEL-PD under test (brown curve 1) at the incident OIL power of 2 mW and detuning of +0.3 nm. Here, for comparison, a similar characteristic for an inherent pin-photodetector is shown (blue curve 2), as well as the response in the absence of an OIL signal (green curve 3).

The following outcomes can be drawn from this sub-section.

• Studying the current responsivity of the OIL-VCSEL-PD vs. the forward DC bias voltage (**Figure 18**) showed that it reaches a maximum of 0.04 A/W at a voltage of 1.5 V, which is 5 times lower compared to the free-running VCSEL-PD (see **Figure 15**).

• Studying the current responsivity of the OIL-VCSEL-PD vs. the detuning between the wavelengths of VCSEL-PD in OIL mode and VCSEL in free-running mode (**Figure 19**) showed that the locking range inside the fundamental mode is near 1.1 nm and the average slope of current responsivity is 0.7 mA/nm, which must be taken into account in further studies.

• Studying the small-signal frequency characteristic of the OIL-VCSEL-PD (**Figure 20**) showed that locking emission of the master laser leads to an approximately 30 dB increase in the gain, but its bandwidth is significantly lower compared to the similar characteristic of **Figure 11**. The reason for this effect is the high loss (7.2 dB) in the optical probe (see Section 2), which must be taken into account in the course of further studies.

Figure 19.
*Photocurrent offset of the OIL-VCSEL-PD under test vs. detuning.*
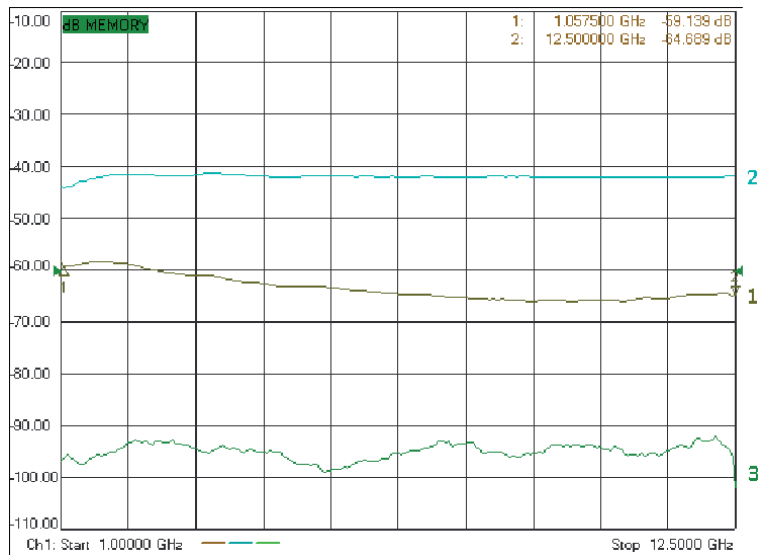
Figure 20.
Small-signal frequency characteristic of the OIL-VCSEL-PD under test.

4. Comparative experimental research using a typical MWP circuit

The previous section was referred to a comparative analysis of the VCSEL-based photodetector properties as a separate device in two modes of its operation, such as free running and optically injection locking. Continuing and expanding the study, in this section, it is considered as an element of a typical MWP circuit including, as described in the Introduction, three cascaded parts: EOC, optical processing unit (OPU), and OEC. Moreover, in this case, for completeness of coverage, three research objects are considered: a pin-photodiode, free-running VCSEL-PD, and OIL-VCSEL-PD. The general testbed for conducting experimental research is presented in **Figure 21**.

In the Figure, the EOC unit contains the tunable semiconductor laser (PurePhotonics PPCL300, 1535–1565-nm wavelength range, 6–13.5-dBm power
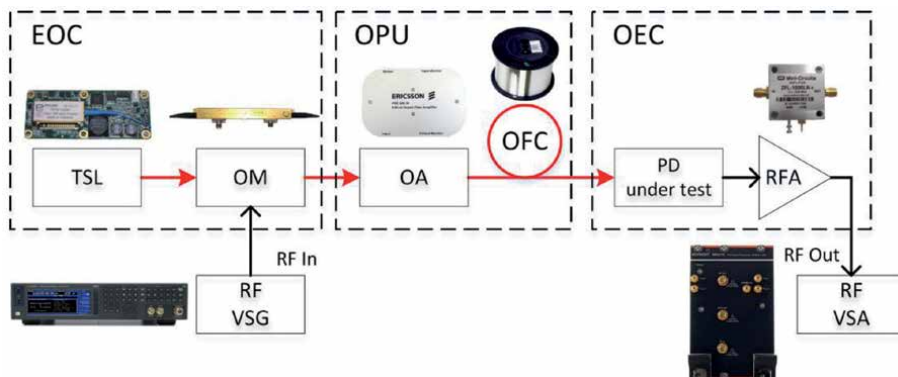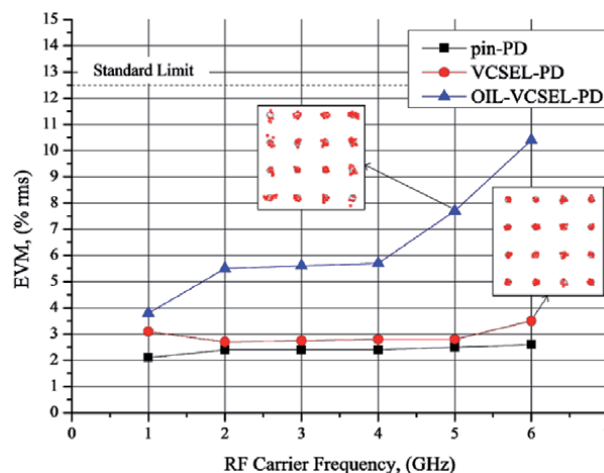

Figure 21.
General testbed for conducting experimental research, where TSL, OM, OA, OFC, PD, RFA, RF VSG and RF VSA stand for tunable semiconductor laser, optical modulator, optical amplifier, optical fiber coil, photodetector, RF amplifier, RF vector signal generator, and RF vector signal analyzer, respectively. (optical connections are painted in red, electrical connections – in black).

range) and the optical modulator (ThorLabs LN05S-FG, 1525–1605-nm wavelength range, 5-dB insertion loss, 35-GHz bandwidth). In addition, the OPU consists of optical amplifier (Ericsson PGE 60830, 1540–1560-wavelength range, up to 20-dB gain, 13-dBm maximum output power) and optical fiber coil (SMF-28+, 5 km). Finally, OEC unit includes PD under test (Finisar, BPDV2150, 43-GHz bandwidth, 0.6-A/W responsivity, or VCSEL-PD, or OIL-VCSEL-PD) and home-made RF amplifier (1–6-GHz operation range, 30-dB gain, 2.2-dB noise figure). Note that in all experiments, the same EOC is used with a TSL different in emitted power and wavelength, respectively. Besides, in connection with the above-mentioned structural features of the photodetectors under test, for the pin-PD a direct connection to the circuit was used, as in **Figure 21**, while VCSEL-based devices were connected to the circuit through an optical circulator (see **Figure 12**).

To provide a practical focus, in the way of the experiments such an important quality indicator for a FOCS and wireless RES as an error vector magnitude (EVM), which in the first approximation is inversely proportional to the square root of the signal-to-noise ratio [25], is evaluated. To implement this measurement, using the VSG (Keysight N8152B), a digital signal at a bitrate of 120 Mbps with 16-position quadrature amplitude modulation (16-QAM) on a RF carrier in the 1–6 GHz band, is applied to the RF input of the OM and the output signal of the RFA is recorded using the VSA (Keysight M9421A).

Figure 22 presents the results of the comparative experiments using the optimal operating regimes that conclude from the Section 3. In the same graph, the horizontal dashed line marks the standard limit for transmitting 16-QAM signals in the emerging 5th generation cellular telecommunications network [26]. For the best vision, there are two insets in the Figure showing constellation diagrams in specific points.

The following outcomes can be drawn from this Figure.

- When using any of three variants of the photodetector under study, the EVM levels, which determines the quality of signal processing in the MWP circuit, turned out to be significantly lower than the threshold value.

- The smallest values of this parameter, i.e. the best processing quality, and independence from the frequency of the RF carrier are obtained when using pin-photodiode, which is determined by its above mentioned bandwidth up to 43 GHz.

Figure 22.
Study of signal quality for a typical microwave-photonics circuit when processing high-speed data with multi-position quadrature amplitude modulation.

- Slightly large values of the EVM are observed, when using a free-running VCSEL-based photodetector. The increase in the EVM at the upper RF carrier frequency noted in the graph is most likely due to its limited bandwidth (see **Figure 17**).

- The largest values of the EVM that increase with the RF carrier are obtained when using an OIL-VCSEL-PD, which is associated with its poorest photo-current responsivity, increased noise due to operating in the laser mode and limited bandwidth (see **Figure 20**) due to the above-mentioned losses in the optical probe.

5. Conclusion

In this Chapter, a detailed comparative experimental study was carry out to pursue advanced performances corresponding to the key parameters of two VCSEL-based photodetectors operating in free-running or optically injection locked mode as well as an inherent pin-photodetector. During the preliminary study, the key static and dynamic parameters were quantitatively determined and the optimal operating modes were derived for both versions of VCSEL-based photodetector as a separate microwave-photonics circuit element. Based on them, a final study was carried out to evaluate the processing quality when the both versions of VCSEL-based photodetectors or an inherent pin-photodetector work as an optical-to-electrical converter of a typical microwave circuit, which can become the core when developing a cost- and power-efficient base station for a mobile cellular telecommunication system of fifth generation [27], as well as for an advanced Wi-Fi system [28] of fiber-wireless architecture, which will significantly increase its service area. As a result, it was confirmed that better processing quality can be obtained by using the free-running VCSEL-based photodetector version.

Further research will focus at a detailed comparative studying the features of the VCSEL-based photodetectors, at expanding their bandwidth to the millimeter wavelength range, as well as at the development of optimal microwave-photonics circuits using one of these devices as an optical-to-electrical converter.

Acknowledgements

Conflict of interest

The authors declare the lack of the 'conflict of interest'.

Author details

Mikhail E. Belkin[1*], Leonid I. Zhukov[1], Dmitriy A. Fofanov[1], Mikhail G. Vasil'ev[2]
and Alexander S. Sigov[1]

1 MIREA - Russian Technological University, Moscow, Russian Federation

2 Kurnakov Institute of General and Inorganic Chemistry, Russian Academy of
Sciences, Moscow, Russian Federation

*Address all correspondence to: belkin@mirea.ru

IntechOpen

References

[1] Gower J. Optical Communication Systems. Second Edition. Prentice Hall, 1993, 696 pp.

[2] Urick, V. J., McKinney, J. D., Williams, K. J. (2015) Fundamentals of Microwave Photonics, Hoboken, New Jersey.

[3] Belkin M. E. "Multiscale Computer Aided Design of Microwave-Band P-I-N Photodetectors," In book "Photodetectors" Ed. By S. Gateva – InTech Open, Chapter 6, pp. 231-250, 2012. https://www.intechopen.com/ books/photodetectors/multiscale-computer-aided-design-of-microwave-band-p-i-n-photodetectors

[4] M.E. Belkin, V. Golovin, Y. Tyschuk, M. Vasil'ev, and A.S. Sigov, "Computer-Aided Design of Microwave-Photonics-based RF Circuits and Systems," In book "RF Systems, Circuits and Components" Ed. by M. Reaz and M. Bhuiyan – InTech Open, Chapter 4, pp. 61-81, 2018. https://www.intechopen.com/books/ rf-systems-circuits-and-components/ computer-aided-design-of-microwave-photonics-based-rf-circuits-and-systems

[5] VCSELs: Fundamentals, Technology and Applications of Vertical-Cavity Surface-Emitting Lasers. Ed. R. Michalzik. Springer Series in Optical Sciences 166; 2013. ISBN 978-3-642-24986-0

[6] Koyama A. F. Recent advances of VCSEL photonics. IEEE Journal of Lightwave Technology 2006. 24(12) 4502-4513

[7] Kapon E., Sirbu A. Long-wavelength VCSELs: Power-efficient answer. Nature Photonics 2009; 3, 27-29 doi:10.1038/ nphoton.2008.266.

[8] Belkin M.E., Belkin L., Loparev A., Sigov A.S., Iakovlev V. Long Wavelength VCSELs and VCSEL-Based Processing of Microwave Signals // In book "Optoelectronics – Advanced Materials and Devices", Ed. by S. Pyshkin and J. Ballato, – InTechOpen, Croatia, 2015, Chapter 6, pp. 231-250. https:// www.intechopen.com/books/ optoelectronics-materials-and-devices/ long-wavelength-vcsels-and-vcsel-based-processing-of-microwave-signals

[9] K. Kishino, M. Unlu, J. Chyi, L. Arsenault, and H. Morkoc, "Resonant-cavity enhanced (RCE) photodetectors," IEEE Journal on Quantum Electronics, vol. 27, pp. 2025-2034, 1991.

[10] X. Duan, Y. Huang, X. Ren, et al., "Long Wavelength Multiple Resonant Cavities RCE Photodetectors on GaAs Substrates," IEEE Transactions on Electron Devices, Vol. 58, No. 11, p. 3948-3953, Nov. 2011.

[11] J. Guo, Y. Zuo, Y. Zhang, et al., "Simulation Research of Nonlinear Behavior Induced by the Charge-Carrier Effect in Resonant-Cavity-Enhanced Photodetectors," IEEE Journal of Lightwave Technology, vol. 25, No 9, p. 2783-2790, Sept. 2007.

[12] M. Casalino, L. Sirleto, L. Moretti, et al., "Fabrication and Characterization of Resonant Cavity Enhanced Silicon Photodetectors at 1.55 μm," 5th International Conference of Group IV Photonics, 2008, p. 1-3.

[13] Qi Wei, Kai Liu, Yo. Huang, et al., "A pair of integrated optoelectronic chips for optical interconnects," Asia Communications and Photonics Conference (ACP), 2018, 2 pp.

[14] T. Knodl, et al., "RCE Photodetectors based on VCSEL Structures," IEEE Photonics Technology Letters, vol. 11, no. 10, p. 1289-1291, 1999.

[15] Belkin M. E. Investigation of the static and dynamic characteristics for a wafer-fused C-band VCSEL in the mode of the optical-electric converter, Technical Physics Letters, 2018, Vol. 44, No. 1, pp. 32-35. DOI: 10.1134/S1063785018010030 © Pleiades Publishing, Ltd., 2018. ISSN 1063-7850

[16] M. E. Belkin, V. Golovin, Y. Tyschuk, and A.S. Sigov. Model of an active optoelectronic switchable element for integrated photonics-based optical beamforming network. 2017 Progress In Electromagnetics Research Symposium - Spring (PIERS), 2017, pp. 1592-1593. https://ieeexplore.ieee.org/document/8262002 (DOI: 10.1109/PIERS.2017.8262002)

[17] Belkin M. E., Alyoshin A., and Fofanov D., "Microwave Photonics Characterization and Application of Long-Wavelength VCSELs in Atypical Regimes," 2-nd International Conference on Photonics Research, InterPhotonics-2019, Antalya, Turkey.

[18] Q. Gu, W. Hofmann, M.-C. Amann, L. Chrostovski, "Optically Injection-Locked VCSEL for Bi-directional Optical Communication," 2008 Conference on Lasers and Electro-Optics (CLEO2008), p. 1-2.

[19] Q. Gu, W. Hofmann, M.-C. Amann, L. Chrostovski, "Optically Injection-Locked VCSEL of a Duplex Transmitter/Receiver," IEEE Photonics Technology Letters, vol. 20, no. 7, p. 463-465, 2008.

[20] Erwin K. Lau, Liang Jie Wong, Ming C. Wu, "Enhanced Modulation Characteristics of Optical Injection-Locked Lasers: A Tutorial," IEEE Journal of Selected Topics in Quantum Electronics, v. 15, no. 3, p. 618-633, 2009.

[21] L. Chrostowski, X. Zhao, and C. J. Chang-Hasnain, "Microwave Performance of Optically Injection-Locked VCSELs," IEEE Transactions on Microwave Theory and Techniques, v. 54, no. 2, p. 788-796, 2006

[22] Fang A.W., Koch B., Norberg, E., et al. Heterogeneous integration as a manufacturing platform for photonic integrated circuits. // IEEE Photonics Conference (IPC), 2013. – P. 87-88.

[23] Belkin, M.E., Iakovlev, V., Wafer fused long-wavelength VCSELs for analog photonics applications, Conference Digest - IEEE International Semiconductor Laser Conference ISLC2016, Kobe, Japan, 2016. art. no. 7765770. https://ieeexplore.ieee.org/document/7765770

[24] Handbook of Optical Components and Engineering. – Ed. by K. Chang, John Wiley & Sons, Hoboken, New Jersey, 2003, 1380 pp.

[25] R. A. Shafik, Md. S. Rahman, AHM R. Islam, "On the Extended Relationships Among EVM, BER and SNR as Performance Metrics," Proceeding of 4th International Conference on Electrical and Computer Engineering, ICECE 2006, 19-21 December 2006, Dhaka, Bangladesh, p. 408-411.

[26] ETSI, "Minimum requirements for Error Vector Magnitude," in TECHNICAL SPECIFICATION, LTE; Evolved Universal Terrestrial Radio Access (E-UTRA); User Equipment (UE) radio transmission and reception (3GPP TS 36.101 version 14.3.0 Release 14), ETSI, 2017-04, p. 215.

[27] M. E. Belkin, T. Bakhvalova, and A.C. Sigov, "Design Principles of 5G NR RoF-Based Fiber-Wireless Access Network"; In book "Recent Trends in Communication Networks", IntechOpen, London, UK, p. 121-145, 2020. DOI: 10.5772/intechopen.90074. Available online: https://www.intechopen.com/online-first/design-principles-of-5g-nr-rof-based-fiber-wireless-access-network

[28] 8802-11-2012 - ISO/IEC/IEEE International Standard - Information technology--Telecommunications and information exchange between systems Local and metropolitan area networks--Specific requirements Part 11: Wireless LAN Medium Access Control (MAC) and Physical Layer (PHY) Specifications.

Edited by Maurizio Casalino
and Jagannathan Thirumalai

This book provides a detailed overview of the most recent advances in the fascinating world of light-emitting diodes (LEDs), organic light-emitting diodes (OLEDs), and photodetectors (PDs). Chapters in Section 1 discuss the different types and designs of LEDs/OLEDs and their use in light output, color rendering, and more. Chapters in Section 2 examine innovative structures, emerging materials, and physical effects of PDs. This book is a useful resource for students and scientists working in the field of photonics and advanced technologies.

IntechOpen